

Physics Reach of the Global Neutrinoless Double-Beta Decay Program
and Systematic Uncertainties of the MAJORANA Project

Victor M. Gehman

A dissertation submitted in partial fulfillment of
the requirements for the degree of

Doctor of Philosophy

University of Washington

2007

Program Authorized to Offer Degree: Physics

University of Washington
Graduate School

This is to certify that I have examined this copy of a doctoral dissertation by

Victor M. Gehman

and have found that it is complete and satisfactory in all respects,
and that any and all revisions required by the final
examining committee have been made.

Chair of the Supervisory Committee:

Steven R. Elliott[†]

Reading Committee:

Steven R. Elliott

John F. Wilkerson

Peter J. Doe

Date: _____

[†]Affiliate Associate Professor, also at Los Alamos National Laboratory

In presenting this dissertation in partial fulfillment of the requirements for the doctoral degree at the University of Washington, I agree that the Library shall make its copies freely available for inspection. I further agree that extensive copying of this dissertation is allowable only for scholarly purposes, consistent with "fair use" as prescribed in the U.S. Copyright Law. Requests for copying or reproduction of this dissertation may be referred to Proquest Information and Learning, 300 North Zeeb Road, Ann Arbor, MI 48106-1346, 1-800-521-0600, to whom the author has granted "the right to reproduce and sell (a) copies of the manuscript in microform and/or (b) printed copies of the manuscript made from microform."

Signature_____

Date_____

University of Washington

Abstract

Physics Reach of the Global Neutrinoless Double-Beta Decay Program and
Systematic Uncertainties of the MAJORANA Project

Victor M. Gehman

Chair of the Supervisory Committee:

Professor Steven R. Elliott[†]

Physics

We present a global analysis technique for extracting information about the mechanism underlying neutrinoless double-beta decay ($0\nu\beta\beta$) by comparing the decay rate to the ground state across a number of isotopes. To this end, we also present work in support of the MAJORANA experiment, which will look for $0\nu\beta\beta$ in ^{76}Ge , aimed at pushing down systematic uncertainties to the level where the inclusion of ^{76}Ge from MAJORANA in this analysis is possible (statistical uncertainty in any $0\nu\beta\beta$ experiment will of course be set by the exposure and half-life, $T_{1/2}^{0\nu}$ for the isotope of interest). We proceed to enumerate likely sources of systematic uncertainty, paying particular attention to the efficacy and uncertainties for background and signal tagging via pulse shape and segmentation analysis, and background fluctuations in the MAJORANA experiment. We will also detail a proposed MAJORANA calibration program designed to reduce these systematic uncertainties.

We find that this global analysis for five different $0\nu\beta\beta$ models is possible if the total uncertainty budget is less than 30% for four isotopes. If these four experiments were to reach an uncertainty budget (statistical plus systematic) of $\approx 20\%$, then this analysis would require matrix element uncertainties of only $\approx 12\%$. If we restrict this analysis to only light Majorana ν exchange (thus testing the different matrix element calculation methods), the total uncertainty budget increases to $\approx 64\%$. This leaves $\approx 31\%$ for the matrix element uncertainty, assuming 20% from the experimental measurement. This global analysis technique is interesting because it is independent of the absolute scale of $T_{1/2}^{0\nu}$ for different isotopes. This means that whatever the actual level of lepton number violation in nature, we can extract information about the exchange mechanism underlying $0\nu\beta\beta$ from the pattern of the decay rates for a variety of isotopes. It is very important to note that this

[†]Affiliate Associate Professor, also at Los Alamos National Laboratory

analysis is based on a set of initial assumptions. Principally, we assume that future changes in the values of $0\nu\beta\beta$ nuclear matrix elements will shift values uniformly across all isotopes, and that one mechanism for $0\nu\beta\beta$ will be found to dominate over the others. These assumptions are stated more completely in the text.

We move from the total uncertainty budget goals from the global analysis to examine several of the more important systematic uncertainties in the MAJORANA experiment. We demonstrate fractional uncertainties in the survival probability for our pulse shape analysis cuts of 6.6% for single-site events and 3.8% for multi-site events. We also suggest some ways that this could be lowered somewhat in MAJORANA data. We also show that for smaller ^{76}Ge exposures, fluctuations in the background and signal levels can lead to systematic shifts in the reconstructed $0\nu\beta\beta$ rate of as much as 5%. These and the other systematic uncertainties expected in MAJORANA give a total systematic uncertainty budget of $\approx 11\%$.

TABLE OF CONTENTS

	Page
List of Figures	iv
List of Tables	xi
Glossary	xv
Chapter 1: The Interconnectedness of $\beta\beta$ Decay	1
1.1 $0\nu\beta\beta$ Mechanism and Matrix Element Tabulation	2
1.2 Summary of Previous Work	7
1.3 Multiple-Isotope Comparison	9
1.4 Model Separation Analysis	11
1.5 Comparison to to Other Neutrino Data	14
Chapter 2: MAJORANA Project Overview and State of the Experimental Field	21
2.1 MAJORANA Project Overview	21
2.2 MAJORANA R&D Detectors	25
2.3 Previous $0\nu\beta\beta$ Experiments	29
2.4 Other Current $\beta\beta$ Experiments	30
2.5 Germanium Array Experiments	33
2.6 Experimental Program Summary	34
Chapter 3: Survey of $0\nu\beta\beta$ Decay Matrix Elements and Associated Uncertainties	35
3.1 Matrix Element Calculations	35
3.2 Sources of Theoretical Uncertainties	39
3.3 Parameter Adjustment	44
3.4 Uncertainties and Their Relative Magnitudes	51
Chapter 4: Systematic Uncertainties and Tolerances in the MAJORANA Experiment	54
4.1 $0\nu\beta\beta$ Rate Expression	54
4.2 Avogadro's Number	56
4.3 Live Time	57
4.4 Detector Mass	59
4.5 Active Mass Fraction	59
4.6 Isotopic Composition	61

4.7	Number of Counts in the Region of Interest	61
4.8	Signal/Background Tagging Efficiencies	64
4.9	Systematic Uncertainty Summary	69
Chapter 5:	Calibration Plan for the MAJORANA Experiment	71
5.1	Criteria	71
5.2	Concerns	73
5.3	Calibration Reference Plan	76
5.4	Characterization and Commissioning Requirements	86
Chapter 6:	Pulse Shape and Segmentation Analysis and Associated Uncertainties	88
6.1	Parametric PSA Overview	88
6.2	Extensions to the Parametric Method	91
6.3	PSA Systematics	97
6.4	Segmentation Cuts and Their Independence from PSA	120
6.5	PSA in the SEGA Detector	124
6.6	Width of Detector Segmentation Boundaries in the CLOVER	126
6.7	Different Segmentation Schemes With SEGA	128
6.8	Pulse Shape and Segmentation Systematic Uncertainty Summary	129
Chapter 7:	Variations and Uncertainties in the Background Model	133
7.1	Parameter Space	135
7.2	Simulation Results	136
7.3	Conclusion From Background Model Simulations	143
Chapter 8:	Conclusions and Path Forward	150
8.1	Global $0\nu\beta\beta$ Analysis	150
8.2	Total Uncertainty Budgets	151
8.3	$0\nu\beta\beta$ and Neutrino Physics as a Whole	153
8.4	Systematics and Calibration	153
8.5	Plans for Future Work	155
Bibliography	157
Appendix A:	Dark Matter Sensitivity of the MAJORANA Experiment	167
A.1	Expected Nuclear Recoil Spectrum From the WIMP Halo	167
A.2	Explored Experiment Configurations	169
A.3	MAJORANA Sensitivity: Signal to Noise	171
A.4	MAJORANA Sensitivity: Annual Modulation	173
A.5	Comparison to Other Experiments	174
A.6	Conclusions	174

Appendix B: Preamp Evaluations for SEGA, MEGA and MAJORANA	178
B.1 Introduction	178
B.2 Preamp Requirements	178
B.3 Supplemental Performance Criteria	179
B.4 Crystal Characterization	179
B.5 Testing methods	183
B.6 PGT RG-11	186
B.7 Amptek A250	192
Appendix C: Scintillation Light Output Studies in Connection to Alternative Designs of the MOON $\beta\beta$ Decay Experiment	195
C.1 Introduction	195
C.2 Scintillation Light Output	196

LIST OF FIGURES

Figure Number	Page
1.1 A hadron-level Feynman diagram of $2\nu\beta\beta$ (left) and $0\nu\beta\beta$ (right) for the light neutrino exchange mechanism.	1
1.2 The two-nucleon or short-range contribution (left), and the long-range 1π (middle), and 2π (right) exchange mechanisms in the heavy-particle exchange framework.	5
1.3 $\Gamma^{0\nu}$ predictions for $M_{0\nu}$ uncertainties of 10% for all 7 $0\nu\beta\beta$ models and all 6 isotopes.	12
1.4 Effective Majorana mass (assuming light, Majorana ν exchange dominates $0\nu\beta\beta$) as a function of the lightest ν mass for $\theta_{12} = 33.9^\circ$, $\theta_{13} = 4.5^\circ$, $\delta m_{12}^2 = 8.0 \times 10^{-5} \text{ eV}^2$, and $\delta m_{23}^2 = 2.5 \times 10^{-3} \text{ eV}^2$	16
1.5 A consistency plot for the neutrino mass eigenvalues m_1 , m_2 and m_3 for various hypothetical measurements. This set of surface plots indicates how measured values of the sum of the neutrino masses, $\langle m_{\beta\beta} \rangle$, $\langle m_\beta \rangle$, and the oscillation results as detailed in Equation 1.12 can constrain the mass eigenvalues. This figure was produced by the author for Reference [48]	20
2.1 Cross-section of the MAJORANA experiment reference design. This figure is from [38].	23
2.2 Detector modules for the MAJORANA experiment reference design. Note the independently removable strings of detectors. This will facilitate keeping more of the MAJORANA array online when part of it will require maintenance, thus maximizing the total live time of the experiment. This figure is a combination of two from [38].	24
2.3 Segmentation schemes being discussed for n-type MAJORANA detectors. From left to right they are: 4×1 , 2×3 , 1×6 , and 6×6 , where $m \times n$ is the number of azimuthal by the number of axial segments. The first three fall into the “modest segmentation” category while the last is considered “highly segmented.” This figure is from [38].	25
2.4 A schematic sketch of the CLOVER detector. This figure is from [49].	26
2.5 A sketch of the SEGA detector[2] (right) showing the segmentation geometry, and the “wiggler” section of the Duke University FEL (left).	27
2.6 A diagram of the WIPP underground (right) showing its location on the North American continent (left). Both panels are from [35].	28
2.7 The first background spectrum taken with the three detectors currently running in the MEGA array. The most prominent feature is the 1460 keV peak from ^{40}K in the salt because the shield was incomplete.	28
2.8 The inside of the Heidelberg-Moscow experiment. Figure taken from [95].	30
3.1 The Woods-Saxon Potential for $A = 76$	37
3.2 The short range correlation function for QRPA calculations from Equation 3.4. The “Distance” on the x-axis is the distance between nucleons.	43

3.3	Running sum of the $2\nu\beta\beta$ and 1^+ component of the $0\nu\beta\beta$ matrix elements for ^{76}Ge and ^{100}Mo as a function of excitation energy, $E_{ex} = E_n - \frac{E_i + E_f}{2}$. Figure from Reference [125].	47
3.4	$0\nu\beta\beta$ matrix elements for ^{76}Ge and ^{100}Mo , both totaled and broken down by parity (with the 1^+ state shown separately). Figure from [125].	49
3.5	$M_{0\nu}$ as a function of g_{pp} . The dots on each plot denote the value of g_{pp} that best reproduces the $2\nu\beta\beta$ rate. Figure from Reference [125].	50
4.1	Percent uncertainty of the detectors active volume as a function of the uncertainty in the dead layers of a closed-end coaxial detector 62 mm diameter by 80 mm tall with a 8 mm diameter by 65 mm depth bore. We assumed an inner dead layer of 0.5 mm and an outer dead layer of 0.5 μm , typical of n-type HPGe detectors.	60
4.2	Percent change in the number of counts in the ROI versus uncertainty in the peak location. The lines on the figure mark the 0.36% uncertainty resulting from a 0.2 keV uncertainty in the peak location. This corresponds to the energy scale uncertainty achieved in the IGEX and Heidelberg/Moscow experiments.	62
4.3	Percent change in the number of counts in the ROI versus uncertainty in the peak width. The lines on the figure mark the uncertainty resulting from a 10% variation in the peak width. This corresponds to the resolution uncertainty achieved in IGEX.	63
4.4	The decay scheme of ^{68}Ge to its stable isotope of ^{68}Zn . Figure taken from [71].	67
5.1	Ratio of the number of counts in E3 to that in E1 for several γ -ray lines in the ^{232}Th spectrum for CLOVER Monte Carlo data (red) and experimental data (blue). See the text for a description of the geometry.	78
5.2	Layer by layer (left) and shell by shell (right) spectra for the Monte Carlo study of the MAJORANA reference design calibration system.	79
5.3	Layer by layer (left) and shell by shell (right) spectra for the Monte Carlo study of the MAJORANA reference design calibration system.	80
5.4	Conceptual drawing of the calibration containment and positioning system to be used in the MAJORANA experiment.	81
5.5	The decay schemes of ^{56}Co (left, from Reference [71]) and ^{232}Th (right, from Reference [38, Figure I.1]). Note that ^{56}Co decays directly to ^{56}Fe via β^+/EC , and has no gaseous elements in its decay chain.	82
5.6	A photograph of the prototype calibration system constructed at LANL. The electrically actuated Swagelok valve came from Albuquerque Valve and Fitting, the plastic tubing from Fisher Scientific, the stepper motor, gear and belt from W. M. Berg and the source garage was fabricated by the CENPA instrument shop at the University of Washington.	83
5.7	A close-up of the garage with its top removed to show the source belt parked inside (left panel) and stepper motor (right panel) sections of the calibration system.	84
5.8	A test spectrum taken with the calibration system prototype. The red trace is the spectrum with the source near the CZT detector, and the blue trace is the spectrum with the source removed.	85
5.9	Catalog photos taken from W.M. Berg's website of different belt materials. The left panel shows the current calibration belt design, and the right panel shows a slightly mechanically sturdier option.	86

6.1	Sample pulses representative of our background events (left) and signal events (right) captured by the LANL CLOVER detector. These two events were isolated using an energy cut in a ^{232}Th data set to pick out a 1588 keV γ (left) and a 1592 keV double-escape peak (right).	89
6.2	Distribution of pulse widths for γ events, DEP events tagged with a simple energy cut, and DEP events tagged with an additional coincidence.	90
6.3	PSA cut keys from ^{232}Th data, populated with 1592-keV DEP (top) and 1588-keV γ -ray (bottom) events. The easiest way to see the difference between these is to look at the contour plot on the top of both of the surface plots.	93
6.4	Single-crystal and PSA cut spectra for five and two-moment analysis.	95
6.5	PSA efficacies as a function of the number of double-escape peaks per detector in the training data set for 10 bins per PSA parameter axis.	99
6.6	PSA efficacies as a function of the number of double-escape peaks per detector in the training data set for 25 bins per PSA parameter axis.	99
6.7	PSA efficacies as a function of the number of double-escape peaks per detector in the training data set for 50 bins per PSA parameter axis.	100
6.8	PSA efficacies as a function of the number of double-escape peaks per detector in the training data set for 100 bins per PSA parameter axis.	100
6.9	PSA efficacies as a function of the fraction of the characterization data in common with the training data.	101
6.10	PSA efficacies for different event classes from ^{232}Th data in the CLOVER detector as a function of event rate read out by the DGF4C boards. The data for this figure were taken from Table 6.3.	104
6.11	Trapezoidal filtering of a preamplifier step with rise time, $L = 4\mu\text{s}$ and flat top time, $G = 1\mu\text{s}$. This figure was taken from Reference [10, pg. 20].	107
6.12	PSA efficacies (top) and FWHM resolution of three γ -ray lines for each CLOVER crystal (bottom) for the three data sets listed in Table 6.6. The top panel has two points in the ‘‘Post-Neutron’’ bin because we analyzed that data twice. The left-hand point in that bin was analyzed with a small training set for comparison to older ^{232}Th data, and the right-hand point was analyzed with a larger training set for comparison to more recent CLOVER data. See the text for more detail. The energy resolution data in each bin is ordered from detector 1 to detector 4.	111
6.13	Energy Dependence of pulse shape analysis cuts for γ and double-escape peak events in terms of the energy of the line being analyzed.	113
6.14	Fractions of population of events contributing to full-energy γ lines from different energy loss mechanisms as a function of energy. This was generated from Monte Carlo studies of a 6 cm \times 6 cm coaxial HPGe detector. This figure is from Reference [99, p. 430].	114
6.15	Range-Energy plot for electrons in two detector media: silicon and sodium iodide. This figure taken from Reference [99, p. 45].	116
6.16	Average PSA survival probabilities for DEP events and γ -ray events above 1 MeV for cuts trained on different DEP lines.	118
6.17	Average PSA survival probabilities for DEP events and γ -ray events above 1 MeV for data taken with the source in different positions around the CLOVER.	118

6.18	Combined pulse shape and segmentation cut survival probability (blue) and product of the individual cut survivals (red) from Monte Carlo data. The PSA cut was constructed by removing events with energy depositions separated by > 3 mm. This figure was taken from Reference [49].	121
6.19	Fraction of γ -ray events removed by the PSA cut versus the radial separation of energy depositions in Monte Carlo data. The red line shows the equivalence between 80% PSA rejection of γ -ray events and 3 mm radial separation resolution. This figure was taken from Reference [49].	122
6.20	Survival probabilities for PSA cuts on FEL data taken with the SEGA detector. The panels are: DEPs in the c-channel (top left), γ -rays in the c-channel (top right), DEPs in the s-channel (bottom left) and γ -rays in the s-channel. In each panel, the singles spectrum (either single central or segmentation channels) is in red, and the PSA cut is in blue.	125
6.21	A measurement of the border width of crystal 1 of the CLOVER. The average fraction of energy assigned to the left and middle positions is plotted as a function of source location. The curve is a fit to the data. See text for discussion of the collimated source. The absolute value of the position scale is arbitrary.	127
6.22	Survival probabilities for several segmentation configurations for DEP events (left) and γ events (right) acquired with the SEGA detector in the FEL. The schemes are enumerated by the label $m \times n$, where m is the number of ϕ segments and n is the number of z segments.	128
7.1	Shifts in peak location (left), continuum background level (middle) and $0\nu\beta\beta$ rate (right) as a function of the strength of the mystery peak at 2030 keV for KKDC-like exposures.	137
7.2	One of the 10000 spectra generated for a KKDC-like exposure (0.83 kmol \times y). The continuum background was 0.11 counts/keV/kg/y, the ^{214}Bi level was set to 0.3, $T_{1/2}^{0\nu}$ was 1.2×10^{25} y, and the mystery peak strength was 0.54 that of the $0\nu\beta\beta$ peak.	137
7.3	Histograms of the continuum level added to the simulation (black) and reconstructed by the fit (red) for each of the 10000 simulated KKDC-like experiments. The top row used a background level of 0.01 counts/keV/kg/y, and the bottom used 0.11 counts/keV/kg/y. The left column was generated for an experiment with no unidentified mystery peak. The middle column had one whose strength was 0.27 that of the $0\nu\beta\beta$ peak. The right column had a mystery peak strength of 0.54 (the level in the KKDC spectrum).	139
7.4	Histograms of the number of $0\nu\beta\beta$ events added to the simulation (black) and reconstructed by the fit (red) for each of the 10000 simulated KKDC-like experiments. The top row used a background level of 0.01 counts/keV/kg/y, and the bottom used 0.11 counts/keV/kg/y. The left column was generated for an experiment with no unidentified mystery peak. The middle column had one whose strength was 0.27 that of the $0\nu\beta\beta$ peak. The right column had a mystery peak strength of 0.54 (the level in the KKDC spectrum).	140
7.5	Shifts in peak location (left), continuum background level (middle) and $0\nu\beta\beta$ rate (right) as a function of the $0\nu\beta\beta$ half-life for M60-like exposure. The 10^{27} year half-life points for the $0\nu\beta\beta$ lifetime plot have been suppressed because they are off scale. Refer to the text for more details.	141

7.6	One of the 10000 spectra generated for M60-like exposures ($3.34 \text{ kmol} \times \text{y}$). The continuum background was 0.001 counts/keV/kg/y (or $4 \times$ the MAJORANA assay goal), the ^{214}Bi level was set to 0.06, $T_{1/2}^{0\nu}$ was $1.0 \times 10^{26} \text{y}$, and the mystery peak strength turned off.	141
7.7	Histograms of the continuum level added to the simulation (black) and reconstructed by the fit (red) for the 10000 simulated M60-like experiments. The top row used a continuum background level of 0.00025 counts/keV/kg/y, the middle used 0.001 counts/keV/kg/y, and the bottom used 0.01 counts/keV/kg/y. The left column was created with a $0\nu\beta\beta$ lifetime of 10^{25}y , the middle with 10^{26}y , and the right with 10^{27}y .	144
7.8	Histograms of the number of $0\nu\beta\beta$ events added to the simulation (black) and reconstructed by the fit (red) for the 10000 simulated M60-like experiments. The top row used a continuum background level of 0.00025 counts/keV/kg/y, the middle used 0.001 counts/keV/kg/y, and the bottom used 0.01 counts/keV/kg/y. The left column was created with a $0\nu\beta\beta$ lifetime of 10^{25}y , the middle with 10^{26}y , and the right with 10^{27}y	145
7.9	Shifts in peak location (left), continuum background level (middle) and $0\nu\beta\beta$ rate (right) as a function of the $0\nu\beta\beta$ half-life for M1000-like exposure.	146
7.10	One of the 10000 spectra generated for M1000-like exposures ($55.7 \text{ kmol} \times \text{y}$). The continuum background was 0.001 counts/keV/kg/y ($4 \times$ the MAJORANA assay goal), the ^{214}Bi level was set to 0.06, $T_{1/2}^{0\nu}$ was $1.0 \times 10^{27} \text{y}$, and the mystery peak strength turned off.	146
7.11	Histograms of the continuum level added to the simulation (black) and reconstructed by the fit (red) for the 10000 simulated M1000-like experiments. The top row used a continuum background level of 0.00025 counts/keV/kg/y, and the bottom used 0.001 counts/keV/kg/y. The left column was created with a $0\nu\beta\beta$ lifetime of 10^{25}y , the middle with 10^{26}y , and the right with 10^{27}y	147
7.12	Histograms of the number of $0\nu\beta\beta$ events added to the simulation (black) and reconstructed by the fit (red) for the 10000 simulated M1000-like experiments. The top row used a continuum background level of 0.00025 counts/keV/kg/y, and the bottom used 0.001 counts/keV/kg/y. The left column was created with a $0\nu\beta\beta$ lifetime of 10^{25}y , the middle with 10^{26}y , and the right with 10^{27}y	148
A.1	Summer (red) and Winter (blue) WIMP nuclear recoil spectra including quenching and finite nuclear radius for a WIMP mass $M_D = 100 \text{ GeV}$ and a cross section per nucleon of $3 \times 10^{-43} \text{ cm}^2$	169
A.2	Results from a neutron moderation study for the dark matter limit in the IGEX experiment. The four curves on the plot correspond to different thicknesses of the neutron moderator in the IGEX shield: (A) no neutron moderator, (B) 20 cm neutron moderator, (C) 40 cm neutron moderator and (D) 80 cm neutron moderator. Curves B and C were actually IGEX production data, and curves A and D were taken later to study neutron backgrounds. The similarity between curves C and D was taken as evidence that the IGEX experiment had eliminated slow neutron backgrounds in their dark matter production data.	170

A.3	(Top) Signal to noise sensitivities for the MAJORANA detector with a threshold of 1 keV (red), 4 keV (green) and 10 keV (blue). (Bottom) Signal to noise sensitivities for the MAJORANA detector with a background at threshold of 0.03 dru (red), 0.06 dru (green) and 0.09 dru (blue).	172
A.4	(Top) Annual modulation sensitivity for thresholds of 1 keV (red) and 4 keV (blue). (Bottom) Annual modulation sensitivity for asymptotic background levels of 0.005 dru (red) and 0.05 dru (blue).	175
A.5	Annual modulation sensitivity for active detector masses of 500 kg (red), 120 kg (green) and 20 kg (blue).	175
A.6	A variety of dark matter sensitivities from experiments around the world: CDMS 2004–2005 7 keV threshold (black line), SuperCDMS projected sensitivity at SNO-Lab(black dash), Cuoricino projected sensitivity (blue dash), XENON10 136 kg d (cyan line), XENON100 projected (green dash), DAMA 3σ result-58000 kg days exposure (red fill), MAJORANA signal to noise sensitivity for thresholds of 1 keV (red line) and 4 keV (magenta line), and MAJORANA annual modulation sensitivity for active masses of 120 kg (blue line) and 500 kg (green line).	176
B.1	Oscilloscope trace of a PGT RG-11 preamplifier. This trace shows the typical aspects of a preamp trace relevant to evaluation. The black trace is the input pulse, the green trace is the preamp response, and the purple trace is the Fourier transform of the preamp response. The bandwidth is measured at the point the Fourier transform transforms from $1/f$ to linear.	180
B.2	Leakage current schematic. The crystal is in series with both feedback components, which are in parallel with each other. In a steady-state situation, the effects of the feedback capacitor can be ignored.	182
B.3	Resolution and centroid curves for the PGT HPGe detector #930. The nominal depletion voltage determined by PGT is +3500 V, but the curves still relax a bit to +3900 V. We decide to run the detector at +3900 V instead of +3500 V.	184
B.4	Circuit diagram for the PGT RG-11B preamp. The bandwidth limiting capacitor, C8, is between stages 1 and 2 of the preamp, circled in red. The adjustment potentiometers R4 (FET current), R12 (FET voltage), R15 (Pole/Zero) and R19 (DC offset) are circled in blue.	186
B.5	The FET current and voltage had to be tuned to eliminate a sustained, fast ripple. If the bandwidth limiting capacitor were too small, the FET could not eliminate the ripple. In this case, the capacitor is 30 pF.	187
B.6	Long time scale behavior of the RG-11B. The time base is 100 μ s per division.	187
B.7	In the left panel, the black trace is the input pulse, green is the RG-11 response, and purple is the FFT of the preamp response. The right panel is a log-linear re-plotting of the FFT (the purple trace in the left panel). From the FFT, we see that the preamp bandwidth is about 150 MHz.	188
B.8	Calibration Spectrum.	190
B.9	RG-11 long time scale preamp response with fit and residuals.	191
B.10	Circuit diagram for the Amptek PC250 preamp motherboard. The compensation capacitor, C6 is circled in red. The adjustment potentiometer, R1 is circled in blue.	192

B.11	Left: best trace of the A250 preamp. The black trace is the input pulse, green is the A250 response, and purple is the FFT of the preamp response. Right: log-linear plot of the FFT from the left panel of this figure. From the graph, the preamp bandwidth is read to be ≈ 29 MHz.	193
B.12	A250 long time scale preamp response with fit and residuals.	194
C.1	A concept drawing (left) and prototype of the detector for the MOON neutrino experiment.	196
C.2	Scintillation counting setup diagram.	198

LIST OF TABLES

Table Number	Page	
1.1	Phase space factors and the assumed nuclear radius scaling factors. The units are $10^{-15}/\text{y}$	6
1.2	$0\nu\beta\beta$ nuclear matrix elements for several light ν exchange models. The matrix elements in this formalism are unit-less.	7
1.3	$0\nu\beta\beta$ nuclear matrix elements for heavy neutrino exchange (upper row) and R-parity violating SUSY models. The matrix elements in this formalism are unit-less.	7
1.4	Products of $0\nu\beta\beta$ nuclear matrix elements and the corresponding phase space factors for right-handed-current interaction models. The units for the η values are $10^{-8}/\text{y}$ and for the λ values are $10^{-12}/\text{y}$	8
1.5	Values of the decay rate in units of $10^{27}/\text{y}$ for the isotopes in our analysis for the chosen LNVP. The light neutrino mass $\langle m_{\beta\beta} \rangle$ was chosen to be 100 meV for the model labeled QRPA($\beta\beta$). The other LNVP's were chosen such that the resultant decay rates for ^{76}Ge were the same. The form of the LNVP was chosen to be unitless.	13
1.6	Limits of required total uncertainties corresponding to each theoretical model and the number of measurements as isotopes are added to the analysis for 90% and 68% confidence. Only the final pair of rows includes all 7 models. The others exclude the RHC models because those models do not have a $M_{0\nu}$ value for ^{116}Cd . The precision of the numbers in this table are approximately $\pm 1\text{-}2\%$	14
2.1	Best reported limits on $0\nu\beta\beta$ half-lives. The mass limits and ranges are those deduced by the authors and their choices of matrix elements cited in the experimental papers. All limits are quoted at the 90% confidence level, except the Klapdor-Kleingrothaus [96] result, where the bounds are for the 99.7% confidence level. Backgrounds are included if given in the original publication. This table is from Reference [38].	29
3.1	This table's text was reproduced from Reference [135]. Original caption: "Pros (+) and cons (-) of the two discussed recipes to fit the parameter g_{pp} . For more explanation on various points see the text."	45
3.2	A sample of calculated matrix elements calculated in QRPA, RQRPA with accompanying uncertainties. This table is partially reproduced from Reference [125, Erratum]. Note that in Reference [125, Erratum], the uncertainty for each matrix element is expressed as a variance (σ^2), whereas here we use standard deviation (σ).	52
3.3	A summary of the systematic uncertainties enumerated mostly in Section 3.2 and an estimate of the typical fractional uncertainty (where such an estimate is meaningful).	53
4.1	μ flux, resulting veto rate and dead time fraction for different overburdens	57

4.2	Survival probabilities of different processes over a range of energy. The quoted uncertainty in the segmentation cut comes from the uncertainty on the fit parameters from the reconstructed spectra. For the pulse shape and combined cuts, the uncertainty also comes from the list of systematic uncertainties detailed in Section 6.3.	68
4.3	Summary table of systematic uncertainties for the MAJORANA $0\nu\beta\beta$ experiment. . .	70
6.1	Survival probabilities of different processes for both the two and five-moment pulse shape cuts. The survival probabilities for both cuts were measured with the same training and characterization data sets, and examined the same three processes: 1588 keV γ -ray, 1592 keV DEP and 2.0 – 2.08 MeV continuum events. Note that the uncertainties quoted in this table are just those from the fit. We also include goodness of fit information for reconstruction of the spectra in the γ -ray/DEP energy region. .	95
6.2	Difference in survival probabilities for PSA cuts (trained on both coincidence-tagged and non-tagged DEPs) between training and characterization data overlaps of 0% and 100% for different event classes. Each survival probability is reported in the form: percent change from 0% to 100% / average fit uncertainty / ratio of percent change to fit uncertainty. As with previous PSA survivals the continuum survival is calculated between 2.0 and 2.08 MeV	102
6.3	PSA Efficacies at different event rates for the CLOVER detector read out via the DGF4C boards. The uncertainties in the survival probabilities for this table are just the error from the fit. Uncertainties in the event rate are the standard deviation of the event rate reported by the DAQ software from run to run. The continuum in the last column, was integrated from 2.0 – 2.08 MeV.	103
6.4	PSA performance for the six part analysis. The results in this table are for an analysis of data set F from training on data sets A through E. The uncertainties listed with the survival probabilities are from the fit. The row labeled “Mean and SD” is the mean and standard deviation of the previous five rows. The last row (labeled “ $\sigma_{SD} - \bar{\sigma}_{Fit}$ ”) is the difference between the standard deviation and the average fit uncertainty. See the text for more detail.	105
6.5	PSA cut survival probabilities comparing data taken under different triggering conditions. For comparison, we also include the survival probability for both of the 39 Hz event rate data sets in Table 6.3. The survival probability uncertainties are once again those from the fit parameters. The last two lines of the table (labeled “Difference”) are the differences between the survival probabilities for each event class in the 0.075 μ s data set and each of the 0.2 μ s data sets. See the text for more detail.	108
6.6	PSA Efficacies for data taken: early in the LANL research program involving the CLOVER, shortly before the annealing process (for both small and large PSA training sets), and immediately after the annealing process.	110
6.7	Variation in PSA survival probabilities for DEP events and γ -ray events above 1 MeV. σ_{SD} is the standard deviation of the survival probability and $\bar{\sigma}_{Fit}$ is the average fit uncertainty for the lines in question. The last row is the difference between the two.	115
6.8	Average PSA survival probabilities for events in all DEP and γ -ray lines above 1 MeV for cuts trained on different DEP lines. σ_{SD} is the standard deviation of the five survival probabilities in this table and $\bar{\sigma}_{Fit}$ is the average fit uncertainty for each cut. The last row is the difference between the two.	117

6.9	Average PSA survival probabilities for DEP events and γ -ray events above 1 MeV for runs with the source in different positions around the CLOVER. σ_{SD} is the standard deviation of the survival probability and $\bar{\sigma}_{Fit}$ is the average fit uncertainty for each data set. The last row is the difference between the two.	119
6.10	Survival probabilities (percentages) of different processes over a range of energy. The first quoted uncertainty comes from Poisson counting statistics, and the second comes from the systematic uncertainty associated with changing the position of the source around the detector. This table was reproduced from Reference [49].	120
6.11	Pulse shape analysis survival probabilities for different event classes for the analysis in Reference [49] and the more recent work in this dissertation. Statistical and systematic uncertainties from Reference [49] have been combined in quadrature. Otherwise, PSA performance from Reference [49] were taken directly from Table 6.10. PSA performance values from this dissertation were taken from Table 4.2.	123
6.12	Survival probabilities for PSA cuts on FEL data taken with the SEGA detector. Results are given for PSA on the internal and external contacts of the detector. The uncertainties are those from the fit parameters.	124
6.13	Survival probabilities for a variety of segmentation cuts in the SEGA detector from the FEL data runs. The uncertainties here result from the fit to the appropriate spectrum. The segmentation schemes are enumerated using the same convention as in Figure 6.22.	129
6.14	Summary table of systematic effects impacting parametric pulse shape analysis. We include the name of each effect, a brief description and the change in survival probability beyond that from the fit parameters for γ -ray and DEP events. The effects are quoted for PSA cuts trained on non-coincidence-tagged DEPs.	132
7.1	Full-energy γ peaks from ^{214}Bi included in this simulation study.	133
7.2	Parameter space explored for the KKDC-like exposure. The two parameters varied for this configuration were: the background level, and strength of the mystery peak.	135
7.3	Parameter space explored for the M60-like exposure. The two parameters varied for this configuration were: the background level, and $0\nu\beta\beta$ lifetime.	136
7.4	Parameter space explored for the M1000-like exposure. The two parameters varied for this configuration were: the background level, and $0\nu\beta\beta$ lifetime.	138
7.5	Number of counts in the continuum for different continuum levels.	142
A.1	Experimental parameters used in the calculation of MAJORANA dark matter sensitivity. Text in blue denotes the configuration of the IGEX experiment.	171
B.1	Sources for resolution measurement. This table does not show all decay peaks, just the largest ones used in the preamp resolution determination. Data comes from the Lawrence Berkeley National Laboratory.	185
B.2	RG-11 performance results.	189
B.3	A250 performance results.	194
C.1	Scintillation output results for ^{137}Cs , $E_\gamma = 660$ keV.	199
C.2	Scintillation output results for ^{207}Bi , $E_\gamma = 570$ keV. Note that no fit was possible for the standard candles with this spectral line.	199

C.3	Scintillation output results for ^{207}Bi , $E_\gamma = 1060$ keV.	200
C.4	Scintillation output results for ^{241}Am , $E_\gamma = 59.6$ keV.	200

GLOSSARY

2DF: “**T**wo-**d**egree-**F**ield Galaxy Redshift Survey.” A large-scale structure survey conducted by the Anglo-Australian Observatory.

ACBAR: “**A**rcminute **C**osmology **B**olometer **A**rray **R**eceiver.” A cosmic microwave background telescope that was deployed at the Viper telescope in Antarctica. It also served as a test run for the detectors that will fly on the Planck mission.

AGATA: “**A**dvanced **G**amma **T**racking **A**rray.” A γ -ray tracking array employing a large array of segmented HPGe detectors for nuclear spectroscopy being developed in Europe.

CALIBRATION TRACK: The electroformed copper tube in which we plan to house the calibration sources used to do the *in situ* calibration of the MAJORANA detectors.

CBI: “**C**osmic **B**ackground **I**mager.” A 13-element interferometer at Llano de Chajnantor Observatory in the Chilean Andes used to study the cosmic microwave background radiation.

CHARGE PULSE: The direct output of the integrating preamplifier, in our case, of a germanium detector.

CLOVER: A detector array commercially available from Canberra consisting of four n-type HPGe detectors with either 2 or 4-fold azimuthal segmentation packaged in a single cryostat.

COBRA: “**C**admium-Telluride **0**-Neutrino Double-**B**eta **R**esearch **A**pparatus.” A $0\nu\beta\beta$ search experiment employing ^{116}Cd currently in the R&D phase.

CUORE: “**C**ryogenic **U**nderground **O**bservatory for **R**are **E**vents.” A $0\nu\beta\beta$ search experiment using ^{130}Te . The prototype for CUORE (called CUORICINO, or “little CUORE”) is currently taking data at the Gran Sasso underground laboratory.

CURRENT PULSE: The time derivative of the charge pulse. The current pulse is proportional to the energy deposition in a detector as a function of time, convolved with the response of the germanium crystal.

DEP: “Double-Escape Peak.” A line that occurs in a detector when a γ -ray has enough energy to undergo $e^+ e^-$ conversion. Both charged leptons lose energy in the detector. When the e^+ stops, it annihilates with an e^- in the detector, and the resultant 511 keV γ -rays escape the detector (“Double-Escape,” get it?). This leaves a line at the energy of the incoming γ -ray minus twice the rest mass of the electron.

DGF: “Digital Gamma Finder.” A product family of digital data acquisition cards from XIA, LLC. They are designed to run under several hardware architectures including CAMAC and compact PCI crates. Most of the data taken with the CLOVER at LANL and SEGA at TUNL, were taken using the DGF-4C (“4C” for four-channel, CAMAC) digitizer cards.

DIRAC PARTICLE: A Fermion (spin $\frac{1}{2}$ particle) that is distinct from its antiparticle.

DUSEL: “Deep Underground Science and Engineering Laboratory.” A proposed underground laboratory to be built in the US, funded by the National Science Foundation.

EVENT CLASSIFIER: A family of machine learning algorithms used to quickly and reproducibly separate events into different subgroups.

EXO: “Enriched Xenon Observatory.” A $\beta\beta$ search experiment currently under development employing ^{136}Xe . The EXO collaboration will deploy a 200 kg prototype at WIPP in the fall of 2007.

EXPONENTIAL LAW OF RADIOACTIVE DECAY: A mathematical formula expressing the decay probability of an unstable nucleus as an exponential function of time.

GAMMASPHERE: A generation γ -ray tracking spectrometer used to study rare and exotic nuclear physics.

GERDA: “GERmanium Detector Array.” A search for $0\nu\beta\beta$ in ^{76}Ge being developed for deployment at the Gran Sasso underground laboratory.

GRETA: “**G**amma **R**ay **E**nergy **T**racking **A**rray.” A γ -ray tracking array employing a large array of segmented HPGe detectors for nuclear spectroscopy being developed in the US.

HEIDELBERG-MOSCOW EXPERIMENT: A ^{76}Ge $\beta\beta$ decay experiment performed at the Gran Sasso underground laboratory.

ICS: “**I**ndividual **C**rystal **S**pectrum.” A spectrum consisting of the energy deposited in individual detectors in an array summed together.

IGEX: “**I**nternational **G**ermanium **E**Xperiment.” A ^{76}Ge $\beta\beta$ decay experiment performed at the Canfranc underground laboratory.

INDEPENDENT PARTICLE MODEL: Another name for the Shell Model.

LEPTON NUMBER: A quantum number assigned to fundamental particles equal to +1 for leptons and -1 for anti-leptons, *i.e.* e^- particles have lepton number +1 and e^+ have lepton number -1 .

LEPTOQUARK: Hypothetical color-triplet bosons that carry both lepton and baryon numbers.

LNVP: “**L**epton **N**umber **V**iolating **P**arameter.” The Lepton Number Violating Parameter quantifies the degree to which Lepton Number Symmetry is violated for a particular process.

LSS: “**L**arge-**S**cale **S**tructure.” Refers to measurements of mass distributions in the Universe on cosmological length scales.

MAJORANA PARTICLE: A Fermion (spin $\frac{1}{2}$ particle) that is identical to its own antiparticle.

MAVAN: **MA**ss-**VA**rying Neutrino. The theory that neutrinos can have an effective mass that comes from the density of the medium through which they are traveling by coupling to a scalar field that preferentially collects around normal matter. This is different from the MSW effect where the coupling is to the electrons in matter through charged current interaction in the forward scattering amplitude.

MEGA: “**M**ulti-**E**lement **G**amma **A**ssay.” A low-background array of p-type HPGe detectors under construction at WIPP as a collaboration between Pacific Northwest National Laboratory, Los Alamos National Laboratory, the University of Washington and the University of Tennessee.

MOON: “**M**olybdenum **O**bservatory **O**f **N**eutrinos.” A $0\nu\beta\beta$ search experiment currently under development employing ^{100}Mo .

MSE: “**M**ulti-**S**ite **E**vent.” An energy deposition in a detector with a spatial extent greater than the detector’s position resolution, so that it appears that a particle may have interacted multiple times in the active volume.

MWE: “**M**eters **W**ater **E**quivalent.” A common normalization for overburden of underground laboratories equal to the depth of water overhead that would provide an equivalent amount of shielding.

MX: This is a name used by the MAJORANA collaboration to denote a configuration of the experiment consisting of X kg active mass of ^{76}Ge

NCT: “**N**umber of **C**uts **T**hreshold” The parameter that sets the number of cuts that an event must pass in the MAJORANA parametric pulse shape analysis when it has been extended to greater than two or three moments.

NEMO: “**N**eutrino **E**ttore **M**ajorana **O**bservatory.” A $\beta\beta$ search experiment at the Fréjus underground laboratory using thin foils of $\beta\beta$ isotope and a large particle tracking array.

NEUTRINO OSCILLATION: A quantum mechanical phenomenon by which a neutrino created with a specific lepton flavor can later be measured with a different lepton flavor.

NORMALIZED MOMENT: One of the moments used in the MAJORANA parametric pulse shape analysis, defined in Equation 6.1. It is generalized to higher moments in Equation 6.2.

PLANCK: A satellite mission that will measure fluctuations in the cosmic microwave background to even greater precision than WMAP already has.

PSA KEY: An object, typically a ROOT histogram, used to define the signal and background regions for the MAJORANA parametric pulse shape analysis.

PSA SENSITIVITY PARAMETER: A number from -1 to 1 that is used to fine tune the relative size of the signal and background regions in the MAJORANA parametric pulse shape analysis.

PSEUDOSCALAR CURRENT: A Current that transforms like a scalar except that it picks up a negative sign under transformations like parity.

PULSE ASYMMETRY: The difference in areas between the first and second halves of a current pulse, normalized by the area of the current pulse. Also referred to as the “Front-Back Asymmetry.”

PULSE WIDTH: The time it takes the charge pulse of a germanium detector to rise from 10% above baseline to 90% of its maximum level.

QRPA: “**Q**uasi**p**article **R**andom **P**hase **A**pproximation.” A method for calculating nuclear transition matrix elements that treats the collective states of nucleons rather than those of individual particles. It includes correlations between all types of quasiparticles in the nuclear system (*i.e.* particle–hole, particle–particle, and hole–hole).

RPA: “**R**andom **P**hase **A**pproximation.” A method for calculating nuclear transition matrix elements that treats the collective states of nucleons rather than those of individual particles. It includes only correlations between particles and holes in the nuclear system.

ROI: “**R**egion of **I**nterest.” The energy range in a spectrum subject to a specific analysis.

R-PARITY: A quantum number introduced in supersymmetric theories. $\mathbb{R} = -1^{2S+3B+L}$, where S is the spin of a particle, B is its baryon number and L is its lepton number. \mathbb{R} is 1 for standard model particles and -1 for supersymmetric ones.

SDSS: “**S**loan **D**igital **S**ky **S**urvey.” A large-scale structure survey conducted at the Apache Point Observatory.

SEGA: “**S**egmented, **E**nriched **G**ermanium **A**ssembly.” A detector made specially for the MAJORANA collaboration by ORTEC. It is an n-type detector with 2-fold axial and 6-fold azimuthal segmentation, fabricated from germanium enriched to 86% in ^{76}Ge .

SHELL MODEL: A method for calculating nuclear transition matrix elements that proceeds analogously to the calculation of states for electrons around atoms.

SNOLAB: An expansion of the underground laboratory originally constructed for the Sudbury Neutrino Observatory funded by the Canadian government.

SSE: “**S**ingle-**S**ite **E**vent.” An energy deposition in a detector with a spatial extent less than the detector’s position resolution, so that it appears to have interacted only once in the active volume.

SUPERSYMMETRY: A symmetry that interchanges bosons (integer spin particles) and fermions (spin $\frac{1}{2}$ particle), meaning that every fundamental fermion would have a boson super-partner, and *vice versa*. Often abbreviated as “SUSY.”

TENSOR CURRENT: A current that transforms like a tensor, of course!

TIGRESS: “**T**RIUMF-**I**SAC **G**amma **R**ay **E**scape **S**uppressed **S**pectrometer.” A γ -ray tracking array being developed at TRIUMF in Vancouver, British Columbia, Canada.

WIPP: “**W**aste **I**solation **P**ilot **P**lant.” A Department of Energy facility approximately 30 miles southeast of Carlsbad, NM designed for the permanent underground disposal of transuranic waste. There are also underground laboratories there connected with the MAJORANA and EXO experiments.

WIPP-N: A roughly 500 g low-background, n-type detector underground at WIPP.

WMAP: “**W**ilkinson **M**icrowave **A**nisotropy **P**robe.” A satellite that measured fluctuations in the cosmic microwave background to previously unprecedented precision.

XIA: “**X**-**R**ay **I**nstrument **A**ssociates.” A company in Hayward, CA that produces the Digital Gamma Finder data acquisition cards, primarily for use with germanium detectors.

ACKNOWLEDGMENTS

While I've only been enrolled at the University of Washington since 2001, I took my first set steps down this road many years before that. My parents, Victor and Sharon, encouraged my interest in science from a very young age. Through them, and their tireless support, I have maintained a passion for science and critical thinking, particularly in physics for as long as I can remember. I would not have been able to complete this Ph.D. without the guidance and hard work of my advisor, Steve Elliott, who first interested me in the MAJORANA experiment and brought me to Los Alamos. Many thanks must also go to the other two members of my reading committee—John Wilkerson and Peter Doe, to whom I am grateful for their careful reading and constructive feedback.

I have had so many guides and friends who have helped me along this road that I cannot mention them all, but I will now try to acknowledge a few of them. First, my siblings—Tom, Matt, James and Molly, my grandparents, and the rest of my family have been the first to cheer at my accomplishments and console me in my setbacks. The entire MAJORANA collaboration has been of immeasurable help, but I would particularly like to thank Craig Aalseth, who first introduced me to pulse shape analysis and Dongming Mei who spent so much time learning about it with me. I would like to thank Reyco Henning and Jason Detwiler for their help with the MaGe simulation framework and numerous other software challenges. Here at LANL, the rest of the Weak Interactions Team—Andrew Hime, Vince Guiseppe, Keith Reilage and Laura Stonehill, have supported me through the day-to-day push on the scientific progress I've made to date.

Last, all of the dear friends I've made and learned mentors with whom I've worked have been with me to share the good times and bad. Specifically, I'd like to thank: Aaron, Al, Jen, Mark, Nancy, Bruce, Mark, Henning, Royce, Beate, Kareem, Helene, Dave, Yeechi, Franklyn, Jeff, Paul, Laura, Minesh, Claire, Karen, Amy, Antonya, Mark (I seem to know a lot of people named Mark...), Mia, Chris, Damian, Rob, Mike and Alexis. I'd especially like to thank Cathy Plesko. Without her endless patience, unfailing kindness and tireless support, this would have been impossible. Thank you again, one and all, who have walked this road with me, and continue to do so. You have been my companions on this journey. I owe you all a debt of gratitude, and I hope I have given back even a fraction of the kindness, love and support I have received from all of you.

DEDICATION

“I’m very glad you asked me that, Mrs Rawlinson. The term ‘holistic’ refers to my conviction that what we are concerned with here is the fundamental interconnectedness of all things. I do not concern myself with such petty things as fingerprint powder, telltale pieces of pocket fluff and inane footprints. I see the solution to each problem as being detectable in the pattern and web of the whole. The connections between causes and effects are often much more subtle and complex than we with our rough and ready understanding of the physical world might naturally suppose, Mrs Rawlinson.

“Let me give you an example. If you go to an acupuncturist with toothache he sticks a needle instead into your thigh. Do you know why he does that, Mrs Rawlinson?”

“No, neither do I, Mrs Rawlinson, but we intend to find out. A pleasure talking to you, Mrs Rawlinson. Goodbye.”

—Douglas Adams, “Dirk Gently’s Holistic Detective Agency”

Chapter 1

THE INTERCONNECTEDNESS OF $\beta\beta$ DECAY

The study of neutrinos in general, and that of double-beta decay ($\beta\beta$) in particular, is among the most exciting fields on the cutting edge of fundamental physics research as it will guide our development of the Standard Model of particle physics. In particular, the case for studying $\beta\beta$ is well-motivated in numerous review articles in the literature [50, 48, 87, 16, 47]. Two-neutrino double-beta decay ($2\nu\beta\beta$) (e.g. ${}^{76}\text{Ge} \rightarrow {}^{76}\text{Se} + 2e^- + 2\bar{\nu}$) is a second-order weak decay process, and is the most rare nuclear decay allowed in the Standard Model. $2\nu\beta\beta$ is observable in even-even nuclei where beta decay is forbidden, and has been observed in ten nuclei. Zero-neutrino double-beta decay ($0\nu\beta\beta$) violates lepton number conservation and is therefore forbidden in the Standard Model. $0\nu\beta\beta$ differs from $2\nu\beta\beta$ by the absence of antineutrinos in the final state (e.g. ${}^{76}\text{Ge} \rightarrow {}^{76}\text{Se} + 2e^-$). Figure 1.1 shows the Feynman diagrams for $2\nu\beta\beta$ and $0\nu\beta\beta$.

The “Standard Model of $0\nu\beta\beta$ ” is the exchange of light Majorana neutrinos (that is, massive neutrinos that are indistinguishable from their own antiparticle). $0\nu\beta\beta$ is the only technique currently under investigation capable of testing the Majorana nature of the neutrino. Furthermore, if the neutrino is a Majorana particle, $0\nu\beta\beta$ is one of the most sensitive probes for the absolute scale of the neutrino mass currently known (though modern β -decay endpoint measurements, and

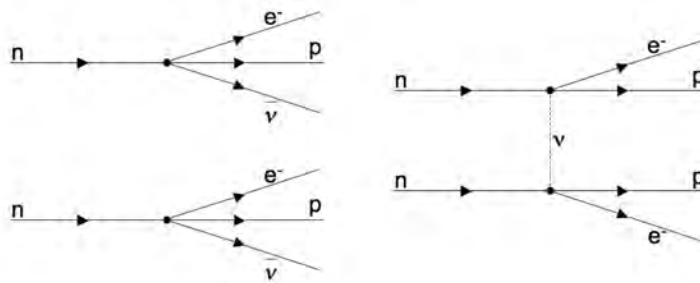


Figure 1.1: A hadron-level Feynman diagram of $2\nu\beta\beta$ (left) and $0\nu\beta\beta$ (right) for the light neutrino exchange mechanism.

model-dependent neutrino mass limits from cosmological observations have similar sensitivities and will be discussed further in Section 1.5.2). While the observation of $0\nu\beta\beta$ would imply the existence of massive Majorana neutrinos [129], several other possibilities exist for the underlying physics mediating the decay.

This dissertation will have a theme of “interconnectedness” running throughout. By “interconnectedness,” we simply mean that results in one sub-area of neutrino physics affects what we expect to see in other sub-areas. This means that by comparing results across a broad range of experimental programs and theoretical predictions, we can extract more physics than we can by examining any individual part of the global analysis. An example of this, already used to great benefit in the neutrino oscillations field, is the joint SNO/KamLAND analysis. The constraints on the mixing angle and mass difference squared from the combined analysis are much more stringent than those from the individual analyses.

To that end, we will begin with a discussion of the use of a suite of experimental results of $0\nu\beta\beta$ ground-state transitions in different nuclei to distinguish exchange mechanism models or transition matrix-element models (for another discussion of this analysis, see Reference [73]). This approach is of immediate interest because of the significant number of next-generation experiments that are proposed or under construction that might provide these data. In particular, motivating the required number of experimental results from different nuclei is critical to the overall $\beta\beta$ program. In Chapter 2, we move on to a discussion of the MAJORANA project [38] (in support of which, most of this work was performed) and several of the other past, current and proposed $0\nu\beta\beta$ searches. Chapter 3 presents an overview of the problem of calculating the $0\nu\beta\beta$ nuclear matrix elements. We then focus in on the MAJORANA experiment, discussing its systematic uncertainties in Chapter 4, and their impact on the total uncertainty budget for the experiment. We discuss our efforts to characterize and mitigate these systematic uncertainties in Chapter 5. Chapter 6 reviews the current state of the pulse shape analysis (PSA) and segmentation analysis techniques for the MAJORANA Project, details the recent research in characterizing the efficacy of these cuts, and proposes several avenues for future research. Chapter 7 discusses shifts in quantities of interest due to fluctuations and uncertainties in the background model of MAJORANA for several possible experimental configurations. Last we finish with some concluding remarks and suggestions for future work in Chapter 8.

1.1 $0\nu\beta\beta$ Mechanism and Matrix Element Tabulation

The $0\nu\beta\beta$ rate can be written:

$$\Gamma^{0\nu} = G^{0\nu} |M_{0\nu}\eta|^2, \quad (1.1)$$

where $\Gamma^{0\nu}$ is the $0\nu\beta\beta$ decay rate, $G^{0\nu}$ is the kinematic phase space factor, $M_{0\nu}$ is the matrix element corresponding to the $0\nu\beta\beta$ transition, and η is a lepton number violating parameter (LNVP). $G^{0\nu}$ contains the kinematic information about the final state particles, and is exactly calculable to the precision of the input parameters (though use of different nuclear radius values in the scaling factors of $G^{0\nu}$ and $M_{0\nu}$ have previously introduced some confusion [41]). $M_{0\nu}$ contains all of the nuclear structure information, and η contains all of the information about lepton number violation.

The LNVP takes on different forms for different $0\nu\beta\beta$ mechanisms. In addition, $M_{0\nu}$ may also depend on the mechanism. Here we consider: light Majorana neutrino exchange, heavy Majorana neutrino exchange, right-handed currents (RHC), and exchange mechanisms that arise from R-Parity violating supersymmetry (RPV SUSY) models. The mechanisms under consideration in this exercise were chosen because they are some of the most qualitatively simple extensions to the Standard Model that include lepton number violation. The individual references chosen to provide matrix elements were picked because they represent the most recent work that included calculations of $M_{0\nu}$ for many isotopes within those mechanisms. The heavy-particle models represent a large class of theories that involve the exchange of high-mass (>1 TeV) particles. For example, leptoquarks [83] have very similar $M_{0\nu}$ to RPV SUSY [82]. Left-right symmetric models can lead to right-handed current models [45] or heavy neutrino exchange models [81]. Scalar bilinears [98] might also mediate the decay but explicit matrix elements have not been calculated yet. For SUSY and left-right symmetric models, effective field theory [121] has been used to determine the form of the effective hadronic operators from the symmetries of the $0\nu\beta\beta$ -decay operators in a given theory. This last paper makes clear the close connection between all the heavy-particle exchange models.

1.1.1 $0\nu\beta\beta$ Mechanisms and the Lepton Number Violating Parameter

In this section we define the LNVP for each of the models.

Light Neutrino Exchange

If the neutrino is a Majorana particle, it can be exchanged between two neutrons and mediate $0\nu\beta\beta$.

If the neutrino is light, the LNVP $\eta_{L\nu}$ has the form:

$$\eta_{L\nu} = \sum_k U_{ek}^2 \xi_k \frac{m_k}{m_e}, \quad (1.2)$$

where the index k spans the light neutrino states, U_{ek} is the (e, k) element of the neutrino mixing matrix, ξ_k is a phase, m_k is a neutrino mass eigenstates eigenvalue, and m_e is the electron mass.

Detailed discussions of light neutrino exchange $0\nu\beta\beta$ and its associated matrix element can be found in References [126, 33, 31, 125, 135, 30, 140]. Further description of the interplay between the LNVP and the neutrino mixing parameters is in Reference [48] and Section 1.5 of this dissertation.

Heavy Neutrino Exchange

Heavy Majorana neutrinos can also contribute to $0\nu\beta\beta$. The LNVP ($\eta_{H\nu}$) however, has a different form:

$$\eta_{H\nu} = \sum_k U_{ek}^2 \xi_k \frac{m_p}{m_k}. \quad (1.3)$$

Here, k runs over the heavy neutrino states, m_k is the mass eigenvalue of the heavy neutrino ($m_k \gg 1\text{GeV}$), and m_p is the mass of the proton. It is important to note that for light neutrino exchange, $\eta_{L\nu}$ is proportional to the light neutrino mass. In contrast, $\eta_{H\nu}$ is inversely proportional to the heavy neutrino mass. The principle difference is that for heavy neutrino exchange, the Majorana neutrino branch of the Feynman diagram of the right panel of Figure 1.1 collapses down to a point, leaving a diagram like the left panel of figure 1.2. Heavy neutrino exchange is discussed at greater length in Reference [140] and references therein.

Right-Handed Currents

In left-right symmetric models [45], right-handed currents can result in interactions leading to $0\nu\beta\beta$. Two parameters are used to describe this phenomenon. η denotes the magnitude of a possible right-handed leptonic current coupling to a left-handed hadronic current in the weak interaction Hamiltonian. λ denotes the magnitude of coupling between a right-handed leptonic and a right-handed hadronic current. For more information about λ and η see Reference [111].

R Parity Violating Supersymmetry

Many supersymmetric (SUSY) R-parity violating extensions to the Standard Model have lepton-number violating interactions between quarks and leptons that can also contribute to $0\nu\beta\beta$ [67, 144, 79, 80, 109, 110, 11, 118]. For the two-nucleon (2N) contribution to $0\nu\beta\beta$ from SUSY, as with $0\nu\beta\beta$ mediated by the exchange of heavy neutrinos, the particles exchanged have extremely high masses and the physics takes place at short distances. Hence, the diagram has a hadron-lepton vertex as shown in the left panel of Figure 1.2. This means that the 2N contribution to $0\nu\beta\beta$ tends to be suppressed because only nuclei very near one another can participate in this reaction. Alternatively, the heavy particle can convert into a virtual π , where the comparatively low-mass π meson can

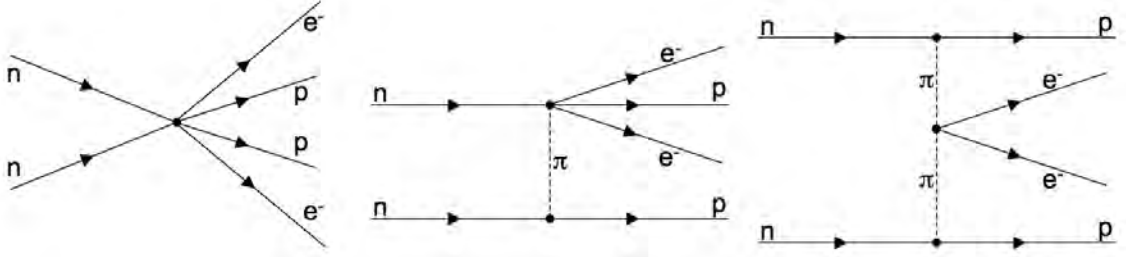


Figure 1.2: The two-nucleon or short-range contribution (left), and the long-range 1π (middle), and 2π (right) exchange mechanisms in the heavy-particle exchange framework.

mediate the $0\nu\beta\beta$ transition between more distant nucleons. This leads to the pion modes tending to dominate over the 2N modes in most models. If one of the initial quarks gets placed into the virtual π , we refer to it as the 1π mode. Similarly, if both are placed into a virtual π , we have the 2π mode. These two modes are discussed in detail in References [67, 144]. Generally, many of the heavy particle exchange models have similar $M_{0\nu}$ with similar short-range and long range components. The 2N exchange and its relative suppression are discussed in References [67, 144, 79, 121]. Figure 1.2 shows the Feynman diagrams for these 3 modes.

For the SUSY $0\nu\beta\beta$ mechanisms, the product of nuclear matrix element M and η_{SUSY} take the form [67]:

$$M\eta_{SUSY} = \eta_T M_q^{2N} + (\eta_{PS} - \eta_T) M_f^{2N} + \frac{3}{8} \left(\eta_T + \frac{5}{3} \eta_{PS} \right) \left(\frac{4}{3} M^{1\pi} + M^{2\pi} \right). \quad (1.4)$$

Here, η_T and η_{PS} are the effective lepton number violating parameters that normalize the tensor and pseudoscalar currents in the lepton number violating part of the effective Lagrangian. M_q^{2N} and M_f^{2N} are the matrix elements for the two-nucleon direct exchange mode, and $M^{1\pi}$ and $M^{2\pi}$ are the matrix elements for the π exchange mode.

1.1.2 Matrix Element Tabulation

We now tabulate the various matrix elements and phase space factors used as inputs in this model separations exercise. The details and sources of uncertainties in the matrix element calculations will be discussed at greater length in Chapter 3. In Table 1.1, we tabulate the phase space integrals in units of $10^{-15}/y$. $G^{0\nu}$ includes a scaling factor (r_0), which is traditionally factored out and combined with a similar factor from the matrix element to conveniently make the matrix element unitless. However a problem arises if authors use matrix elements and phase space integrals from different sources and are not careful to make certain that they are scaled by the same value of r_0

[41]. In Table 1.1 the numerical value of r_0 used is noted for each reference.

Table 1.1: Phase space factors and the assumed nuclear radius scaling factors. The units are $10^{-15}/y$.

Ref.	^{48}Ca	^{76}Ge	^{82}Se	^{96}Zr	^{100}Mo	^{116}Cd	^{128}Te	^{130}Te	^{136}Xe	^{150}Nd
[140] ^a		7.93	35.2	73.6	57.3	62.3	2.21	55.4	59.1	269
[28] ^b	75.8	7.60	33.5	69.7	54.5	58.9	2.17	52.8	56.3	249

$$^a r_0 = 1.1 \text{ fm}$$

$$^b r_0 = 1.2 \text{ fm}$$

Table 1.2 contains matrix elements for light neutrino exchange calculated in either the QRPA or shell model framework. There are literally dozens of other matrix element calculations that are not tabulated here. As discussed in References [48, 125], many of the previous calculations are outdated. We chose the QRPA values for light neutrino exchange in the table, because we consider them to be the state of the art. We include values for the QRPA from References [140, 111] for comparison only, since we use values for heavy neutrino exchange and right-handed currents from those references, respectively. For reference [111] we used the values it reports for $M_{GT} - M_F$. Comparisons between these and the other matrix elements should be done with care however, because the authors do not explicitly state the value they used for r_0 . For the Shell Model, we used the published values from Reference [31] except for the cases of ^{100}Mo and ^{116}Cd , where we have taken the liberty of using the values from Reference [119] because those values weren't included in Reference [31]. Since the values in Reference [119] have not yet been published, one must consider their use preliminary and only indicative of the anticipated final results.

In Table 1.3, we tabulate the matrix elements arising from heavy neutrino and SUSY particle exchange. The choice of reference for the heavy neutrino exchange mode was made due to its estimates of $M_{0\nu}$ for numerous isotopes. For the SUSY mode, it is the only comprehensive set of calculations done after the importance of the 1π and 2π modes was realized. We assumed that the 1π and 2π terms in Equation 1.4 dominate, and the values in the table are taken from Reference [67] as:

$$M_{SUSY} = \left(\frac{4}{3} M^{1\pi} + M^{2\pi} \right). \quad (1.5)$$

Table 1.2: $0\nu\beta\beta$ nuclear matrix elements for several light ν exchange models. The matrix elements in this formalism are unit-less.

Ref.	^{48}Ca	^{76}Ge	^{82}Se	^{96}Zr	^{100}Mo	^{116}Cd	^{128}Te	^{130}Te	^{136}Xe	^{150}Nd
[140] ^a		2.8	2.64	1.49	3.21	2.05	2.17	1.8	0.66	3.33
[125, Err.] ^b		3.92	3.49	1.20	2.78	2.42	3.23	2.95	1.97	4.16
[33] ^c		3.33	3.44	3.55	2.97	3.75		3.49	4.64	
[111] ^d		4.19	3.92		2.12		4.29	3.47	1.57	6.08
[31] ^e	0.720	1.39	2.19				0.86	1.19	0.75	
[119] ^f		1.6	1.7	0.4	0.3	1.9	2.0	1.6		

^apnQRPA, $r_0 = 1.1$ fm

^bRQRPA, $g_A = 1.25$, tune coupling parameters to reproduce correct $2\nu\beta\beta$ rate, $r_0 = 1.1$ fm

^cpnQRPA, tune coupling parameters to reproduce single β rate of intermediate nucleus, $r_0 = 1.2$ fm

^dpnQRPA, this paper doesn't explicitly state the r_0 value. See the text for more detail.

^eShell Model, published, $r_0 = 1.2$ fm

^fShell Model, unpublished, $r_0 = 1.2$ fm

Table 1.3: $0\nu\beta\beta$ nuclear matrix elements for heavy neutrino exchange (upper row) and R-parity violating SUSY models. The matrix elements in this formalism are unit-less.

Ref.	^{48}Ca	^{76}Ge	^{82}Se	^{96}Zr	^{100}Mo	^{116}Cd	^{128}Te	^{130}Te	^{136}Xe	^{150}Nd
[140] ^a		32.6	30.0	14.7	29.7	21.5	26.6	23.1	14.1	35.6
[67] ^b		-625	-583	-429	-750	-435	-691	-627	-366	-1054

^apnQRPA, $r_0 = 1.1$ fm

^bpnRQRPA, $r_0 = 1.2$ fm

Table 1.4 provides the matrix elements arising from right-handed currents as calculated by Reference [111]. Again we chose this reference because it provided values for a number of isotopes. However, it does not provide a value for ^{116}Cd . Therefore, in the analysis described below, these two theories require special treatment.

1.2 Summary of Previous Work

If $0\nu\beta\beta$ is observed, it will demonstrate that neutrinos are massive Majorana particles regardless of the underlying physics of the process [129]. The prospect of finding a distinctive experimental fingerprint for this underlying physics would then become extremely interesting. Various techniques

Table 1.4: Products of $0\nu\beta\beta$ nuclear matrix elements and the corresponding phase space factors for right-handed-current interaction models. The units for the η values are $10^{-8}/\text{y}$ and for the λ values are $10^{-12}/\text{y}$.

Ref.	^{48}Ca	^{76}Ge	^{82}Se	^{96}Zr	^{100}Mo	^{116}Cd	^{128}Te	^{130}Te	^{136}Xe	^{150}Nd
[111] ^a		0.44	1.54		3.50		0.15	2.25	0.83	29.5
[111] ^b		0.14	1.01		1.05		0.007	1.05	0.20	26.8

^a_{pn}QRPA(η)

^b_{pn}RQRPA(λ)

have been discussed previously. The use of the kinematic distributions to discern right-handed currents (RHC) from light neutrino mass processes was described in Reference [45]. Reference [4] discusses the use of the angular distribution as a function of particle physics model. In Reference [138], the author also proposes examining the ratio the rates of $0\nu\beta\beta$ to the 2^+ excited state to that for $0\nu\beta\beta$ to the ground state in the same isotope as a signature for RHC. Reference [142] discusses using relative rates of the decay to the first excited 0^+ state and the ground state to discern the light neutrino mode, the heavy neutrino mode, and SUSY processes. Reference [32] discusses the potential of using $\mu \rightarrow e$ and $\mu \rightarrow e\gamma$ in combination with $0\nu\beta\beta$ to prove that the light ν mechanism is dominant. Reference [122] discusses the relative contributions to $\Gamma^{0\nu}$ from light neutrinos and heavy particle exchange. In this dissertation, we revisit the approach of comparing rates of the ground state transition in multiple nuclei to determine the $0\nu\beta\beta$ mechanism.

There are many other, more exotic particle physics models that can lead to lepton number violation and $0\nu\beta\beta$. For example, singlet neutrinos in extra dimensions can lead to double beta decay [24]. In this case the Kaluza-Klein spectrum of neutrino masses spans values from much less to much greater than the nuclear Fermi momentum. Therefore one cannot separate the nuclear and particle physics and the effective neutrino mass depends on the nuclear matrix element. The decay rate also depends on unknowns such as the brane shift parameter and the extra dimension radius and therefore is highly model dependent. Also, mass varying neutrinos (MAVANS) might lead to decay rates that depend on the density of the matter in which the process occurred [90].

Three recent articles [12, 26, 44] have considered the question of the required number of $0\nu\beta\beta$ experiments. Reference [12] took a very pessimistic view of nuclear theory and $\beta\beta$. That paper took *all* previous calculations of $M_{0\nu}$ and considered them as samples of a parent distribution of the true value. This led to a very wide distribution of possible anticipated results for a given $\langle m_{\beta\beta} \rangle$ and hence a requirement that an impractically large number of measurements be performed. Many of

the calculations, however, have been found to be in error, or have been updated and hence replaced by more recent calculations. (See Reference [125] for a summary discussion.) If one performs a more coherent analysis neglecting these outlying results, the situation is improved.

Reference [26] concludes that $0\nu\beta\beta$ measurements in 3 nuclei would be an important tool in the solution of the nuclear matrix element problem. This reference does not address the question of discerning the various mechanisms for $0\nu\beta\beta$, although it does point out that it is an interesting one. It also does not quantify the confidence one would derive from 3 measurements nor does it quantify the required precision.

During the writing of this dissertation, Reference [44] became available. This paper estimates the ratio of rates for $0\nu\beta\beta$ for a number of mechanisms but doesn't estimate the number or required measurements or their required precision. The paper does estimate the spread in ratios for a number of particle physics models and suggests pairs of isotopes that would be most useful for separating certain models.

1.3 Multiple-Isotope Comparison

To compare theoretical calculations and prospective experimental results, we calculate the predicted rate for each considered model using Equation 1.1. The LNVP and $M_{0\nu}$ appear as a product, therefore if one obtains a decay rate from a lone nucleus, the two factors cannot be individually separated. To address this, we normalized the LNVPs for each model so that all reproduce identical decay rates for ^{76}Ge . The absolute normalization was chosen for $\langle m_{\beta\beta} \rangle = 100$ meV with the matrix elements in Reference [125, erratum]. This sets the scale of η to correspond to $0\nu\beta\beta$ lifetimes just within the reach of the current set of proposed experiments. This absolute scale for the LNVP is arbitrary for this analysis and is only chosen for definiteness. Our arguments concerning the uncertainty requirements and the number experimental results do not depend upon it.

Our model space will consist of seven different theories enumerated below chosen from those described in Section 1.1.2. Because the RHC model does not have a $M_{0\nu}$ for ^{116}Cd , our primary analysis uses only the first 5 of these models. A secondary analysis tests the impact of including the two RHC models. The $0\nu\beta\beta$ models considered in this exercise are:

1. QRPA($\beta\beta$): Light ν exchange, RQRPA with coupling constants tuned to reproduce the $2\nu\beta\beta$ rate [125]
2. QRPA($\beta\beta$): Light ν exchange, pnQRPA with couplings tuned to reproduce the β -decay rates for the intermediate nucleus in the $2\nu\beta\beta$ reaction [33]

3. SM: Light ν exchange, shell model [31, 119]
4. Heavy ν : Heavy ν exchange [140]
5. SUSY: R-parity violating supersymmetry – 1π and 2π exchange modes [67]
6. RHC- η : Right-handed current [111]
7. RHC- λ : Right-handed current [111]

For each of these models, we simulated 10000 potential sets of decay-rate results for a group of isotopes with *measured* decay rates according to a Gaussian distribution whose mean was defined by the predicted decay rate and its variance defined as a fraction of that mean. We then compared each simulated result group to each of the models to discern the predictive power of selecting the correct model. We made this comparison by calculating χ^2 . The model that best fit the simulated set was chosen as that with the lowest χ^2 value. We then tabulated the number of simulated sets for which the best fit set was also the correct set. We then determined the largest total uncertainty that would result in the correct choice being selected 90% and 68% of the time. This analysis was done not only for varying uncertainty, but also for a varying number of isotopes included in the analysis. Alternatively, one could tabulate the number of times a wrong model was chosen as the correct model and determine how well one can reject a given model.

The six $\beta\beta$ isotopes used in this analysis are: ^{76}Ge , ^{82}Se , ^{100}Mo , ^{116}Cd , ^{130}Te , and ^{136}Xe . These six were chosen because they are proposed for use in future experiments and have $M_{0\nu}$ calculations available for a variety of models.

The analysis presented below is by no means restricted to this set of $0\nu\beta\beta$ models and isotopes. In fact, one would anticipate that the theories will improve and experimenters will invent new techniques that employ other isotopes. Most importantly, the nuclear theory is not entirely settled. Therefore, although we use the $\Gamma^{0\nu}$ values quoted in Table 1.5 as indicative of the difference between the various models, we recognize that the predictions are likely to evolve. It is clear that this work rests on a number of assumptions, including:

1. We have made the implicit assumption that the present differences in the model predictions are indicative of the true differences.
2. It is conceivable that future calculations will include additional microphysics (e.g nuclear deformation) that will affect different isotopes differently. Our analysis assumes that any uncertain-

ties in the models shift each $M_{0\nu}$ similarly. If a model has a systematic shift in its predictions for all isotopes that alters all $M_{0\nu}$ by an equivalent fraction, that would not alter this analysis in choosing the correct theory, but would result in a shift in the value of the deduced LNVP.

3. We have assumed that within each set of theoretical values for $M_{0\nu}$, each calculation for the individual isotopes is of equivalent accuracy.
4. Finally, we have also assumed that one and only one model is correct. That is, we have assumed that if two mechanisms are contributing to $\Gamma^{0\nu}$ (e.g. light neutrino and heavy particle exchange), one mechanism dominates and any interference is negligible.

These assumptions notwithstanding, the analysis can provide useful guidance indicating how precise measurements should be and how many measurements are required.

1.4 Model Separation Analysis

We used the calculated $\Gamma^{0\nu}$ for each isotope as the mean values of a set of probability distributions for $\Gamma^{0\nu}$ and assumed a fraction of those values as the uncertainties. The explicit values are plotted in Figure 1.3 with 10% uncertainties shown to provide a qualitative indication of how well the various models can be discerned at this chosen uncertainty level. Numeric values are given in Table 1.5. This table is very useful for identifying which models will be difficult to separate. For example, the SUSY and heavy neutrino models give very similar decay rates for each isotope to within a somewhat uniform factor of about 2. Hence it will be hard to separate these two models from each other. Also the table shows the interesting case of the shell model estimate for ^{100}Mo . This isotope shows a large disagreement (greater than a factor of 10) with several of the other models. Hence, this Table indicates that Mo is a key isotope for separating the models. We should, however note the caveat regarding the reference for the shell model calculations discussed above. This value has not yet been published, and is therefore less well-vetted in comparison to the other calculations.

To determine the number of isotopes required to obtain sufficient separation, we varied the number of isotopes included in the analysis. By design, the analysis does not include all isotopes, and therefore, the order in which isotopes were added to the analysis had to be chosen. We chose four isotope orderings; by atomic number, by largest spread in predicted $\Gamma^{0\nu}$, by an assumed likely order of actual results, and an alternate ordering to examine the effect of ^{100}Mo . The “experimental readiness” (third) ordering and the choice of the isotopes is clearly arbitrary and reflects the opinions, as opposed to any prescience, on the part of the author. Note: ^{76}Ge is first in each list is because, as mentioned in Section 1.3, we normalized the LNVPs to reproduce the same rate in that isotope.

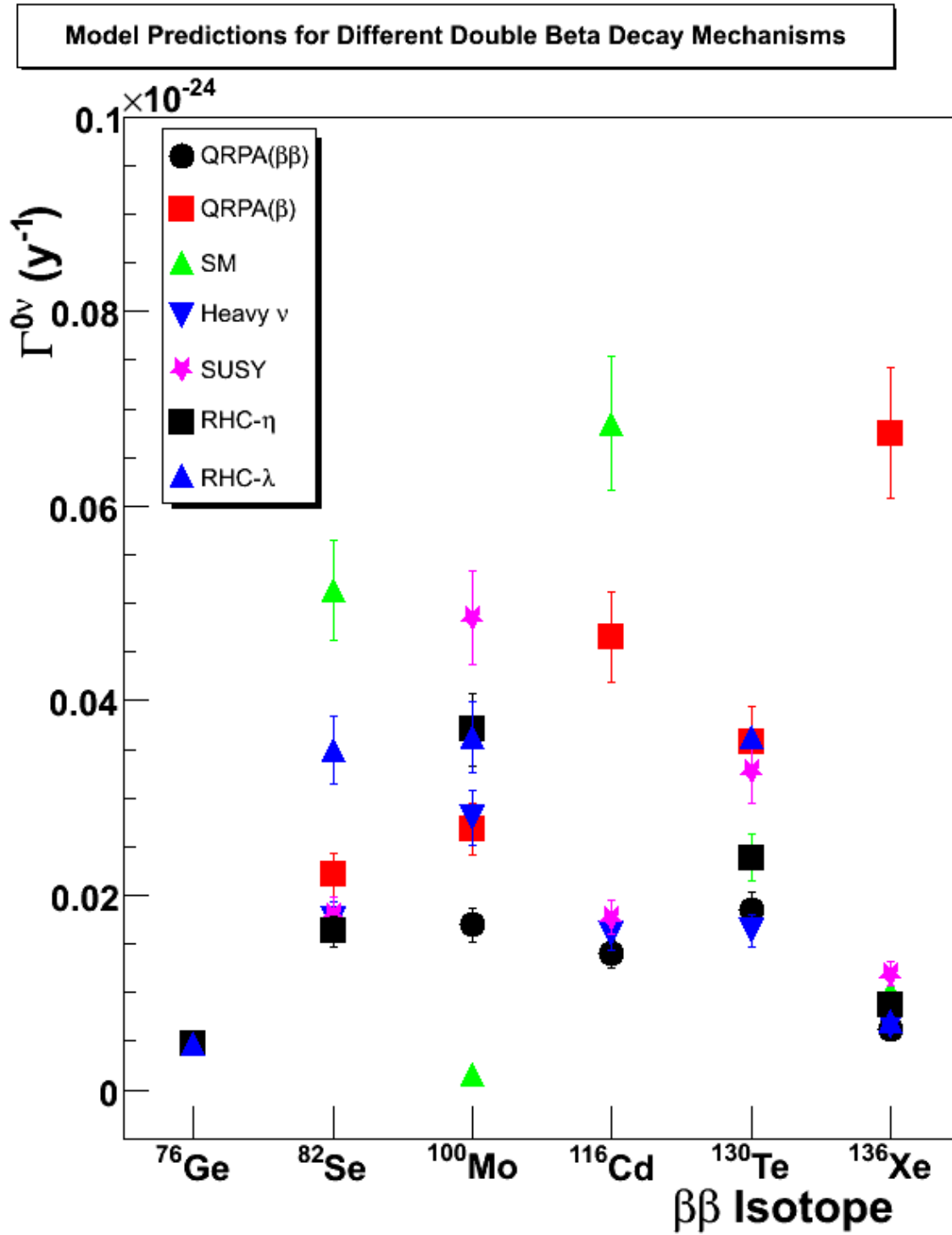


Figure 1.3: $\Gamma^{0\nu}$ predictions for $M_{0\nu}$ uncertainties of 10% for all 7 $0\nu\beta\beta$ models and all 6 isotopes.

Table 1.5: Values of the decay rate in units of $10^{27}/\text{y}$ for the isotopes in our analysis for the chosen LNVP. The light neutrino mass $\langle m_{\beta\beta} \rangle$ was chosen to be 100 meV for the model labeled QRPA($\beta\beta$). The other LNVP's were chosen such that the resultant decay rates for ^{76}Ge were the same. The form of the LNVP was chosen to be unitless.

Model	LNVP	^{76}Ge	^{82}Se	^{100}Mo	^{116}Cd	^{130}Te	^{136}Xe
QRPA($\beta\beta$)	1.96×10^{-7}	4.67	16.42	16.96	13.97	18.46	6.31
QRPA(β)	2.30×10^{-7}	4.67	22.11	26.82	46.49	35.81	64.52
SM	5.52×10^{-7}	4.67	51.42	1.57	68.50	23.89	10.13
Heavy ν	2.35×10^{-8}	4.67	17.54	27.99	15.95	16.37	6.51
SUSY	1.23×10^{-9}	4.67	18.02	48.56	17.76	32.81	11.93
RHC- η	1.03×10^{-9}	4.70	16.29	37.02		23.80	8.75
RHC- λ	1.86×10^{-7}	4.70	34.88	36.26		36.26	7.04

1. Atomic number: ^{76}Ge , ^{82}Se , ^{100}Mo , ^{116}Cd , ^{130}Te , ^{136}Xe
2. $\Gamma^{0\nu}$ spread: ^{76}Ge , ^{136}Xe , ^{116}Cd , ^{100}Mo , ^{82}Se , ^{130}Te
3. Likely order of experimental results: ^{76}Ge , ^{130}Te , ^{136}Xe , ^{100}Mo , ^{82}Se , ^{116}Cd
4. Alternate order to study ^{100}Mo : ^{76}Ge , ^{130}Te , ^{136}Xe , ^{116}Cd , ^{82}Se , ^{100}Mo

All of the $\beta\beta$ isotopes treated in this article have proposals for upcoming Fiorini-style internal source experiments (that is, experiments consisting of detectors made from material containing the $\beta\beta$ decay isotope) with the exception of ^{82}Se and ^{100}Mo . The MAJORANA[38, 37] and GERDA [130] collaborations will use ^{76}Ge . The COBRA experiment [146] will use ^{116}Cd . CUORE [7] will use ^{130}Te , and the EXO collaboration [120] will use ^{136}Xe . ^{82}Se is one of the $\beta\beta$ isotopes proposed for use by the SuperNEMO collaboration [14] in a tracking apparatus. The MOON collaboration [59] plans to use ^{100}Mo in a large multi-layer sandwich of molybdenum foil and plastic scintillators. All of these experiments are discussed in greater detail in Section 2.4. Table 1.6 summarizes the results of the simulations.

When we examine Table 1.6, we see that while the order in which the isotopes are added to the analysis clearly affects the required uncertainties, but this effect is fairly small. While the predictions from several of the models examined in this study indicate that certain isotopes (^{100}Mo in particular) are more important in performing this analysis, it is premature to plan out the future of the world $\beta\beta$ program based on this because of the assumptions and uncertainties in the underlying nuclear

Table 1.6: Limits of required total uncertainties corresponding to each theoretical model and the number of measurements as isotopes are added to the analysis for 90% and 68% confidence. Only the final pair of rows includes all 7 models. The others exclude the RHC models because those models do not have a $M_{0\nu}$ value for ^{116}Cd . The precision of the numbers in this table are approximately $\pm 1\text{-}2\%$.

Isotope Ordering	Confidence Level	Number of Isotopes				
		2	3	4	5	6
Atomic Number	90%	<2%	8%	15%	19%	19%
	68%	<2%	19%	25%	31%	34%
$\Gamma^{0\nu}$ Spread	90%	< 2%	5%	17%	17%	19%
	68%	4%	13%	31%	31%	34%
Experimental Readiness	90%	4%	5%	19%	19%	19%
	68%	8%	12%	30%	32%	34%
Alternative Ordering (^{100}Mo added last)	90%	4%	5%	7%	7%	19%
	68%	8%	11%	17%	18%	34%
Experimental Readiness (Light ν ONLY)	90%	8%	18%	44%	48%	47%
	68%	14%	35%	64%	64%	62%
Experimental Readiness (All 7 models, no ^{116}Cd)	90%	<2%	5%	14%	16%	—
	68%	<2%	11%	22%	24%	—

theory. At this point it is far more important when deciding which $\beta\beta$ isotopes to pursue to consider which are experimentally accessible. The results of this study lead us to the conclusion that in a four or five isotope analysis including all but the right-handed current models, a total uncertainty budget of $\approx 30 - 32\%$ is required to correctly choose the underlying mechanism 68% of the time (or $\lesssim 20\%$ for 90% accuracy). If we restrict our consideration to the light neutrino exchange models, the total uncertainty budget gets relaxed to around 44% and 64% for four isotopes at 90% and 68% accuracy. This is important from the standpoint of testing matrix element calculation techniques.

1.5 Comparison to to Other Neutrino Data

There has been a remarkably successful worldwide neutrino physics program outside of $\beta\beta$ studies over the past decade that has illuminated much of this heretofore dark corner of physics. We now have initial values for the neutrino mixing matrix elements, the differences between the squares of the neutrino masses as well as the number of light active neutrino species.

There is, however much still to learn. We now outline what we have learned about the neutrino sector and its ramifications for a program of $\beta\beta$ decay research. For much of the following discussion,

we will assume that light neutrino exchange dominates $0\nu\beta\beta$. Reference [48] has a more detailed discussion of this subject.

We begin this discussion by revisiting the expression for the LNVP for light neutrino exchange in Equation 1.2, and using it to explicitly define the effective $\beta\beta$ mass [48]:

$$\begin{aligned} \langle m_{\beta\beta} \rangle &= m_e \eta_{L\nu} = \sum_k U_{ek}^2 \xi_k m_k \\ &= m_1 U_{e1}^2 + m_2 U_{e2}^2 e^{i(\alpha_2 - \alpha_1)} + m_3 U_{e3}^2 e^{-i(\alpha_1 + 2\delta)}, \end{aligned} \quad (1.6)$$

where as before, m_e is the electron mass and $\eta_{L\nu}$ is the LNVP for light neutrino exchange. U_{ek}^2 is the element of the neutrino mixing matrix connecting the electron neutrino with mass eigenstate k . ξ_k is a phase and m_k is the neutrino mass eigenvalue corresponding to mass eigenstate k . The second line of Equation 1.6 writes out the sum explicitly including the two Majorana phases α_1 and α_2 , and Dirac phase δ . The phases in Equation 1.6 are ± 1 if CP is conserved.

1.5.1 Neutrino oscillation parameters

Now, we further discuss the various neutrino oscillation parameters that affect the physics of $0\nu\beta\beta$ and discuss how uncertainties in these quantities can hinder the extraction of $\langle m_{\beta\beta} \rangle$ from a $0\nu\beta\beta$ result (again assuming light-neutrino exchange to be the dominant $0\nu\beta\beta$ mechanism). One of the major contributions from the oscillation experiments is the differences in the squares of the neutrino mass eigenvalues

$$\delta m_{ij}^2 \equiv m_j^2 - m_i^2, \quad (1.7)$$

where m_i and m_j are again the neutrino mass eigenvalues. The oscillation experiments have also extracted some of the values in the neutrino mixing matrix. We parameterize the mixing matrix as

$$U = \begin{pmatrix} c_{12}c_{13} & s_{12}c_{13} & s_{13}e^{-i\delta} \\ -s_{12}c_{23} - c_{12}s_{23}s_{13}e^{i\delta} & c_{12}c_{23} - s_{12}s_{23}s_{13}e^{i\delta} & s_{23}c_{13} \\ s_{12}s_{23} - c_{12}c_{23}s_{13}e^{i\delta} & -c_{12}s_{23} - s_{12}c_{23}s_{13}e^{i\delta} & c_{23}c_{13} \end{pmatrix} \begin{pmatrix} e^{i\frac{\alpha_1}{2}} & 0 & 0 \\ 0 & e^{i\frac{\alpha_2}{2}} & 0 \\ 0 & 0 & 1 \end{pmatrix} \quad (1.8)$$

Here, s_{ij} and c_{ij} are the sine and cosine respectively of the mixing angle θ_{ij} between neutrino mass eigenstates i and j . As in Equation 1.6, δ is a Dirac phase much like the phase in the CKM matrix, and α_1 and α_2 are phases affecting only Majorana particles.

We now summarize the results of the oscillation experiments [13]. The global analysis of the SNO and KamLAND experiments gives us $\delta m_{sol}^2 \equiv \delta m_{12}^2 = 8.0_{-0.4}^{+0.6} \times 10^{-5} \text{ eV}^2$, and $\theta_{sol} \equiv \theta_{12} = 33.9_{-2.2}^{+2.4} [53]$. The Super-Kamiokande experiment gives $\delta m_{atm}^2 \equiv \delta m_{23}^2 = 2.5_{0.6}^{+0.5} \times 10^{-3} \text{ eV}^2$, and $\theta_{atm} \equiv \theta_{23} \sim 45^\circ [66]$. The CHOOZ experiment gives a limit of $\theta_{13} < 13^\circ (90\% \text{ CL}) [60]$. Some

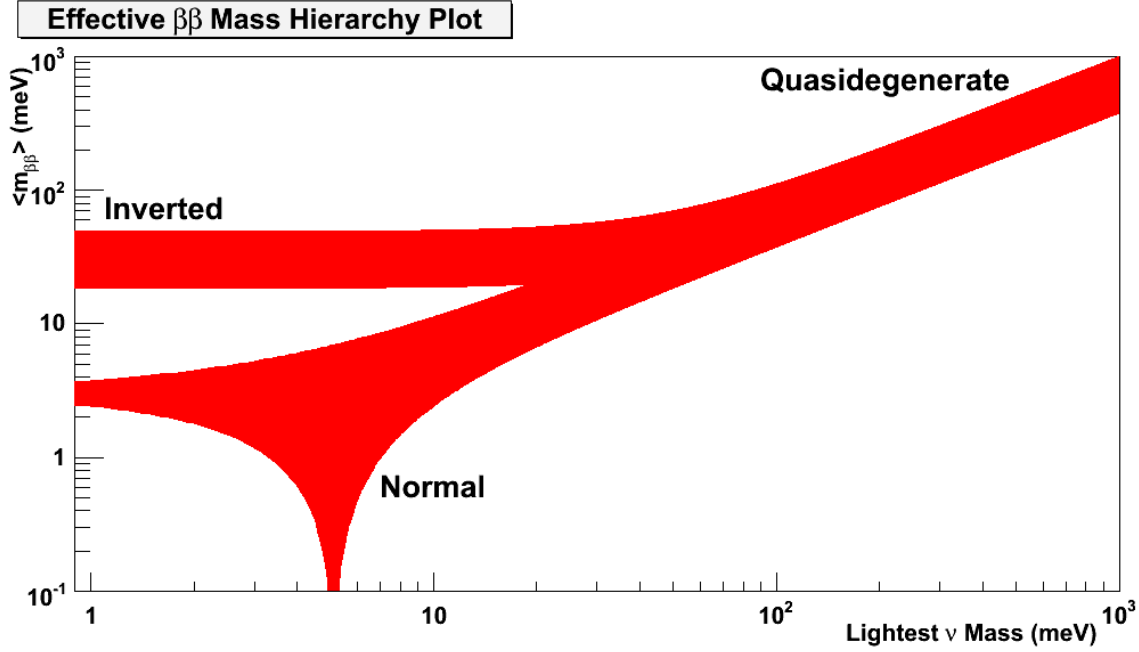


Figure 1.4: Effective Majorana mass (assuming light, Majorana ν exchange dominates $0\nu\beta\beta$) as a function of the lightest ν mass for $\theta_{12} = 33.9^\circ$, $\theta_{13} = 4.5^\circ$, $\delta m_{12}^2 = 8.0 \times 10^{-5} \text{ eV}^2$, and $\delta m_{23}^2 = 2.5 \times 10^{-3} \text{ eV}^2$.

other authors have obtained slightly different numerical results for these quantities (particularly those involving the combined solar/reactor neutrino experiments) over the years, and the limit on θ_{13} depends on the value of δm_{23}^2 used in the analysis. For these reasons, and the fact that the precise values of these parameters are always under review, the following discussion is also subject to revision. Any conclusions drawn from it should be considered as indicative of possible future analyses, and contingent on the actual values of these parameters as we come to understand the neutrino sector more precisely.

The solar/reactor data gives us the sign of δm_{sol}^2 , revealing that ν_1 is lighter than ν_2 . The limits on θ_{13} tell us that the third eigenstate ν_3 contains little or no ν_e . The atmospheric neutrino experiments, however are not sensitive to the sign of δm_{atm}^2 , so we do not know whether ν_3 is heavier or lighter than ν_1 and ν_2 . If ν_3 is the heaviest eigenstate, then we call the mass spectrum the “normal hierarchy.” If ν_3 is lighter, then we call the mass spectrum the “inverted hierarchy”. If all three masses are much greater than δm_{atm}^2 , we call the mass spectrum “quasidegenerate,” regardless of which eigenstate is the lightest. Which of these three hierarchies is actually the correct model is central to the question of the absolute mass scale of the neutrino.

The values of and uncertainties for the oscillation parameters in Equation 1.6 constrain the range of $\langle m_{\beta\beta} \rangle$ values for any value of the lightest ν eigenmass. Figure 1.4 shows these allowed regions for the oscillation parameters as quoted above and $\theta_{13} = 4.5^\circ$. The bands come from the unknown phases in the mixing matrix. The edges are defined by the CP-conserving values of the phases, $e^{i(\alpha_1 - \alpha_2)} = \pm 1$. At high values of the lightest neutrino mass, the mass spectrum is solidly quasidegenerate, and the bands in Figure 1.4 overlap. For a lightest neutrino mass below ~ 30 meV, the degenerate band splits into the normal and inverted hierarchies. Figure 1.4 shows us that for an appropriately precise value of $\langle m_{\beta\beta} \rangle$ (assuming light neutrino exchange dominates $0\nu\beta\beta$), we can identify the appropriate band and therefore constrain the eigenvalue of the lightest neutrino mass state. However, it is also important to remember that there are uncertainties in the oscillation parameters and the matrix elements are not accounted for in the figure.

1.5.2 Absolute Mass Scale

We know that at least one of the neutrino states has a mass $> \sqrt{\delta m_{atm}^2} \approx 45$ meV. This therefore sets the scale for the sensitivity goals of future neutrino mass experiments (actually, most current $0\nu\beta\beta$ experiments are designed for sensitivity for the quasidegenerate mass scale with the option to scale up to an experiment sensitive to the atmospheric scale). We now detail the potential of other mass measurements.

There are several techniques for the measurement of the mass of the neutrino. Reference [25] has a nice summary of these. The best and most mature of these are $0\nu\beta\beta$ decay (only if the neutrino is a Majorana particle), β -decay and cosmological observations. These three techniques complement one another because they arise from differently weighted sums over the mass eigenvalues and mixing-matrix parameters, as shown in Equation 1.12. β -decay measures an incoherent sum over the neutrino masses because a real neutrino is emitted in the decay. The effective neutrino mass one extracts from $0\nu\beta\beta$ (assuming light-neutrino exchange dominates) is a coherent sum of the Majorana neutrino masses because no real neutrino is emitted (instead, a virtual neutrino is exchanged between nucleons). The cosmology constraints come from the gravitational impact of the neutrino density which is, in turn proportional to the sum of all three neutrino masses.

The current best limit from β -decay $\langle m_\beta \rangle \leq 2200$ meV (95% CL) comes from tritium beta decay [143, 107]. This limit, combined with results from the oscillation experiments, show that for at least one neutrino:

$$45 \text{ meV} \leq m_i \leq 2200 \text{ meV}. \quad (1.9)$$

The next generation of ${}^3\text{H}$ β -decay experiments is the KATRIN collaboration [36]. They are building

a very large spectrometer (24 m long by 10 m wide) at the Karlsruhe Institute of Technology in Karlsruhe, Germany. The KATRIN collaboration aims to reach a sensitivity to $\langle m_\beta \rangle$ approaching 200 meV [72].

Massive neutrinos should also contribute to the matter density of the Universe on cosmological scales [77] by an amount,

$$\Omega_\nu h^2 = \frac{\Sigma}{92.5 \text{ eV}}, \quad (1.10)$$

where Ω is the neutrino mass density as a fraction of the critical density, h is the dimensionless Hubble constant, and $\Sigma \equiv m_1 + m_2 + m_3$ is just the simple sum of the neutrino masses. h differs from the standard Hubble constant H_0 (the recessional velocity per unit distance of objects across cosmological length scales) in that it is normalized by $100 \text{ km s}^{-1} \text{ Mpc}^{-1}$, making it dimensionless. Since the neutrinos are light, they only cluster with cold dark matter for scales larger than

$$\frac{1}{k} \sim 33 \sqrt{\frac{1 \text{ eV}}{m_\nu \Omega_m h}} \text{ Mpc}, \quad (1.11)$$

where k is a wave number corresponding to fluctuations in the cosmic microwave background (CMB). Perturbations get suppressed for smaller values of k , allowing measurements of large scale structure (LSS) to provide constraints on the neutrino mass. These constraints are however, rather weak unless combined with precise measurements of other cosmological parameters, which also affect the size of perturbations. The WMAP collaboration [56] has taken cosmological data of unprecedented precision supplementing LSS data from the 2dF galaxy survey [62], CBI [65], ACBAR [57] and the Lyman- α forest [63].

Cosmological observations have been used in numerous combinations [19, 61, 58, 76, 42] to derive limits on Σ much lower than those currently available to laboratory experiments. There has also been at least one claim for a nonzero value of $\Sigma = 0.64 \text{ eV}$ [5]. There has also been some work in this field examining the impact of prior distributions on the neutrino mass limit calculated in this way [103].

In the future, measurements from the Sloan Digital Sky survey [137] and the PLANCK satellite [39] may limit values of Σ to as low as 40 meV [85]. Still, the determination of Σ from cosmological observations tends to be stymied by the number of correlated parameters that need to be precisely measured to extract a value. Therefore, cleaner laboratory-based measurements of the neutrino mass will remain important regardless of the ultimate sensitivity of the cosmological limits. Because β -decay endpoint experiments will be hard-pressed to attain a sensitivity near $\sqrt{\delta m_{atm}^2}$, $0\nu\beta\beta$ experiments will remain particularly important. In fact, these three techniques for extracting an absolute neutrino mass scale are complimentary, and progress on all fronts will be required for healthy scientific progress.

1.5.3 The Majorana phases

We see the explicit form of the effective Majorana neutrino mass and its dependence on the Majorana phases in Equation 1.6. CP conservation imposes the condition that these relative phases are an integer multiple of π . Mathematically, the two relative phases $\alpha \equiv (\alpha_2 - \alpha_1)$ and $\beta \equiv (-\alpha_1 - 2\delta)$ can impact observables in $0\nu\beta\beta$ searches, but are in practice, extremely difficult to determine. We will now discuss the physical impact of these phases by expanding on our earlier discussion of comparing results of multiple $0\nu\beta\beta$ experiments to include results from other neutrino mass results. We can illuminate the main thrust of this global, global analysis through a hypothetical set of measurements. Figure 1.5 is a consistency plot showing the constraints for three neutrino species and two phases using the following parameters:

$$\begin{aligned}
\Sigma &= m_1 + m_2 + m_3 = 700 \text{ meV} \\
\delta m_{21}^2 &= m_2^2 - m_1^2 = \delta m_{sol}^2, \quad \delta m_{32}^2 = m_3^2 - m_2^2 = +|\delta m_{sol}^2| \\
\langle m_\beta \rangle^2 &= m_1^2 U_{e1}^2 + m_2^2 U_{e2}^2 + m_3^2 U_{e3}^2 = 232 \text{ meV} \\
\langle m_{\beta\beta} \rangle^2 &= m_1^2 U_{e1}^4 + m_2^2 U_{e2}^4 + m_3^2 U_{e3}^4 + 2m_1 m_2 U_{e1}^2 U_{e2}^2 \cos(\alpha) \\
&+ 2m_1 m_3 U_{e1}^2 U_{e3}^2 \cos(\beta) + 2m_2 m_3 U_{e2}^2 U_{e3}^2 \cos(\alpha + \beta) = 159 \text{ meV}
\end{aligned} \tag{1.12}$$

The phases α and β were taken to be 2.0 and 2.5 radians respectively, and U_{e3} was taken to be 0.03.

While these surfaces intersect at a point, $0\nu\beta\beta$ decay is the only measurement included in Figure 1.5 that can access these phases (assuming light neutrino exchange is the proper mechanism for $0\nu\beta\beta$). Therefore a second pair of phases would produce a result consistent with the one depicted above. This means that two experiments sensitive to the phases would be required to unambiguously determine both. Furthermore, we have ignored the uncertainty in the measured parameters, and these will undoubtedly muddy any conclusions extracted via this method. Still, it is exciting to note that these seemingly disparate experimental techniques can, when combined, form a much more complete picture of the neutrino sector. As with the global $0\nu\beta\beta$ analysis described earlier in this chapter and in reference [73], the price for gaining more information from such a cross technique analysis is tighter uncertainty requirements than would otherwise be necessary for a simple discovery experiment.

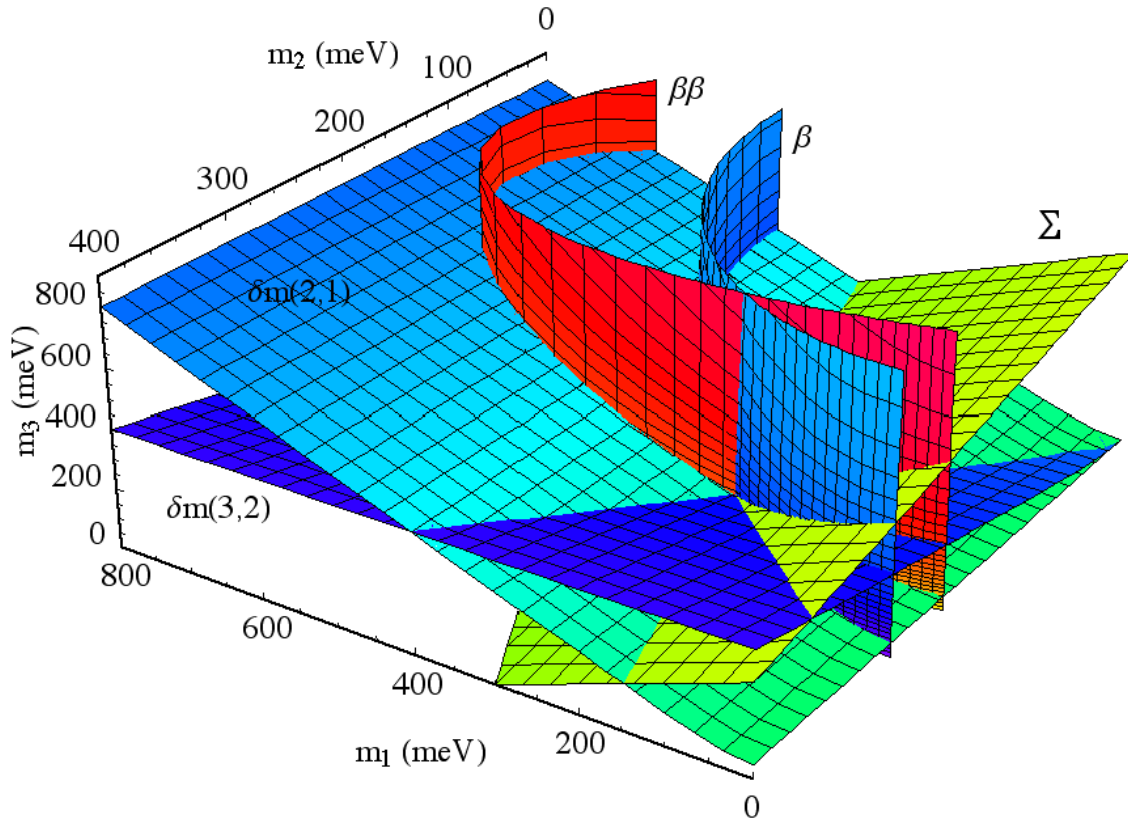


Figure 1.5: A consistency plot for the neutrino mass eigenvalues m_1 , m_2 and m_3 for various hypothetical measurements. This set of surface plots indicates how measured values of the sum of the neutrino masses, $\langle m_{\beta\beta} \rangle$, $\langle m_\beta \rangle$, and the oscillation results as detailed in Equation 1.12 can constrain the mass eigenvalues. This figure was produced by the author for Reference [48]

Chapter 2

MAJORANA PROJECT OVERVIEW AND STATE OF THE EXPERIMENTAL FIELD

We now present a global experimental overview of the state of the field. Because the work in this dissertation was performed in direct support of it, we begin with a description of the MAJORANA experiment itself. We will then move on to an overview of the current and recent MAJORANA research and development (R&D) work related to this dissertation. Then, we will move on to a summary experimental work connected to other $\beta\beta$ experiments, beginning with the previous generation and then moving on to the current slate of experiments either proposed or under way. Last, we will briefly outline the γ -ray tracking experiments using large arrays of germanium detectors, because they use similar apparatus as well as potentially some of the same analysis techniques.

2.1 MAJORANA *Project Overview*

If the MAJORANA project were to be summarized in one sentence, it would be:

“Our collaboration proposes to construct an array of 86% enriched ^{76}Ge crystals contained in an ultra-low-background structure.” [38]

More specifically, the physics goals of the MAJORANA collaboration’s first phase search for $0\nu\beta\beta$ are to:

- Demonstrate that backgrounds at or below 1 count/ton/year in the $0\nu\beta\beta$ decay peak 4-keV region of interest (1 count/ROI/t-y) are achievable, which would justify scaling up to a detector mass of one ton or larger.
- Use these demonstrated backgrounds to make a “down select” between the MAJORANA and GERDA (see Section 2.4.1) detector array technologies.
- Unambiguously test the KKDC claim of an observation of $0\nu\beta\beta$ in ^{76}Ge corresponding to $\langle m_{\beta\beta} \rangle \approx 400$ meV [96], and probe the quasidegenerate neutrino mass region down to ≈ 200 meV.

To attain these goals, we propose the expansion of the internal-source technique originally introduced by Fiorini [70] using high-purity Ge (HPGe) crystals. We believe that ^{76}Ge offers the best combination of capabilities and sensitivities for a next-generation $0\nu\beta\beta$ experiment, specifically because:

- The detectors would consist of elemental Ge, maximizing the source-to-total-mass ratio.
- ^{76}Ge has an endpoint value above most (but not all) naturally occurring radioactive backgrounds, with $Q_{\beta\beta} = 2.039$ MeV.
- ^{76}Ge has a comparatively well-understood nuclear matrix element, $M_{0\nu} \approx 3.9$ [125, erratum].
- ^{76}Ge has a reasonably slow $2\nu\beta\beta$ rate, $T_{1/2}^{2\nu} = (1.4 \pm 0.2) \times 10^{21}$ y [54].
- Germanium detectors have superior energy resolution, 0.16% at 2.039 MeV. This combined with the slow $2\nu\beta\beta$ rate will minimize $2\nu\beta\beta$ contamination in the $0\nu\beta\beta$ ROI. Even more important is the enhanced signal to noise ratio that results from better resolution.
- The fact that intrinsic high-purity Ge diodes are semiconductor devices means that the processes used in their production eliminates or minimizes U and Th chain impurities.
- A close-packed array of Ge detectors would provide powerful signal-to-background discrimination techniques: granularity, pulse-shape analysis, segmentation, and timing cuts.
- There is a demonstrated ability to enrich ^{76}Ge from the natural abundance of 7.44% to 86%.
- The MAJORANA experiment offers well-understood technologies and is available now: commercial segmented Ge diodes and existing, well-characterized large Ge arrays.

The advantages of ^{76}Ge are especially clear when one considers the fact that the most sensitive $0\nu\beta\beta$ half-life limits to date have been obtained using Ge detectors ($T_{1/2}^{0\nu} > 1.9 \times 10^{25}$ y, 90% CL), in the IGEX and Heidelberg-Moscow experiments.

As of November 2006, the reference design is based on modules, with space for 57 close-packed, 1.1 kg, enriched, possibly segmented germanium crystals enclosed in an ultra-pure copper cryostat. This maximizes the concentration of detectors while minimizing the mass of structural materials. These modules would be contained in a graded shield consisting of a low-background inner layer surrounded by structural material and additional γ and neutron shielding, which are, in turn surrounded by an

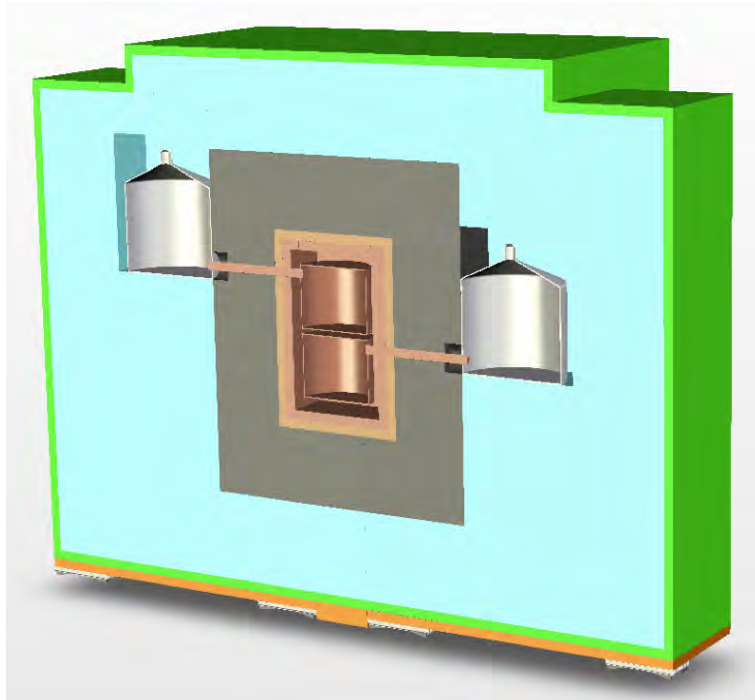


Figure 2.1: Cross-section of the MAJORANA experiment reference design. This figure is from [38].

active veto system. A cross section of the proposed detector apparatus is shown in Figure 2.1, and a schematic of a detector module is shown in Figure 2.2. The reference design is, as with most experiments in the planning and R&D phase, a moving target that responds to the requirements of and resources available from the funding agencies.

This reference design draws on the Collaboration’s extensive experience in past $2\nu\beta\beta$ and $0\nu\beta\beta$ experiments, solar and reactor ν oscillation experiments, large-array γ -ray tracking detectors, as well as recent advances in the production of ultra-low-background construction materials, germanium detector technology and electronic signal processing. The modular design is inherently scalable, with the proposed first phase consisting of 60 kg active mass which the Collaboration will use to demonstrate the backgrounds required to reach the inverted hierarchy scale in light Majorana neutrino mass. This prototype phase would be used to make a down-select between the MAJORANA and GERDA designs (the GERDA experiment is described in Section 2.4.1). This initial phase would also be sensitive to effective $T_{1/2}^{0\nu}$ values corresponding to Majorana neutrino masses in the quasidegenerate region. The MAJORANA collaboration is also actively pursuing R&D to minimize the cost and schedule for a future 1000 kg-scale experiment.

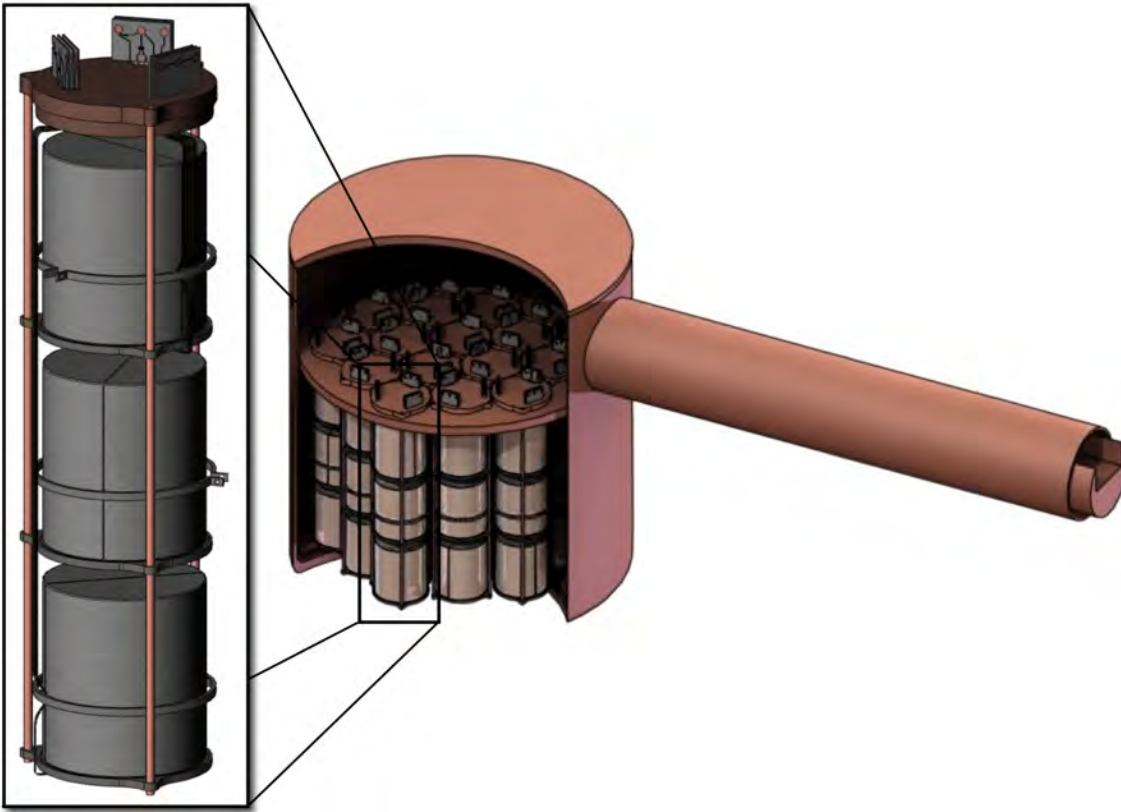


Figure 2.2: Detector modules for the MAJORANA experiment reference design. Note the independently removable strings of detectors. This will facilitate keeping more of the MAJORANA array online when part of it will require maintenance, thus maximizing the total live time of the experiment. This figure is a combination of two from [38].



Figure 2.3: Segmentation schemes being discussed for n-type MAJORANA detectors. From left to right they are: 4×1 , 2×3 , 1×6 , and 6×6 , where $m \times n$ is the number of azimuthal by the number of axial segments. The first three fall into the “modest segmentation” category while the last is considered “highly segmented.” This figure is from [38].

There are currently four candidate detector designs for the MAJORANA array: unsegmented p-type, point-contact p-type (P-PC), modestly segmented n-type, and highly segmented n-type. Cartoons of the n-type segmentation schemes (three of the modest segmentation designs and one highly segmented design) can be found in Figure 2.3. All four detector designs have both strengths and weaknesses, and the collaboration as a whole will be strongly engaged in the decision as to the final choice for the MAJORANA experiment. The initial MAJORANA prototype phase will likely consist of two modules with 30 kg of detectors in each. The reference plan is still for the cryostats to each be big enough to hold 60 kg, giving us a simple way to test our ability to reliably make large cryostats as well as scale up the mass of the experiment. One cryostat will contain enriched P-PC detectors and the other will hold unenriched, highly-segmented n-type detectors.

2.2 MAJORANA R&D Detectors

We will now describe the research and development detectors being used in support of the MAJORANA experiment, focusing on those from which the data in this dissertation were taken.

2.2.1 The CLOVER

The CLOVER is a commercially available detector from Canberra [29]. It is a close packed array of four, twofold segmented, n-type detectors in a single cryostat. The individual crystals have a relative efficiency of 26% (this corresponds to a mass of roughly 800 g). The detector is instrumented with four high-resolution, cold-FET energy readouts (one for the central contact of each crystal), and three low-resolution, warm-FET position readouts (corresponding to the left two, middle four and right two segments of the detector). See Figure 2.4 for more detail. Coincidences between the energy

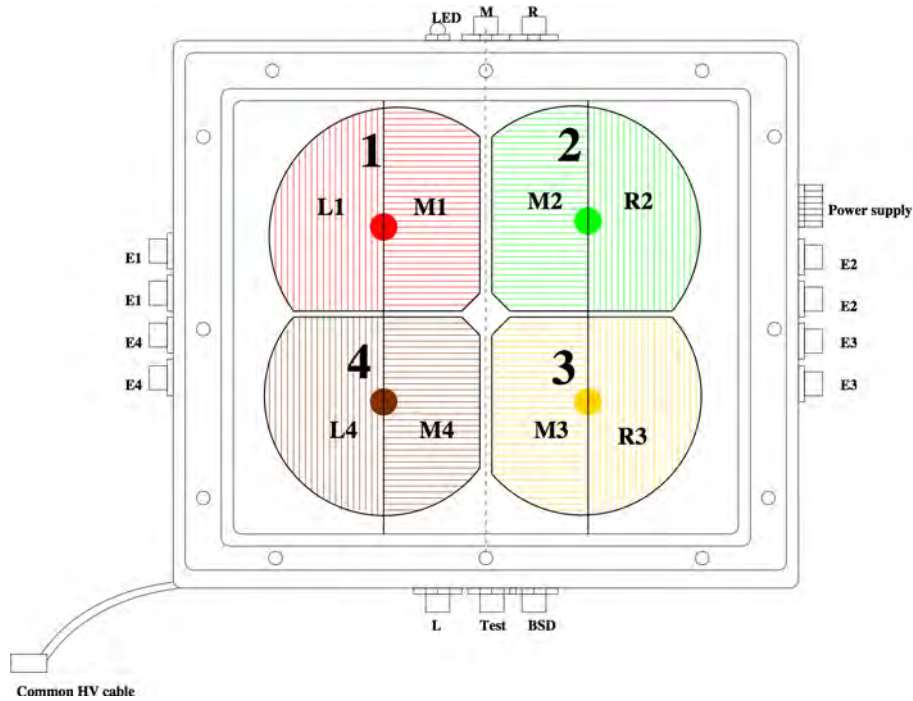


Figure 2.4: A schematic sketch of the CLOVER detector. This figure is from [49].

and position readouts tell us which segment(s) recorded energy depositions. The CLOVER is a good off-the-shelf test bed for many of the analysis techniques we hope to use in MAJORANA because it is several segmented n-type detectors in a single cryostat.

2.2.2 SEGA

The Segmented Enriched Germanium Array (SEGA) is a custom detector built for the MAJORANA collaboration by ORTEC [116]. It is a segmented n-type detector with two axial segments (or “c-channels”) on the central contact and six azimuthal segments (or “s-channels”) on the outer contacts. See the right panel of Figure 2.5. It is also fabricated out of elemental germanium enriched to 86% in ^{76}Ge , making it the only enriched, segmented detector in the world. Interesting SEGA data were taken with the High-Intensity γ -Ray Source (HI γ S), a free electron laser (FEL) located at the Triangle Universities Nuclear Laboratory (TUNL) on the campus of Duke University. The SEGA/FEL data used HI γ S as a γ source with a tunable energy. We took these data in two modes: one with the energy of the γ beam at $Q_{\beta\beta}$ for ^{76}Ge , and another in which the double escape peak energy from the beam coincided with $Q_{\beta\beta}$.

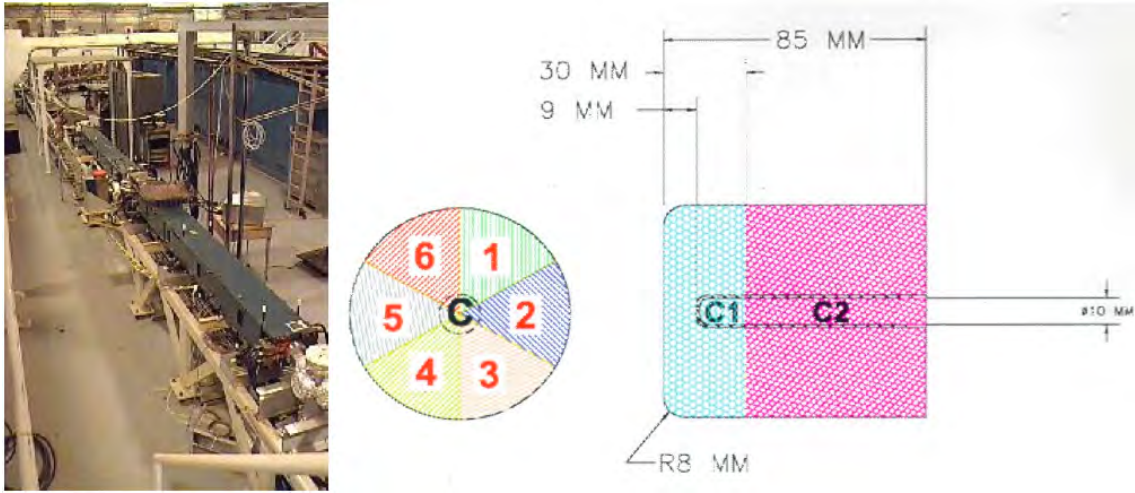


Figure 2.5: A sketch of the SEGA detector[2] (right) showing the segmentation geometry, and the “wiggler” section of the Duke University FEL (left).

2.2.3 Detectors at WIPP

There has been a concerted MAJORANA R&D effort at the Waste Isolation Pilot Plant (WIPP) near Carlsbad, NM. WIPP is a U.S. Department of Energy facility whose primary mission is the permanent internment of transuranic radioactive waste. It is 2150 ft. beneath the surface of the largest oak forrest in the world [123]. This corresponds to an overburden of 1600 MWE.

The MAJORANA collaboration is operating two germanium detectors in our underground laboratory at WIPP. WIPP-n is an n-type detector that has been underground at WIPP in a low-background cryostat since the late 1990’s. It was used as an R&D detector by another student at LANL in support of a prospective dark matter search. We plan to use it primarily for material assay, but we are also using it to study α backgrounds in n-type HPGe detectors. The Multi-Element Gamma Assay (MEGA) was produced by Pacific Northwest National Laboratory, with significant contributions from Los Alamos National Laboratory and the University of Washington. It is also being used for MAJORANA prototyping and R&D because it has similar shielding and cooling requirements and has a large electro-formed copper cryostat. The MAJORANA collaboration recently installed the first three detectors in the MEGA cryostat (at the time of writing, there are actually four detectors in the MEGA cryostat, one of which has either cable connection problems or a front-end electronics board failure). The first background spectrum from the three operational detectors in the MEGA cryostat is in Figure 2.7.

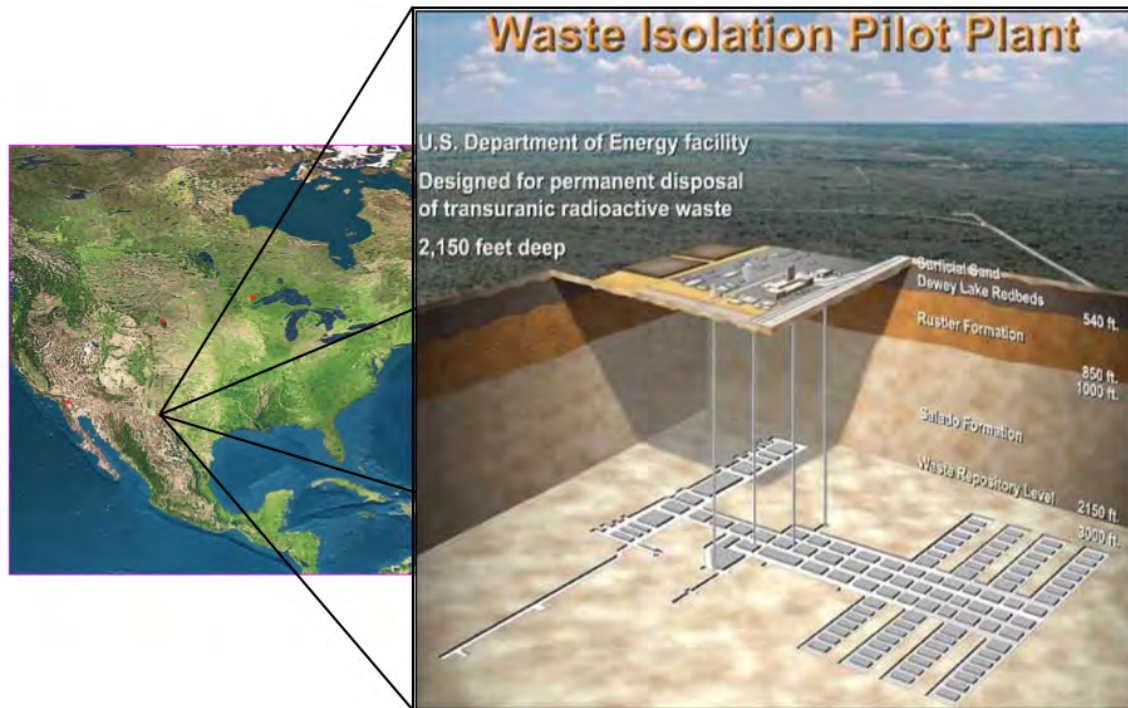


Figure 2.6: A diagram of the WIPP underground (right) showing its location on the North American continent (left). Both panels are from [35].

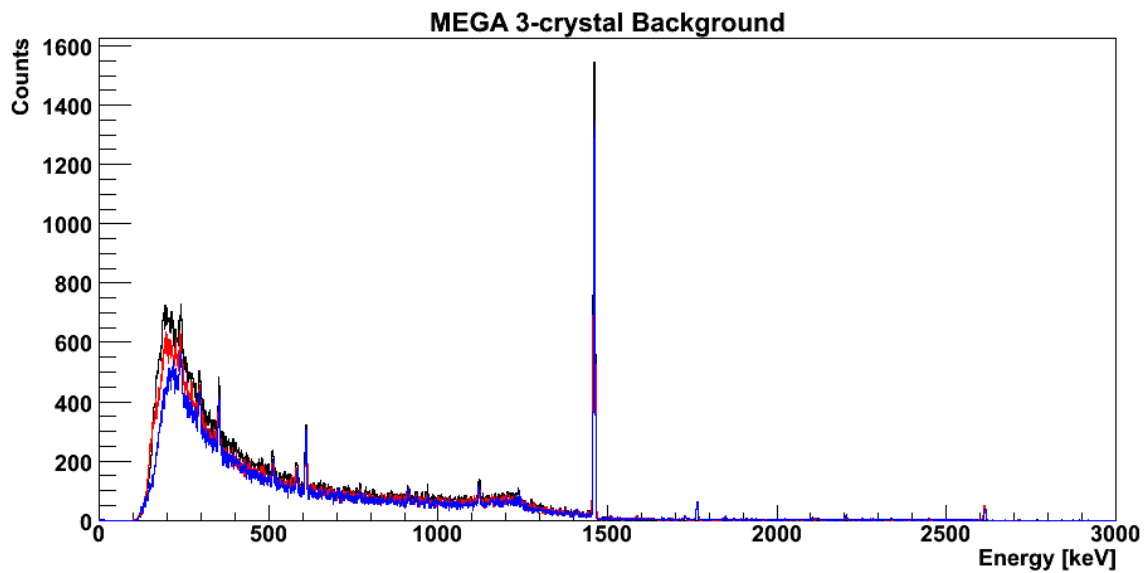


Figure 2.7: The first background spectrum taken with the three detectors currently running in the MEGA array. The most prominent feature is the 1460 keV peak from ^{40}K in the salt because the shield was incomplete.

2.3 Previous $0\nu\beta\beta$ Experiments

In the past few decades, several $\beta\beta$ decay nuclei have been studied using a variety of experimental techniques. Table 2.1 lists the best $0\nu\beta\beta$ half-life limits and deduced effective $\langle m_{\beta\beta} \rangle$ limits for different nuclei (assuming the dominance of light Majorana ν exchange). We can see from Table 2.1 that the most sensitive experiments are the ones where the source and detector are one and the same (*i.e.* Fiorini-style experiments). It is also apparent that the most sensitive experiments to date are the Ge-based Heidelberg-Moscow (HM) and International Germanium Experiment (IGEX) experiments, both of which are completed. The $0\nu\beta\beta$ half-life limit of $T_{1/2}^{0\nu} > 1.9 \times 10^{25}$ y set by the Heidelberg-Moscow collaboration [97] was acquired with five Ge crystals, enriched to 86% in ^{76}Ge , with a total mass of 10.96 kg. The IGEX collaboration [1] obtained a limit of $T_{1/2}^{0\nu} > 1.6 \times 10^{25}$ y using six similarly enriched Ge crystals with a total mass of 8.9 kg. The longest half-life bound corresponds to an effective Majorana ν mass $\langle m_{\beta\beta} \rangle$ of $< 0.32 - 1$ eV, depending on the nuclear matrix elements chosen. Using the recommended ^{76}Ge matrix element from the most recent Renormalized QRPA (RQRPA) calculations [125], $\langle m_{\beta\beta} \rangle$ is < 0.55 eV.

Table 2.1: Best reported limits on $0\nu\beta\beta$ half-lives. The mass limits and ranges are those deduced by the authors and their choices of matrix elements cited in the experimental papers. All limits are quoted at the 90% confidence level, except the Klapdor-Kleingrothaus [96] result, where the bounds are for the 99.7% confidence level. Backgrounds are included if given in the original publication. This table is from Reference [38].

Isotope	Half-Life	$\langle m_{\beta\beta} \rangle$ (eV)	Exposure (kg y)	Background $(\frac{\text{counts}}{\text{keV kg y}})^a$	Reference
^{48}Ca	$> 1.4 \times 10^{22}$	$< 7.2 - 44.7$	4.23		[113]
^{76}Ge	$> 1.9 \times 10^{25}$	$< 0.32 - 1$	35.5	0.19	[94]
^{76}Ge	$> 1.6 \times 10^{25}$	$< 0.33 - 1.35$	8.9	0.06	[1]
^{76}Ge	$= 1.2 \times 10^{25}$	$= 0.24 - 0.58$	71.1	0.11	[96]
^{82}Se	$> 2.1 \times 10^{23}$	$< 1.2 - 3.2$	13		[15]
^{96}Zr	$> 1 \times 10^{21}$	$< 16.3 - 40$	0.0084		[9]
^{100}Mo	$> 5.8 \times 10^{23}$	$< 0.6 - 2.7$	1.76		[15]
^{116}Cd	$> 1.7 \times 10^{23}$	$< 2.2 - 4.6$	0.15	0.03	[43]
^{128}Te	$> 7.7 \times 10^{24}$	$< 1.1 - 1.5$	Geoch.	Geoch.	[22]
^{130}Te	$> 3.0 \times 10^{24}$	$< 0.41 - 0.98$	10.85		[8]
^{136}Xe	$> 4.5 \times 10^{23}$	$< 0.8 - 5.6$	4.84	4.5	[21]
^{150}Nd	$> 3.6 \times 10^{21}$	$< 4.9 - 17.1$	0.015		[17]

^aMost documents generated by the MAJORANA collaboration refer to backgrounds in cnts/ROI/t/y, where the ROI for ^{76}Ge detectors is 4 keV.



Figure 2.8: The inside of the Heidelberg-Moscow experiment. Figure taken from [95].

A recent claim of observation of $0\nu\beta\beta$ in Ge has been put forth by Klapdor-Kleingrothaus *et al.* References [97, 94, 96]. Their assertion has been very controversial [1, 93, 78, 69, 145], and it is strongly dependent on the background model assumed in the analysis. In Klapdor-Kleingrothaus's most recent results from 71.7 kg-years of ^{76}Ge exposure [96], a $0\nu\beta\beta$ signal was claimed with a 4.2σ significance corresponding to a half-life of 1.2×10^{25} y. This result has a background rate in the region-of-interest of 0.11 cts/keV/kg/y, and implies at the 3σ level an $\langle m_{\beta\beta} \rangle$ from 0.24 – 0.58 eV. A debate of the veracity of this result is beyond the scope of this document, but there is a clear need to definitively verify or refute this result. If the Klapdor-Kleingrothaus result is verified, it will be critical to measure the decay rate with an uncertainty small compared to the nuclear matrix element uncertainty. To refute the result, an experiment must have sensitivity to exclude the result with convincing statistics and reduced backgrounds.

2.4 Other Current $\beta\beta$ Experiments

There are currently three collaborations that are funded or partially funded and are constructing or planning to construct next-generation internal source $0\nu\beta\beta$ experiments with active masses from 40 – 200 kg: GERDA, EXO and CUORE. The COBRA collaboration is proceeding with extensive

R&D efforts pursuant to a next-generation internal source $0\nu\beta\beta$ experiments. Last, we will discuss the NEMO and MOON collaborations, which while not using the internal source techniques exploited by the rest of the community, are also exciting experimental programs. The NEMO collaboration has published some impressive $2\nu\beta\beta$ results and have some intriguing plans to enhance their sensitivity to $0\nu\beta\beta$, and the MOON collaboration is pushing forward with a very aggressive R&D program.

2.4.1 GERDA

The GERmanium Detector Array (GERDA) experiment [3] is a project that will be sited at the Gran Sasso underground facility. It uses ^{76}Ge as its $\beta\beta$ source and plans to field ≈ 40 kg of detectors. Their enriched ^{76}Ge detectors will be suspended in a large cryogenic bath of liquid argon. Liquid argon is expected to have low radioactivity, and also acts as shielding from external background radiation. The collaboration will start with 18 kg of existing detectors from other experiments (IGEX and Heidelberg-Moscow) and later add additional segmented detectors for a total mass of ≈ 40 kg. The GERDA collaboration expects to eventually attain sufficient statistics to test the Klapdor-Kleingrothaus *et al.* claim. The GERDA and MAJORANA collaborations have reached an agreement to share resources and knowledge (where appropriate) in their parallel development of these two different detector designs. The ultimate goal is to combine the the two Collaborations in a future experiment that will employ the most appropriate technology for reaching a $\langle m_{\beta\beta} \rangle$ sensitivity < 50 meV.

2.4.2 EXO

The Enriched Xenon Observatory (EXO) collaboration is constructing EXO200, a detector consisting of 200 kg of 80% enriched ^{136}Xe . To improve the energy resolution, EXO200 will combine scintillation light from the liquid Xenon and ionization from drifting $\beta\beta$ electrons. They have estimated they will be able to test the Klapdor-Kleingrothaus *et al.* claim at the 2σ significance level [75] as well as set a much stronger limit on $2\nu\beta\beta$ in ^{136}Xe (which is hitherto unobserved). They expect to start installing the detector and collecting data at the Waste Isolation Pilot Plant in 2007. The EXO collaboration is also proceeding with R&D and design work for a ton-scale EXO. For this stage of the experiment, the EXO Collaboration hopes to also include the ability to tag and trap the daughter Ba ion, allowing for an extremely clean population of $\beta\beta$ events.

2.4.3 CUORE

The Cryogenic Underground Observatory for Rare Events (CUORE) collaboration is proposing to build a large array of cryogenic bolometers to measure the energy released in the decays of ^{130}Te in crystals of TeO_2 at the Gran Sasso underground laboratory [7]. The crystals from which these bolometers are made need not be enriched because ^{130}Te has a high natural isotopic abundance (34.1%). CUORE is envisioned as consisting of 19 towers of bolometers, giving a total TeO_2 mass of 750 kg. This corresponds to a ^{130}Te mass of 206 kg. They expect to start collecting data in 2011. The CUORE Collaboration is currently operating a prototype detector called CUORICINO (or “little CUORE”) underground at Gran Sasso, which is essentially one of the 19 CUORE towers. New results from CUORICINO are intriguing because its sensitivity is beginning to approach that of the ^{76}Ge experiments [8].

2.4.4 COBRA

The Cadmium-Telluride O-neutrino double-Beta Research Apparatus [146], is a proposed $\beta\beta$ experiment that would use CdZnTe detectors to search for the $\beta\beta$ decay of ^{116}Cd and ^{130}Te at the Gran Sasso underground laboratory. CdZnTe detectors are intriguing because they are semiconductor devices, meaning that they have many of the cleanliness and energy resolution benefits of HPGe detectors (though their energy resolution is typically a factor of five to eight worse than a good HPGe detector). They also tend to be much smaller than HPGe detectors, meaning that their γ detection efficiency of these detectors drops dramatically as a function of energy. From an experimental operations standpoint, one of the most attractive features of CdZnTe detectors is that they also operate at room-temperature. This removes the need for cooling, making them much easier to run (though moderate cooling similar to that provided to high-end CCD cameras can substantially improve their energy resolution). COBRA is probably the least developed experiment of the six discussed in this chapter, but the properties of CdZnTe detectors coupled with the possibility of making a $\beta\beta$ search with two isotopes simultaneously makes this an exciting experiment.

2.4.5 NEMO

The Neutrino Ettore Majorana Observatory (NEMO) experiment is a tracking and calorimetry detector array at the Fréjus underground laboratory. This experiment differs from most of the others in this section because they are all (with the exception of MOON) Fiorini-style internal source detectors, while NEMO uses a separate set of foils as its source. This has the advantage of being able to measure the two electrons in the final state of $\beta\beta$ reactions as separate tracks, and the

disadvantage of a poor source mass to mass ratio (the NEMO-3 detector has a maximum capacity of ≈ 10 kg). The NEMO detectors have been very successful in measuring $2\nu\beta\beta$, particularly in ^{82}Se , ^{100}Mo , ^{116}Cd and ^{150}Nd . The collaboration is also working on R&D for SuperNEMO which would be modular in design and have the capacity for ≈ 100 kg of source material.

2.4.6 MOON

The Molybdenum Observatory Of Neutrinos [59] is a dual-purpose experiment for real-time observation of p-p chain solar neutrinos as well as for the search for $0\nu\beta\beta$ in ^{100}Mo . Solar neutrinos would be observed by their capture on ^{100}Mo . This capture is followed by two subsequent β decays, the second of which has a 15.8 s half-life. This reaction can be shown as: $^{100}\text{Mo} + \nu \rightarrow ^{100}\text{Tc} + \beta \rightarrow ^{100}\text{Ru} + \beta$. $0\nu\beta\beta$ will, of course be observed as two simultaneous β 's in the detector. The MOON detector has two possible designs. The first is essentially many layers of thin Mo foil and plastic scintillator laced with wavelength shifting fibers to facilitate light transport. The second is an array of scintillating fibers coated with a thin layer of Mo. ^{100}Mo has a decent natural abundance (9.6%), but probably not sufficient to avoid the need for isotopic enrichment. The primary problems facing the MOON experiment are the fast $2\nu\beta\beta$ rate along with limited energy resolution of plastic scintillator. The many layers inherent to both designs also means that there is an enormous amount of surface area to keep clean, making construction of the full experiment more difficult.

2.5 Germanium Array Experiments

We now move from discussing other $\beta\beta$ experiments, to discussing other experiments using large arrays of HPGe detectors. These are primarily used for accelerator-based, low-energy nuclear structure measurements where high efficiency and resolution as well as nearly 4π coverage are required. The currently running experiments are: Gammasphere [20] in the United States and Euroball [132] in Europe. The TRIUMF-ISAC Gamma Ray Escape Suppressed Spectrometer (TIGRESS) [55] currently being constructed in Canada. There are currently two next-generation arrays in development: the Gamma Ray Energy Tracking Array (GRETA) [104] in the US and the Advanced GAMMA Tracking Array (AGATA) [133] in Europe. The next-generation arrays use clusters of highly-segmented (typically 6×6), hexagonal, tapered detectors to achieve close packing and nearly perfect spherical coverage. In fact, gaps between detectors typically range from a few to less than ten millimeters. Both GRETA and AGATA will also exploit advanced three-dimensional position reconstruction of energy depositions in the array by examining not just the pulse(s) from a segment(s) where an energy deposition actually took place, but also the pulses induced in other segments in the array. Because

the induced pulses on the segmentation contacts are essentially image charges, the magnitude and configuration of these image charges can very tightly constrain the location of any energy depositions in the detectors.

There is a significant overlap between GRETA and the MAJORANA project, to the great benefit of both collaborations. Both are building large, close-packed arrays of germanium detectors. Additionally, the MAJORANA project is exploring the prospect of using highly-segmented detectors and full position reconstruction techniques similar to those used in the GRETA experiment and Gretina, its working prototype. Both MAJORANA and the advanced γ -ray tracking arrays will require the procurement of many advanced germanium detectors from at least one manufacturer, though radiological cleanliness will be the principle challenge for MAJORANA whereas the complexity of the non-standard detector geometries will be the primary difficulty for the γ -ray trackers.

2.6 Experimental Program Summary

We have now introduced the world-wide experimental program interrelated with the work performed for this dissertation. We began by describing the MAJORANA experiment in some detail, paying specific attention to the R&D detectors and facilities. The efforts involving these detectors are aimed at optimizing the design of the MAJORANA experiment and developing novel analysis techniques to mitigate backgrounds while maximizing the number of signal events preserved in the experiment. We discussed the previous generation of $\beta\beta$ experiments, focusing on those that also used ^{76}Ge , then moved on to an overview of current and proposed $\beta\beta$ experiments contemporary with MAJORANA. This discussion of contemporary experiments began with other $\beta\beta$ experiments, and closed with other large arrays of germanium detectors. Both programs are closely related to MAJORANA. The past and current $\beta\beta$ programs share the problems of understanding and mitigating backgrounds while maintaining an experiment with a high duty cycle over a long period of time. The germanium detector arrays have similar problems to MAJORANA in terms of required cooling power, signal routing and data processing.

Chapter 3

SURVEY OF $0\nu\beta\beta$ DECAY MATRIX ELEMENTS AND ASSOCIATED UNCERTAINTIES

The nuclear matrix elements are the largest source of theoretical uncertainty in predicting the $0\nu\beta\beta$ rate from a given particle and nuclear physics model, and the leading source of uncertainty in the model separation analysis described in Section 1.4. Historically, there has been roughly a factor of two disagreement in the various methods for calculating the matrix elements for $0\nu\beta\beta$. If this situation did not improve, the analysis in Section 1.4 would be impossible. We shall now present an overview of the current state of the field in calculating $M_{0\nu}$, and show that much of the historical difference in these calculations has stemmed from different assumptions about the underlying physical models previous authors have used. We will demonstrate that the real difference in the calculation of $M_{0\nu}$ is much lower than a factor of two, given similar initial assumptions. This still begs the question of the validity of those underlying assumptions, but it is indeed encouraging that the $0\nu\beta\beta$ theory community is beginning to converge to a standard set of methods for this work.

3.1 *Matrix Element Calculations*

The nuclear matrix element in Equation 1.1 contains the information about the nuclear structure of the reaction, and is influenced by the exchange mechanism considered for the transition. We discuss the process by which authors calculate the numerical values of $M_{0\nu}$. Two formalisms have been used to make this calculation: the shell model and the quasiparticle random phase approximation (QRPA). We begin with a discussion of the matrix elements by briefly discussing shell model calculations, and then focus in on the QRPA method and its relatives. We move on to enumerating the uncertainties associated with the QRPA family of calculations. We will then delve into two competing methods for normalizing the unfixed parameters in the QRPA model calculations. This last point is extremely important because, as we will show, much of the difference in previous $M_{0\nu}$ calculations comes from the fact that they have made different assumptions regarding their input physics. Finally, we close this chapter by listing the cumulative uncertainties in the $0\nu\beta\beta$ matrix element calculations for ^{76}Ge and several other $\beta\beta$ isotopes. For the balance of this document we will adopt the conventions for matrix element definitions used in Reference [125]. We take the nuclear matrix element to be defined

as:

$$M^{0\nu} = \left(\frac{g_A}{1.25}\right)^2 \left\langle f \left| \frac{M_F^{0\nu}}{g_A^2} + M_{GT}^{0\nu} + M_T^{0\nu} \right| i \right\rangle \quad (3.1)$$

Here, $|i\rangle$ and $\langle f|$ are the initial and final ground state wave functions. For details on why this slightly peculiar parameterization in terms of g_A , refer to the above reference. The M's ($M_F^{0\nu}$, $M_{GT}^{0\nu}$ and $M_T^{0\nu}$) are the Fermi, Gamow-Teller, and Tensor operators respectively (details about the explicit forms of these operators are found in Reference [140]). We now discuss the shell model and QRPA methods for calculating nuclear matrix elements. More information about each technique can be found in Reference [124].

3.1.1 Shell Model

The shell model (also sometimes referred to as the “Independent Particle Model”) grew out of the realizations in the 1940’s and 50’s that the nuclei behaved not just as a collective fluid (the liquid drop model of the nucleus had been hitherto fantastically successful), but also as a collection of individual bound particles. This paradigm shift was largely driven by the discovery of “Magic Numbers” of nucleons mirroring the stable states associated with closed electron shells in atomic physics. In fact, shell model calculations proceed very analogously to those for electron shells—matrix elements are calculated using some number of particles in some state interacting through a potential. The principle difference lies in the fact that in the nuclear shell model case, the potential does not arise from a simple electrostatic interaction with some essentially infinitely massive core with only small corrections for the particles in question interacting with each other. Instead, the nuclear potential comes from interactions with the nucleons with each other (mostly through two-body interactions, but some authors add three-body interactions into their models as well), via a collection of several complicated potentials. Nevertheless, we can treat this aggregate two-body potential as an effective potential. One of the most common central potentials used in shell model calculations is a modification to the Fermi function, known as the Woods-Saxon (WS) potential:

$$V^{WS}(r) = \frac{-V_0}{1 + e^{\frac{r-R_0}{a}}} \quad (3.2)$$

Typical parameter values for the WS potential are: $R_0 = r_0 A^{1/3}$ (where $r_0 \approx 1.2$ fm), $V_0 \approx 50$ MeV, and $a \approx 0.5$ fm. This potential (for $A = 76$) is shown in Figure 3.1. Because the WS potential does not have eigenfunctions that can be given in a closed, analytic form, many authors make the approximation of using a harmonic oscillator or infinite square well potential. These approximations are fine for situations in which the author is only interested in single-particle ground states, but they quickly become unphysical when dealing with excitations or multiple particles because both

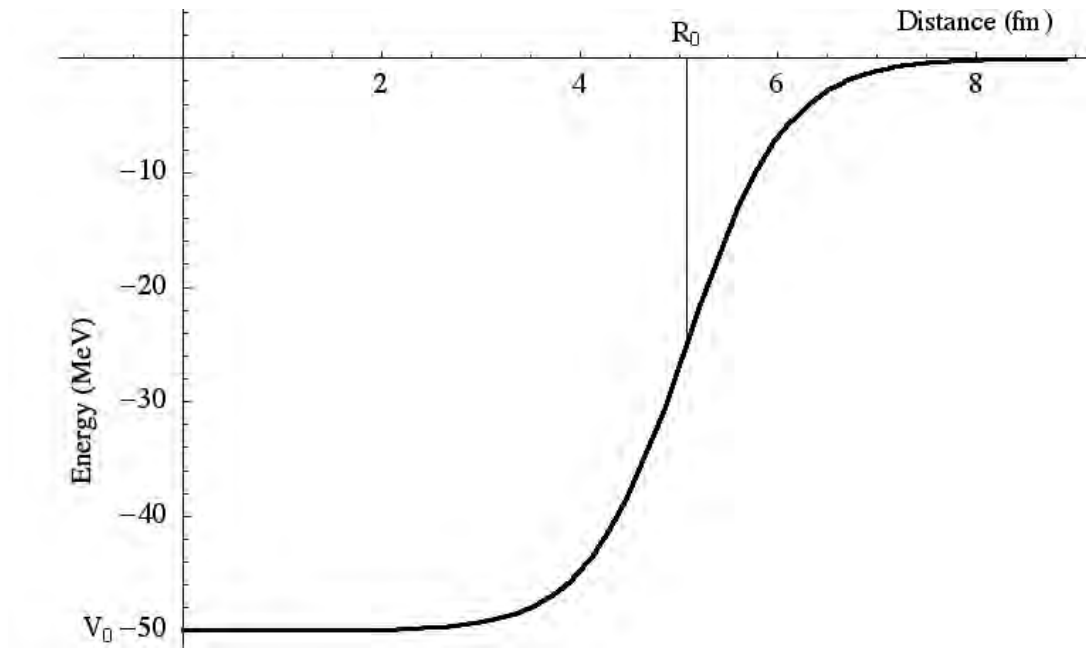


Figure 3.1: The Woods-Saxon Potential for $A = 76$

potentials are infinite. This means that it is very easy to accidentally wander into regions where the energies of interest would actually be in the continuum rather than bound to the nucleus. Modern computing techniques, however allow most authors to calculate energy levels and matrix elements in terms of the WS potential.

We run into further complications when applying the shell model to the nuclear many-body problem (compared to calculations involving electron levels) in that there are two kinds of particles to consider: protons and neutrons (as opposed to just worrying about electrons in the calculation of atomic shells). This means that we must treat protons and neutrons differently when allowing them to interact in a nuclear system (the simplest example of this is that protons have a coulomb interaction that must be accounted for whereas neutrons do not). Excitations to nuclear systems in the shell model are treated analogously to a Fermi gas of nucleons being excited above (or relaxed back below) a Fermi energy determined by the number and type of nucleons present (typically parameterized by Z and A). Applications of the shell model to the calculation of $0\nu\beta\beta$ matrix elements can be found in Reference [31].

3.1.2 QRPA Family

The Quasiparticle Random Phase Approximation (QRPA) family of calculations can most easily be thought of as a quantum mechanical recasting of the liquid drop model of the nucleus. Authors who work in the QRPA framework treat mostly collective states rather than those of independent particles. QRPA calculations tend to use much of the mathematical language used to describe superconductivity, including BCS-like wave functions analogous to those derived by Bardeen, Cooper and Schrieffer (hence the acronym) to describe the “bosonized” pairs of electrons in superconducting materials. For more information on BCS theory, see References [18, 131]. The difference between this and the original liquid drop model is that the collective vibrations in QRPA are actually vibrations in the different wave functions of the nucleus rather than the density of some mysterious, positively charged nuclear fluid. Typically these vibrations fall into one of four categories:

- Breathing modes: These are vibrations in the radial part of the spatial wave function (we treat only the radial part because the collective angular dependence is determined by the angular momentum quantum numbers of a given state).
- Twist modes: These are collective motions of the nucleus in which different parts of the nucleus are rotating, but in such a way that the orbital angular momentum of the nucleus remains constant. The name of this mode is very suggestive and exceptionally useful in visualizing this type of motion.
- Spin modes: These are just vibrations in the spin part of the wave function, again with the constraint that the total spin of the nucleus is constant.
- Isospin modes: These involve the protons or neutrons in a nucleus vibrating either in or out of phase with one another, causing vibrations in the isospin wave function.

Breathing and twisting modes were included in the liquid drop model whereas spin and isospin modes, being inherently quantum mechanical in nature, were not.

What differentiates QRPA from Random Phase Approximation (RPA) calculations is that RPA only includes correlations between particles and holes in the nuclear system. This works very well for nuclei close to closed shells, but breaks down once we examine nuclei farther away. At this point the particle-particle and hole-hole correlations (that is those between other types of quasiparticles, hence the name) also become large enough to affect the nuclear states and single particle-motion. QRPA is the particular extension to this quantum mechanical liquid drop model that includes all

quasiparticle correlations (there is also a particle-particle RPA which only includes particle-particle correlations, and is something of an intermediate step between RPA and QRPA). The application of QRPA to $0\nu\beta\beta$ matrix elements is detailed in Reference [125] and Reference [135].

It is important to realize the relative strengths and weaknesses of the QRPA and shell model families. QRPA is capable of including an effectively unlimited number of single-particle states, but a limited number of particle-hole configurations. The opposite is true of the shell model. In this light, it is encouraging that the two methods arrive at similar answers. Most of the calculations being done in this area are in the QRPA or Renormalized QRPA (RQRPA) framework. Encouraging work, however continues in the shell model, and confidence in this technique will only improve as computing speeds and numerical methods become more advanced. Overviews of the matrix element calculations are available in the literature [68, 136]. Recent works by Rodin *et al.* [125] and Suhonen [135] provide a spirited, written debate concerning the implementation of QRPA. This debate has helped elucidate why the collection of previous QRPA calculations have resulted in numerous differing results. In particular, the free parameters in the theory can be normalized differently. Additionally, not all calculations have included the same input physics in their descriptions of the virtually excited states of the intermediate nucleus.

3.2 Sources of Theoretical Uncertainties

In the last few years, there has typically been a roughly factor of two to three disagreement globally in the numerical values of the matrix elements calculated in QRPA and related methods. Many have started simply taking the mean of these values as the central value and the standard deviation as the uncertainty [12]. This would be a valid approach if the spread in these matrix element calculations were due to the results of these calculations sampling some random distribution. Instead it seems that much of the disagreement in the values of these matrix elements comes from different choices of the constants parameterizing the strengths of the various interactions in the theory as well as differing assumptions regarding the underlying micro-physics. It has been shown [125] that when the same parameters are used in the construction of this calculation, the level of disagreement in the resulting matrix elements drops to the level of approximately 20%. The question now becomes how one appropriately adjusts these different parameters in a rigorous and systematic manner. See Reference [125] for more information on QRPA uncertainties.

3.2.1 *The Quasiparticle Mean Field*

To make these problems computationally tractable, we consider the model space available to these calculations as finite. To compensate for this, nearly all authors fit the pairing interactions to reproduce the pairing gaps in nuclear binding energies. The only problem with this technique is that it breaks down for nuclei with closed neutron and proton shells (such as ^{136}Xe and ^{116}Sn respectively). Some authors instead modify the single particle energies near the Fermi surface (mostly considering the Woods-Saxon potential discussed in Section 3.1.1) so that they correctly reproduce the low-energy quasiparticle spectra of the neighboring odd mass nuclei.

3.2.2 *Many-Body Approximations*

The base QRPA method works in the quasi-boson approximation in which the commutator of the bi-fermion operators (that is, the operators that annihilate or create neutrons and protons) are replaced with their expectation values in the BCS ground state. In doing so, the quasi-boson approximation violates the Pauli exclusion principle. This is tantamount to ignoring the off-diagonal elements in these operators. The renormalized QRPA (or RQRPA) uses QRPA states instead of BCS states to get the above expectation value, and this does a better job of accounting for the real values of these commutators. This subsequently produces a more accurate calculation [141, 125].

3.2.3 *Coupling Constants*

There are three main coupling constants in these calculations: g_{pair} , g_{ph} , and g_{pp} . The parameter g_{pair} sets the strength of the nucleon-nucleon pairing force. The numerical value of the $0\nu\beta\beta$ matrix element seems to depend rather weakly on this parameter. The coupling constant g_{ph} is for the particle-hole interaction. Most people doing this calculation tend to adjust this one so that it reproduces the giant Gamow-Teller resonance, or some other collective state. Values of g_{ph} between about 0.8 and 1.0 do not change the $0\nu\beta\beta$ matrix element by more than about 10%. Last, g_{pp} scales the strength of the particle-particle interaction. The adjustment of this parameter is far more controversial than the others, and will be discussed at length in Section 3.3. Also there has been considerable debate over the quenching of the axial-vector coupling constant for $\beta\beta$ calculations. Most authors adopt values of either 1.0 or 1.25. The authors of Reference [125] tabulate values of $M_{0\nu}$ for both, and as long as they adjust g_{pp} to reproduce the $2\nu\beta\beta$ rate, changes to $M_{0\nu}$ are less than 10%.

3.2.4 *Perturbative Effects*

This covers several inputs to the calculations that lead to small corrections in $M_{0\nu}$. First, there are two higher order, momentum dependent terms in the nucleon current, namely the induced pseudoscalar, and weak magnetism terms. They come into play because the virtual neutrino has such a high momentum (≈ 100 MeV on average). This leads to the Tensor Term sometimes seen in the expression for $M_{0\nu}$. The magnitude of this term varies slightly from nucleus to nucleus, but generally represents a roughly 30% reduction in the value of the matrix element.

Second, we account for the finite size of the nucleon through the momentum dependence of the nucleon form factors (see Reference [140] for details). Previously this effect was neglected because it was expected to be small (and it was compared to the factor of 2 – 3 estimated uncertainty in $M_{0\nu}$ when calculated in the QRPA framework). In fact, when one takes the finite nucleon size into account, it lowers the value of $M_{0\nu}$ by about 10%, a significant fraction of the current uncertainty thus making it an important correction.

Last, the shape of the nucleus has typically been assumed to be spherically symmetric. For the initial and final nuclei, this is nearly experimentally true (though deformation could affect the intermediate nucleus if it passes through a sufficiently excited state). However, since we are now being forced to concern ourselves with effects on the order of 10% or so, the effects of nuclear deformation bear examination. There has been some progress in recent years in the calculation of $2\nu\beta\beta$ matrix elements of ^{76}Ge accounting for aspheric deformations [139]. The authors of Reference [139] saw nontrivial differences from this effect, and one might guess that there would be a similar effect in the $0\nu\beta\beta$ matrix elements. ^{150}Nd is a $\beta\beta$ decay isotope many physicists would like to examine due to its rather large phase space factor ($\approx 2.7 \times 10^{-13} \text{ y}^{-1}$ compared to a value on the order of 10^{-15} y^{-1} for most isotopes) and high endpoint energy (3.367 MeV compared to more typical values of 1–2 MeV). The problem is that ^{150}Nd is a highly deformed nucleus and therefore a notoriously difficult one to treat in any framework. Obviously more work on this area is extremely desirable.

3.2.5 *Size of the Model Space*

Early calculations of the $0\nu\beta\beta$ matrix elements, unsurprisingly used rather small model spaces. Mostly, they only included two major shells near the Fermi surface. Some later calculations have moved on to using up to five major shells. In general, results from calculations involving larger model spaces are suppressed compared to those calculated in smaller ones for the same value of g_{pp} (≈ 1). To complicate matters further, authors using different model spaces obtain significantly different results for the tuning of g_{pp} . The origin of this difference is not at all well understood. In particular,

Reference [134] shows that if you add the $N = 2$ shell to the $N = 3$ and 4 shells in the model space, the value of the $0\nu\beta\beta$ matrix element for ^{76}Ge drops by around a factor of 3. This is very surprising because the $N = 2$ shell lies so far from the Fermi surface, and intuitively one would not think that it would have much influence. Results from Reference [125] and Reference [126], however contradict this result, showing relatively small effects on $M_{0\nu}$ from the model space.

3.2.6 Closure Approximation

The $0\nu\beta\beta$ matrix elements are usually calculated assuming that the intermediate nuclear states exhibit closure, *i.e.* that:

$$\sum_{n,\pi} |J_n^\pi\rangle \langle J_n^\pi| = \mathbb{1} \quad (3.3)$$

This means that the energies of the intermediate states ($E_n - E_i$) are replaced by an average of this quantity that works out to ≈ 10 MeV. This obviously, immensely simplifies the numerical calculations. The authors of Reference [126] have examined the details of this assumption and any effects on the matrix element are less than 10% because the virtual neutrino has a momentum of ≈ 100 MeV (*i.e.* much larger than the differences in the nuclear excitation energies).

3.2.7 Two-Nucleon, Short-Range Correlations

Most calculations account for the correlations between nucleons by simply multiplying the two-particle wave functions by a Jastrow correlation function:

$$f(r) = 1 - e^{-\gamma_1 r^2} (1 - \gamma_2 r^2) \quad (3.4)$$

with $\gamma_1 = 1.1 \text{ fm}^{-2}$ and $\gamma_2 = 0.68 \text{ fm}^{-2}$. This correlation function is shown in Figure 3.2. This technique is something of an “industry standard” for $M_{0\nu}$ calculations and has not heretofore been particularly controversial, except that the short-range correlations reduce the $0\nu\beta\beta$ matrix elements more for higher g_{pp} values. This lead many authors to claim that an accurate determination of g_{pp} was therefore all the more important. More details on this argument are in Reference [140]. More recently, the authors of Reference [100] claimed that use of the Jastrow correlation function actually over suppresses the two-particle wave functions at short distances (In fact we can see from Figure 3.2 that Equation 3.4 drops to zero at short ranges). The simple multiplication also changes the wave function normalization. The authors of Reference [100] argue that a much more elegant solution to the short-range correlation problem is to use a unitary operator to account for these correlations. The results in Reference [100] indicate that this operator-based approach tends to lead

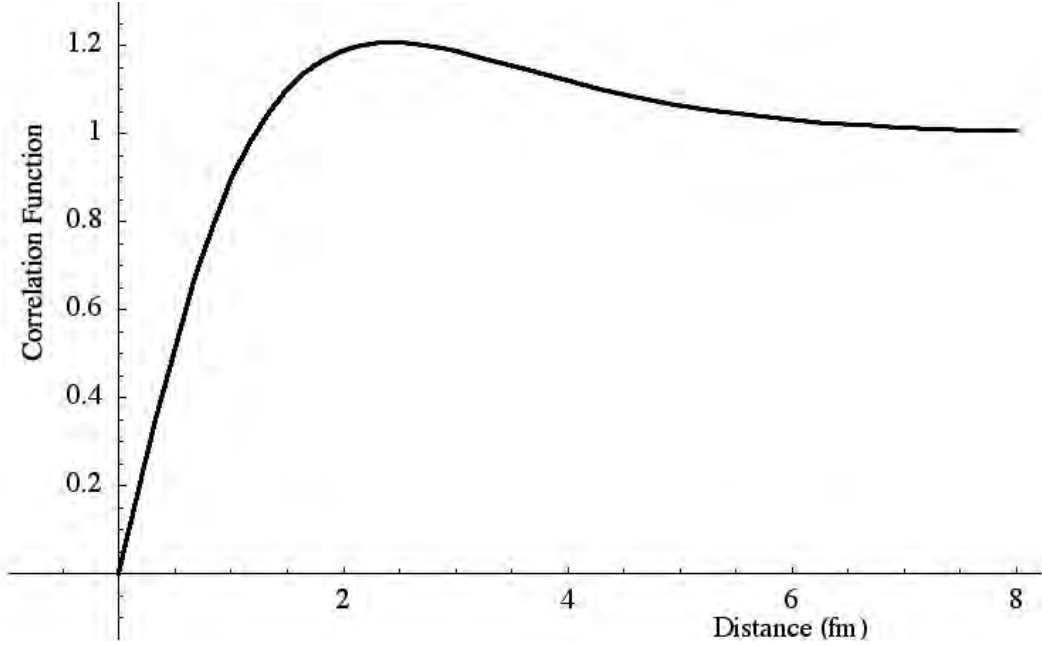


Figure 3.2: The short range correlation function for QRPA calculations from Equation 3.4. The “Distance” on the x-axis is the distance between nucleons.

to a 7–16% reduction in $M_{0\nu}$ (compared to 30–40% with the Jastrow method). Furthermore, because the operator-based method tends to affect the different multi-poles of $M_{0\nu}$ more uniformly than the Jastrow method, the dependence of $M_{0\nu}$ on g_{pp} is mitigated. The value of g_{pp} is still important, but Reference [100] gives the $0\nu\beta\beta$ theory community another avenue they can pursue in refining their understanding of $M_{0\nu}$ calculations.

3.2.8 Overlap of Intermediate Nuclear States

An overlap factor is often included in QRPA calculations to account for the fact that, in the usual approximation scheme, the intermediate states generated from the initial and final nuclei are not perfectly orthogonal. Typically this overlap factor is of the simple form:

$$X^i X^f - Y^i Y^f, \quad (3.5)$$

where X and Y are sets of amplitudes that come from solving the QRPA eigenvalue problem. They are defined in Reference [89]. The problem with this approach is that the $\beta\beta$ decay problem deals with the ground (or vacuum) states of both the initial and final nuclei. The overlap factor of the initial and final BCS ground states is an important part of that for the intermediate nuclear states.

This initial to final overlap factor is ≈ 0.8 for spherical nuclei (it would be 1 if the states lined up properly), and is commonly neglected in $\beta\beta$ matrix element calculations. If an author fits g_{pp} to the $2\nu\beta\beta$ rate, the dependence of the final nuclear matrix element is significantly reduced since the initial and final states are the same as in $0\nu\beta\beta$, and the overlap factor gets absorbed into the adjustment of g_{pp} . This factor is much more important in QRPA calculations for deformed nuclei.

3.2.9 Phase Space Integrals

The expression for the $0\nu\beta\beta$ rate (Equation 1.1) contains the phase space integral $G_{0\nu}$ which is ostensibly “precisely calculable” (to the precision of the input parameters for the calculation of course). The “uncertainty” arising from something exactly calculable like a two-particle phase space is perhaps something of a poor choice of words. The problem is that most authors scale the expression for $M_{0\nu}$ by the nuclear radius R to make it unit-less. We then compensate for this scaling factor by including a $1/R^2$ into the phase space integral $G^{0\nu}$. The nuclear radius takes the form

$$R = r_0 A^{1/3} \quad (3.6)$$

The value of r_0 is not precisely defined, but is of order 1 fm. There is a corresponding spread in the values different authors use for r_0 , ranging typically from 1.0 to 1.3 fm (the correct values should probably be fit out of scattering data for each nucleus). This can result in an error of as much as $\approx 70\%$ ($1.3^2 \approx 1.7$). This is, in principle, a simple error to avoid. We simply have to either ensure that we use values of $M_{0\nu}$ and $G^{0\nu}$ from the same reference or that we appropriately re-scale their product by the ratio of their r_0 's. This is sometimes difficult because not all authors are explicit in their choice of the numerical value of r_0 . As a result, great care must be taken when combining values of $M_{0\nu}$ and $G^{0\nu}$ from different references.

3.3 Parameter Adjustment

As stated in Section 3.2.3, there are three coupling constants in the (R)QRPA calculations in question: g_{pair} , g_{ph} , and g_{pp} . Like any theory with empirical coupling constants, these have to be adjusted to reproduce some appropriate set of experimental data. The adjustment of the first two is not controversial, and there is overwhelming consensus in the community as to appropriate values. On the other hand, the adjustment of g_{pp} has become somewhat contentious in the past few years. There are two competing methods for the appropriate way to normalize g_{pp} . Some authors argue that we should adjust g_{pp} to reproduce the rates of the β^- decays and the β^+/EC of the intermediate nucleus in the $\beta\beta$ process. Others argue that we should instead adjust g_{pp} to reproduce the $2\nu\beta\beta$ rate. Arguments for both approaches are detailed in the next two sections.

3.3.1 Normalizing to the Weak Decays of the Intermediate Nucleus

The argument for normalizing the g_{pp} parameter in this way is detailed in Reference [135], and we present a summary of it here. The crux of the case for this approach is that since $2\nu\beta\beta$ proceeds mostly via the 1^+ state of the intermediate nucleus (a phenomenon referred to as single-state dominance), the $2\nu\beta\beta$ matrix elements are much more sensitive to g_{pp} than the $0\nu\beta\beta$ matrix elements (since $0\nu\beta\beta$ depends on a much broader spectrum of J^π states). The author of Reference [135] goes on to argue that this means we need to use another method to fix g_{pp} , and claims that the way to do so is to tune g_{pp} so that the QRPA calculation correctly produces the lifetimes of the various weak decays of the intermediate nucleus (WDIN). He includes a table in his paper (Table 3 in Reference [135], reproduced here as Table 3.1) that lists seven points enumerating the relative strengths and weaknesses of each technique. We begin with the rows on the table in which the author claims a

Table 3.1: This table’s text was reproduced from Reference [135]. Original caption: “Pros (+) and cons (–) of the two discussed recipes to fit the parameter g_{pp} . For more explanation on various points see the text.”

Point	Fit to β^- and/or EC decay(s)	Fit to $2\nu\beta^-\beta^-$ decay
1	One, two or more observables can be used for the fit (+)	Only one observable can be used for the fit (–)
2	Direct access to grass-root-level deficiencies of a nuclear model (+)	Two or more compensating errors may conspire to produce a good $2\nu\beta^-\beta^-$ rate (–)
3	The beta-decay properties better reproduced (+)	The $2\nu\beta^-\beta^-$ decay properties better reproduced (+)
4	Error limits from comparison of the experimental and computed $2\nu\beta^-\beta^-$ decay rate (+)	Advisable to check against data on β^- decays
5	Largely eliminates the model-space dependance of the computed $0\nu\beta^-\beta^-$ decay rates (+)	Largely eliminates the model-space dependance of the computed $0\nu\beta^-\beta^-$ decay rates (+)
6	Can be extended to study forbidden contributions, e.g., 2^- , in $0\nu\beta^-\beta^-$ decay (+)	No access to a possible variation of g_{pp} from multipole to multipole (–)
7	Can access $\beta\beta$ decays where no $2\nu\beta\beta$ data exists	Can access $\beta\beta$ decays where no direct β -decay data exists (+)
Balance	$7 \times (+)$	$3 \times (+)$ and $3 \times (-)$

positive aspect of the WDIN method and a negative for the $2\nu\beta\beta$ normalization. Point 1 claims

that the WDIN technique can fit more than one observable compared to the $2\nu\beta\beta$ technique, which only has one observable. This is true since the intermediate nucleus can, in principle decay via β^- , β^+ , or electron capture, whereas $2\nu\beta\beta$ is only one observable. Point 2 is closely tied to point 1, in that the different decay channels available to the intermediate nucleus allows us to try and unfold some of the deficiencies in whatever nuclear model we are considering. The author of Reference [135] also claims that because the $2\nu\beta\beta$ matrix element depends essentially on a sum of many states, more than one compensating error can “conspire to produce a good $2\nu\beta^-\beta^-$ decay rate” in spite of underlying problems with the physical model (*i.e.* that a nuclear model could have offsetting physics errors that still give an accurate $2\nu\beta\beta$ rate in spite of underlying inaccuracies). In point six, the author of Reference [135] points out that the WDIN method can be extended to study the contributions of forbidden multipoles to the $0\nu\beta\beta$ amplitude. This is impossible in the $2\nu\beta\beta$ fit since it only accesses the sum of all the amplitudes. Next we examine the rows in the table that have positive aspects for both approaches. These points stem directly from the fact that both techniques are tuned to different process. Point three, for instance states that WDIN better reproduces the β decay rate while the $2\nu\beta\beta$ method better reproduces the $2\nu\beta\beta$ rate. Not surprising really... Both remove much of the dependence on the size of the model space, and both can access isotopes that the other technique cannot. The final (and summarizing) line of the table states that the $2\nu\beta\beta$ method has a total of three positive aspects, three negative and one neutral, while the WDIN has at total of seven positive points.

3.3.2 Normalizing to the $2\nu\beta\beta$ Rate

The argument for normalizing g_{pp} to the $2\nu\beta\beta$ rate is detailed in Reference [125]. First, the authors of Reference [125] claim that the $2\nu\beta\beta$ rate is suitable for this parameter tuning because the initial and final states are identical as those for $0\nu\beta\beta$. This is important because of the approximations to the wave functions and their altered normalization as discussed previously in Section 3.2.7 and Section 3.2.8. They go on to state that the $2\nu\beta\beta$ method is a better one because the WDIN rates are only known for three nuclear mass numbers (100, 116, and 128). Next, they argue that the so-called single state dominance for the $J^\pi = 1^+$ state in $2\nu\beta\beta$ is not as overwhelming as previously thought. While it is certainly true that the 1^+ state has a larger contribution to the $2\nu\beta\beta$ state than the other multipoles, the other higher states have nontrivial contributions as well. There is also the dilemma that the β and β^+/EC matrix elements move in opposite directions when we vary g_{pp} . This makes it difficult to choose one of them to use to normalize g_{pp} . It is far more appropriate to use the sum of all channels in the amplitude. This is most easily done by examining the $2\nu\beta\beta$ rate.

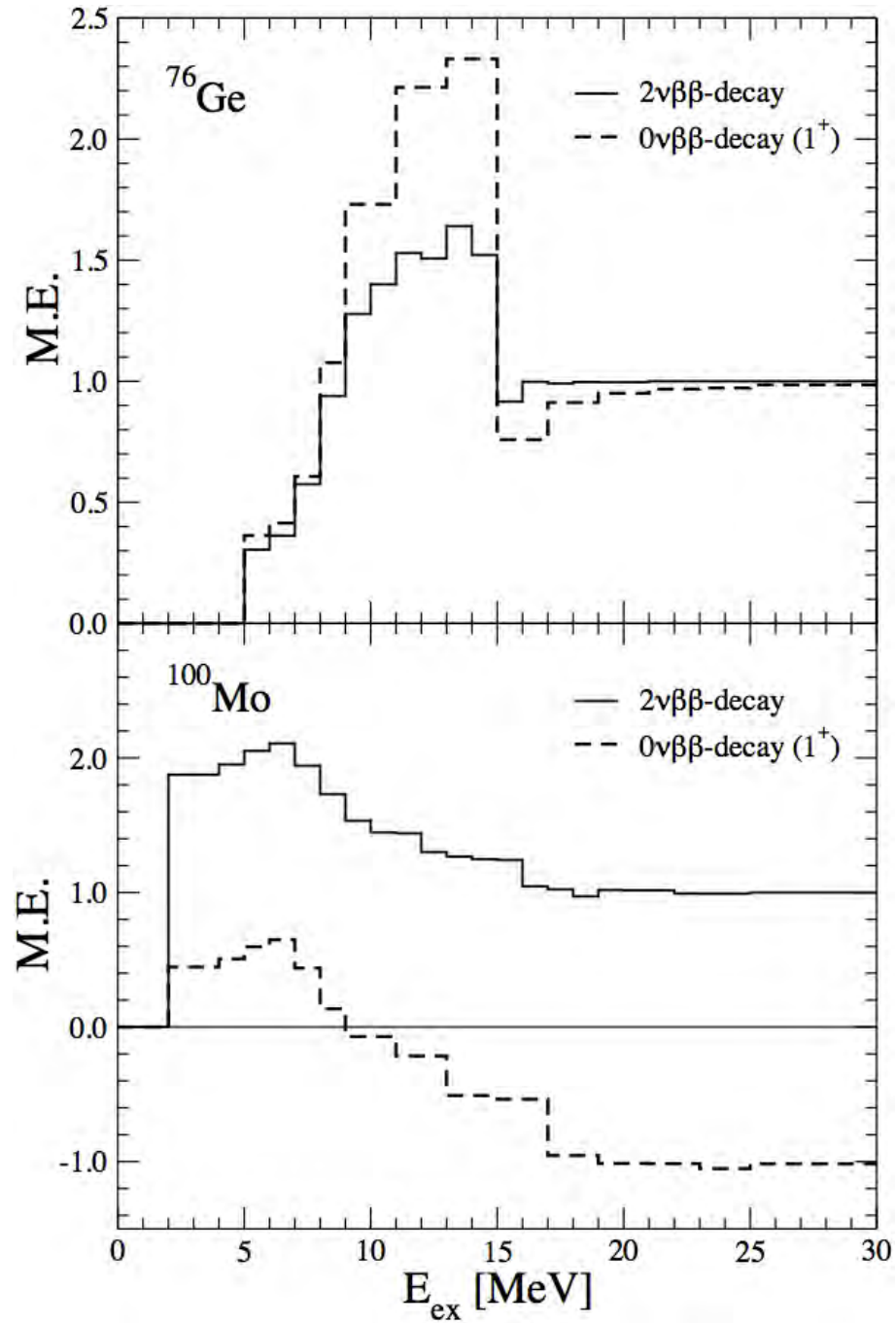


Figure 3.3: Running sum of the $2\nu\beta\beta$ and 1^+ component of the $0\nu\beta\beta$ matrix elements for ^{76}Ge and ^{100}Mo as a function of excitation energy, $E_{ex} = E_n - \frac{E_i + E_f}{2}$. Figure from Reference [125].

We see in Figure 3.3 that while the $2\nu\beta\beta$ matrix element is certainly not identical to the $0\nu\beta\beta$ 1^+ multipole, they are obviously correlated. By making sure that the $2\nu\beta\beta$ matrix element is well matched by a calculation, authors effectively constrain the 1^+ part of the $0\nu\beta\beta$ matrix element. Figure 3.4 shows the $0\nu\beta\beta$ matrix elements for ^{76}Ge and ^{100}Mo , decomposed in to even and odd parity, the 1^+ state specifically and the total matrix element. This shows that any single state dominance visible in the $2\nu\beta\beta$ matrix elements is wiped out in the $0\nu\beta\beta$ case (though the 1^+ multipole still contributes heavily to the total). Thus there is no real reason to pick any one particular state or transition for the adjustment, making the sum accessed in the $2\nu\beta\beta$ transition more attractive.

The authors of Reference [125] also take great pains to demonstrate that adjusting g_{pp} to the $2\nu\beta\beta$ rate removes the dependence on the other model parameters while they claim that the author of Reference [135] doesn't go through the same exercise for the WDIN technique. The 1^+ multipole contributing to $M_{0\nu}$ has a slope much steeper than the others under variation of g_{pp} , making it especially important to properly constrain (see Figure 3.5).

Last, the authors of Reference [125] argue that while the WDIN technique can be used to properly reproduce the β^- decay rates of intermediate nuclei for mass numbers for which we have data, it cannot also simultaneously reproduce the β^+/EC amplitude (the other component of that decay). This is an inherent drawback of the QRPA method since it was never intended as a way to describe the detailed properties of non-collective states. This is still more reason to use the $2\nu\beta\beta$ rate to adjust g_{pp} since, once again, it is a sum over all intermediate states.

Furthermore, the matrix elements from Reference [125, Erratum] are more consistent with the shell model calculations than those from Reference [135]. To quantify this, we define the average fractional difference between the two QRPA calculations and the shell model as:

$$D = \frac{1}{N} \sum_{i=1}^N \frac{A_i - B_i}{B_i}, \quad (3.7)$$

where N is the number of isotopes under consideration, $\{A_i\}$ is the set of matrix elements from one of the QRPA calculations and $\{B_i\}$ is the set of shell model matrix elements. We then read off the matrix element values from Table 1.2 for: ^{76}Ge , ^{82}Se , ^{96}Zr , ^{100}Mo , ^{116}Cd , ^{130}Te and ^{136}Xe (chosen because they cover all of three models we are examining here) for the two QRPA calculation methods and the shell model calculations (making $N = 7$ for this). We find that for the matrix elements from Reference [125, Erratum], $D = 2.2$, and for those from Reference [135], $D = 3.8$. This better agreement with the shell model combined with the very convincing arguments made in Reference [125] lead us to quote values of $M_{0\nu}$ calculated using g_{pp} normalized to reproduce the $2\nu\beta\beta$ rate for the balance of this document. Still, the fact that even in the best case QRPA and shell

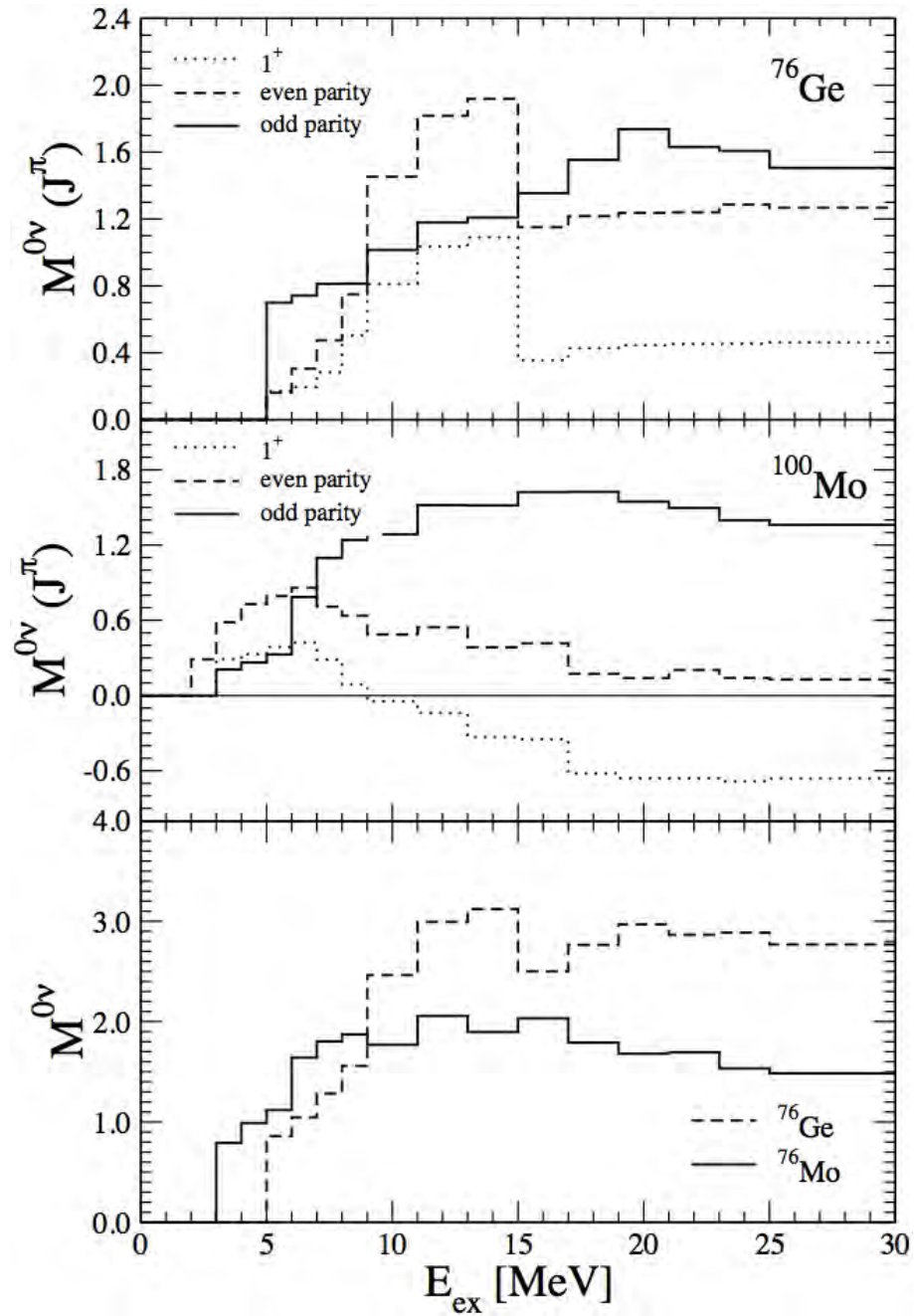


Figure 3.4: $0\nu\beta\beta$ matrix elements for ^{76}Ge and ^{100}Mo , both totaled and broken down by parity (with the 1^+ state shown separately). Figure from [125].

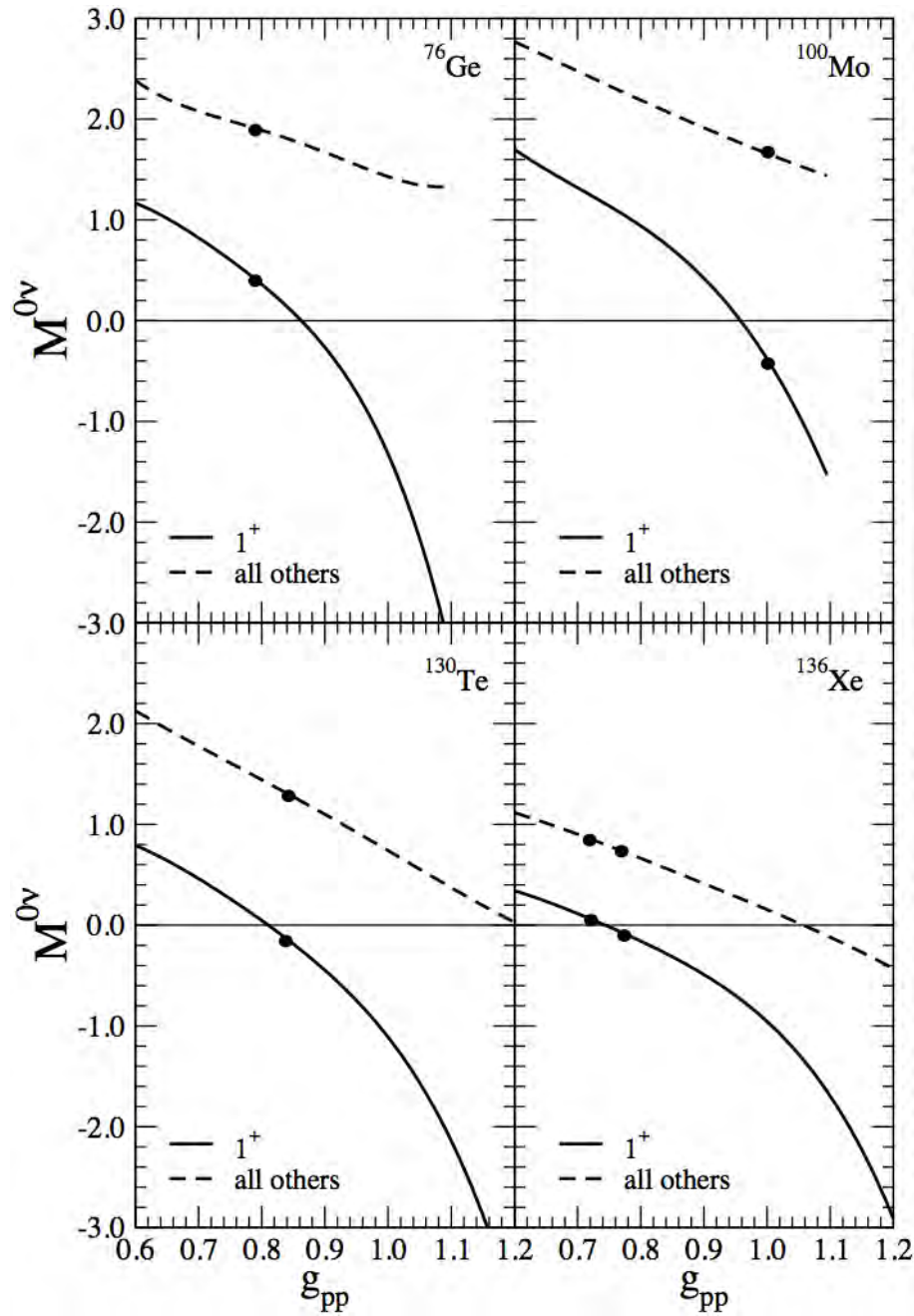


Figure 3.5: $M_{0\nu}$ as a function of g_{pp} . The dots on each plot denote the value of g_{pp} that best reproduces the $2\nu\beta\beta$ rate. Figure from Reference [125].

model calculations have an average disagreement of a factor of 2 means that there is still significant theoretical work to be done in reconciling these two techniques.

3.4 *Uncertainties and Their Relative Magnitudes*

Here we reproduce part of a table from Reference [125, Erratum]. It includes the matrix element, the method used to calculate them with its uncertainty, as well as the uncertainty associated with measurements of the $2\nu\beta\beta$ rate. Once again, the QRPA family calculations are presented with g_{pp} adjusted to reproduce the $2\nu\beta\beta$ rate. The message that the reader should take from Table 3.2 is that the theoretical uncertainties in the matrix element calculated in this way will tighten considerably after the next round of $\beta\beta$ experiments regardless of any observation of $0\nu\beta\beta$, because all of them will have high-statistics $2\nu\beta\beta$ lifetime measurements.

Last, we create a summary table of the sources of uncertainty in the $0\nu\beta\beta$ matrix elements. The particular values will of course depend on the actual isotope under consideration, and correlations between these uncertainties could confound any attempt to estimate the absolute matrix element uncertainties by simply adding the rows of this table in quadrature as we have done in the last row of Table 3.3. Still, it will serve as a useful comparison between the magnitude of theoretical compared to systematic and statistical uncertainties from a future experimental program. It is furthermore quite encouraging that this estimated total is 30–40% instead of the historical factor of 2 spread in $M_{0\nu}$ calculations.

Table 3.2: A sample of calculated matrix elements calculated in QRPA, RQRPA with accompanying uncertainties. This table is partially reproduced from Reference [125, Erratum]. Note that in Reference [125, Erratum], the uncertainty for each matrix element is expressed as a variance (σ^2), whereas here we use standard deviation (σ).

Transition	g_A	$M_{0\nu}$ (RQRPA)	$M_{0\nu}$ (QRPA)	$\sigma_{2\nu\beta\beta}$
$^{76}\text{Ge} \rightarrow ^{76}\text{Se}$	1.25	3.92 ± 0.35	4.51 ± 0.41	± 0.22
	1.00	3.46 ± 0.36	3.83 ± 0.37	± 0.24
$^{82}\text{Se} \rightarrow ^{82}\text{Kr}$	1.25	3.49 ± 0.36	4.02 ± 0.39	± 0.28
	1.00	2.91 ± 0.30	3.29 ± 0.35	± 0.28
$^{96}\text{Zr} \rightarrow ^{96}\text{Mo}$	1.25	1.20 ± 0.37	1.12 ± 0.17	$^{+0.35}_{-0.48}$
	1.00	1.12 ± 0.33	1.21 ± 0.26	$^{+0.35}_{-0.50}$
$^{100}\text{Mo} \rightarrow ^{100}\text{Ru}$	1.25	2.78 ± 0.44	3.34 ± 0.44	± 0.14
	1.00	2.34 ± 0.35	2.71 ± 0.37	± 0.14
$^{116}\text{Cd} \rightarrow ^{116}\text{Sn}$	1.25	2.42 ± 0.40	2.74 ± 0.44	± 0.14
	1.00	1.96 ± 0.36	2.18 ± 0.40	± 0.14
$^{128}\text{Te} \rightarrow ^{128}\text{Xe}$	1.25	3.23 ± 0.35	3.64 ± 0.36	± 0.30
	1.00	2.54 ± 0.28	2.85 ± 0.28	± 0.32
$^{130}\text{Te} \rightarrow ^{130}\text{Xe}$	1.25	2.95 ± 0.35	3.26 ± 0.35	$^{+0.51}_{-0.28}$
	1.00	2.34 ± 0.26	2.59 ± 0.24	$^{+0.52}_{-0.28}$
$^{136}\text{Xe} \rightarrow ^{136}\text{Ba}^a$	1.25	1.97 ± 0.36	2.11 ± 0.33	
	1.00	1.59 ± 0.30	1.70 ± 0.26	
$^{136}\text{Xe} \rightarrow ^{136}\text{Ba}^b$	1.25	1.67 ± 0.36	1.78 ± 0.33	
	1.00	1.26 ± 0.30	1.35 ± 0.26	
$^{150}\text{Nd} \rightarrow ^{150}\text{Sm}$	1.25	4.16 ± 0.40	4.74 ± 0.45	$^{+0.24}_{-0.44}$
	1.00	3.30 ± 0.40	3.72 ± 0.45	$^{+0.24}_{-0.44}$

^a 2ν upper limit

^b 2ν vanishes

Table 3.3: A summary of the systematic uncertainties enumerated mostly in Section 3.2 and an estimate of the typical fractional uncertainty (where such an estimate is meaningful).

Effect	Section	Uncertainty
Quasiparticle Mean Field	3.2.1	
Many-Body Approximations	3.2.2	
Coupling Constants	3.2.3	10%
Perturbative Effects	3.2.4	10%
Size of the Model Space	3.2.5	
Closure Approximation	3.2.6	10%
Short-Range Correlations	3.2.7	20%
Intermediate State Overlap	3.2.8	small
Phase Space Scaling Factors	3.2.9	<70%
Adjusting g_{pp} from $2\nu\beta\beta$	3.3	10–20%
Estimated Total:		30–40%

Chapter 4

SYSTEMATIC UNCERTAINTIES AND TOLERANCES IN THE MAJORANA EXPERIMENT

Systematic uncertainties are a blanket group covering nearly all experimental uncertainty not arising directly from counting statistics in an experiment. They are typically addressed by taking high-statistics data sets with known calibration sources (either radioactive sources or electronic pulsers). In this section, we begin our discussion by deriving and examining the expression by which we will calculate (or place a limit on) the $0\nu\beta\beta$ rate from quantities that we will measure either with or about the MAJORANA experiment. This, of course differs from the rate one calculates from nuclear structure models and the degree of lepton number violation one expects. After we have arrived at the expression for the rate measured by MAJORANA, we will then step through each quantity in that expression and estimate its uncertainty.

4.1 $0\nu\beta\beta$ Rate Expression

We start with the expression for the *Exponential Law of Radioactive Decay* [101] for the number of radioactive nuclei present in a sample at time t :

$$N(t) = N_0 e^{-\Gamma t} \quad (4.1)$$

Here, N_0 is the number of atoms of interest in the initial sample, and Γ is the decay rate, or one over the lifetime τ of the nucleus (τ is related to the half-life by the expression, $t_{1/2} = \ln(2) \tau \approx 0.693 \tau$). First we normalize Equation 4.1 such that it becomes the probability density for any one atom decaying over time. We also then expand this in a polynomial series since any time over which we are able to count is of less than a part in 10^{25} of $T_{1/2}^{0\nu}$ (because typical experimental live times are of order a few years, and typical $0\nu\beta\beta$ lifetime sensitivities are greater than 10^{25} years):

$$p(t) = \Gamma e^{-\Gamma t} \approx \Gamma + \mathcal{O}(\Gamma t) \quad (4.2)$$

If we integrate Equation 4.2 over some counting time T and multiply by the number of atoms in the original sample, we get the number of decays observed in time T :

$$N_D(T) = N_0 \int_0^T p(t) dt \approx N_0 \Gamma T \quad (4.3)$$

We can more conveniently express N_0 as:

$$N_0 = \chi' N_A \frac{M}{\mathcal{M}} = \frac{N_A M \chi'}{\sum_k \chi_k A_k} \quad (4.4)$$

Here, M is mass of the sample, N_A is Avogadro's Number, χ' is the enrichment fraction for the isotope of interest and \mathcal{M} is the molar mass of the sample. We express \mathcal{M} as a sum over the number of isotopic species (over which the index k runs) where each term is the product of the atomic weight A_k of that isotopic species with its enrichment fraction χ_k . In general, \mathcal{M} must also account for information about whatever the molecular compound from which the detectors are made. This isn't an issue for HPGe detectors, but is for a variety of other techniques. For our experiment, we will count some number of decays and then calculate a rate from that result. We therefore substitute Equations 4.4 into 4.3, solving for the $0\nu\beta\beta$ rate Γ :

$$\Gamma = \frac{N_D}{N_0 T} = \frac{\sum_k \chi_k A_k}{T N_A M \chi'} N_D \quad (4.5)$$

The number of decays, N_D is actually found by either subtracting an expected background from the total number of counts in a region of interest (ROI) or fitting out the strength of a spectral feature on top of some background:

$$\Gamma = \frac{\sum_k \chi_k A_k}{T N_A M \chi'} (N_C - N_B) \quad (4.6)$$

N_C and N_B are the total number of counts and the expected background in the ROI of the final, fully cut spectrum. We can now start to see some of the places into which systematic and statistical uncertainties will begin to creep. Both N_C and N_B can be expressed as the product of an efficiency and the total number of counts in the "Individual Crystals Spectrum" (ICS). The ICS is the spectrum constructed by filling a histogram with the raw, un-summed output of each individual detector with no cuts applied (*i.e.* no granularity, pulse shape, segmentation, *etc.* cuts).

The ROI is plainly important in determining N_C and N_B , but there is a subtlety when talking about the uncertainty in their difference. If the ROI is very large and the signal for which an experiment is looking is quite small, then N_C and N_B will both be rather large numbers of events. The difference of two large numbers is often a very difficult quantity to know precisely because the scale of the uncertainties in question is set by the numbers themselves, making the uncertainty in the difference comparatively quite large when the numbers are very near one another. Experimenters can address this problem by making the ROI as small as possible while still maintaining a large fraction of the signal events. This is why the excellent energy resolution of germanium detectors is such an advantage for the MAJORANA experiment. Because MAJORANA is searching for a narrow peak at a well-known energy, the ROI to be selected very tightly around the location of that peak.

This minimizes the number of background events that must be subtracted from the total in the ROI to extract the number of signal events in the experiment.

To further complicate things, the entire mass of each detector is not active (*i.e.* energy depositions in some parts of the detector will not result in signals), and this non-active mass fraction is specific to each detector. This means that the lifetime expression needs to involve a sum over detectors. Since this measurement will be made by summing over a presumably large number of runs, we will also need to treat the expression for Γ as a sum over production data runs. With these considerations in mind, we now rewrite Equation 4.6 as:

$$\Gamma = \frac{\sum_{r=1}^{N_{runs}} \sum_{i \in D_r} N_{Tri} (\eta_{Cri} - \eta_{Bri}) (\sum_k \chi_{ki} A_k)}{N_A \sum_{r=1}^{N_{runs}} \sum_{i \in D_r} T_{ri} \alpha_i M_i \chi'_i} \quad (4.7)$$

N_{runs} is the number of production runs in the data set, and r is the index of a particular run. D_r is the set of all crystals in run r , and i is an index running over D_r . N_{Tri} is the total number of counts in the ROI of the ICS for crystal i in run r . η_{Cri} is the efficiency for the combination of all the signal/background cuts to fill the final spectrum, and η_{Bri} is the efficiency for background events contaminating the final spectrum. T_{ri} is the live time for detector i in run r . M_i is the “scale mass” of detector i (the physical mass one would measure on a scale), α_i is the active mass fraction of detector i , and χ'_i is the enrichment fraction for the isotope of interest of detector i (^{76}Ge , for the MAJORANA experiment).

Each of these quantities (with the exception of the number of runs and the detectors operating for each run) has a systematic uncertainty associated with it, and we will discuss each of them below. We will also estimate the fractional level of each uncertainty, and discuss plans to characterize and/or mitigate them.

4.2 Avogadro’s Number

Though it is often treated as such, Avogadro’s Number is not *actually* a fundamental constant, and it has a small uncertainty associated with it. It is defined by the number of atoms in 12 g of ^{12}C . According to the Committee on Data for Science and Technology (CODATA) [115], the recommended value for N_A is:

$$N_A = (6.0221415 \pm 0.0000010) \times 10^{23} \frac{\text{atoms}}{\text{mol}}$$

This corresponds to a fractional uncertainty of 1.7×10^{-7} . As we will see below, this is exceedingly small compared to the other uncertainties that we will consider.

4.3 Live Time

Uncertainties in T_{ri} arise from uncertainties in the live time from the system clocks used in the various anti-coincidence cuts. These anti-coincidence cuts will also have an efficiency uncertainty that will be discussed in Section 4.8. In this section, we will estimate the dead time fraction from each cut, and then estimate from that the approximate uncertainty. We will close this section with a discussion of the characterizing triggering efficiency, which is also important for understanding the live time.

4.3.1 Active Veto

According to Reference [38], the active veto dead time can be estimated as:

$$f = Rw = FAw \quad (4.8)$$

where f is the dead time fraction, R is the μ rate through the veto shield, w is the time window. F is the μ flux, and A is the cross-sectional area of the veto. If we assume the shield has a square cross section, 2 m on a side (*i.e.* $A = 4 \text{ m}^2$), and $w = 1 \text{ s}$, we can create a table of values for f depending on the μ flux, and therefore on depth. The MAJORANA collaboration is really only

Table 4.1: μ flux, resulting veto rate and dead time fraction for different overburdens

Overburden	μ Flux	Veto Rate	Dead Time Fraction
2000 m.w.e.	$10^5 \text{ m}^{-2}\text{y}^{-1}$	0.013 Hz	1%
4000 m.w.e.	$3 \times 10^3 \text{ m}^{-2}\text{y}^{-1}$	$4 \times 10^{-4} \text{ Hz}$	4×10^{-4}
6000 m.w.e.	$2 \times 10^2 \text{ m}^{-2}\text{y}^{-1}$	$2 \times 10^{-5} \text{ Hz}$	2×10^{-5}

considering sites with > 4000 m.w.e. of over burden, but even with as little as 2000 m.w.e., the dead time fraction will only be $\approx 1\%$. The uncertainty in this dead time fraction will be exceedingly small because it will be set by the system clock of the DAQ system. This will lead to something on the order 10^{-6} for a roughly 1 MHz clock and a one second anti-coincidence window. The veto rate will not only come from cosmic rays, but will also come from natural radioactivity in the underground laboratory and in the veto paddles themselves. We can see from Table 4.1 that for total veto rate in the neighborhood of 0.01 Hz, the dead time stays around 1%. It does, however grow linearly with the background rate, so the dead time can become prohibitively high very quickly if we do not take care to avoid contamination on the veto paddles and maintain clean room conditions in the MAJORANA underground laboratory.

4.3.2 Granularity/Segment-Anti-Coincidence

The dead time from segmentation anti-coincidence in MAJORANA will be quite small. A prospective $0\nu\beta\beta$ event would be rejected if it is in coincidence with (*i.e.* preceded or succeeded by another event within some time coincidence window). The time coincidence window will be of order a μs because of the fast response time of Ge diode detectors. The IGEX experiment demonstrated a background rate of 3×10^{-4} Hz/kg for energies greater than 200 keV [86]. Even making the rather conservative assumption of a 10 to 100 fold increase for a threshold as low as 3 keV, this would give us an event rate for a 120 kg array (one of the possible MAJORANA configurations) of roughly 1 Hz. The MAJORANA experiment should be markedly cleaner than IGEX, making the actual rate in MAJORANA likely much lower than 1 Hz. The time window for signals to be considered part of the same event we have used in our work with the CLOVER has typically been 100 ns. This gives us an anti-coincidence dead time fraction of $\approx 10^{-7}$. The 100 ns anti-coincidence window corresponds to four clock ticks in the Digital Gamma Finder (DGF) digitizer card, used by many groups within the MAJORANA collaboration. If we assume a margin of error of one clock tick on either side of the window, the dead time fractional uncertainty becomes $\approx 5 \times 10^{-8}$.

4.3.3 Single-Site Time Correlation

There will also be dead time arising from single-site time correlation (SSTC) cut. The dead time arising from this cut will of course depend on the cut duration, as well as on the detector rates at different energies. We expect that the dead time arising from this cut to be less than that from the active veto cut, and that the resulting uncertainty will also be extremely small. We can make this argument on similar grounds to that for the dead time uncertainty for the anti-coincidence cut. Even though the duration of the time window for the SSTC cut is much longer than for the anti-coincidence cuts, it will still be made using the digitizer system clocks, meaning that it will have an absolute uncertainty similar to one over the rate of the system clock. This would make the fractional uncertainty roughly 25 ns divided by the SSTC time window (something like a fraction of an hour to a few hours for most radioactive backgrounds we would try to mitigate with this technique), or $\approx 10^{-11}$. For the ^{68}Ge decay chain, the SSTC time window would be between three to five half-lives, or 3.4 to 5.6 hours for a 67.6 minute half-life. This would lead to a fractional uncertainty of 1.7×10^{-12} . The resulting dead time from this cut is found by examining the “gross” rate for ^{68}Ge (15.76 counts/ROI/t-y, from Reference [38, Table 4.2]). If we assume 1 kg detectors, the 3.4 to 5.6 hour SSTC time window leads to a dead fraction of 6×10^{-6} to 1×10^{-5} . The uncertainty on the efficacy of this cut will be discussed in Section 4.8.2, again using ^{68}Ge as an example.

4.3.4 Trigger Efficiency

Another factor for which we must account in the calculation of the live time is the trigger efficiency. Unless there is some problem with the DAQ hardware, this should be one for events above our hardware threshold because of the very low rates expected for MAJORANA production data. At 2.039 MeV, $Q_{\beta\beta}$ for ^{76}Ge is comfortably above this threshold (which will be something like 1 – 5 keV), but we may have to think about this for both the MAJORANA $2\nu\beta\beta$ measurement and the SSTC cut. We would likely characterize this efficiency with an electronic pulser by scanning the amplitude of the input pulses across where we think the threshold should be. It would also be advisable to vary the rise time of the input pulses to check for any dependence on that.

4.4 Detector Mass

The mass of each detector is obtainable simply by weighing it. We can attain fractional uncertainties in detector mass of roughly 10^{-5} with a typical electronic balance. To actually achieve that level, we must also account for the buoyancy force from air displaced by the detector. The ratio of an object’s buoyancy in air to its weight is just the ratio of the density of the air in which it is being weighed to its own density. In this case, that ratio is $\approx 2 \times 10^{-4}$, for air at standard temperature and pressure ($1.3 \times 10^{-3} \text{ g/cm}^3$) and germanium (5.3 g/cm^3 —the detectors in MAJORANA will be slightly more dense than this because they will be enriched to a higher concentration of ^{76}Ge than natural germanium). This is a straightforward affect to correct for, but even if we neglected it entirely, we will see that fractional uncertainties of 10^{-4} are well below the level that will affect the total uncertainty of the MAJORANA experiment.

4.5 Active Mass Fraction

This is sometimes also called the “fiducial volume” of our detectors. It will be measured by determining the dead layer of each crystal. Most likely, this will be done by characterizing each crystal before deployment with a source, measuring the relative attenuation of low-energy γ -ray lines from that source. The absolute location and intensity of the source is not particularly important, and the active volume of the crystal can then be determined to a very low uncertainty [38, Section 3.12.2]. Once we have a good initial characterization, later studies of relative rates in the MAJORANA array can be made with *in situ* calibrations to monitor for changes over time.

It is true that the relative dead layer effect for internal $\beta\beta$ decay events versus external γ -rays still needs to be determined. This comes from the fact that the internal boundary of the dead layer is not as precisely defined as the external boundary (*i.e.* the surface of the crystal). Ideally, this internal

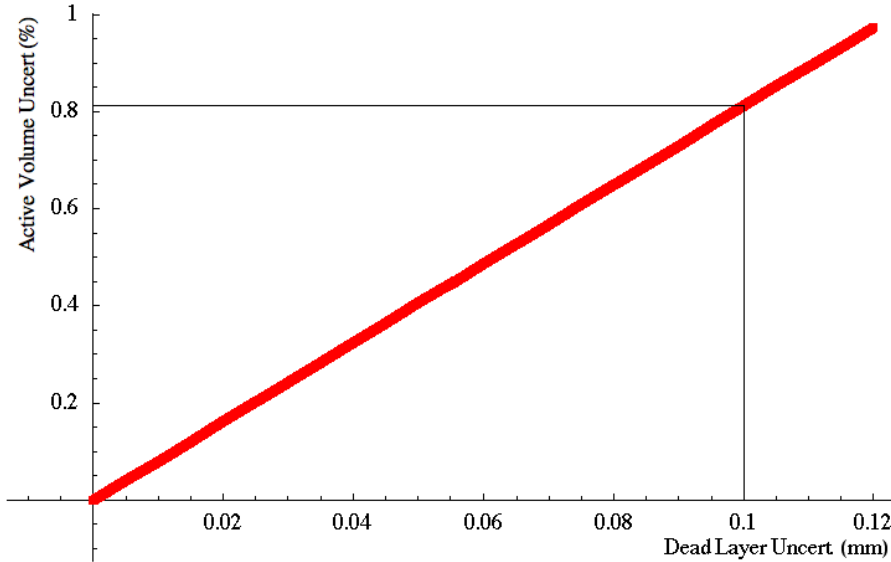


Figure 4.1: Percent uncertainty of the detectors active volume as a function of the uncertainty in the dead layers of a closed-end coaxial detector 62 mm diameter by 80 mm tall with a 8 mm diameter by 65 mm depth bore. We assumed an inner dead layer of 0.5 mm and an outer dead layer of 0.5 μm , typical of n-type HPGe detectors.

boundary represents an interface between two different chemical compositions (the doped surface layer and the bulk germanium) [99]. Still, the approximate thickness of the dead layer is known, and this can be used to place an upper limit on this uncertainty. For an uncertainty of 100 microns on all dead layers of a 62 mm \times 80 mm detector, we obtain a fractional uncertainty of $\approx 0.8\%$ in the active volume of the detector. We show the dependence of the active volume uncertainty on the dead layer uncertainty in Figure 4.1.

In addition to monitoring the active mass we will need to make sure that we know which detectors in the array are actually functioning at any given time. If a detector goes off line because of loss of high-voltage or preamplifier power, then there will be fewer ^{76}Ge atoms contributing to the experiment. This is equivalent to dropping α_i to zero for detector i . Unless we account for this in the analysis of the final MAJORANA spectrum, we would obtain too low a result or place a limit that is not stringent enough for the $0\nu\beta\beta$ rate. The magnitude of this affect is proportional to the amount of time the detector was “off” before it was discovered times its active mass (*i.e.* the lost exposure from that detector). For an array of 60 equal-mass detectors, one detector being inactive for the entire data run would mean a loss of one sixtieth of the exposure, corresponding to a decrease of $\approx 1.7\%$. Since we can expect at least a few counts per day from all of the detectors

in the array over their entire energy range, it seems unlikely that a completely non-functioning detector would go unnoticed for more than about a day. One day out of a five-year run would push this exposure loss down to approximately one part in 10^5 . Simply interrogating every detector on a roughly hourly basis would push this down by another factor of ≈ 24 , well below the level of systematic uncertainties strongly affecting the experiment. Hourly pulser pings, are a better way of monitoring the detectors than waiting for background events because it would allow for a simple way to check the stability of the gain for each detector as well. A simple alarm if any detector's response to a pulse of known amplitude fell outside of an acceptable range would alert the detector operators that a specific crystal has malfunctioned.

4.6 Isotopic Composition

This is where uncertainty in the enrichment level enters the rate expression. Once we obtain our enriched isotope, we will take samples of this material and analyze it via some form of mass spectroscopy, most likely either Gas Chromatography Mass Spectroscopy (GCMS) or Inductively Coupled Plasma Mass Spectroscopy (ICPMS). These techniques have typical uncertainties of 1 – 2%.

4.7 Number of Counts in the Region of Interest

The number of counts in the region of interest is where the statistical uncertainty enters. If the $0\nu\beta\beta$ half-life for ^{76}Ge lies just below the current limits or is consistent with the claim in Reference [38], five years of run time for the 120 kg configuration of the MAJORANA experiment will be able to measure the half-life with a statistical uncertainty of $\approx 10 - 20\%$. This sets the maximum acceptable scale for the total systematic uncertainty.

Detector Gain

Part of the uncertainty in the number of counts in the region of interest centers around actually defining the region of interest for each detector and adding the individual crystal spectra together. If the gain for a detector is imprecisely known, then a given peak may actually be at a different energy than the one assumed by the analysis. If there are too few counts in the peak to do a proper fit, then an error in the definition of the ROI will ensue. Both IGEX and the Heidelberg/Moscow achieved typical full-width, half-maximum (FWHM) detector resolutions of four keV ($1\sigma \approx 1.5$ keV). For a ROI of similar width, one could expect an ROI efficiency of 83.8%. A gain uncertainty of 0.2 keV (achieved in IGEX) at 2039 keV would introduce a fractional uncertainty of approximately 0.36%. It is also important to note that this uncertainty is single-sided, *i.e.* a change in the gain always

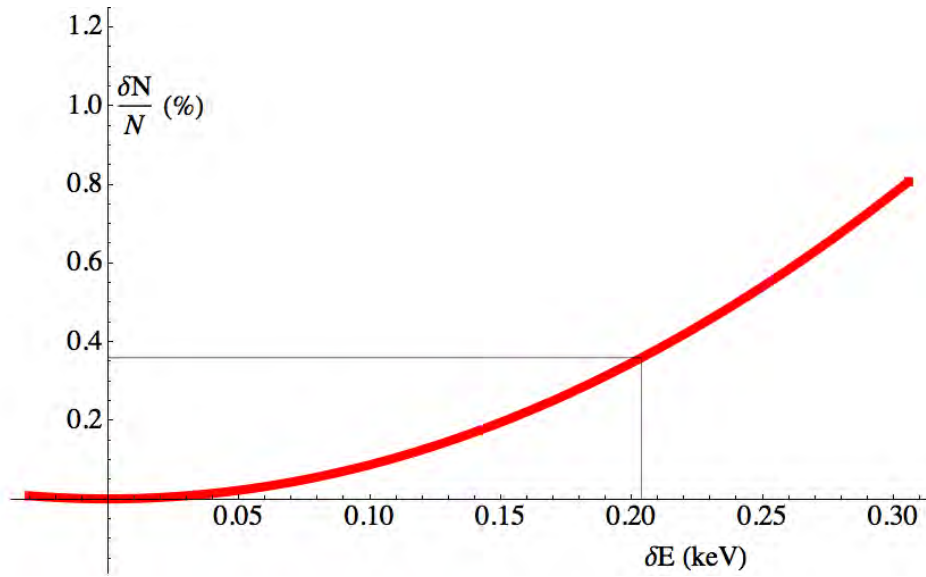


Figure 4.2: Percent change in the number of counts in the ROI versus uncertainty in the peak location. The lines on the figure mark the 0.36% uncertainty resulting from a 0.2 keV uncertainty in the peak location. This corresponds to the energy scale uncertainty achieved in the IGEX and Heidelberg/Moscow experiments.

decreases the number of counts in the ROI. This is different from changes in detector resolution (discussed below), for which any individual change can, depending on its direction, enhance or detract from the number of counts in the ROI.

$\beta\beta$ Endpoint

The actual endpoint of $0\nu\beta\beta$ for ^{76}Ge is a well known quantity ($Q_{\beta\beta} = 2039.006 \pm 0.050$ keV [46]). We can see from Figure 4.2 that this corresponds to an uncertainty of less than 0.1%.

Bin Width

There is also the question of adding together spectra with different gains and therefore subtly different bin widths. The output of our DAQ system will be inherently binned because it is digitized. This leads to two problems. First, a histogram of raw ADC values will in general not have bin edges that line up with those in whatever calibrated energy histogram we try to analyze. Second, due to the small nonlinearity of the detectors, the width of the bins in the calibrated histogram spectra are no longer constant. We can solve this problem by identifying bins in the raw ADC spectrum that overlap two bins in the calibrated energy spectrum, then filling one or the other of the bins

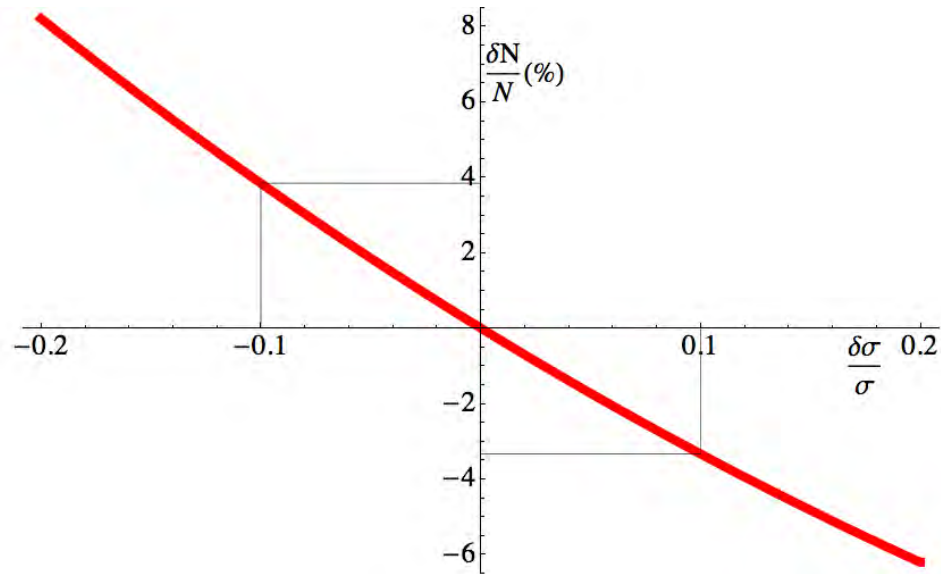


Figure 4.3: Percent change in the number of counts in the ROI versus uncertainty in the peak width. The lines on the figure mark the uncertainty resulting from a 10% variation in the peak width. This corresponds to the resolution uncertainty achieved in IGEX.

in the energy spectrum with a probability equal to the fraction of the raw ADC bin that overlaps either of the calibrated energy bins. This procedure makes certain that each bin in the calibrated energy spectrum has Poisson-distributed statistics, and therefore that goodness-of-fit calculations are meaningful in an absolute sense. Please refer to Reference [91, Section 4.2.3] for more details.

Detector Resolution

If the resolution of our detectors at $Q_{\beta\beta}$ is imprecisely known, we introduce an uncertainty similar to the one from the gain. The principle difference is that it is two-sided and asymmetric. If the FWHM resolution is uncertain to 10%, as was achieved by the IGEX experiment (4.0 ± 0.4 keV), we can see from Figure 4.3 that the resulting uncertainty in the number of counts in the ROI would be $\approx 3 - 4\%$. This is, by far the largest detector-related uncertainty for the MAJORANA experiment, and it would therefore be wise to try and lower it from what was achieved in IGEX. The use of ^{56}Co as a calibration source might help to lower the energy resolution uncertainty because it has a strong γ -ray at 2034.8 keV, very near $Q_{\beta\beta}$ in ^{76}Ge . This is preferable in many ways to ^{232}Th , the calibration source primarily under consideration for MAJORANA, because the nearest γ -rays in that decay chain to $Q_{\beta\beta}$ are 1630.6 keV (from ^{228}Ac) and 2614.5 keV (from ^{208}Tl). This forces experimenters to interpolate between these two energies when estimating line widths as a function

of energy. Having a strong γ -ray only ≈ 4 keV from $Q_{\beta\beta}$ would make this interpolation far more accurate, greatly reducing this systematic uncertainty. Possible calibration sources are discussed further in Section 5.3.1. There are unfortunately, a number of logistical challenges associated with the use of ^{56}Co as a calibration source (mostly due to its relatively short half-life of 77 days). There are also γ -ray lines at 2021.8 and 2052.9 keV from ^{214}Bi (part of the ^{238}U decay chain). At around 4.5 billion years, ^{238}U has a much longer half-life than ^{56}Co , but these lines are both extremely weak. It might therefore be difficult to pick them out of the continuum in a source run, especially in the inner detectors of the array. The question is whether the 3 – 4% uncertainty from detector resolution is “good enough” given the rest of the uncertainties in the experiment. It is certainly well below the 10 – 20% statistical uncertainty arising from the observation 25–100 $0\nu\beta\beta$ events, but if an additional set of calibration runs from a different source would reduce this uncertainty dramatically, it would probably be worth undertaking.

4.8 *Signal/Background Tagging Efficiencies*

This section covers all the signal and background tagging efficiencies. Some of these are anti-coincidence or time correlation cuts, and as discussed in Section 4.3, have uncertainties associated with their ensuing dead time. This section will cover the uncertainties in the actual signal survival probability and background contamination. For all of these background/signal tagging cuts, there is a trade off between the amount of background rejected and the amount of signal preserved. For some, like the granularity and segmentation cuts, the level of this trade off is set by the detector geometry (though the energy thresholds in both hardware and analysis can adjust the levels of background rejection and signal preservation). Others, like the time correlation and pulse shape cuts have signal and background sensitivities that are completely adjustable in post processing analysis.

4.8.1 *Anti-coincidence Cuts*

This is a category of background reduction cuts including: granularity, segmentation and active veto cuts. The granularity and segmentation cuts seem like very simple ones to make, and being essentially a multiplicity filter, they are. There are, however, a number of ways that signal events could be mistaken for background or that background events could masquerade as signal. We could lose two-electron events to detector-to-detector or segment-to-segment anti-coincidence via: accidental coincidence, electronic crosstalk or Bremsstrahlung radiation. There is also a possibility that background events (particularly external γ -rays) could mimic the multiplicity pattern for two-electron events. Single or very localized Compton scatters are the biggest problem here.

Granularity Cut

The MaGe simulation group has performed a detailed Monte Carlo study of $0\nu\beta\beta$ events as well as numerous backgrounds in a 60 kg MAJORANA module [38, Table 4.3]. The Monte Carlo predicts a 96% survival for $0\nu\beta\beta$ events, with losses coming mostly from the decay electrons losing energy via Bremsstrahlung radiation (96% is an upper limit since the simulation did not include electronic crosstalk or accidental coincidences). Over all, we can expect a granularity cut efficacy of 17% for background events. This number comes from an average over a number of simulated backgrounds with survival probabilities ranging from 3 – 4% for ^{60}Co in the copper parts to 100% for (α, n) neutrons. The statistical uncertainty in each term of this average is of order 0.1 to 1%, and we can expect the fractional uncertainty in this efficacy to be $\approx 1\%$. The efficacy of the granularity cut is dependent on the details of the background model because different backgrounds originating from different locations in the detector array will have different associated multiplicities. We will, of course, measure this efficacy using *in situ* calibration data. We can take a rough estimate of the statistical uncertainty to be $\approx 1\%$ (*i.e.* 10000 events) for the event types we can generate with a calibration source. The granularity cut survival from the *in situ* calibration data will be used to normalize the survival probabilities from Monte Carlo simulations because it is impossible to place a source into some of the locations from which contamination will originate. This means that the final granularity cut systematic uncertainty will be a combination of the statistical uncertainties from counting events in both the calibration data and the Monte Carlo simulation.

Segmentation Cut

The segmentation cut will obviously be dependent on the particular segmentation geometry used in the MAJORANA detectors. The Monte Carlo study in Reference [38, Table 4.3] estimates the segmentation cut survival for $0\nu\beta\beta$ events to be 95% for a 3×2 (axial \times azimuthal) segmentation scheme. There are similar caveats that apply to this number as to the granularity cut $0\nu\beta\beta$ survival described above. The third column of Table 4.2 reports results for the segmentation cut in the CLOVER detector for a variety of events at different energies. Reference [49] discusses this work in detail. The segmentation cut efficacy is dependent on a number of factors, but its fractional uncertainty tends to hover between 1 – 3%. We will determine this number in the MAJORANA experiment through the taking of large characterization and calibration data sets and then using those to normalize the Monte Carlo predictions (as described above for the granularity cut), but this 1 – 3% uncertainty can serve as an upper limit on what we can expect.

Active Veto

The active veto cut has an efficiency uncertainty associated with it too. The loss of signal events to the active veto is going to be quite improbable because even Bremsstrahlung radiation from $0\nu\beta\beta$ will be, in all probability, stopped by the intervening shielding. The accidental coincidence rate between the veto and the array will also be vanishingly small even at very modest depths (according to Table 4.1, the dead time fraction will be only 1% for a veto rate of a fraction of a count per second). There is also a non-zero probability that external radiation would enter the detector array without depositing energy in the active veto shield. While it is highly improbable that a direct μ could enter the MAJORANA array without first depositing energy in the active veto, spallation neutrons created by cosmic ray μ interacting with the walls of the laboratory could. The fractional uncertainty on the rate arising from this affect will be rather large, and the only way to mitigate it is to go deep to avoid the cosmic rays. A reasonable first assumption for the active veto efficiency is 90%, and the combination of characterization on the surface with cosmic ray μ and external source calibrations underground will help quantify the performance of the veto paddles. An uncertainty of 1% is not unreasonable assuming that approximately 10000 events per veto paddle can be captured from a well-calibrated γ -ray source.

4.8.2 Single-site Time Coincidence

The SSTC essentially extends the anti-coincidence time window for certain specific energy depositions. An example of this is the cut to remove ^{68}Ge background events (decay scheme from the table of isotopes shown in Figure 4.4). This involves tagging the 11-keV x-ray from the electron capture of ^{68}Ge so that the β^+ emission of ^{68}Ga can be vetoed (with an endpoint of 2.9211 MeV, this could contribute background counts in the region of interest). ^{68}Ga has a half-life of ≈ 68 minutes, so we would need to veto signals from that particular detector for something like four to six half-lives. Background from events passing the SSTC efficiency would come from the efficiency for capturing the ^{68}Ga x-ray as well as the probability that ^{68}Ga will decay with a β^+ of energy in the ROI after the veto for that crystal has expired. Uncertainty in this background would arise from how well we know each of these quantities. Once again, we should reiterate that the uncertainties discussed in Sections 4.8.1 and 4.8.2 also have separate, but related uncertainties associated with the live time for the experiment.

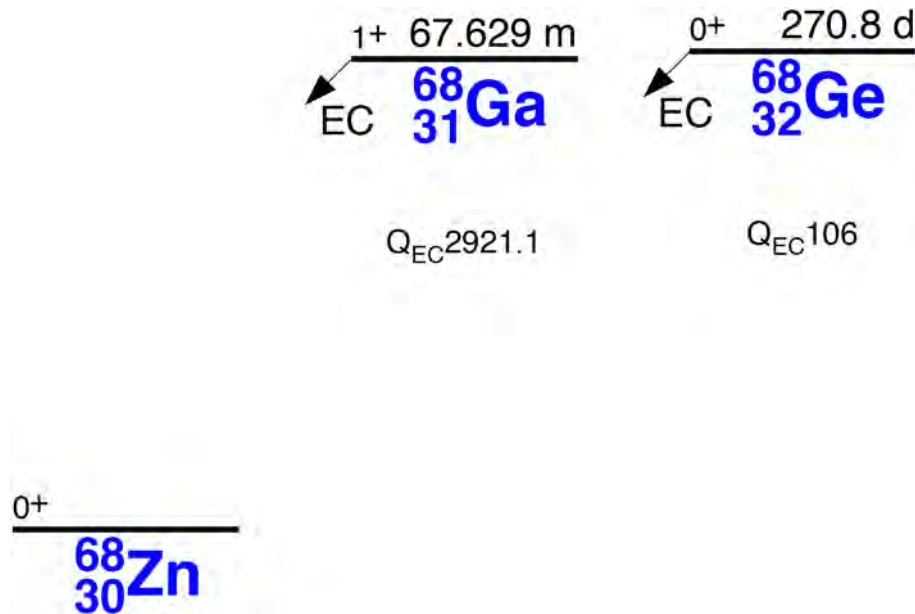


Figure 4.4: The decay scheme of ^{68}Ge to its stable isotope of ^{68}Zn . Figure taken from [71].

4.8.3 Pulse Shape Analysis

Uncertainty in the acceptance of the PSA cut will also contribute to the efficiency uncertainty. The PSA acceptance will be characterized by calibration runs with high-energy γ -ray lines (^{232}Th , and possibly ^{56}Co). The survival probability for signal will come from that for double-escape peak events, and that for backgrounds will come from the survival probability for γ lines and Compton continua. Uncertainties in these survival probabilities will be rooted primarily in counting statistics from the runs used to characterize the PSA efficacy, and hence the strength of the calibration source and length of the calibration runs. Section 5.3.2 describes a Monte Carlo study of the MAJORANA calibration system, in terms of getting the number of counts required to *train* the PSA cuts into the inner detectors of the MAJORANA module. We will leave a discussion of this study to the calibration plan, but getting the few hundred counts into the inner detectors required to reach a few percent fractional uncertainty will take something like a day or more. A discussion of how to lower these required counting times can be found in Chapter 5.

We have made some progress in estimating the uncertainties associated with the pulse shape and segmentation cuts using the CLOVER as a function of many systematic effects. These are typically variations of the method used to implement the PSA cuts. In Table 4.2, we present results of this systematic uncertainty study along with nominal values for the efficacy of pulse shape analysis and

segmentation cuts for γ , DEP and continuum events. Details of the study of these systematic effects can be found in Section 6.3. The systematic uncertainties for the pulse shape cuts will almost

Table 4.2: Survival probabilities of different processes over a range of energy. The quoted uncertainty in the segmentation cut comes from the uncertainty on the fit parameters from the reconstructed spectra. For the pulse shape and combined cuts, the uncertainty also comes from the list of systematic uncertainties detailed in Section 6.3.

Process	Energy (MeV)	Segmentation (%)	Pulse Shape (%)	Both Cuts (%)
$^{228}\text{Ac } \gamma$	1.588	69.1 ± 1.5	29.0 ± 1.9	21.8 ± 1.5
$^{208}\text{Tl DEP}$	1.592	93.3 ± 3.2	65.6 ± 2.5	61.4 ± 3.2
Compton Cont.	2.0 - 2.08	79.8 ± 0.9	45.4 ± 2.3	38.8 ± 3.2

certainly be significantly lower for detectors in the MAJORANA experiment. This is because many of the details varied in this study would be very clearly defined in the final MAJORANA detector. For now however, the uncertainties in table 4.2 can serve as upper limits on what we could expect in MAJORANA.

There has also been significant discussion of using pulse shape and segmentation cuts similar to those used in GRETA/GRETINA, AGATA, and other γ -ray tracking experiments. These algorithms use a complicated combination of primary and image charge pulses to track the deposition of energy through a large array of detectors. This method however would be very expensive both in terms of money and computational power. This is because the γ -tracking analysis requires a series of complicated many-parameter fits and would also require a significant increase in the amount of front-end electronics close to the detectors. This could possibly result in a substantial increase in background for the MAJORANA experiment because these electronic components are notoriously difficult to keep clean. Still, it is true that the γ -tracking analysis will provide a rich palette of information about each event in the MAJORANA data stream. Some fairly detailed work in both Monte Carlo and small parts assay will need to be done in parallel with fielding the MAJORANA prototype cryostat with highly-segmented detectors. This combined simulation and experimental program will be crucial as the MAJORANA collaboration makes the decision about which detector design would best scale to 1000 kg. We will discuss pulse shape analysis cuts more in Chapter 6.

4.8.4 Background Model

One of the primary criticisms of the Heidelberg–Moscow experiment has been that their $0\nu\beta\beta$ claim is strongly dependent on the level of the continuum background underneath the peaks in and around

the ROI, and therefore on the background model for the experiment as a whole. We need to address this dependence in the MAJORANA experiment. To this end, we performed some simple Monte Carlo studies. The actual values of the shifts and uncertainties will, of course depend on the details of the ^{76}Ge exposure, the continuum and other background levels, and most importantly, the $0\nu\beta\beta$ rate. This, of course, leads to a rather wide distribution of potential results. Specifically, large exposure, low background and fast $0\nu\beta\beta$ rate will naturally lead to small shifts in quantities reconstructed from the final spectrum known very precisely. On the other hand, low exposure, high background and slow $0\nu\beta\beta$ will lead to large shifts known to rather poor precision. We will discuss these Monte Carlo studies and the spectrum of possible outcomes at greater length in Chapter 7, but a good range for these uncertainties in a positive MAJORANA result is 0 – 5%.

4.9 Systematic Uncertainty Summary

We now present a summary of the systematic uncertainties discussed in this chapter in Table 4.3. As we can see, the MAJORANA experiment will have a total systematic uncertainty of $\approx 11\%$ in its $0\nu\beta\beta$ rate measurement or limit. This value is lead by the pulse shape analysis cut efficacies. This is partly because of the difficulty in getting the necessary counting statistics in the data sets used to characterize the cuts, but also due to a number of other systematic factors we will discuss in Section 6.3. The next largest uncertainty is that arising from the background level. We will devote Chapters 6 and 7 respectively to these topics. First however, we will discuss the calibration plan at greater length in Chapter 5.

Table 4.3: Summary table of systematic uncertainties for the MAJORANA $0\nu\beta\beta$ experiment.

Quantity	Nominal Value	Parameter Affected	Rate Unc.
Avogadro's Number	$6.022 \times 10^{23} \pm 1 \times 10^{17}$	N_A	1.7×10^{-7}
Veto window	$1 \text{ s} \pm 1 \times 10^{-6} \text{ s}$	T_{ri}	1×10^{-6}
Live time frac.	$(1 - 10^{-7}) \pm 5 \times 10^{-8}$	T_{ri}	5×10^{-8}
SSTC window	$< 1 \text{ hour} \pm 25 \text{ ns}$	T_{ri}	$\approx 10^{-11}$
Detector mass	$\approx 1 \text{ kg} \pm 10 \text{ g}$	M_i	$\approx 10^{-5}$
Active fraction	$99.0\% \pm 0.8\%$	α_i	$\approx 0.8\%$
Enrichment	$86\% \pm 1\text{-}2\%$	χ_k, χ_i	$\approx 1 - 2\%$
Detector gain	$2039.006 \text{ keV} \pm 0.2 \text{ keV}$	N_{Tri}	$\approx 0.4\%$
$Q_{\beta\beta}$	$2039.006 \text{ keV} \pm 0.050 \text{ keV}$	N_{Tri}	$< 0.1\%$
Bin width	Depends on DAQ electronics	N_{Tri}	negligible
Energy resolution	$4.0 \text{ keV (FWHM)} \pm 0.4 \text{ keV}$	N_{Tri}	$3 - 4\%$
Continuum Background	$1 \frac{\text{count}}{\text{tonne year ROI}}$	N_{Tri}	$0 - 5\%$
Granularity eff.	$17\% \pm 0.017\%$	η_{Bri}	1%
	$100\% \pm 1\%$	η_{Cri}	1%
Segmentation eff.	Depends on detector geometry	η_{Bri}	$2 - 3\%$
	$\approx 90 - 100\%$	η_{Cri}	$2 - 3\%$
Active veto eff.	$10\% \pm 1\%$	η_{Bri}	1%
	$\approx 100\%$	η_{Cri}	1%
SSTC eff.	$10\% \pm 0.1$	η_{Bri}	1%
	$99\% \pm 1\%$	η_{Cri}	1%
PSA eff.	$29\% \pm 1.9\%$	η_{Bri}	6.6%
	$66\% \pm 2.5\%$	η_{Cri}	3.8%
Estimated Total			$\approx 11\%$

Chapter 5

CALIBRATION PLAN FOR THE MAJORANA EXPERIMENT

This MAJORANA calibration program is the primary way in which we will push down the systematic uncertainties of the experiment. Calibration touches nearly every aspect of the experiment and presents numerous technical challenges. We now detail the requirements and difficulties inherent to calibrating the MAJORANA experiment, and then discuss the specifics of the plan for carrying out MAJORANA calibration. We will then close this chapter with an outline of what will be required for the characterization data acquired when we will take possession of new detector, and commissioning data that will be taken when we bring a new MAJORANA module online.

5.1 Criteria

Here we lay out the requirements for calibrating the large array of germanium detectors that will make up the MAJORANA experiment. In general, the total time spent calibrating the detectors should be relatively short compared to the length of time spent taking production data. There should be many independent sets of calibration data, each collected frequently enough to check the MAJORANA array for stability while containing enough data to populate the calibration spectra of the array's inner detectors. The data rate for the calibration runs must also be low enough that event pileup and pulse shape deformation are kept to a minimum. The source used in calibration runs must also have a double-escape peak (DEP) or two near $Q_{\beta\beta}$ for ^{76}Ge so that we can also train our pulse shape analysis algorithms.

5.1.1 Detectors

When we think of calibrating an experiment, the energy scale is the first and most obvious aspect of that experiment to which we refer. We calibrate the energy scale by subjecting each detector in the array to a variety of events of known energy. These are typically γ -rays from radioactive sources. Most of the R&D work for the MAJORANA experiment has used the γ lines from ^{232}Th since it has lines from less than 100 keV to 2.6 MeV. The 2.6-MeV line leads to a fairly strong DEP at 1592 keV. The energy scale would then be made by fitting the centroids of these lines and mapping those onto their known energies. We would fit the energy as a function of the raw output of detectors (*i.e.*

an ADC value) with an analytic expression, probably a polynomial of somewhere between second and fourth-order [91]. The size of the quadratic and higher terms in this fit compared to the linear term would allow us to characterize the linearity of the response of the detectors. Examining the width of these lines will allow us to extract the resolution of the detectors as a function of energy. Knowing the array's resolution will help us to tell bin-by-bin statistical fluctuations from real peaks resulting from physical events. Understanding the resolution of each detector will also help to reduce the systematic uncertainty associated with detector resolution described in Section 4.7.

Another important systematic uncertainty we will have to consider is the fraction of each detector that comprises its active mass. Germanium diode detectors have an inherent dead layer that comes from the surface properties of the semiconductor. There is an additional non-active region of each crystal that comes from the magnitude of the electric fields inside the germanium. Given sufficiently accurate knowledge of the geometry of each crystal we can calculate what the field strength should be in all parts of each detector, but we must also endeavor to measure the active fraction of each detector in some way. The non-active region of these detectors should be something on the order of a fraction of a millimeter in depth from the surface. This means that if we look at the relative attenuation of low energy (tens to a hundred keV or so) lines from external sources, we should be able to estimate the thickness of the non-active region of the detectors since the range of these lines in germanium metal is of this order. This does not have to be done *in situ* but could instead be done in the detector characterization process before a string of detectors is installed into the MAJORANA array. The focus of this dissertation is on the *in situ* calibration of the MAJORANA experiment, so we will leave detailed investigation of this process to future work.

5.1.2 Electronics

We will also want to characterize and monitor many of the electronic attributes of the MAJORANA experiment. This will largely be an exercise in interrogating our detectors with a pulser. This pulser will need to have a short (< 10 ns) rise time, and a large (> 100 μ s) fall time. This will allow us to monitor the stability of the baseline of the detectors, as well as check the gain of the detector electronics provided we record the voltage height of each pulse as we inject it. The details of the electronics calibration will not be considered here.

5.1.3 Array Response to Contamination

One other capability that will be useful in the MAJORANA experiment is the ability to localize spot contamination inside the experiment. This would be important for finding and eliminating

“hot spots” in the experiment once it is constructed. These “hot spots” could come from any number of sources including, but not limited to mishaps or breaches in clean room procedures during construction or failures in quality assurance during the procurement of components of the experiment. To characterize our ability to localize contamination in the experiment, we would likely want to be able to place a source (probably either ^{232}Th , ^{238}U or ^{60}Co since these will be our leading backgrounds in the copper and lead that will comprise the shielding and support structure for the MAJORANA experiment, see Section 2.1 or Reference [38] for more details) of known activity and reproducible position into different locations in and around the detector array. We will cover details of these types of calibration runs below in Section 5.3.

5.1.4 *Efficiencies*

There are also a number of aspects of the MAJORANA experiment that can be most simply called “efficiencies.” These are: the absolute efficiency for $\beta\beta$ capture, the active veto efficiency and the signal and background cuts (granularity, segmentation, pulse shape analysis and single-site time correlation). We will address the $\beta\beta$ capture efficiency with a combination of DEP events in calibration data and detailed Monte Carlo studies. The active veto efficiency will be characterized by combining Monte Carlo studies with the cosmic ray rate in the veto system as well as with calibrated sources before and perhaps after deployment of the veto shield. The background and signal tagging efficiencies will be measured directly by selecting specific types of events in calibration data sets. We will discuss the details of each of these in Section 5.3.

5.2 *Concerns*

We now cover some of the concerns and problems that could arise from the process of calibrating the MAJORANA experiment. First, the calibration apparatus must not introduce any new radiological backgrounds into the detector either from the source itself in the form of radon emanation from a ^{232}Th source, or by opening up the γ and neutron shielding to allow external radiation into the heart of the detector. Second, the calibration runs, as discussed in Section 5.1, must take place in an amount of time short compared to typical production data runs. This is to minimize interference with the operation and to maximize the live time of the experiment. The sources used in all calibration runs should be placed into the array so that their position is reproducible from calibration run to calibration run. The inner detectors of the array will also be shielded from external radioactivity, including calibration sources. This will mean that those detectors will be populated with calibration events much more slowly than the outer ones. Last, at least some of the calibration sources will have

to emit γ lines with energies sufficiently high that the MAJORANA array will observe enough DEPs in each detector to calibrate the pulse shape analysis cuts.

5.2.1 *Zero Contamination*

Calibration of the MAJORANA experiment must leave no additional radioactivity in the detector array. This includes both residual radioactivity from the calibration source(s) or the introduction of environmental Rn gas. The entire MAJORANA shield will be enclosed in a radon exclusion device. Radon exclusion is usually achieved with a thin stainless steel box around the outside of the shield, but we will also examine the option of using some sort of plastic because these materials tend to be lower in radiological background. They also, unfortunately tend to allow radon gas to permeate through them. This problem could be mitigated though, by over-pressuring the inside of the shield with boil-off from a liquid nitrogen dewar. We will mitigate the problem of γ and neutron radiation entering the shield through the calibration ports by configuring them such that there is no direct “line of sight” into the shield. See Figure 5.4 in Section 5.3 for more details.

5.2.2 *Minimal Interference*

Calibration must not take more than a nominal amount of time away from production mode running. This nominal amount of time should be on the order of a few hours per week. Unfortunately, it appears that this will be insufficient to populate the inner crystals with enough DEPs to train the pulse shape analysis algorithms using the supervised parametric methods described in this dissertation. This is based on the Monte Carlo studies discussed in Section 5.3. The tension between limiting the total amount of calibration time required and the need to train our PSA algorithms will lead us to having a regular, few hours per week calibration run that will be used just to set the energy scale of the array, and a less frequent PSA training run that we will use to define the signal and background regions of the pulse shape parameter space for our PSA cut algorithms.

5.2.3 *Position Reproducibility*

All calibration sources should be able to be placed back to the same physical location within a nominal tolerance of ≈ 1 mm. This tolerance is small enough to be less than the likely pointing accuracy of the MAJORANA detector array, but large enough to be easily attainable with off-the-shelf stepper motors. We will use the absolute rates and widths of different lines as a function of energy to check the stability and state of health for each detector in the array. This position reproducibility will allow us to neglect any spatial variation in the sources that we will use to calibrate the array.

Position reproducibility will also be important in the use of calibration data to verify and validate the Monte Carlo simulations of the MAJORANA array. The prototyping work described in Section 5.3.3 used computer-controlled stepper motors for source positioning. For the full MAJORANA experiment we will also use a computerized stepper motor to push the calibration sources through the shield, but we will also deploy a hardware interlock to independently verify the position of the calibration source. We are currently exploring several possibilities for this interlock system and will be testing the feasibility and performance of these ideas with the calibration prototype.

5.2.4 *Array Self-Screening*

Array self-screening is one of the aspects of the detector that will allow us to lower the background of the inner part of the experiment. We pay for this however, when we try to calibrate those inner detectors. There is (according to Monte Carlo studies and measurements made with the CLOVER) roughly a factor of five to ten attenuation in the strengths of γ lines through each shell of detectors. As long as we intend to place all of the detectors in a single, roughly cylindrical cryostat, there is nothing we can do about this except use stronger calibration sources and count for longer times during calibration runs.

Pulse pileup and the event rate the data acquisition system can accept, will tend to limit the strength of the calibration sources we can use. Pulse pileup will limit the throughput of our calibration runs independently of the data acquisition hardware. This is because in order to get clean pulses for the training of our pulse shape cut algorithms, we will need several (five to ten) time constants of our preamplifiers to ensure that each pulse is not riding on top of the exponential tail of the previous one. Most germanium detector preamplifiers have a decay time of 50 to a few hundred μs , leading us to a few thousand counts per second per detector as an absolute upper limit for the rate on our calibration runs. Our experience with the CLOVER detector at LANL implies that this upper event rate is as low as a few hundred counts per second as an overall rate per digitizer board. This work was done using the DGF4C digitizer boards from X-Ray Instrument Associates (XIA) [10], which run on a CAMAC architecture. CAMAC boards have a fairly limited throughput across the backplane of the crate, and this hard limit could be pushed up if we use data acquisition cards based on a compact-PCI or VME architecture for the MAJORANA experiment.

5.2.5 *Double-Escape Peaks*

Since we are using double-escape peaks as surrogate single-site events to calibrate our pulse shape cuts, we need at least one DEP near $Q_{\beta\beta}$. We can get these DEPs with a wise choice of calibration

source. ^{232}Th is the traditional choice for the training of PSA algorithms. It has a 2614 keV γ -ray which yields a DEP at 1592 keV, and a long half-life (1.4×10^{10} years). It, however only has one of these high-energy lines that can give strong DEPs. Much of the PSA R&D work at LANL has been also been done with ^{56}Co . ^{56}Co has the benefit of several strong γ lines up to approximately 3.6 MeV, yielding strong DEPs stretching from 1576 keV up to 2429 keV. This allows us to examine the energy dependence of the efficacy of our PSA cuts through the $0\nu\beta\beta$ ROI. ^{56}Co however, has a fairly short half-life at only about 77 days. We will discuss the details of the calibration plan in Section 5.3, and specifically the sources to be used in Section 5.3.1.

5.2.6 Time Stability

In addition to understanding and characterizing the aspects of the detector array being addressed by the calibration program, we must also monitor them for stability. Shifts in the gain or resolution, for instance, are excellent state of health indicators for the array. Changes in the rates in each detector for data taken during calibration runs can inform the collaboration of problems with the source positioning hardware, or a reduction in the active region of the detectors. Furthermore, tracking the rate for production data will allow us to tell when there are transient contaminations arising from things like radon either emanating from the calibration system or leaking in through some breach in the shield.

5.3 Calibration Reference Plan

Here, we discuss the details of the reference plan for the radioactive source calibration of the different systems in the MAJORANA detector array. There are a number of often conflicting requirements for calibrating different aspects of the experiment. In order to have a complete source calibration program for the MAJORANA detector array, we propose four types of source calibration runs:

- Energy scale characterization
- PSA training
- Veto efficiency measurement
- Localized contamination response

These four calibration modes will allow us to calibrate and characterize the different properties of the MAJORANA detector array. Once again, this is the *in situ* source calibration program, and it is

in addition to the initial characterization and commissioning data. These will be undertaken upon taking possession of new detectors, and immediately after module construction, respectively. Both will be discussed in Section 5.4. We will now go through the different aspects of the calibration plan, discussing: the sources to be used, the time required for the different types of calibration runs, containment and packaging to be used, and intended delivery methods for calibration sources.

5.3.1 Sources

For the first two calibration modes listed in Section 5.3, we propose the use of spatially extended wire sources. The energy scale and resolution for the MAJORANA array can be calibrated and characterized primarily with the use of ^{232}Th sources. Thorium wires are commercially available from Goodfellow [40]. These wires are 0.22 mm in diameter, and have an activity of approximately $0.716 \frac{nCi}{cm}$. PSA training runs can use either ^{56}Co or ^{232}Th wires. We have not identified a vendor for ^{56}Co wires, but it is straightforward to make ^{56}Co by placing a sample of ^{56}Fe in a low-energy (few MeV) proton beam. ^{56}Co is created by (p, n) reactions on ^{56}Fe . Making our own source does however leave the problem of calibrating its strength to the collaboration.

The veto system efficiency will be calibrated using both the cosmic ray μ rate on the surface, and well-calibrated γ -ray sources underground. The specific γ -ray source is not particularly important, only that it has several well-spaced lines to characterize the threshold of the veto panels, and that its activity be precisely calibrated. Precision calibrated sources are available from a number of commercial laboratories. The localized contamination runs should be done with sources corresponding to background contaminants likely to occur outside the germanium detectors themselves. This means that ^{232}Th , ^{238}U and ^{60}Co will be our candidate sources. The sources for these runs could be simple “pellets” introduced through reentrant ports reaching part or all of the way into the shield.

5.3.2 Schedule

As discussed above, there are two competing forces at work when trying to decide the length of the different sorts of calibration runs. We need the calibration data to provide sufficient statistics for each calibration task, but we need to do so in a manner that is as unobtrusive as possible to the day-to-day operation of the experiment. The most stringent statistics requirements will come from the PSA training runs. These require the accumulation of at least 400 DEP events per detector in the training data set (we address the performance of our PSA algorithm as a function of the size of the training set in Section 6.3.1).

We wanted to perform a Monte Carlo study of a single MAJORANA reference design module with

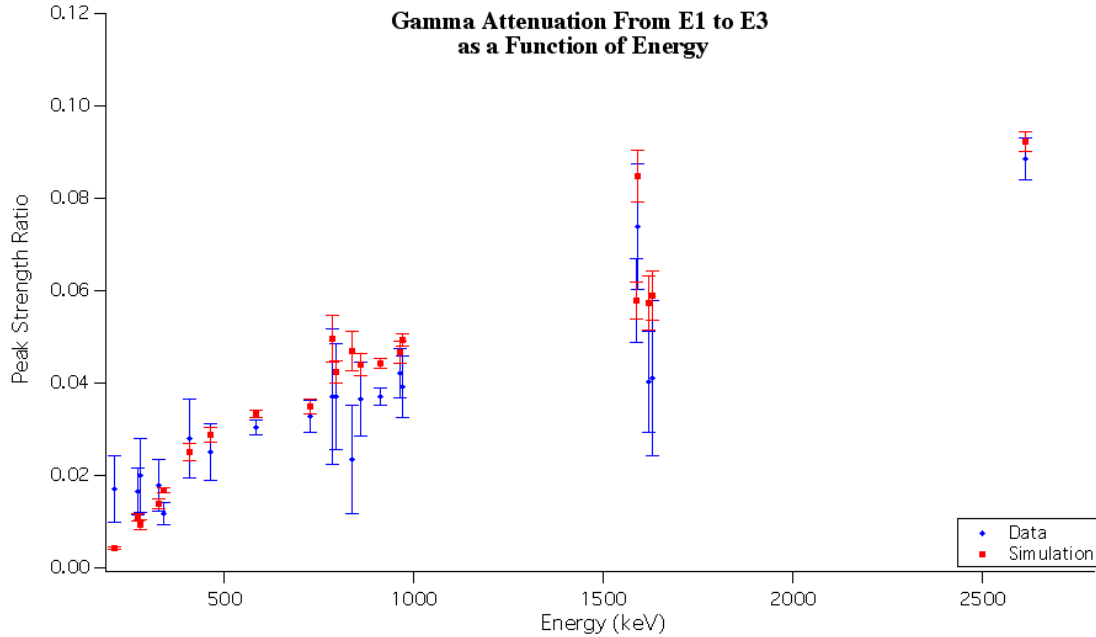


Figure 5.1: Ratio of the number of counts in E3 to that in E1 for several γ -ray lines in the ^{232}Th spectrum for CLOVER Monte Carlo data (red) and experimental data (blue). See the text for a description of the geometry.

a ^{232}Th wire source described in Section 5.3.1 to determine the amount of time required to generate a PSA training data set. First, we needed to check that the Monte Carlo correctly handled the attenuation of γ -ray lines through a layer of detectors. To this end, we simulated 10 cm of thorium wire wrapped roughly 90° around the quadrant of the CLOVER containing detector E1 (refer to Figure 2.4 for an illustration of the CLOVER). We then examined the ratio of the number of counts in the detector on the opposite corner of the CLOVER (E3) to that in E1 for several γ -ray lines in the ^{232}Th spectrum. We compared it to real data taken in this configuration and present these results in Figure 5.1. We can see from Figure 5.1 that the simulation of γ -ray attenuation agrees with data to within the statistical uncertainties. With renewed confidence the Monte Carlo software, we moved on to the MAJORANA reference design cryostat. If we refer back to Figure 2.2, which depicts the MAJORANA reference design module, we can see that each removable string of detectors consists of three crystals. This forms three horizontal layers in the cryostat. There are also three concentric shells of detectors, consisting of: the one innermost string, the six strings surrounding it in the interim shell, and the twelve outermost strings of the module. We simulated 10^7 events from the ^{232}Th decay chain and constructed the calibration spectra by horizontal layer and by concentric shell

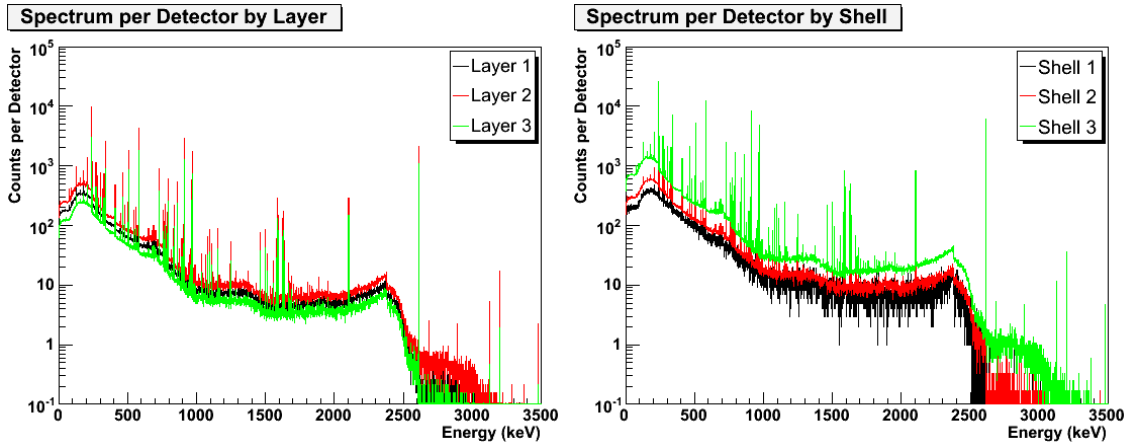


Figure 5.2: Layer by layer (left) and shell by shell (right) spectra for the Monte Carlo study of the MAJORANA reference design calibration system.

in the module, normalized to counts per detector. These are shown in Figure 5.2. If we zoom in on the energy region around the DEP and γ -ray lines used to train our PSA cuts (see Figure 5.3), we see that the center string of detectors collects just over 100 DEP counts per detector. This is roughly one fourth of the minimum we would need to construct a full training data set for the PSA cuts. The 10^7 Monte Carlo events displayed in Figure 5.2 correspond to a roughly 19-hour run with a single strand of the 0.22 mm diameter thorium wire from Goodfellow. This means that in order to get a full PSA training set, we would need to run for more than three days with a single strand of thorium wire. This is considerably longer than the amount of time we would like to perform calibration runs in a given week. This run time could be reduced significantly by using two or three strands of the thorium wire in the calibration track, as well as by deploying a calibration track (like the one pictured in Figure 5.4) around each layer of detectors in each module. Still, pushing the counting time down to even as low as twelve hours is more than we would like to have the experiment in calibration mode each week. This is the fact that leads us to notion of separating out the energy scale calibration from the PSA training runs. One hour per week with two or three strands of thorium wire would be sufficient to calibrate the energy scale of the experiment. This would allow us to count for the roughly one day (assuming we deploy three thorium wire sources) required for PSA training on a less frequent schedule. Even more importantly, this scheme would allow us to train the PSA cuts on the entire training data set and then have a separate set of calibration data we could use to monitor the efficacy of the PSA cuts (a much more detailed discussion of the need for this can be found in Section 6.3.2).

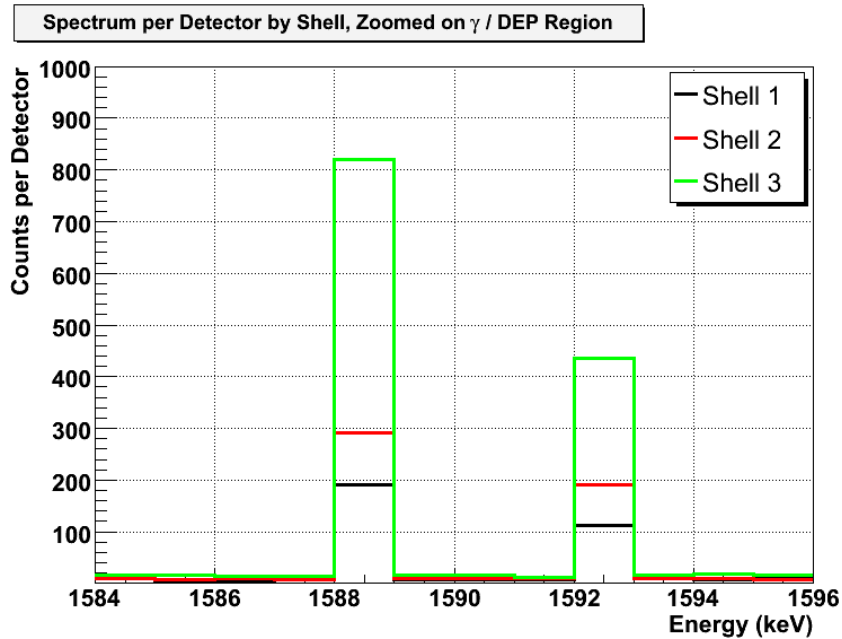


Figure 5.3: Layer by layer (left) and shell by shell (right) spectra for the Monte Carlo study of the MAJORANA reference design calibration system.

The schedule for the other two types of calibration runs (veto efficiency and localized contamination) is less critical to the operation of the experiment. We suggest that they will be performed extensively just after the deployment of the first MAJORANA module as well as subsequent to deployment of a second or third, etc. Afterward, these types of calibration tests could be performed on a monthly or even quarterly basis to check for deviations from the original efficiency results. In particular, we could use the cosmic ray μ rate to monitor the stability of the veto efficiency, *i.e.* if there were a sudden drop in the cosmic ray μ rate, it would perhaps be an indication of some problem with the veto system and therefore reason to perform a detailed efficiency calibration.

5.3.3 Calibration Prototype System

Now we discuss the containment and positioning hardware proposed for the MAJORANA project and the prototyping work done at LANL to develop it. Many of the technical challenges to be overcome in the design of the containment and positioning hardware revolve around the requirements detailed in Section 5.2. The first and most important aspect of the calibration hardware is the calibration source track. This “track” is a tube made from electroformed copper that will wrap around the exterior of the module and exit the shield near the point where it enters. The wire sources will be

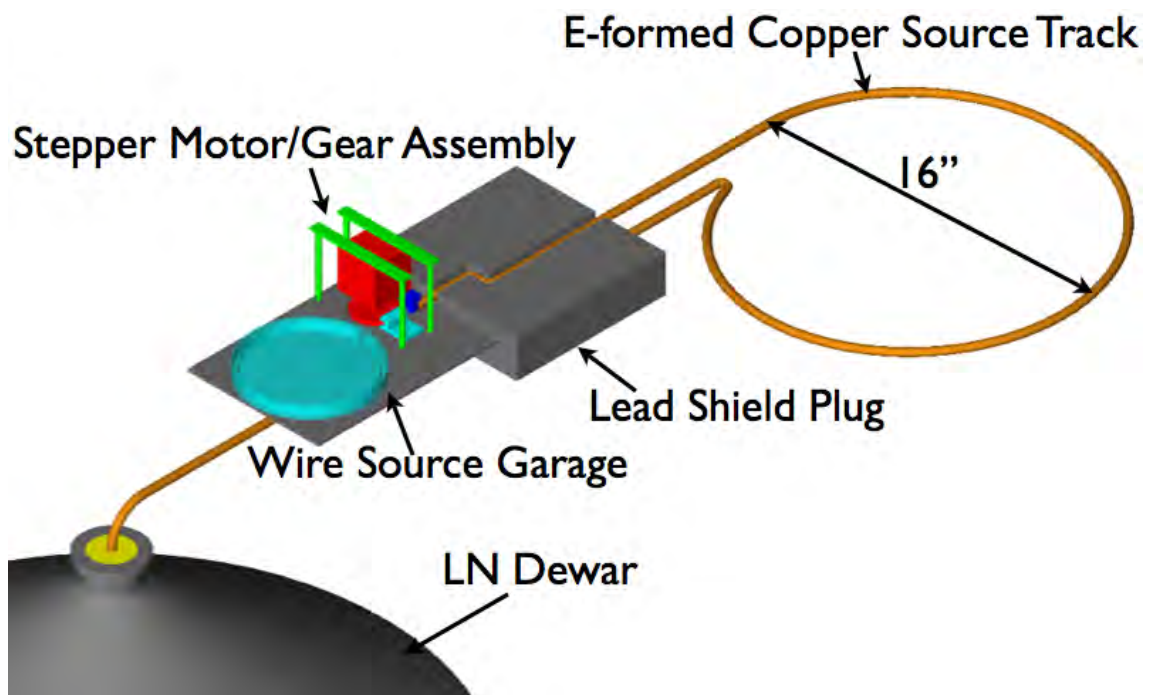


Figure 5.4: Conceptual drawing of the calibration containment and positioning system to be used in the MAJORANA experiment.

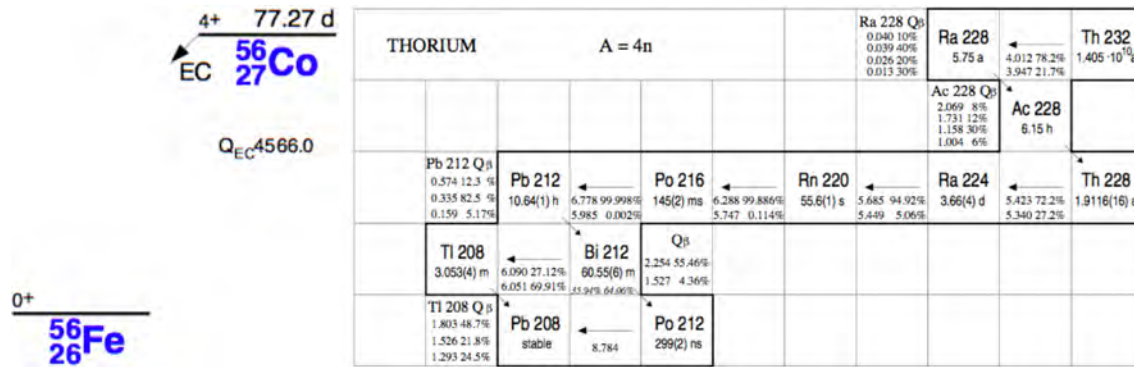


Figure 5.5: The decay schemes of ^{56}Co (left, from Reference [71]) and ^{232}Th (right, from Reference [38, Figure I.1]). Note that ^{56}Co decays directly to ^{56}Fe via β^+ /EC, and has no gaseous elements in its decay chain.

glued to a mechanical belt that will get fed through the containment tube by a gear and stepper motor assembly as shown in Figure 5.4.

For the thorium wire sources entering the shield for energy scale calibration and PSA training runs, there are two possible origins for contamination from the source itself. First, we must guard against dust from the wire being deposited inside the electroformed copper tube. We will address this by coating all of the wire sources in Teflon[®] and possibly by also evaporating a thin layer of copper onto the wire prior to Teflon[®] coating. This will likely not, however eliminate the second possible source of contamination from the thorium wire sources: radon emanation. ^{220}Rn is part of the decay chain of ^{232}Th , and will therefore emanate from the thorium wire. The ^{56}Co wire source will not suffer from this problem because ^{56}Co has no gaseous elements in its decay chain (see Figure 5.5). Both sources can allow for the introduction of environmental radon into the experiment. We will mitigate this problem by sealing off the calibration tube when not in use and by venting it with the boil-off from a liquid nitrogen dewar after each calibration run. Figure 5.4, shows the conceptual design for the calibration system.

We have constructed a prototype for the calibration system in our laboratory at LANL, depicted in Figure 5.6. The heart of the calibration system is the gear/stepper motor system and source garage. A close-up of these two sections of the prototype can be seen in Figure 5.7. The thorium wire source is mounted on the dark blue belt material shown in both panels of Figure 5.7, and it is held into place by a metal guide that fits around the gear. The left panel of Figure 5.7 shows the design of the source garage. It is essentially a spiral track into which the calibration belt gets fed when not in use. This design works quite well in this prototype phase, but we will discuss some

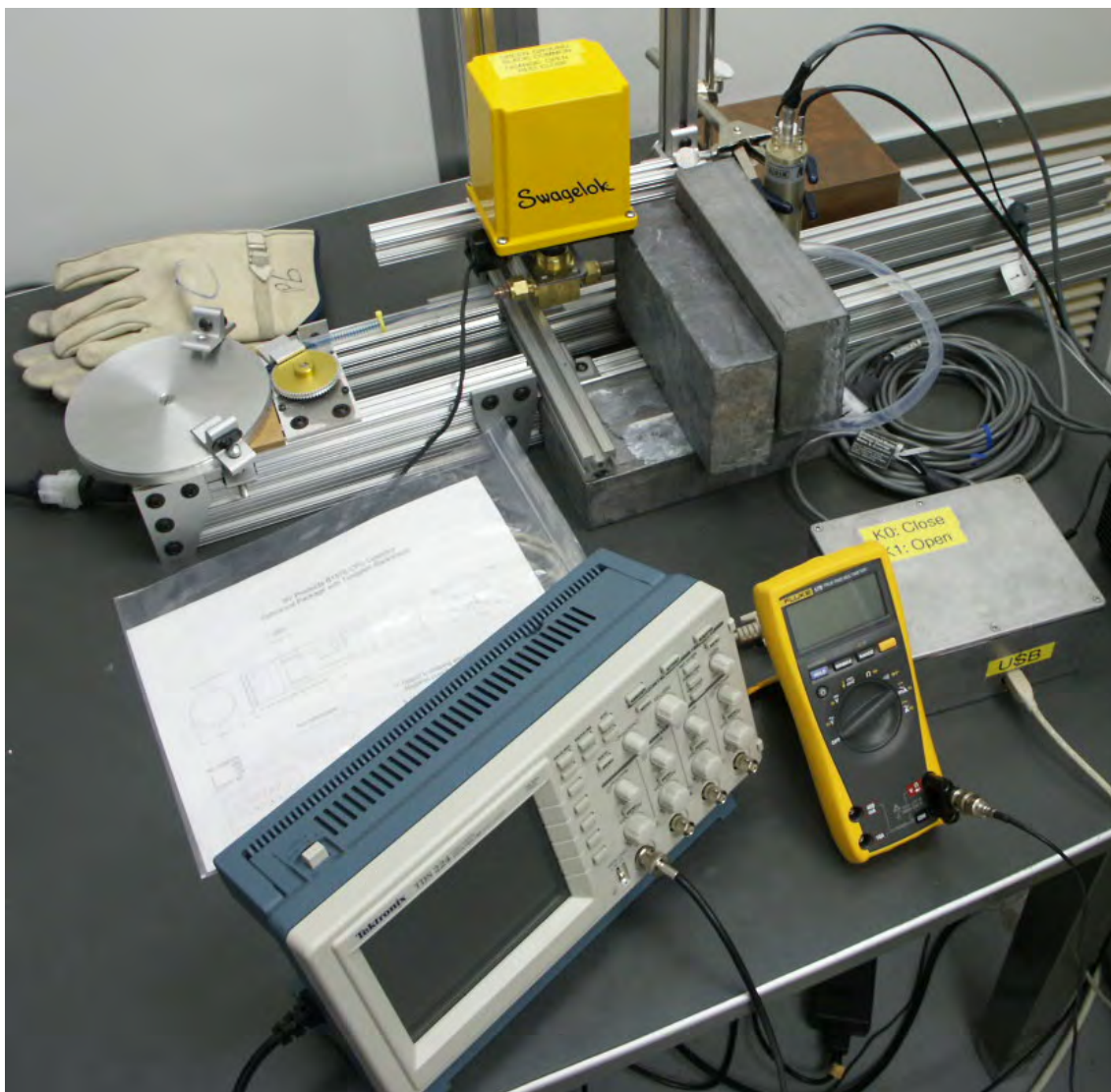


Figure 5.6: A photograph of the prototype calibration system constructed at LANL. The electrically actuated Swagelok valve came from Albuquerque Valve and Fitting, the plastic tubing from Fisher Scientific, the stepper motor, gear and belt from W. M. Berg and the source garage was fabricated by the CENPA instrument shop at the University of Washington.



Figure 5.7: A close-up of the garage with its top removed to show the source belt parked inside (left panel) and stepper motor (right panel) sections of the calibration system.

potential improvements to this design in Section 5.3.4.

We now present a sample calibration spectrum taken with the prototype system. The data were read out with a DGF4C digitizer board[10], controlled by the Object-oriented Real-time Control and Acquisition (ORCA) software[84]. ORCA also ran the slow control systems (*i.e.* the stepper motor and valves). For simplicity of operations, we took this spectrum with a Cadmium-Zinc-Telluride (CZT) detector. We described CZT detectors at greater length in our discussion of the COBRA experiment in Section 2.4.4. ORCA also has a scripting host that we used to automate this exercise. The script for this calibration test: counted with the source out for 90 minutes in MCA mode, opened the valve and pushed in the source, counted for another 90 minutes in MCA mode, and then pulled the source out and closed the valve.

The localized contamination response runs will use either a commercially available linear slide or a gear and stepper motor assembly like the prototype for source positioning. The ports will also be made of electroformed copper, and the sources will be pellets sealed in stainless steel. These too will have to be sealed off with valves and purged with liquid nitrogen boil-off. The veto efficiency runs will not require precise source positioning techniques since they will be outside the experiment proper, but we will have to mark the location of the source on each panel so that it can be placed back in the same location each time.

5.3.4 Lessons Learned From the Calibration Prototype

We now discuss several changes and improvements to the prototype design that, from our experience during its initial construction and operation, we think would be useful in fielding an eventual

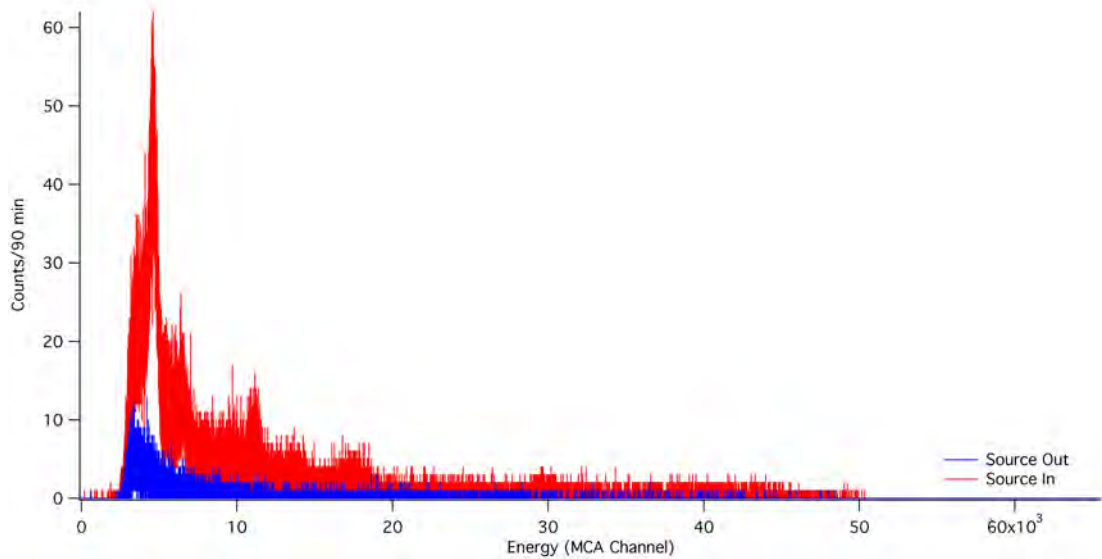


Figure 5.8: A test spectrum taken with the calibration system prototype. The red trace is the spectrum with the source near the CZT detector, and the blue trace is the spectrum with the source removed.

MAJORANA calibration system. First, the total length of the track is currently constrained by the amount of the belt that can be pushed into the garage before friction causes the belt material to bind up and go no further. This length corresponds to a loop diameter of approximately six inches. This is clearly not large enough for a MAJORANA-type cryostat, but we have several ideas for beating this friction limit. The belt material from W. M. Berg is a simple braided steel cable surrounded by molded polyurethane which forms the teeth into which the gear bites. They also sell belt material with two wire cores that is the same width as the single core belt material currently in use. This will serve both to stiffen the belt material and largely take away one direction in which it could flex. We could special order some belt material made from thin solid core wire or thicker braided wire, it too would serve to strengthen the belt. In fact, it is very likely that we will have to special order a belt (or more likely, several of them) for the calibration system because of the difficulty of attaching the wire source to the belt. The current design does this with simple electronic heat shrink, but a far more elegant design would be to simply make a section of the belt out of the thorium wire and then splice that into a larger one for the calibration system. This would obviously require the fabrication of a special part either by the MAJORANA collaboration or the manufacturer. We could also redesign the source garage to be wider, or even coat its inside with Teflon® or some other low-friction material. Both of these options would substantially reduce the friction between the belt

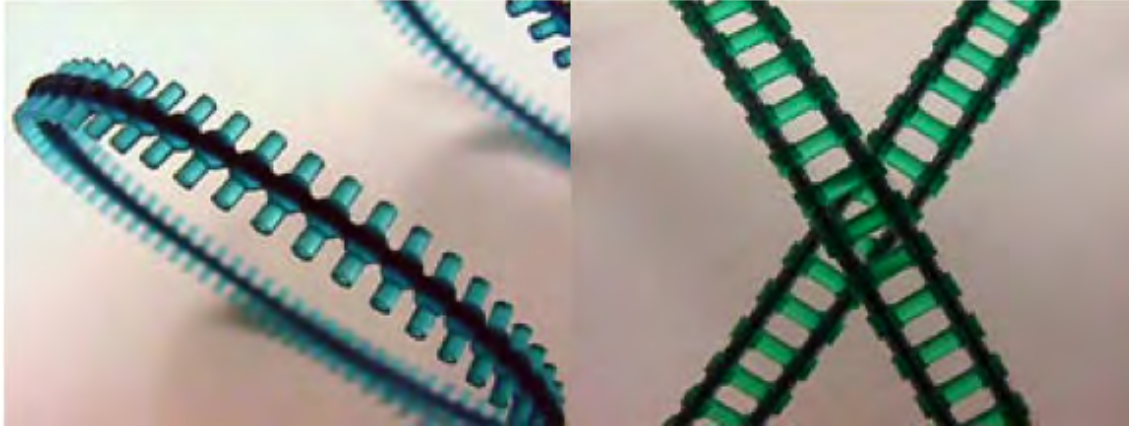


Figure 5.9: Catalog photos taken from W.M. Berg’s website of different belt materials. The left panel shows the current calibration belt design, and the right panel shows a slightly mechanically sturdier option.

and the garage walls thereby allowing more material inside the garage and increasing the available length of the source delivery belt.

Second, it would be useful to have some independent way to know where the source actually is. Currently, we “know” the source’s location by counting the number of ticks that the stepper motor has moved the source in or out. This is fine as long as we are certain of the source location at the start of the calibration program. Some sort of interlock that stopped the motor when it was pulled completely out of the shield would accomplish this. On a related note, there is currently nothing other than the skill of the operator to keep the calibration system from closing the valve while the source is inside the shield, potentially snapping the belt cable. An engineering control or hardware interlock to keep this from happening will be required.

Last, this will probably not be a major difficulty, but we did not actually implement a purge system for the calibration prototype. This would involve adding a second valve to the calibration system that worked simultaneously with the first. We would also need to attach a source of clean nitrogen gas to the system. This would most likely be boil-off from a liquid nitrogen dewar.

5.4 Characterization and Commissioning Requirements

One of the main focuses of this dissertation is on lowering the systematic uncertainties in the MAJORANA experiment. To this end, we have concerned ourselves primarily with the *in situ* calibration program for the experiment. There is an entirely separate program that centers around the initial characterization of new detectors once the collaboration takes possession of them from the

manufacturers, and another that will focus on the data taken shortly after a MAJORANA module's deployment and commissioning. We will not go into great detail about these programs, but we will outline some requirements for them.

The initial characterization data will consist of high-statistics source data that will try to characterize the thickness of the outer non-active region for each detector. Should the MAJORANA collaboration choose a segmented detector geometry, we will also have to interrogate the boundaries between segments with a well-collimated, low-energy source. We will not be able to generate PSA training keys for the detector at this stage because it will be in a different cryostat with different electronic characteristics from the final MAJORANA module.

Last, the commissioning data for new MAJORANA modules will also be high-statistics source runs, but these data will focus on benchmarking the system-wide performance of a new module. This will include getting initial values for most of the systematic uncertainties discussed listed in Table 4.3. This is the initial set of data that will likely be used to normalize the Monte Carlo results. It is also possible that instead of doing separate runs during production data taking to generate PSA training sets for the array, we could simply use commissioning data to generate these keys. It would however be wise to take intermittent, high-statistics calibration runs throughout production runs to monitor for stability of the MAJORANA PSA performance.

Chapter 6

PULSE SHAPE AND SEGMENTATION ANALYSIS AND ASSOCIATED UNCERTAINTIES

One of the key contributions to the background discrimination power of the MAJORANA experiment is the powerful combination of pulse shape analysis with detector segmentation. In this chapter, we will begin with an examination of the concepts behind analyzing pulse shapes in germanium detectors. We will detail some extensions that can be made to the heretofore published PSA work applied to germanium detector technology. We will then move on to some work on the specific systematic uncertainties associated with making pulse shape cuts. We will then examine some different segmentation schemes with data from a rather highly segmented detector, and then discuss the effectiveness combining pulse shape analysis with single segment multiplicity cuts and the independence of the two techniques. Last, we will close with a summary of the systematic effects that can impact pulse shape analysis.

6.1 *Parametric PSA Overview*

Pulse shape and segmentation analysis, like most of the background tagging techniques to be employed in the MAJORANA experiment, exploit the single-site nature of the signal and the multi-site nature of most backgrounds of similar energy. Figure 6.1 shows the difference between typical pulses indicative of our signal events (represented by a double-escape peak event) and our backgrounds (represented by a γ -ray event). While it is obvious that these two classes of events are qualitatively different “by eye,” quantifying the difference between them in such a way that a computer can quickly and reliably tell them apart is both quite difficult and the primary aim of the MAJORANA pulse shape analysis cuts. These cuts are largely an extension of the PSA work done in support of the IGEX experiment, and discussed at greater length in Reference [2, 49]. This method relies on moments calculated from digitized waveforms from the germanium detector(s). The waveforms analyzed for our PSA are recorded from the output of the integrating preamplifiers for the detector system. We refer to this as the “charge pulse.” Most of the pulse shape moments used in background rejection strategies are calculated from the “current pulse,” which we recover by taking the time derivative of the charge pulse. This is because the current pulse is actually proportional to the energy deposited in the detector as a function of time (after being convolved with the transfer

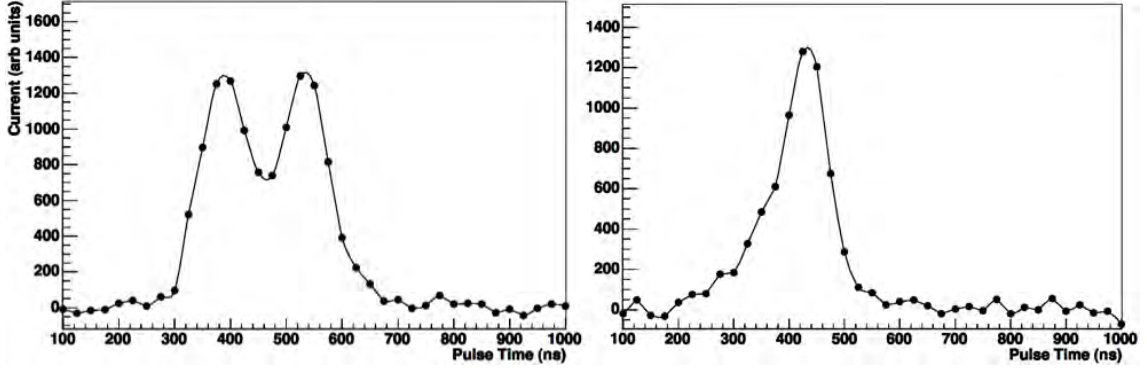


Figure 6.1: Sample pulses representative of our background events (left) and signal events (right) captured by the LANL CLOVER detector. These two events were isolated using an energy cut in a ^{232}Th data set to pick out a 1588 keV γ (left) and a 1592 keV double-escape peak (right).

functions of the detector and preamplifier systems, of course).

The PSA cut algorithm must first be “trained” on calibration data, at which time, the training software associates typical values of the pulse shape moments with each class of events (single and multi-site). It makes this association by storing the pulse shape parameters for each class of training events in a multidimensional histogram we refer to as a “PSA Key.” Histogram bins which contain more events from one class of events become associated with that class. Then, when the analysis software examines the pulse shape parameters from production data, a pulse with parameters that fall into a given histogram bin becomes classified as whatever event type is associated with that bin. Previous pulse shape analysis algorithms used by the MAJORANA collaboration have made use of three parameters for these cuts:

- Pulse width, defined as the time between when a charge pulse rises 10% above the baseline level, and when it reaches 90% of its full height.
- Front-back asymmetry, defined as the difference in the area of the first and second halves of the current pulse, normalized by the total area of the current pulse.
- Normalized moment, defined essentially as the moment of inertia of the current pulse were it treated as a mass distribution. It is calculated using the expression:

$$I_2 = 12 \frac{\sum_{i=N_0}^N j_i \Delta t^2 (i - i_{mid})^2}{\sum_{i=N_0}^N j_i \Delta t}, \quad (6.1)$$

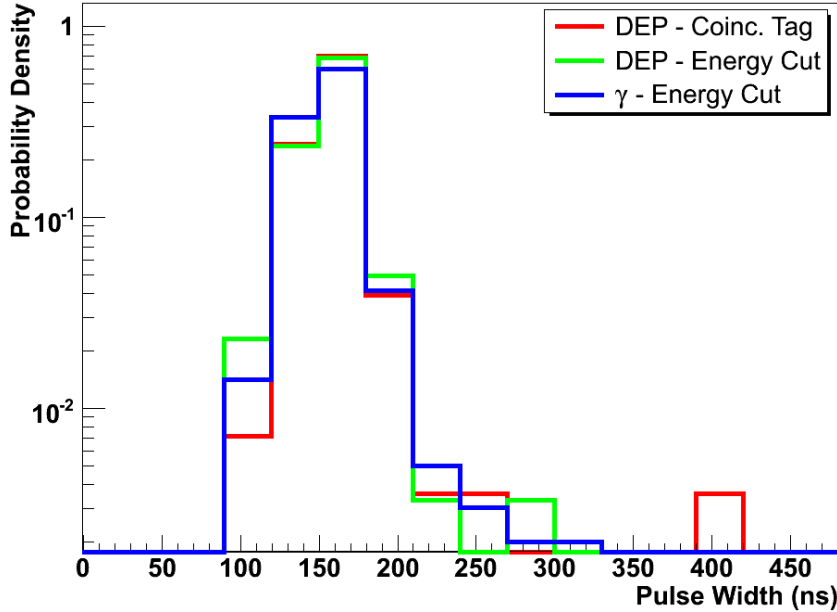


Figure 6.2: Distribution of pulse widths for γ events, DEP events tagged with a simple energy cut, and DEP events tagged with an additional coincidence.

where the pulse runs from time indices N_0 to N , with i_{mid} halfway between. j_i is the amplitude of the current pulse at time index i , and Δt is the period between samples of the digitizer.

The details of how the association of specific moment values with certain event classes (and therefore the actual cut) was made for IGEX data can be found in Reference [2]. This work trains the PSA cuts by organizing pulse shape moments calculated from DEP events in the training data in a three dimensional PSA key histogram, then sorting the bins in that histogram in order of descending content (*i.e.* the bin with the most counts in it would be first and the bins with zero counts in them would be at the end). The PSA training software then steps down that list and stops when some nominal fraction of the total DEP events are included (typically, this is 80%). The event-by-event analysis software then calculates the moments for each pulse and determines into which bin in the above key histogram it falls. If that bin is one of those on the list defined by the DEP training data, the software classifies that event as single-site, and it passes the cut.

In the R&D work at LANL supporting the MAJORANA experiment, we have taken a slightly different approach [49]. First, the IGEX analysis used all three of the above parameters, while the MAJORANA R&D work used only the second and third in the list. This was because the pulse width was extremely degenerate between the different event classes (see Figure 6.2). Instead, we

populated different **two**-dimensional key histograms with moments from training data corresponding to **both** DEP and γ events. For the results reported in Reference [49], we then fit a two-dimensional analytical expression to both, and normalized that expression to one such that it could be treated as a probability density. We then classify each event as whichever type has the higher probability given its moments.

The PSA (and segmentation) work throughout this chapter relies on the ratio of peak and continuum strengths before and after cuts are made to calculate the survival probability of those cuts for different event classes. For flat, featureless continua, this is simply an exercise in counting the number of events in an energy window. The resulting uncertainties are then just those arising from Poisson fluctuations. However, for peaks on top of continua, the situation is more complicated. We wish to separate out the strength of the peak from that of the continuum on which it rests. We do so by performing a standard χ^2 fit in the ROOT framework [34]. In this case, the fit model is a flat background plus a Gaussian peak (or two when the peaks are close enough in energy for the spectrum not to fall back to the continuum level between them—this is the case for the 1588 keV γ -ray and 1592 keV DEP). To extract a peak’s strength, we simply calculate its area from the fit parameters. The uncertainty in this area comes from the uncertainty in the fit parameters and the expression for the area of a Gaussian using standard error propagation techniques. We can then take the ratio of these peak areas to calculate the survival probability for that cut. We again propagate uncertainty through the expression to obtain the survival probability uncertainty. Throughout this chapter, when we refer to the “fit uncertainty,” this is the quantity under discussion.

6.2 Extensions to the Parametric Method

Having shown the utility of parametric pulse shape analysis in the tagging of signal and background events, the notion of extensions to and improvements upon this method becomes quite interesting. We will now discuss three extensions to and one departure from the parametric pulse shape analysis method described in Section 6.1. First, we will discuss some structural changes made to simplify and computationally streamline the PSA cuts and their training as well as some efforts to allow for the fine-tuning of their sensitivity. We will then detail efforts to add several higher order moments beyond those included in References [2, 49]. Next we will discuss plans to use some simple machine learning algorithms to better define the signal and background regions in our cuts. Last we will summarize the PSA cuts used in the full position reconstruction analysis used in γ -ray tracking experiments, such as GRETA and Gretina. Unfortunately, only the structural changes have been implemented and systematically tested. PSA performance with the higher moments has been pre-

liminarily implemented with data from the CLOVER detector, but no detailed analysis of its efficacy under varying experimental conditions has yet been performed. The rest of these extensions to the current state of MAJORANA pulse shape analysis will be left to future work.

6.2.1 *Structural Improvements*

In the time since the publication of Reference [49], we have made some changes to the methods used for that work. Instead of fitting a complicated analytical function to the key histograms, we simply normalize them to unity directly and use the key histograms themselves as the probability densities. This is much cheaper computationally, but does require somewhat larger training data sets. The fit method from Reference [49] required approximately 200 DEP and γ -ray events per detector, while the key histogram method requires roughly two to three times that number. Additionally, we also started to select training DEPs in two different ways: one in which we make a simple energy cut in the single-crystal spectra, and another where we look for two-crystal events with the DEP energy in one detector, and one of the two e^+ annihilation γ -rays in another. This coincidence tag limits the number of DEPs available for training in the clover, but it also provides a very clean population of DEP events. Most of the PSA cuts presented in this dissertation were made with single-crystal, energy cut-selected DEPs. When both analyses were made however, the non-coincidence tagged DEPs in this chapter are denoted with a subscript “NC” (for “No Coincidence”). Examples of these keys for single-crystal, energy cut-selected DEP and γ -ray events are in Figure 6.3. We have also added a fine-tuning parameter to these cuts that gets added to the γ probability and subtracted from the DEP probability when making the cut. This allows us to tune the selectivity of the PSA cuts, making them more stringent for higher values of this parameter and more lax for lower values.

6.2.2 *More Moments*

An obvious extension to the parametric PSA method is the addition of more moments to the analysis. This is essentially an attempt to incorporate more “handles” into the analysis for us to use in the discrimination between different event types. We will now discuss in detail the methods by which this was investigated.

Definition of Higher Order Moments

We define the third and fourth moments of the current pulses analogously to the way in which the normalized (second) moment was defined in Reference [2]. We modify Equation 6.1 to be essentially the n th moment of the current pulse, once again normalized by the area to minimize any energy

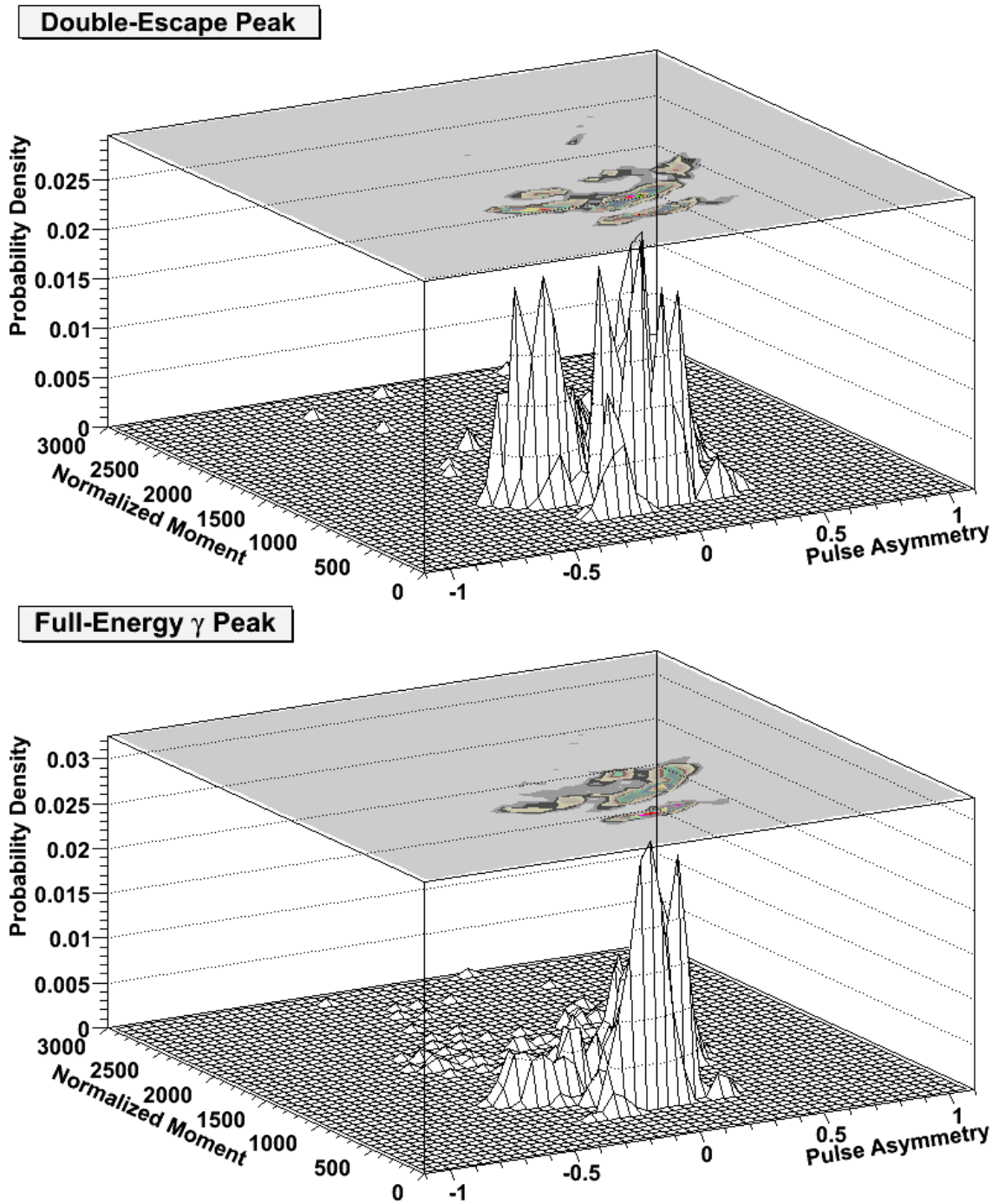


Figure 6.3: PSA cut keys from ^{232}Th data, populated with 1592-keV DEP (top) and 1588-keV γ -ray (bottom) events. The easiest way to see the difference between these is to look at the contour plot on the top of both of the surface plots.

dependence in the form of the moment itself:

$$I_n = \frac{\sum_{i=N_0}^N j_i \Delta t^n (i - i_{mid})^n}{\sum_{i=N_0}^N j_i \Delta t}. \quad (6.2)$$

As with the normalized moment, I_n is the n th moment of a pulse that runs from N_0 to N with i_{mid} at the center. j_i is the current at time step i , and Δt is the clock period of the digitizer. There is a limit to the utility of adding many more moments to this analysis because, above a certain level, higher order moments begin to lose real physical significance. This is analogous to a situation in which an analyst performs a fit with too many degrees of freedom to very few data points. The charge pulses in the CLOVER had typical rise times (where information about energy deposition lives) of $\approx 0.5 - 1 \mu s$, corresponding to roughly 20 to 40 digitizer points. We stopped adding higher moments with the fourth. This is because the addition of two more moments was a significant increase in the dimension of our parameter space, but the fourth moment is likely well below the point where mathematical moments would lose significance. It is quite possible that the addition of a few more pulse shape moments would further improve PSA performance, and we will address that question in future work.

Signal and Background Regions

We now have a total of five moments to examine in our expanded parametric PSA study: width, asymmetry, normalized second, normalized third and normalized fourth moment. Nearly all of the analysis for this study was done in the ROOT framework [34]. When there were only two or three moments in the analysis, we simply stored the PSA key(s) as root histogram objects. The ROOT framework however, only has histogram objects defined up to dimension three. How then can we store and access all of the information about where the different populations of training events live in our now five-dimensional PSA parameter space?

We answer this dilemma by constructing two-dimensional histograms for every combination of two of the five PSA parameters, and examining the results of the PSA cut done by comparing each couplet of parameters. We simply loop over all of the pairs of PSA parameters and tally the number of PSA cuts that a particular event passes. This allows us to set a threshold on the minimum number of cuts an event must pass to be called a single-site event. We refer to this required number of cuts as the Number of Cuts Threshold (NCT). Operationally, the NCT serves as a coarse adjustment of the selectivity of our PSA cuts, while the tuning parameter described in Section 6.2.1 is a more fine adjustment.

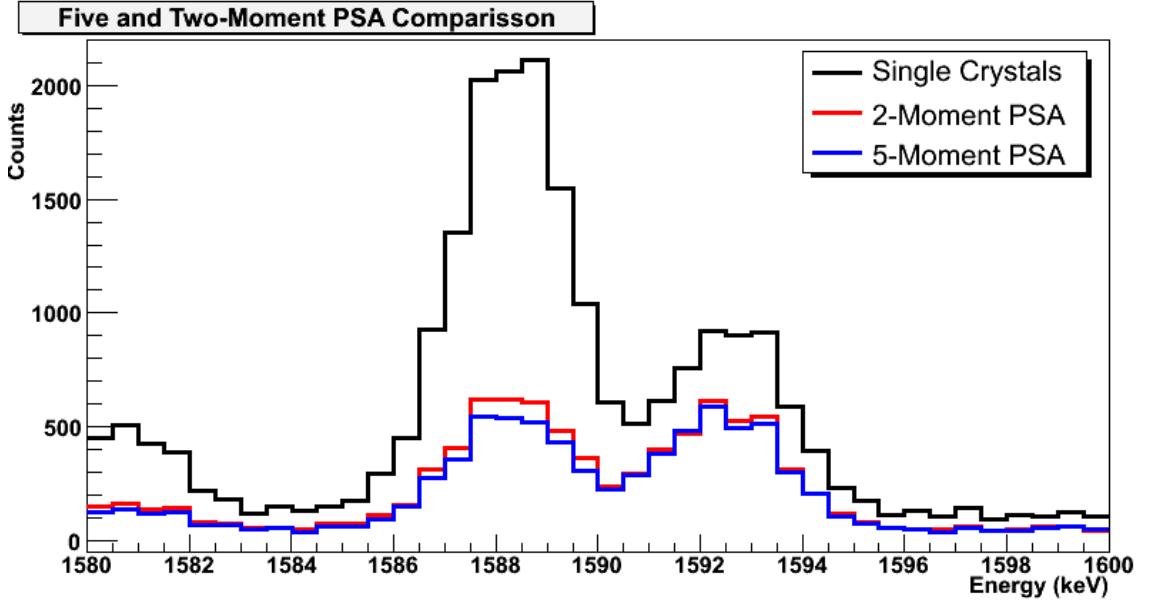


Figure 6.4: Single-crystal and PSA cut spectra for five and two-moment analysis.

Preliminary Results in the CLOVER Detector

The PSA survival probabilities reported in Table 4.2 and most of the rest of this dissertation used only two-moment pulse shape analysis because that technique was systematically tested under a variety of experimental circumstances. We now report some preliminary results on the effectiveness of adding these higher order moments to parametric PSA in the CLOVER. We set the NCT to six, because that most closely reproduced the DEP survival probability quoted in Table 4.2. We

Table 6.1: Survival probabilities of different processes for both the two and five-moment pulse shape cuts. The survival probabilities for both cuts were measured with the same training and characterization data sets, and examined the same three processes: 1588 keV γ -ray, 1592 keV DEP and 2.0 – 2.08 MeV continuum events. Note that the uncertainties quoted in this table are just those from the fit. We also include goodness of fit information for reconstruction of the spectra in the γ -ray/DEP energy region.

Cut Type	Survival Probabilities (%)			χ^2 per Degree of Freedom
	γ -ray	DEP	Continuum	
Two-Moment	29.0 ± 0.9	65.6 ± 2.5	45.4 ± 0.6	$47.6/31 = 1.5$
Five-Moment	25.0 ± 0.8	64.3 ± 2.4	41.7 ± 0.6	$48.4/31 = 1.6$

can see from Table 6.1 and Figure 6.4 that for the single data set examined, the five-moment pulse shape analysis out-performs the two-moment cuts clearly but not dramatically. Any conclusions drawn from this analysis are, of course subject to the limits of the fit reconstruction. For equivalent DEP survival, γ -ray and continuum events are rejected more effectively by better than four times the fit uncertainty. This is particularly exciting because it corresponds to reductions in survival probability of $\approx 13\%$ and $\approx 8\%$ respectively for γ -ray lines and continuum events. As noted in the caption of Table 6.1, the uncertainties in this table are only those from the fit and do not include other systematic uncertainties as those from Table 4.2 do. This comparison using only the fit uncertainty is legitimate because these two analyses were performed using exactly the same training and characterization data. Furthermore, both cut spectra have similar goodness of fit behavior, meaning that any deviation from the fit model (two Gaussian peaks plus a flat background) is likely quite similar in both.

While the increase in PSA performance for the CLOVER was not overwhelming, it is nonetheless useful because no additional hardware and only marginally more computational power were required. It is also true that the CLOVER, because of its small size and only modest segmentation, has pulses with very simple time structure. Larger, more highly segmented detectors have more complex time structure, and the addition of higher pulse shape moments will therefore likely be of much greater utility in separating different event classes for such detectors. As mentioned above, we intend to also explore the addition of at least two to three more moments to this analysis and check for further improvement.

6.2.3 Better Signal and Background Region Definition

At its core, the pulse shape analysis we are doing for the MAJORANA experiment is one manifestation of a more general family of algorithms, known in the machine learning community as “Event Classifiers.” There are a number of very subtle algorithms for improving the efficacy of event classifiers used in machine learning research. One such algorithm is known as “boosting.” The idea behind this technique is that once the mask applied to the training data that actually makes the event classification is constructed (in our case, this would be the signal and background regions in our parameter space), the training software modifies that mask slightly and re-checks the training data to examine the efficacy of the new cuts. This process is iterated many times until an asymptotically good solution is reached. There are also a number of machine learning algorithms that do not require training. These are known as “Unsupervised Learners.” These algorithms simply group events together in clusters in whatever parameter space is used to classify events. Unsupervised learners

are a very attractive option because they would remove the need for very large calibration sets and thereby remove one of the principle difficulties in the MAJORANA calibration program. It is, however more difficult to understand the discrimination power of unsupervised cuts ahead of production data taking, so we must bear that in mind if we decide to pursue them. There are many subtleties in the details of how any of these algorithms are implemented and further exploration of novel PSA techniques could, be quite an involved project worthy of a dissertation in its own right. Further work along these lines is an intriguing prospect for improving the power of single and multi-site event discrimination with no additional hardware requirement for the experiment.

6.2.4 γ Tracking Techniques

There has been debate in the MAJORANA collaboration about the utility of incorporating some of the γ -ray tracking techniques from the GRETA/Gretina analysis into the MAJORANA experiment. Any large decision that will directly affect the entire experiment, like this one, must be weighed in terms of a cost/benefit analysis. Implementing the GRETA-style position reconstruction analysis in MAJORANA will require a significant investment on a number of fronts. Principally, γ -ray tracking requires the detectors in the array to be rather highly segmented because it studies not only the primary pulse on the central contact of the detector, but also the induced pulses on all of the external contacts. Designs for the GRETINA prototype detectors have been segmented 5×8 and 6×6 . However, examining the induced pulses has been shown to be at least moderately effective with SEGA-like segmentation, so 5×8 or 6×6 could be quite a bit more segmentation than would be necessary in MAJORANA. It is the comparison of pulses across many segments that enables the full position reconstruction for energy depositions. This technique indisputably would offer the most information about each event in the MAJORANA data stream, but the increased number of front-end electronic parts, heat load for the cryogenic system, and general complexity of the detectors themselves makes fielding an array of highly segmented detectors more difficult than some other detector designs. The MAJORANA collaboration will continue to investigate the feasibility of implementing γ -ray tracking techniques with ongoing Monte Carlo efforts as well as the part of the MAJORANA prototype detector made from highly segmented detectors.

6.3 PSA Systematics

In Reference [49], we discussed systematic uncertainties in the PSA cuts as characterized with the CLOVER detector in a fairly general way. In this reference, the statistical uncertainties came from the fit parameters used to calculate the number of counts in each peak. The systematic uncertainties

came from the differences in survival probabilities between runs where the source was placed in different locations around the CLOVER cryostat. We will investigate a number of other sources of pulse shape analysis uncertainty as well as more specific ways to mitigate them.

6.3.1 PSA Parameter Histogram Binning and Training Set Size

The PSA parameter histogram keys have a finite number of bins in each axis. It is therefore interesting to examine the manner in which the binning of these axes affects both: PSA performance, and the required size of the training data set. To examine this dependence, we construct a series of figures showing PSA performance as a function of training set size for several different PSA parameter axis binnings. Figures 6.5 through 6.8 show this performance for: 10, 25, 50 and 100 bins per PSA parameter axis.

The first thing we see when examining these figures is that as binning in the PSA parameter histograms becomes finer, the survival probabilities for each event class reach their asymptotic values for larger training data sets. Also, we find that making the binning finer generally improves PSA performance, but there is a point of diminishing returns around 50 bins per axis (*i.e.* increasing the number of bins from 10 to 25 to 50 improves the separation of DEP and γ -ray events, but increasing from 50 to 100 bins per axis does not even at very large training set sizes). This is because finer binning in PSA parameter space allows for the resolution of finer structure in the signal and background regions. Once you have already captured the available structure however, increasing resolution does not help to discriminate between different event classes. We therefore chose the optimal conditions for our ensuing PSA studies by picking the binning that allows the best performance with the lowest number of training events. Because large-training set performance does not improve between 50 and 100 bins per PSA parameter axis, we chose 50 for all other studies presented in this dissertation. We now further examine Figure 6.7 to pick out the minimum size of the training set. We see that the best DEP/ γ separation is reached when there are more than approximately 400-600 DEP events per detector in the training data. This corresponds to between four and eight 25,000-spill data files captured with the CLOVER using the DGF4C digitizer cards without demanding the coincidence tag, or more that sixteen if we do.

6.3.2 Independence of Training and Characterization Data Sets

We now discuss the importance of training PSA cuts and characterizing their efficacy on different data sets. If the same events used to train PSA cuts are subsequently used to characterize their efficacy, then sample bias will creep in as another systematic effect. This (especially when combined

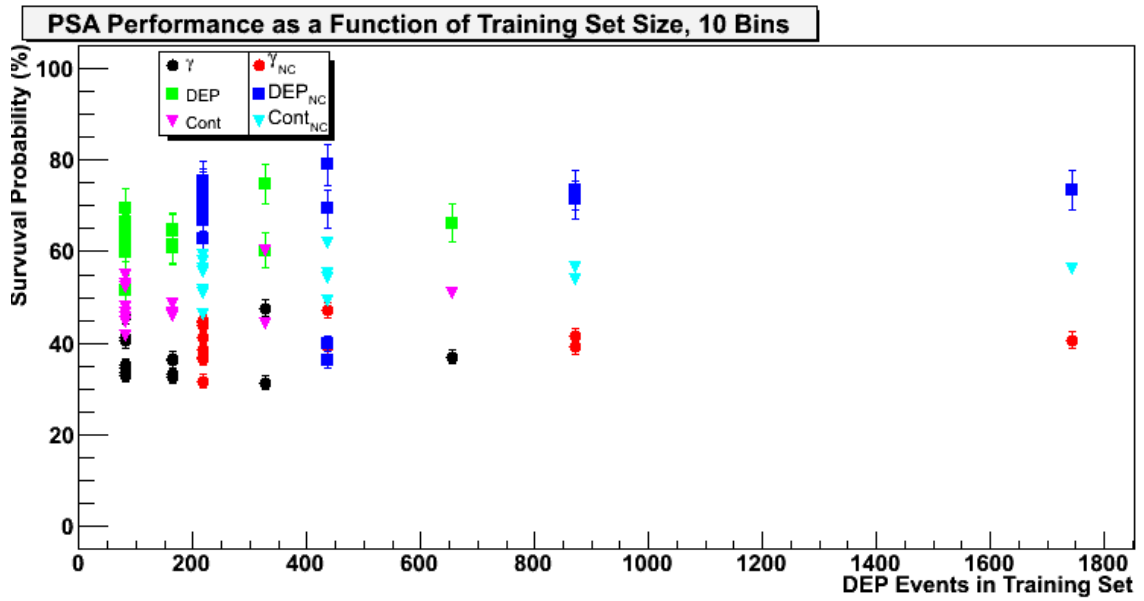


Figure 6.5: PSA efficacies as a function of the number of double-escape peaks per detector in the training data set for 10 bins per PSA parameter axis.

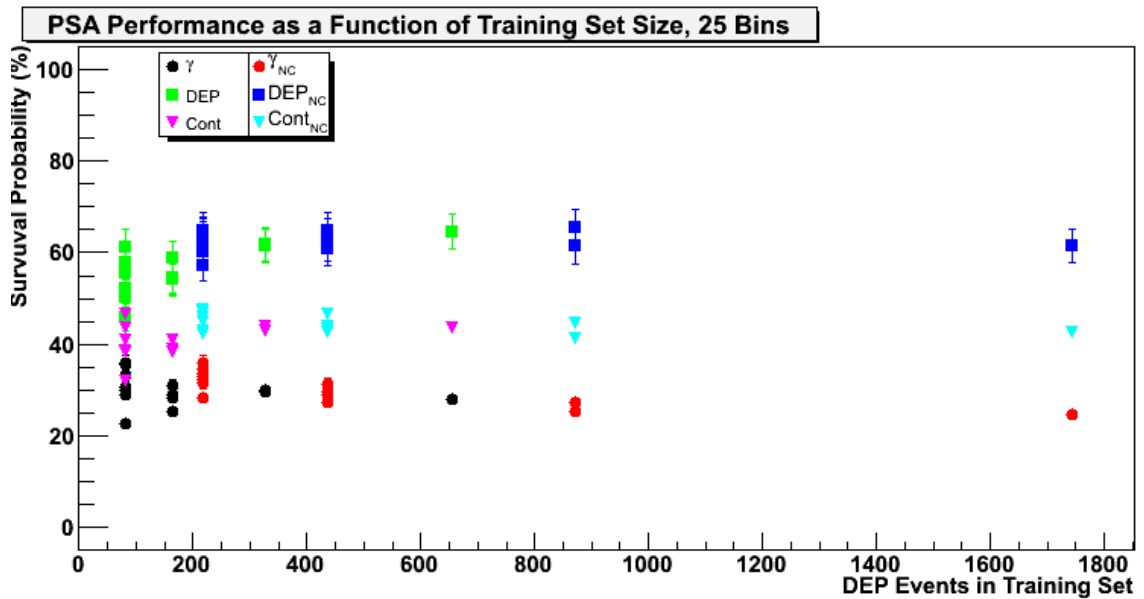


Figure 6.6: PSA efficacies as a function of the number of double-escape peaks per detector in the training data set for 25 bins per PSA parameter axis.

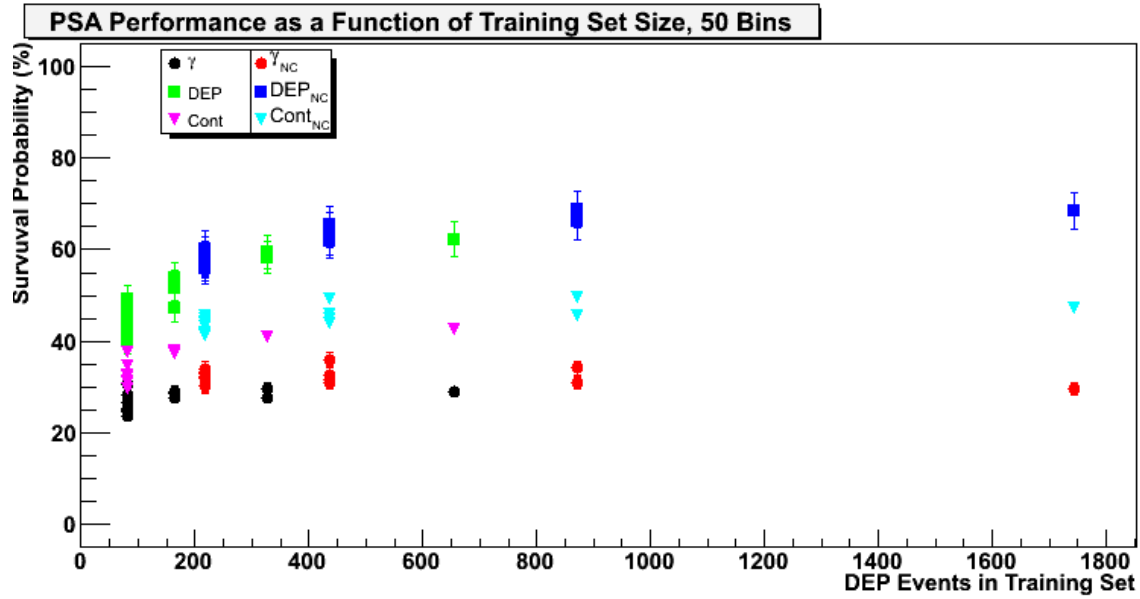


Figure 6.7: PSA efficacies as a function of the number of double-escape peaks per detector in the training data set for 50 bins per PSA parameter axis.

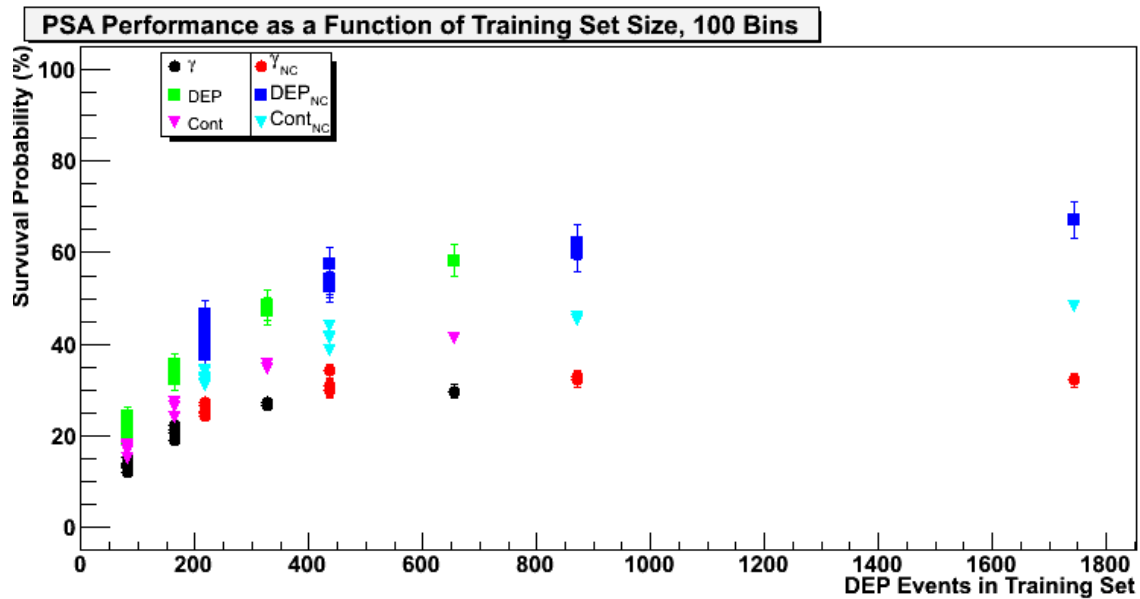


Figure 6.8: PSA efficacies as a function of the number of double-escape peaks per detector in the training data set for 100 bins per PSA parameter axis.

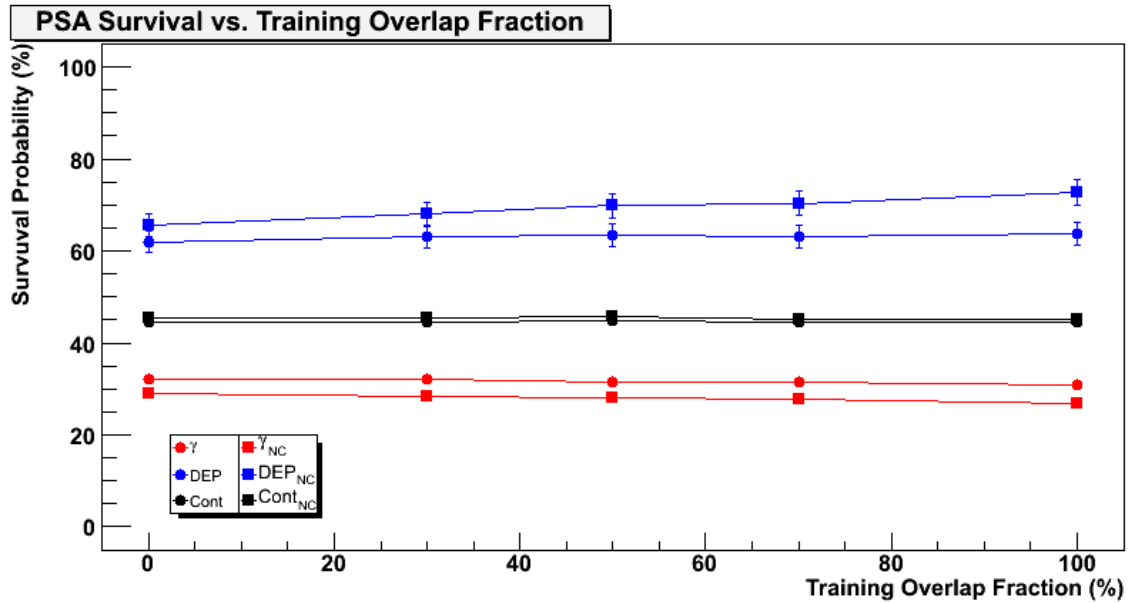


Figure 6.9: PSA efficacies as a function of the fraction of the characterization data in common with the training data.

with a comparatively small number of training events) will tend to make pulse shape cuts appear more effective than they actually are because any fluctuations in the signal and background regions will get frozen into the PSA keys. Then, when the same data is run through the event classifier, these fluctuations get treated as real differences. This effect is most easily mitigated by building a “wall of separation” between training and characterization data.

To examine how strongly sample bias can affect our PSA performance, we took the training keys constructed for a particular data set, and used them to analyze several characterization data sets of the same size (there were ten 25,000-spill files in each one). Each characterization set had a different number of files in common with the training set. We show the results of this study in Figure 6.9.

We can see, unsurprisingly that as the overlap fraction increases, the separation of DEP and γ -ray events also increases. For comparison, we also included survival probabilities for pulse shape analysis trained on coincidence-tagged DEP’s. To help quantify the effect of sample bias, Table 6.2 reports the total change in survival probability (that is, the difference in survival probability between 0% and 100% overlap) compared to the average fit uncertainties for each event class in the two analyses. Upon examination of Table 6.2, we find that DEP and γ -ray events for the non-tagged cuts are most strongly affected by sample bias, each changing favorably by just less than three times the fit uncertainty. The affect is nearly eliminated for those event classes in the tagged cuts, with γ -ray

Table 6.2: Difference in survival probabilities for PSA cuts (trained on both coincidence-tagged and non-tagged DEPs) between training and characterization data overlaps of 0% and 100% for different event classes. Each survival probability is reported in the form: percent change from 0% to 100% / average fit uncertainty / ratio of percent change to fit uncertainty. As with previous PSA survivals the continuum survival is calculated between 2.0 and 2.08 MeV

Event Class	Coincidence-Tagged	Non-Tagged
γ -ray	-1.0%/0.9% / - 1.1	-2.3%/0.9% / - 2.6
DEP	+1.7%/2.4% / + 0.7	+7.1%/2.6% / + 2.7
Continuum	0.0%/0.6%/0.0	+0.3%/0.6% / + 0.5

survival dropping by just one unit of fit uncertainty and DEP survival dropping by a fraction of that. This is because the coincidence-tagged training DEPs never actually enter the characterization data stream, as they are all two-crystal events (with an annihilation γ -ray in one detector and the DEP in another). The characterization analysis treats only single-crystal events, thus keeping sample bias from playing a strong role. This could be useful in training pulse shape cuts in the MAJORANA modules. Even the smaller prototype modules are much larger and have many more detectors than the CLOVER. This will mean that the efficiency for capturing a DEP in one detector with one or both annihilation γ -rays in others will be considerably higher in the MAJORANA reference design module than it is in the CLOVER. These extra two and three-crystal DEP events might therefore play an important role in training MAJORANA pulse shape analysis. Last, we examine the continuum survival probabilities in Table 6.2 and find that they are essentially independent of overlap fraction for the same reason: we do not actually train on continuum events, so there are none in the training data regardless of number of files overlapping with the characterization data set.

6.3.3 Event rate and Pulse Pileup

Now, we will examine the possibility that there could be a rate dependence in our PSA performance. As discussed in Section 5.2.4, charge pulses from germanium detectors have a relatively short ($\approx 1 \mu\text{s}$) rise time, containing all of the information about energy deposition. This is followed by a much longer fall time characterized by the RC time constant of the detector's preamplifier (typically around $50 \mu\text{s}$). In Section 5.2.4, we claim that PSA calibration data sets should have an absolute maximum rate of about one to two thousand counts per second because at this rate, pulses from a detector will begin to be deformed slightly by the tail of the preceding one. The pulse shape data in this dissertation were taken at a broad range of rates from as low as $\approx 40 \text{ Hz}$ up to $\approx 650 - 900 \text{ Hz}$. The

≈ 40 Hz data were taken at a rate clearly below this 1 – 2 kHz threshold, while at ≈ 900 Hz, the event rate is beginning to approach it. Still, the fraction of a pulse overlapping another following it by ten time constants should only be at the level of $\approx 5 \times 10^{-5}$. Dead time of the DGF4C data acquisition system used for this dissertation is actually a much bigger problem at rates approaching 1 kHz. The live time in the DGF4C system drops below 90% at around 80 – 90 Hz, drops below 80% by ≈ 200 Hz and by 1 kHz has dropped to $\approx 40\%$. Once again, we think that this dead time comes from the DGF4C boards communicating with the host computer across the backplane of the CAMAC crate, so switching to a VME or compact-PCI architecture for data acquisition will do much to enhance the live time of the system.

We now report our efforts to test the rate dependence of PSA with the CLOVER. We adjusted the rate at which we collected data by placing different amounts of our ^{232}Th source (meaning that we added varying numbers of segments of a thoriated welding rod) inside a lead shield with the CLOVER, centered on the front face of the cryostat, approximately two inches away from it. Event rates ranged from ≈ 40 to ≈ 500 Hz. At each rate, we collected 375,000 spills of data for each of the three highest rates (98, 143 and 531 Hz), corresponding to ≈ 1500 DEPs in the single-crystal spectrum. The lowest rate (39 Hz) had double this data set because we performed this test last and kept the system running while we decided what affect to examine next. As a result, there are two independent data sets at this lowest rate. Each of these runs (531, 143, 98 and each 39 Hz data set) took slightly less than one week each. We trained the PSA cuts on the first two thirds and characterized their efficacy with the last third of each of the five data sets. PSA results are reported in Table 6.3 and displayed in Figure 6.10.

Table 6.3: PSA Efficacies at different event rates for the CLOVER detector read out via the DGF4C boards. The uncertainties in the survival probabilities for this table are just the error from the fit. Uncertainties in the event rate are the standard deviation of the event rate reported by the DAQ software from run to run. The continuum in the last column, was integrated from 2.0 – 2.08 MeV.

Rate (Hz)	DEP (%)	γ -ray (%)	Continuum (%)
530.8 ± 39.1	63.2 ± 4.5	31.1 ± 1.9	46.8 ± 1.1
143.1 ± 0.1	66.9 ± 3.6	29.2 ± 1.3	46.4 ± 0.9
97.6 ± 0.3	66.9 ± 3.8	33.1 ± 1.5	48.2 ± 0.9
38.8 ± 0.1	64.8 ± 4.2	35.9 ± 1.7	45.9 ± 0.9
38.8 ± 0.1	68.1 ± 4.0	34.0 ± 1.7	46.2 ± 0.9

We find that the PSA event classification power depends only quite weakly on the event rate. We

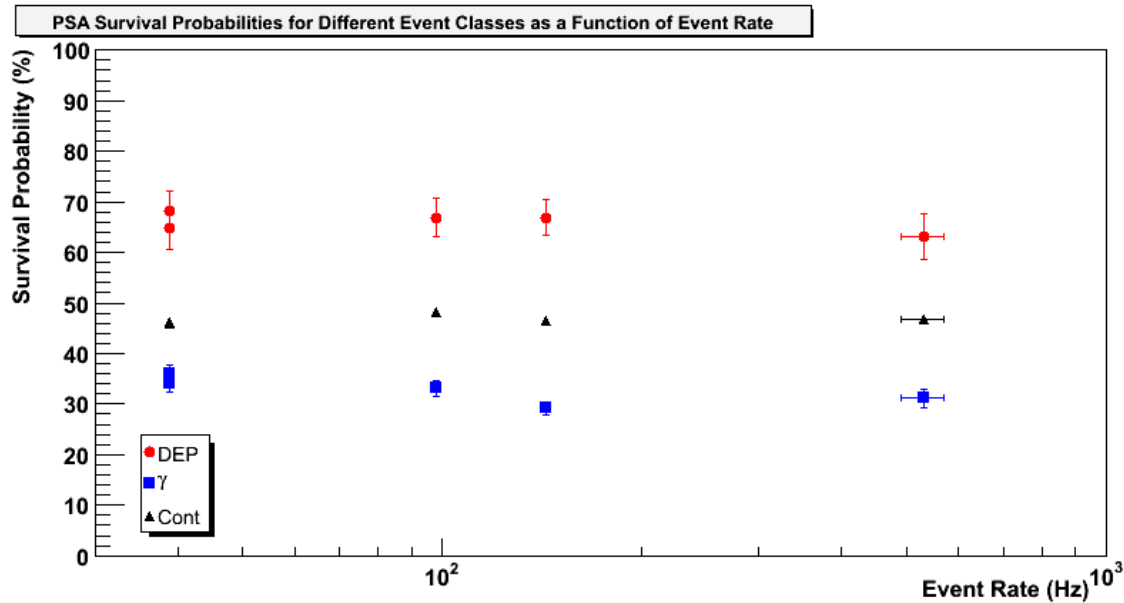


Figure 6.10: PSA efficacies for different event classes from ^{232}Th data in the CLOVER detector as a function of event rate read out by the DGF4C boards. The data for this figure were taken from Table 6.3.

do find that for the 531 Hz data, DEP survival drops slightly (approximately 1 unit of fit uncertainty). That, combined with the fact that DAQ system dead time is a problem at a considerably lower rate, leads us to the conclusion that we should hold the event rate in our calibration runs down to approximately 100 to 150 Hz. If we keep our calibration rates down to this level, it should not only avoid problems associated with dead time, but also systematic shifts in our PSA performance associated with high-event rate pulse deformation.

6.3.4 Different Training Sets

Throughout the course of MAJORANA experiment, we will no doubt take many pulse shape analysis training data sets (assuming of course, that we continue to use supervised learning algorithms that require training data for our PSA). This will be necessary to test for stability of the MAJORANA detector array over time, but what if there is an uncertainty in pulse shape analysis performance from training on different data sets taken under ostensibly the same conditions? This could arise from fluctuations in the signal and background regions. We would expect them, *a priori* to be quite small (especially for large training data sets containing several hundred DEP events and many more γ -ray events), but this uncertainty needs to be addressed. We will now attempt to do so by dividing

a large data set into many pieces, training the PSA algorithm on different parts of that data set, and then analyzing the remaining part using each trained cut. We will then examine the standard deviation of the survival probabilities compared to the uncertainty from the fit for each PSA cut spectrum.

To this end, we took the data sets described in Section 6.3.3 recorded at the three lowest rates (39, 98 and 143 Hz), and split them into six equal parts labeled A–F. There were a total of 60 25,000-spill data files, so each of the six parts contained ten data files with a roughly equal number taken at each event rate. We trained our PSA cuts independently on each of the first five parts (A–E). We then used those five signal and background regions to analyze the sixth. We characterized the spread in these results with the standard deviation of the survival probabilities. If the spread in results for this analysis is smaller than or similar to the errors from the fits on the individual results, then the fit errors place an upper limit on this training set uncertainty. If the spread is larger than the fit errors, then we can use the difference between the spread and the fit uncertainty to estimate the additional uncertainty from fluctuations in the training data.

Table 6.4: PSA performance for the six part analysis. The results in this table are for an analysis of data set F from training on data sets A through E. The uncertainties listed with the survival probabilities are from the fit. The row labeled “Mean and SD” is the mean and standard deviation of the previous five rows. The last row (labeled “ $\sigma_{SD} - \bar{\sigma}_{Fit}$ ”) is the difference between the standard deviation and the average fit uncertainty. See the text for more detail.

Training	Results from Analyzed Set		
Data Set	DEP (%)	γ -ray (%)	Continuum (%)
A	66.3 ± 2.7	33.5 ± 1.1	46.6 ± 0.6
B	65.8 ± 2.7	33.9 ± 1.1	46.9 ± 0.6
C	66.0 ± 2.7	33.8 ± 1.1	47.3 ± 0.6
D	67.2 ± 2.7	35.9 ± 1.1	48.2 ± 0.6
E	65.7 ± 2.7	32.6 ± 1.1	45.9 ± 0.6
Mean and SD	66.2 ± 0.6	33.9 ± 1.2	47.0 ± 0.9
$\sigma_{SD} - \bar{\sigma}_{Fit}$	-2.1	+0.1	+0.3

Table 6.4 shows us that the uncertainty arising from different training sets is quite small. The standard deviation for DEP survivals is markedly less than the average fit uncertainty. For γ -ray and continuum events, it is only slightly larger, with an excess of 0.1% and 0.3% respectively. It is

also worth noting that these values seem to be driven by training set D which is something of an outlier, having consistently higher survival probabilities for all event classes. We will include these numbers as is, but it is likely that they are, in fact, upper limits on this uncertainty.

6.3.5 *Triggering Conditions*

The triggering conditions for the data acquisition system can influence PSA and segmentation cut efficacy essentially by changing the population of events that end up in an experiment's data stream. For instance, if we arrange our triggering parameters to ignore pulses with comparatively slow rise times, this will preferentially ignore multi-site events. If an experiment's data acquisition system preferentially ignores multi-site events, then the background tagging cuts implemented for that experiment could appear to be less effective while the signal tagging efficacy would remain largely unchanged.

For the DGF4C data acquisition boards, there are three parameters that the user can adjust to configure the triggering conditions:

- **Threshold:** Generally, lower threshold values will lead to the best energy resolution. It is however true that setting it too low can cause the count rate in the detector to increase, resulting in noise peaks at the high and low-energy edges of the spectrum. Setting the threshold too high, particularly at high count rates, can allow low-energy events to sneak into the data stream and pile up with higher energy events. This can distort the shape of peaks in the spectrum, adding exponential tails to their high-energy side.
- **Rise Time:** Longer rise time causes the DGF4C boards to average the baseline over a longer time, helping to remove electronic noise from the spectrum. This in turn, helps to remove high-energy side tails on peaks. The rise time is labeled as “L” in Figure 6.11.
- **Flat Top Time:** Increasing the flat top time helps the DGF4C boards to trigger on pulses with slower rise times. This results in a sharper cut off at threshold. It can also, depending on the geometry of the detectors used in an experiment, change the ratio of single to multi-site events in the data stream. The flat top time is labeled as “G” in Figure 6.11.

This last point in the above list is perhaps most interesting to the question of single and multi-site event populations. Longer trigger flat top times allow the DGF4G boards to trigger on slower rising pulses in addition to those with shorter rise times. Multi-site events should tend to have slightly longer rise times than single-site events (though the difference is quite small in the CLOVER). We

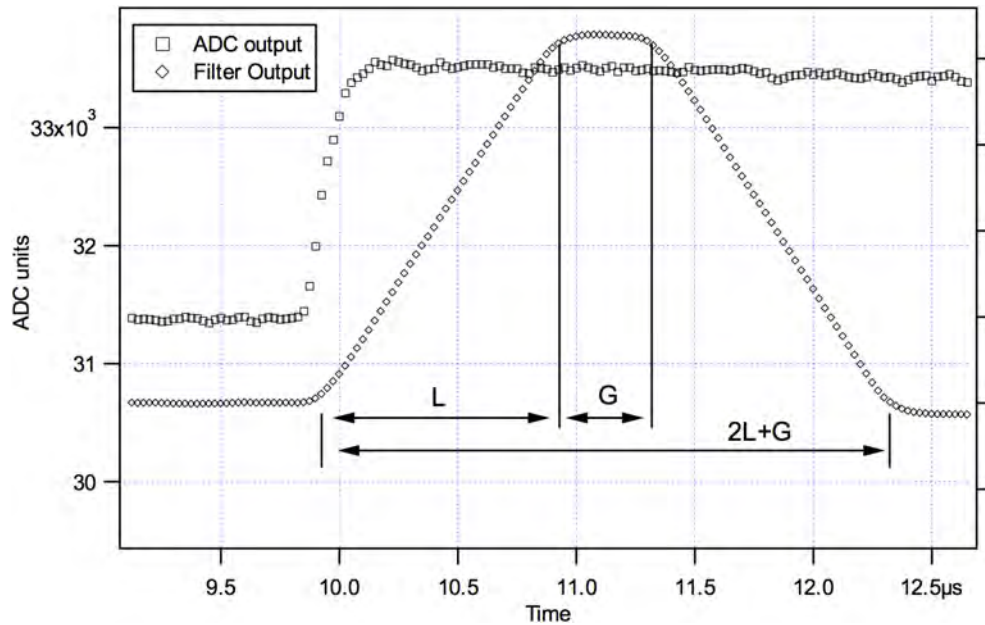


Figure 6.11: Trapezoidal filtering of a preamplifier step with rise time, $L = 4\mu\text{s}$ and flat top time, $G = 1\mu\text{s}$. This figure was taken from Reference [10, pg. 20].

can therefore predict that changing the trigger flat top will alter the ratio of single to multi-site events in the data stream, thereby potentially changing the PSA cut survival probabilities for different event classes.

To examine this possibility, we constructed the following program. After we acquired the last data used in the rate and training set dependence studies detailed in Sections 6.3.3 and 6.3.4 respectively, we reduced the the trigger flat top time from $0.2\mu\text{s}$ to $0.075\mu\text{s}$ because this was the lowest value we used for the CLOVER. Aside from that, the experimental configuration was unchanged. We took the same size data set as we did for each event rate during the study detailed in Section 6.3.3, and analyzed it in the same way (*i.e.* trained on two thirds of the data set and analyzed the remaining third). Because of the extra data at the end of the event rate study, doubling the amount of 39 Hz data, we included the survival probabilities for both independent 39 Hz analyses for the trigger flat top at $0.2\mu\text{s}$. We present results in Table 6.5. In this table, the survival probabilities listed for a trigger flat top of $0.2\mu\text{s}$ are taken directly from the two rows for an event rate of 38.8 Hz in Table 6.3. To facilitate comparison, we also include the difference between the survival probabilities for each event class. These differences are the survival probability from the $0.075\mu\text{s}$ minus those from each of the $0.2\mu\text{s}$ data sets.

Table 6.5: PSA cut survival probabilities comparing data taken under different triggering conditions. For comparison, we also include the survival probability for both of the 39 Hz event rate data sets in Table 6.3. The survival probability uncertainties are once again those from the fit parameters. The last two lines of the table (labeled “Difference”) are the differences between the survival probabilities for each event class in the 0.075 μs data set and each of the 0.2 μs data sets. See the text for more detail.

Flat Top	DEP (%)	γ -ray (%)	Continuum (%)
0.075 μs	64.8 ± 3.7	29.0 ± 1.5	40.2 ± 0.7
0.2 μs	64.8 ± 4.2	35.9 ± 1.7	45.9 ± 0.9
0.2 μs	68.1 ± 4.0	34.0 ± 1.7	46.2 ± 0.9
Difference	0.0 ± 5.6	-6.9 ± 2.3	-5.7 ± 1.1
	-3.3 ± 5.4	-5.0 ± 2.3	-6.0 ± 1.1

Upon examination of Table 6.5 (particularly the differences in PSA performance), we find that the survival probabilities for DEP events remained unchanged when we lowered the trigger flat top time. Those for γ -ray and continuum events however, are substantially lower with a shorter flat top time. This leads us to the conclusion that PSA performance can be affected by triggering conditions, and that the trigger filter parameters should be tuned for each detector in the MAJORANA array to maximize the power of pulse shape analysis as well as energy resolution and other characteristics. It also important that once a detector’s triggering conditions are established, the collaboration be very reluctant to change them. If the trigger filter parameters are held constant, the uncertainty they contribute to the PSA efficacy is zero. If the trigger filters for some of the detectors change, then we must include this affect in our estimate of the uncertainties for our pulse shape cut survival probabilities.

Returning to the above list of DGF4C triggering parameters, it is also possible in principle, for the trigger threshold to affect the survival probability of the segmentation cuts. If the threshold for the segmentation contacts on all of the MAJORANA detectors were set to an unreasonably high level (say, one corresponding to an MeV, or so), then the segmentation cut efficacy would drop precipitously because the segmentation contacts would not record any but fairly high energy depositions. For the MAJORANA experiment, there will be a significant effort to push the trigger thresholds on all of the detectors down to below 10 keV, so that we can observe the ^{68}Ga electron capture x-ray for the SSTC cut discussed in Section 4.8.2. If the trigger thresholds for all MAJORANA detector segments are at this level, the threshold effect on the single-segment survival probability will be negligible.

6.3.6 Detector Damage

Resolving individual Compton scatters requires very good timing resolution (order 100 ns), and if the detector is damaged in some way, that timing resolution will get worse. One possible source of such damage would be crystal defects in the germanium from exposure to a high fluence of neutrons. Between the times when the ^{232}Th data for Reference [49] and that for the systematic checks in this section were taken, we undertook a study that involved activating the material in the CLOVER with a neutron source to mimic $2\nu\beta\beta$ to excited states of ^{76}Ge [91]. According to Reference [91] and the references contained therein, there is a critical neutron fluence leading to damage in germanium detectors around 10^8 n/cm². The experimental program detailed in this reference was focused on the observation of the decay of products of neutron capture on germanium isotopes. To facilitate this, there were several inches of polyethylene between the AmBe neutron source and the CLOVER to moderate the neutron energies down to the point where neutron capture is more probable. At the neutron fluxes produced by the source used in this experiment, it would have taken over three months of exposure to reach a fluence of 10^8 n/cm², even neglecting the moderator. Reference [91] therefore asserts that it is very unlikely that the CLOVER detector was damaged during this experiment because it was only exposed for approximately three weeks. However, the author of Reference [91] and related references therein quote the above critical fluence as the level at which the energy resolution of HPGe detectors will begin to degrade. It is possible that a much lower fluence may cause sufficient damage to slightly alter the pulse *shapes* from the detector while only very slightly degrading energy resolution.

We attempted to test for neutron damage in the CLOVER. One of the ways to repair radiation damage in HPGe detectors is to re-anneal them. This process involves a simple baking of the detector for an extended period of time at temperatures high enough to repair damage to the crystal lattice but low enough to keep the dopants and other surface treatments from drifting. This temperature is typically around 100°C. We re-annealed the CLOVER in this way, then took another set of ^{232}Th data. We then calculated the PSA survival probabilities for that data set and checked it against those for the data from Reference [49] and some of the data taken shortly before we annealed. Much of the data originally taken for Reference [49] has been lost or corrupted since the analysis for that publication was performed, so we were unable to attain the necessary size training data set. To make a comparison between these data and the more recent studies, we took the mean and standard deviation of the points from Figure 6.7 corresponding to just over 200 DEP events per detector, since that was the training set closest in size to the one available in the “Pre-Neutron” data taken for Reference [49]. This was also the data set used to generate the other “Post-Neutron” survival

probability (albeit with a larger training set). We report the results of this exercise in Table 6.6. We also display these results graphically in Figure 6.12, along with the FWHM resolution for each of the detectors the CLOVER.

Table 6.6: PSA Efficacies for data taken: early in the LANL research program involving the CLOVER, shortly before the annealing process (for both small and large PSA training sets), and immediately after the annealing process.

Data Set	DEP (%)	γ -ray (%)	Continuum (%)
Pre-Neutron	53.6 ± 9.3	39.8 ± 5.1	45.9 ± 2.8
Post-Neutron, Small Training	57.9 ± 1.3	32.3 ± 1.5	43.3 ± 1.6
Post-Neutron	66.9 ± 3.6	29.2 ± 1.3	46.4 ± 0.9
Post-Anneal	65.6 ± 2.5	29.0 ± 0.9	45.4 ± 0.6

Table 6.6 and the top panel of figure 6.12 tell us clearly that the size of the training data set affects PSA performance much more strongly than the level of neutron fluence to which the CLOVER was exposed. If we compare pulse shape cut survivals with the same size training set (that is, comparing the “Pre-Neutron” points to the first “Post-Neutron” points, and the second “Post-Neutron” points to the “Post-Annealing” points in the top panel of Figure 6.12), we see that all event classes are unaffected to within fit uncertainties by either the neutron fluence or the annealing process. In total, we see little or no affect on CLOVER PSA performance from its exposure to neutrons during the data-taking for Reference [91]. This is further supported by the lower panel in Figure 6.12, in which we see that the resolution of three of the four detectors actually improves with each successive data set. The exception to this is detector E4, whose resolution worsens uniformly by approximately half a keV for each γ -ray energy in the “Post-Neutron” data set. It is unlikely that the neutron fluence would have affected only this one detector. E1 and E4 were both on the same side of the CLOVER as the neutron source, and E1 does not show this behavior. It is more likely that the energy filtering parameters were tuned more carefully for the “Pre-Neutron” and “Post-Annealing” data sets for detector E4. This assertion is further supported by the uniformity of the energy resolution increase in the “Post-Neutron” data in that detector. The energy resolution of HPGe detectors is typically parameterized by a quadrature sum of three terms: one from the statistical fluctuation in the number of charge carriers created in a detector, one from inefficiencies in the collection of the charge carriers, and one from the electronic noise of the detector system. Reference [99, Section

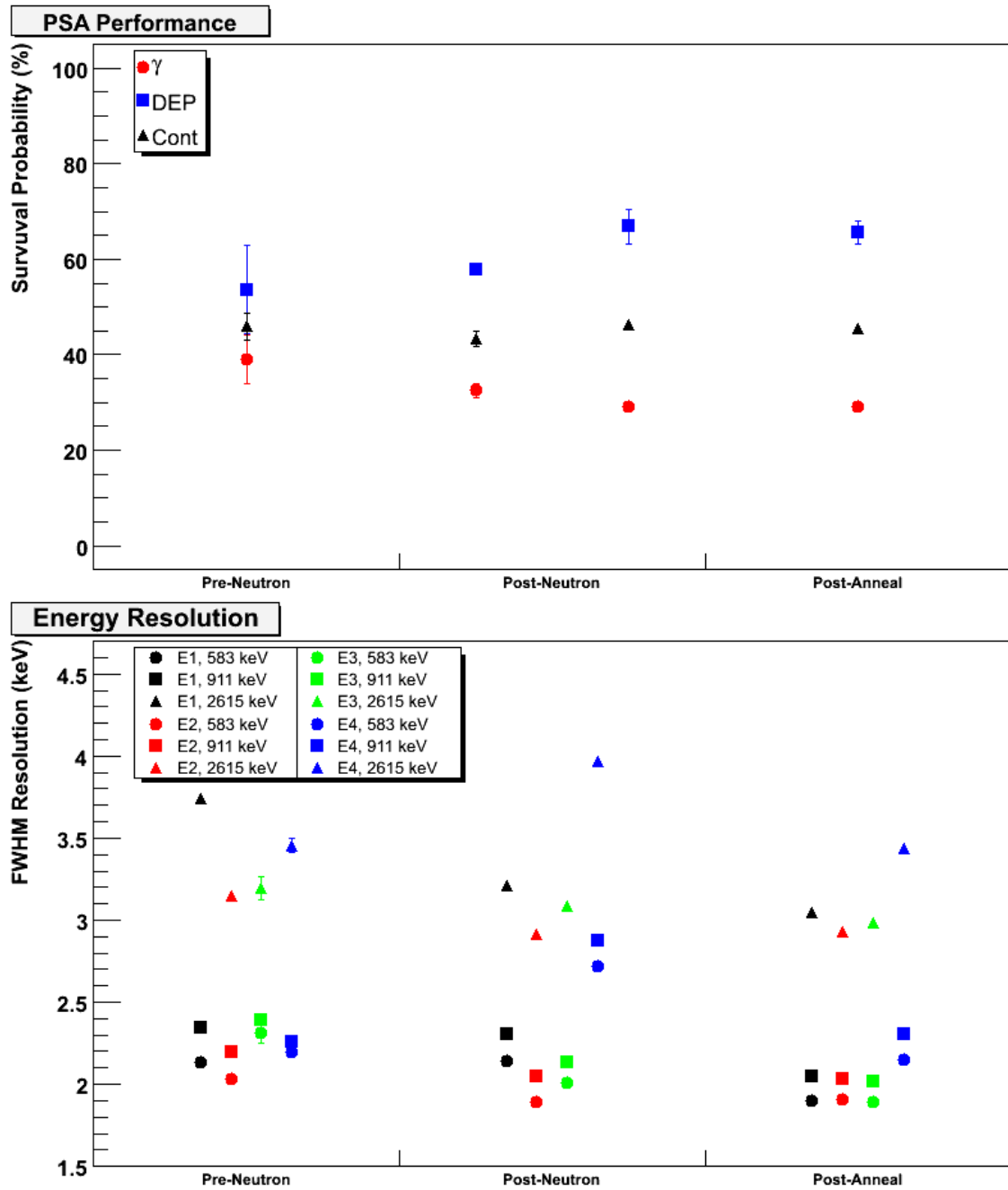


Figure 6.12: PSA efficacies (top) and FWHM resolution of three γ -ray lines for each CLOVER crystal (bottom) for the three data sets listed in Table 6.6. The top panel has two points in the “Post-Neutron” bin because we analyzed that data twice. The left-hand point in that bin was analyzed with a small training set for comparison to older ^{232}Th data, and the right-hand point was analyzed with a larger training set for comparison to more recent CLOVER data. See the text for more detail. The energy resolution data in each bin is ordered from detector 1 to detector 4.

12.III.B] has a detailed discussion of each. The first two terms increase in magnitude with the energy of the incident γ ray, while the remaining part due to detector electronics is constant. Crystal damage would result in increased charge carrier trapping in the detectors. This would tend to most strongly affect the charge collection term, with perhaps a smaller effect on the charge carrier creation part. Both of these would affect the FWHM of the 2615 keV γ -ray line much more strongly than that of the 583 or 911 keV lines. The fact that all three γ -ray lines have uniformly worse energy resolution in the “Post-Neutron” data in detector E4 points to this being an electronic affect.

We could further test the effects of neutron damage on pulse shape analysis in HPGe detectors by taking a new detector and measuring its PSA survival probabilities for each event class. We could then expose it to increasing levels of neutron fluence, stopping periodically to check its PSA performance. After the detector had been sufficiently exposed to a sufficiently high fluence to draw some conclusions about neutron damage, we could then re-anneal it to check how much its performance improved. This would, unfortunately require purchasing a new detector with the express intent of degrading its performance, so it may be difficult to actually perform this test.

6.3.7 Energy and Source Position Dependence With ^{56}Co

The goal of pulse shape analysis cuts is to distinguish between event classes based on the multiplicity of their scattering in detectors. We would therefore expect that types of events whose scattering multiplicity depends on energy (in the ranges to which we are sensitive), would exhibit an energy dependence in their PSA survival probabilities. We would also like to have the option of adding single-site events other than the 1592 keV double-escape peak in the ^{232}Th spectrum to our library of training events (DEPs from other sources or even $2\nu\beta\beta$ events are such possibilities). We would like to characterize the changes in our pulse shape analysis arising from training our PSA cuts on different single-site events. We also want to make sure that our PSA performance does not depend on the location outside the cryostat from which the training and characterization events originate. To test for all of these affects, we took data with the CLOVER and a ^{56}Co source (^{56}Co was chosen for this study because of its broad range of strong γ -ray lines and DEPs—it is discussed in Sections 5.2.5 and 5.3.1) in three positions around the CLOVER (on top, to the side, and in front of the detector).

Analyzed Line Energy

Figure 6.13 was constructed by training our PSA software on the 1576 keV DEP and 1771 keV γ -ray lines from ^{56}Co using data taken with the source in all three positions around the CLOVER. We

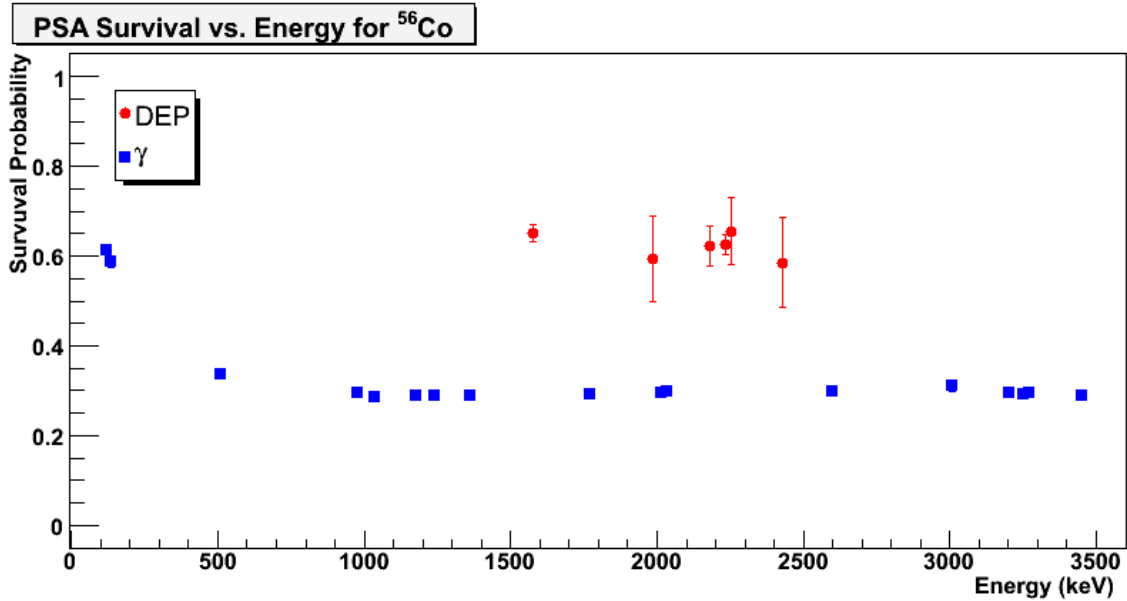


Figure 6.13: Energy Dependence of pulse shape analysis cuts for γ and double-escape peak events in terms of the energy of the line being analyzed.

then plotted the survival probabilities for different lines in the spectrum as a function of energy. Full-energy γ -ray lines in Figure 6.13 indeed show a strong energy dependence, exhibiting a sharp increase in survival probability at lower energies. Once above a critical threshold of ≈ 1 MeV, however, their survival probabilities are quite stable. Double-escape peaks, in the energy range available (which spans $Q_{\beta\beta}$), show no energy dependence. This is because the range of γ -rays in germanium stretches from less than a millimeter up to a few centimeters in the energy range in question (≈ 0.1 to 3.6 MeV for ^{56}Co). The range changes over these energies, because the dominant scattering processes change from the photoelectric effect at low energy, to Compton scattering and e^+/e^- pair production at higher ones. A plot of the fraction of simulated full energy γ -ray events with different multiplicities as a function of energy is shown in Figure 6.14. Energy depositions from two charged leptons (such as DEPs and $\beta\beta$ events) have a much shorter range in germanium, and thus show minimal energy dependence in Figure 6.13. If we examine Figure 6.15, we can read off the range times the medium density for electrons of a given energy. While germanium was not one of the detector media on this plot, we see that when the data is displayed in this way, the curves for silicon diodes and sodium iodide scintillators are nearly coincident. This gives us at least “factor of order one” confidence that the curve for HPGe detectors would be very close to these two. We read off a value of $\approx 0.7 \frac{\text{g}}{\text{cm}^2}$ for electrons with ≈ 1 MeV of energy, allowing us to calculate their range δ

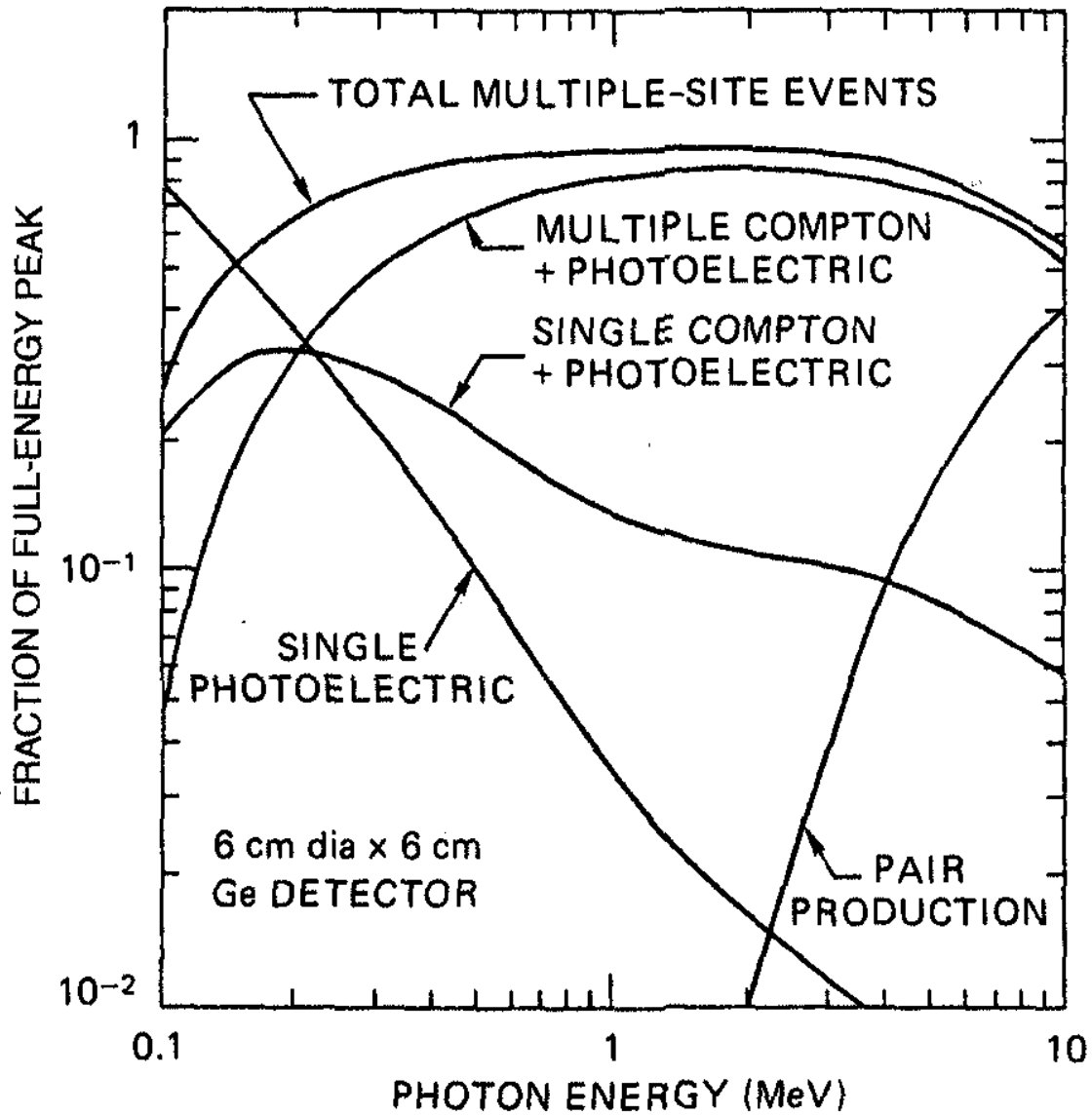


Figure 6.14: Fractions of population of events contributing to full-energy γ lines from different energy loss mechanisms as a function of energy. This was generated from Monte Carlo studies of a 6 cm \times 6 cm coaxial HPGe detector. This figure is from Reference [99, p. 430].

in cm:

$$\delta\rho = 0.7 \frac{\text{g}}{\text{cm}^2}, \quad \delta = \frac{0.7 \frac{\text{g}}{\text{cm}^2}}{\rho} = \frac{0.7 \frac{\text{g}}{\text{cm}^2}}{\frac{A_{Enr}}{A_{Nat}} \rho} = 0.13 \text{ cm} \approx 1 - 2 \text{ mm} \quad (6.3)$$

1–2 mm is comfortably below the $\approx 3-4$ mm position separation resolution we have demonstrated with the parametric PSA method in Reference [49] and later in this chapter. It is, however close enough that the possibility of pushing that resolution down lower to distinguish these events from even shorter range ones like α particles is very intriguing. Essentially, we find that over the energy range available in ^{56}Co data (which more than covers the energies of interest for tagging $0\nu\beta\beta$ and $2\nu\beta\beta$ events), DEPs at different energies behave nearly the same, while γ -ray events can interact through several different processes. It is also interesting to note that the very low-energy γ -lines in Figure 6.13, whose interaction will be dominated by single photo-absorption (a very spatially localized process), have nearly identical behavior under PSA as the DEP lines. As noted above, the γ -ray lines in Figure 6.13 have nearly identical survival probabilities above ≈ 1 MeV. To quantitatively examine the PSA survival variation of DEP and γ -ray events over 1 MeV, we simply take the survival probabilities for all of these lines and once again compare their standard deviation in their survival probabilities to their average fit uncertainty. We tabulate these results in Table 6.7. We can see that

Table 6.7: Variation in PSA survival probabilities for DEP events and γ -ray events above 1 MeV. σ_{SD} is the standard deviation of the survival probability and $\bar{\sigma}_{Fit}$ is the average fit uncertainty for the lines in question. The last row is the difference between the two.

Event Class	σ_{SD} (%)	$\bar{\sigma}_{Fit}$ (%)	$\sigma_{SD} - \bar{\sigma}_{Fit}$ (%)
DEP	0.02	0.06	-0.04
γ	0.006	0.005	+0.001

there is no variation beyond the fit uncertainties for DEP lines. For γ -ray lines, it is exceedingly small, at the level of only 0.001%

Training DEP Energy

We now examine the variation in pulse shape analysis from the use of different DEP lines to train the cut. For this study, we train each analysis on the 1771 keV γ -line, but on five different DEP lines in the ^{56}Co spectrum from 1576 to 2429 keV. Once again, we trained the cuts on approximately two thirds of the data and analyzed the remainder. As with the preceding ^{56}Co study, DEP and γ -ray survivals are averaged for all twelve γ -ray and five DEP lines above 1 MeV. We tabulate these

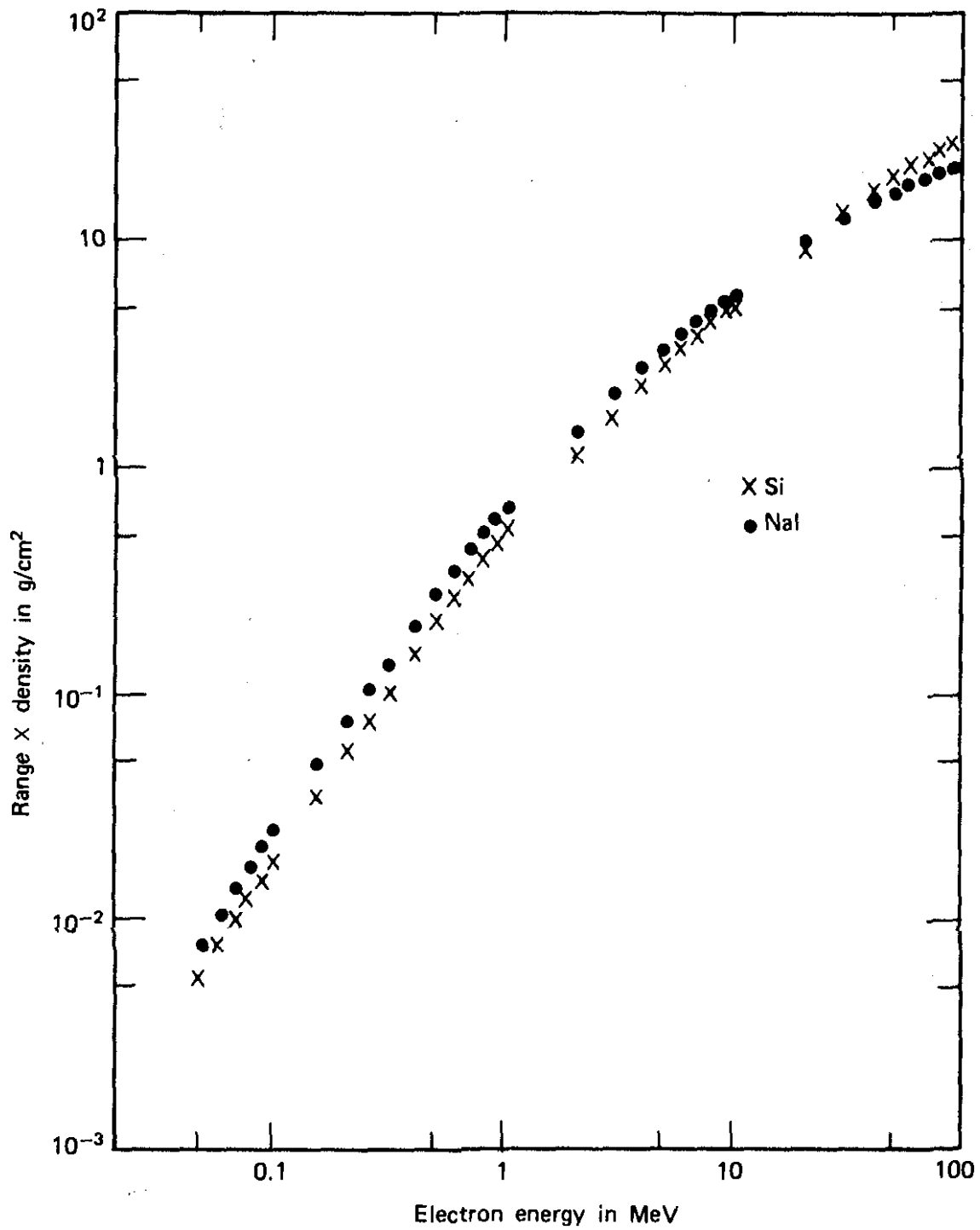


Figure 6.15: Range-Energy plot for electrons in two detector media: silicon and sodium iodide. This figure taken from Reference [99, p. 45].

results in Table 6.8 and display them in Figure 6.16. We again quantify the excess uncertainty from this affect by looking at the difference between the standard deviation and average fit parameter uncertainty for the survival probabilities of the cuts trained on the different DEPs. We find variation

Table 6.8: Average PSA survival probabilities for events in all DEP and γ -ray lines above 1 MeV for cuts trained on different DEP lines. σ_{SD} is the standard deviation of the five survival probabilities in this table and $\bar{\sigma}_{Fit}$ is the average fit uncertainty for each cut. The last row is the difference between the two.

Training DEP	DEP (%)	γ (%)
1576 keV	62.2 ± 2.8	29.4 ± 0.2
2180 keV	62.0 ± 2.8	31.0 ± 0.2
2231 keV	63.5 ± 2.8	30.8 ± 0.2
2250 keV	62.9 ± 2.8	31.8 ± 0.2
2429 keV	60.1 ± 2.8	34.1 ± 0.2
σ_{SD}	1.3	1.7
$\bar{\sigma}_{Fit}$	2.8	0.2
$\sigma_{SD} - \bar{\sigma}_{Fit}$	-1.5	+1.5

of the training DEP contributes an uncertainty of 1.5% for γ -ray events and no excess uncertainty for DEP events.

Source Location Dependence

To examine the dependence of our PSA performance on the position of the source used to collect the data, we return to pulse shape cuts trained on the 1576 and 1771 keV DEP and γ -ray lines. The survival probabilities are again averaged for all DEP and γ -ray lines above 1 MeV. We assess the uncertainty from this variation in the same way as in other parts of Section 6.3, by looking at the difference between the standard deviation of the survival probabilities under this variation and the uncertainty from the fit parameters. We tabulate and display the results from this study in Table 6.9 and Figure 6.17. We once again find no variation in the DEP survival in excess of the fit uncertainties, and a relatively small one for γ events at 0.8%.

6.3.8 Detector Geometry

As discussed in Section 2.1, the current plan for the MAJORANA prototype module is to populate it with two types of detectors: point-contact p-type and, highly-segmented n-type. We must under-

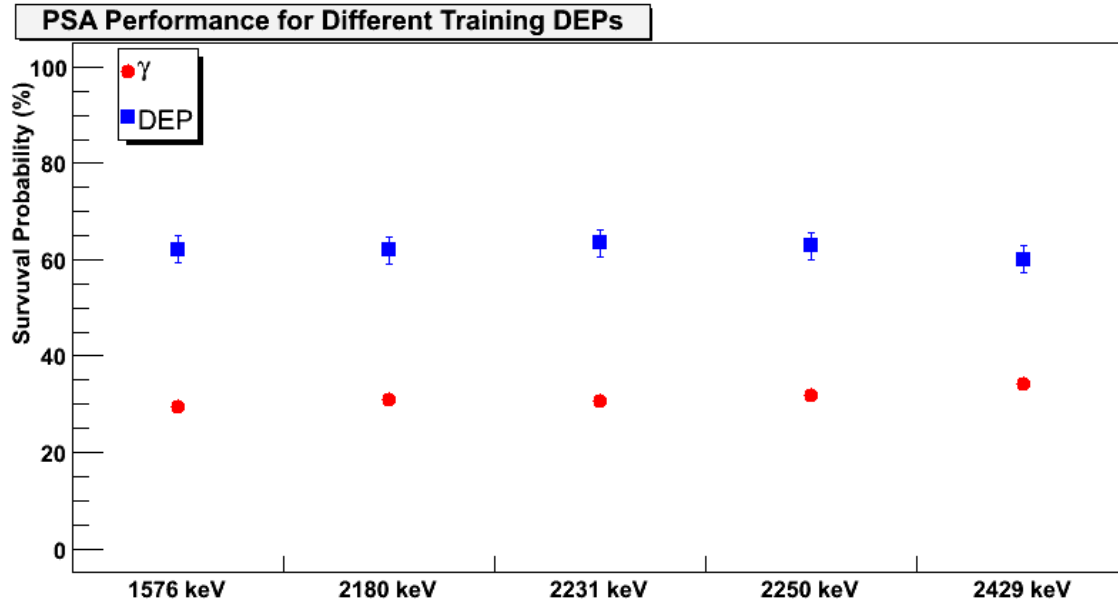


Figure 6.16: Average PSA survival probabilities for DEP events and γ -ray events above 1 MeV for cuts trained on different DEP lines.

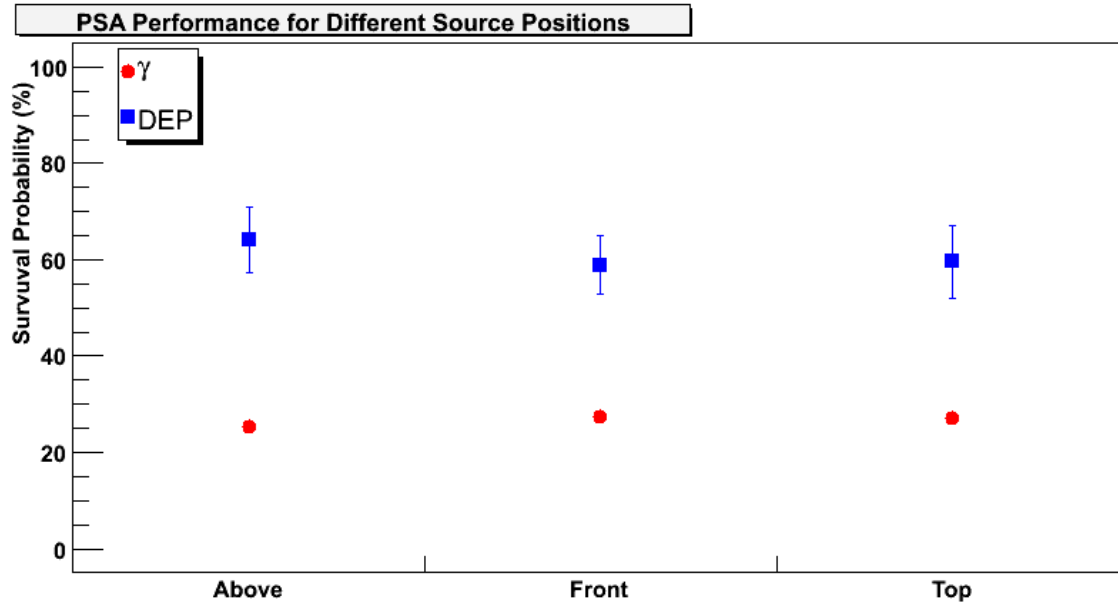


Figure 6.17: Average PSA survival probabilities for DEP events and γ -ray events above 1 MeV for data taken with the source in different positions around the CLOVER.

Table 6.9: Average PSA survival probabilities for DEP events and γ -ray events above 1 MeV for runs with the source in different positions around the CLOVER. σ_{SD} is the standard deviation of the survival probability and $\bar{\sigma}_{Fit}$ is the average fit uncertainty for each data set. The last row is the difference between the two.

Source Position	DEP (%)	γ (%)
Above	64.0 ± 6.8	25.3 ± 0.3
Front	58.9 ± 6.1	27.3 ± 0.3
Top	59.6 ± 7.6	27.1 ± 0.4
σ_{SD}	2.8	1.1
$\bar{\sigma}_{Fit}$	6.8	0.3
$\sigma_{SD} - \bar{\sigma}_{Fit}$	-4.0	+0.8

stand that the pulse shape analysis survival probabilities will be different in each detector design, especially if we perform a γ -ray tracking analysis in the highly-segmented detectors. The MAJORANA collaboration and $\beta\beta$ community as a whole must remember that it is very difficult to compare pulse shape analysis survival probabilities across different detector designs. This need for an ‘‘apples to apples comparison’’ can explain some of the discrepancy between our PSA results in this dissertation and those shown in the Heidelberg-Moscow experiment [94, 96]. Four of the five detectors used in Heidelberg-Moscow experiment were well over 2 kg, considerably larger than the ≤ 800 g detectors in the CLOVER. The IGEX experiment used detectors of a similar size to those from the Heidelberg-Moscow experiment, and the data sets presented in Reference [2] were from a similar detector to those. The PSA survival this detector was 80% for DEP events and 26% for γ -ray events. Larger detectors will have a much higher ratio of multiple to single Compton scatters, making pulse shape analysis more effective.

The design (particularly the size) of the detectors for the MAJORANA experiment will be constrained by a wide variety of factors, including: the cost and risk associated with the manufacturing process, instrumenting and cabling the detectors, cooling the array, background rejection power (including pulse shape analysis) and anticipated failure rate. Thus, a lengthy debate over optimal detector design is beyond the scope of this dissertation. Still, the power of pulse shape analysis, especially combined with other background rejection techniques in detectors for which we can actually collect data, is an important input for the ongoing process of selecting a MAJORANA detector design. Furthermore, comparison between PSA survival probabilities for current detectors, future MAJORANA designs and those from past experimental programs is an interesting topic and should

be addressed in future Monte Carlo study.

6.4 Segmentation Cuts and Their Independence from PSA

We now discuss the interplay between pulse shape analysis and detector segmentation (also covered extensively in Reference [49]). In this section, we refer to segmentation analysis not as the GRETA-style γ tracking analysis described in Section 6.2.4, but as a simple multiplicity filter, as detailed in Section 2.2. Table 6.10 lists the PSA and segmentation survival probabilities for ^{232}Th obtained for Reference [49]. We can see by comparing the last two columns in Table 6.10 that the combination

Table 6.10: Survival probabilities (percentages) of different processes over a range of energy. The first quoted uncertainty comes from Poisson counting statistics, and the second comes from the systematic uncertainty associated with changing the position of the source around the detector. This table was reproduced from Reference [49].

Process	Energy (MeV)	Segmentation	Pulse Shape	Both Cuts	Product
$^{228}\text{Ac } \gamma$	1.588	$66 \pm 1.2 \pm 0.7$	$20 \pm 0.5 \pm 1.0$	$7 \pm 0.3 \pm 0.4$	13
$^{208}\text{Tl DEP}$	1.592	$97 \pm 2.4 \pm 1.2$	$75 \pm 2.0 \pm 2.1$	$73 \pm 2.0 \pm 4.0$	73
$^{208}\text{Tl SEP}$	2.103	$63 \pm 1.4 \pm 1.8$	$45 \pm 1.1 \pm 4.5$	$20 \pm 0.7 \pm 2.0$	28
Continuum	2.0 - 2.1	$81 \pm 1.6 \pm 2.0$	$43 \pm 0.9 \pm 3.0$	$30 \pm 0.6 \pm 2.0$	35
$^{208}\text{Tl } \gamma$	2.615	$70 \pm 2.0 \pm 4.1$	$17 \pm 0.7 \pm 2.2$	$8 \pm 0.5 \pm 0.4$	12

of the two cuts is clearly lower than the product of the survival probabilities corresponding to the individual cuts. This is because the two cuts (pulse shape analysis and segmentation) operate preferentially on different populations of events. Pulse shape analysis is capable of resolving the spatial extent of events in the direction parallel to the electric field lines inside the detectors, which tend to radiate from the central contact of the crystal to its outer surface. The segmentation masks for germanium detectors partition them in the axial and/or azimuthal directions. This means that events spatially extended in the radial direction will tend to be tagged by the pulse shape cuts, while those extended in the other two will tend to be identified by the single-segment cut. To test this, we performed some Monte Carlo studies [49], to examine a number of different segmentation schemes. We note from Table 6.10 that we measured the combined and product survival probabilities for 1588 keV γ events to be 7% and 13% respectively for twofold azimuthal segmentation, while the Monte Carlo study that generated Figure 6.18 predicts 9% and 13%. It is also apparent upon examination of Figure 6.18 that the combined cut survival probability eventually crosses and becomes less powerful than the simple product of the two. We surmise that this occurs because as azimuthal segmentation

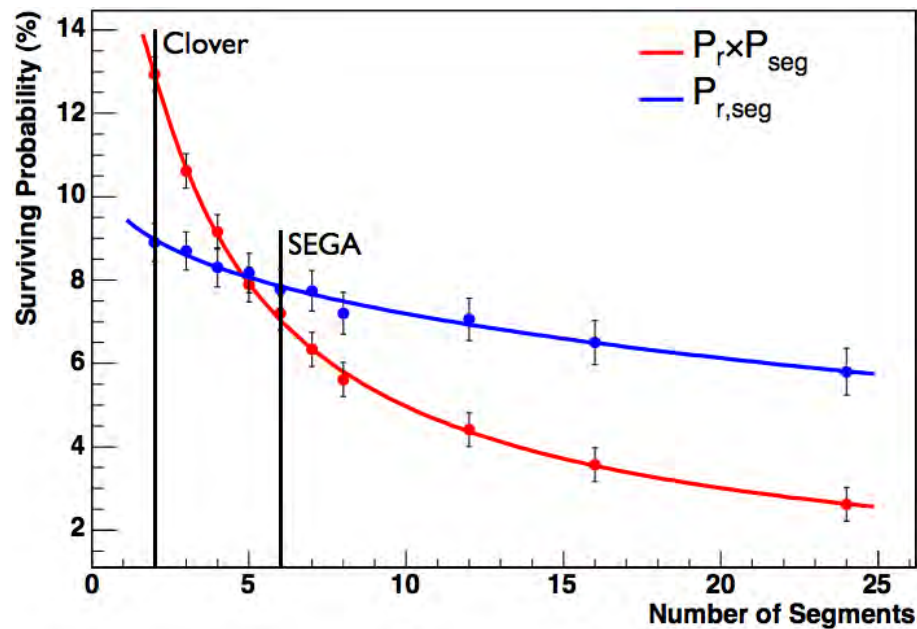


Figure 6.18: Combined pulse shape and segmentation cut survival probability (blue) and product of the individual cut survivals (red) from Monte Carlo data. The PSA cut was constructed by removing events with energy depositions separated by > 3 mm. This figure was taken from Reference [49].

becomes increasingly fine, the population of events identified by each individual cut overlaps to a greater degree. As the segmentation becomes finer, the azimuthal angle subtended by a set of energy depositions required to confine it to a single slice of the detector becomes smaller. At some critical value (approximately five azimuthal segments according to the Monte Carlo), it becomes more likely that a multi-site energy deposition will be tagged by both cuts than by only one. Once again, it is important to reiterate that the segmentation cut applied here is only a multiplicity filter, and that the γ tracking style analysis from highly segmented detectors would likely do much better.

We can also use this simulation data to estimate the effective radial separation of events in the CLOVER that our PSA is capable of resolving. We read off the PSA survival probability for γ -ray events measured for [49] as 20%, corresponding to a rejection power (one minus the survival probability) of 80%. We then construct a curve of the fraction of events in the simulation data stream with energy depositions separated by more than a given length along the radial direction of the crystal. From this curve, we can then read off that an 80% rejection probability for γ -ray events corresponds to an effective radial separation resolution of 3 mm (shown as the red line in Figure 6.19). This is, in fact, how the 3 mm separation resolution used to generate the PSA cut for Figure 6.18 was chosen. Last, we point out that the Monte Carlo that generated Figures 6.18 and 6.19 only

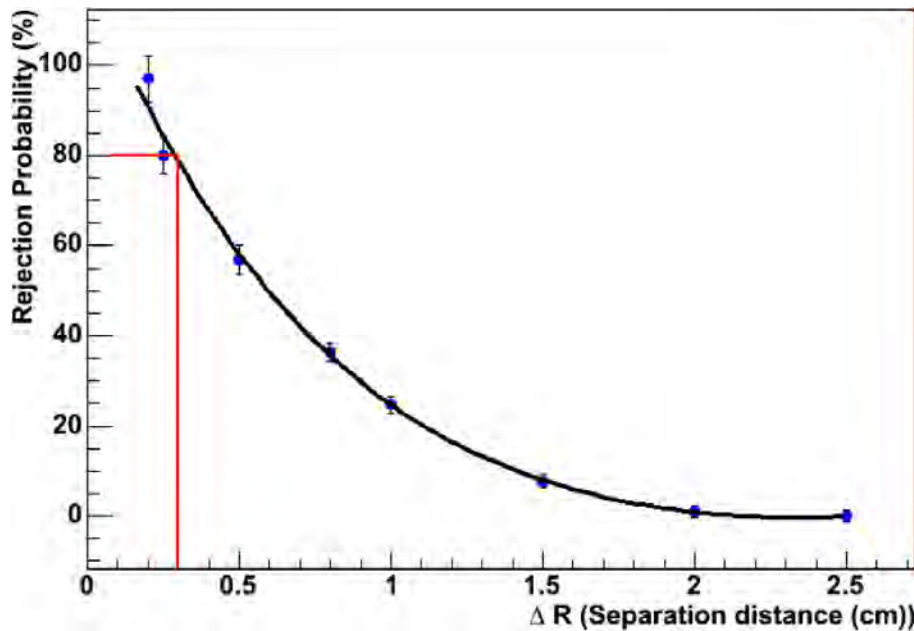


Figure 6.19: Fraction of γ -ray events removed by the PSA cut versus the radial separation of energy depositions in Monte Carlo data. The red line shows the equivalence between 80% PSA rejection of γ -ray events and 3 mm radial separation resolution. This figure was taken from Reference [49].

dealt with the 1588 keV γ -ray and not one near $Q_{\beta\beta}$. These energies are however, close enough that γ -ray energy loss mechanisms and scattering multiplicities should be quite similar.

We can see that the pulse shape survival probabilities for DEP and γ -ray events taken from Table 6.10 are different from those reported in the rest of this chapter, and the nominal values quoted in Tables 4.2 and 4.3. The survival probabilities for continuum events are however, quite consistent. For easier comparison, we have reproduced the survival probabilities for both bodies of work here in Table 6.11. Note that the total uncertainty for the continuum events has been estimated at $\approx 5\%$ of its nominal value, to lie between the fractional uncertainties of DEP and γ -ray events. It was not possible to examine all of the systematics for continuum events near $Q_{\beta\beta}$ because of the γ -ray line at 2034 keV in the ^{56}Co spectrum.

We spent a great deal of time searching for possible reasons for this discrepancy in PSA performance. In fact, many of the systematic uncertainties examined in Section 6.3 were thought of during brainstorming about what could be different between the data in Reference [49] (which was taken very early in our CLOVER experimental program) and data taken since then. The first difference between the analysis for Reference [49], and that for subsequent data sets, was the approximately

Table 6.11: Pulse shape analysis survival probabilities for different event classes for the analysis in Reference [49] and the more recent work in this dissertation. Statistical and systematic uncertainties from Reference [49] have been combined in quadrature. Otherwise, PSA performance from Reference [49] were taken directly from Table 6.10. PSA performance values from this dissertation were taken from Table 4.2.

Process	Reference [49] (%)	This Work (%)
$^{228}\text{Ac } \gamma$	20 ± 1.1	29.0 ± 1.9
$^{208}\text{Tl DEP}$	75 ± 2.9	65.6 ± 2.5
Continuum	43 ± 3.1	45.4 ± 2.3

25% overlap between the training and characterization data in Reference [49] (*i.e.* the cuts were trained on 25% of a total data set that was then used to characterize their efficacy). If we go back to our training overlap study in Section 6.3.2, we can look at the point on Figure 6.9 for 30% overlap. Survival probabilities for this configuration were: $28.3 \pm 0.9\%$, $68.1 \pm 2.5\%$, respectively for γ -ray and DEP events. This “buys us” some, but certainly not all of the difference between the two analyses. The analysis in Reference [49] also used a much smaller training data set (at only 200 DEP events per detector) than nearly all of the work in this dissertation. It is likely that smaller training sets will tend to amplify the sample bias effects from training/characterization data overlap. The last remaining difference is the mechanics of the way in which the pulse shape cuts were made. One of the structural changes described in Section 6.2.1 made to the PSA cuts was a transition from performing the event by event comparison with a many-parameter fit to the asymmetry-normalized moment parameter space, to using a simple histogram of that space for each population of training events. It is true that the fit method required fewer training events to attain what certainly appears to be somewhat better performance. The reason we transitioned away from that method was the extremely complicated form of the fit equation required to capture the structure in the parameter space. The fit equation required for the PSA results in Reference [49] was a sum of over twenty multi-variate Gaussian and Lorentzian functions for a total of well over one hundred fit parameters (a normalization, two location coordinates and a width along each axis, for a total of five parameters for each multivariate term in the fit equation). For subsequent work, the author decided that simply using the PSA parameter space histograms would be a much more robust and reproducible way to perform pulse shape analysis in a wider variety of circumstances. It is quite telling that the total uncertainties from the results in Reference [49] are comparable or even larger than the more recent ones even though a thorough search of systematic uncertainties was not done.

Last, if we refer back to Table 4.2, we see that the product of the two survival probabilities (PSA and segmentation) is consistent to within error bars with the survival probability of the combined cut, rather than being substantially higher. This is because the effective radial separation resolution is slightly greater than the 3 mm quoted in Reference [49] and earlier in this section. This radial separation resolution does not worsen dramatically when we use the slightly lower γ -ray rejection probabilities we have demonstrated in this document. When we read off this resolution coming from the $\approx 70\%$ rejection (30% survival) of γ -ray events, it only grows from 3 mm to ≈ 4 mm. All in all, we recommend the more conservative survival probabilities quoted in Table 4.2 be taken as the nominal PSA and segmentation performance.

6.5 PSA in the SEGA Detector

Now, we show pulse shape analysis results for the SEGA data taken during the FEL run described in Section 2.2.2. We examined the efficacy of pulse shape analysis on both the inner central contacts (c-channels) and outer segmentation contacts (s-channels) of the detector. We take the PSA efficacies to be the ratio of the peak strengths in the appropriate pulse shape analyzed spectrum to that for the appropriate single contact (c-channel or s-channel) spectrum. Here, the PSA algorithm was trained on approximately two thirds of the data with the FEL beam energy at 3 MeV (and the resultant 2 MeV DEP). We then analyzed both the remaining third of the 3 MeV data to measure the survival probabilities for the 2 MeV DEP and the 3 MeV γ -ray, and the entire data set with the FEL beam energy at 2 MeV to measure the survival probability of 2 MeV γ -rays. Results are tabulated in Table 6.12 and displayed graphically in Figure 6.20.

Table 6.12: Survival probabilities for PSA cuts on FEL data taken with the SEGA detector. Results are given for PSA on the internal and external contacts of the detector. The uncertainties are those from the fit parameters.

Event Class	C-Channel PSA (%)	S-Channel PSA (%)
DEP (2 MeV)	59.7 ± 7.8	66.6 ± 1.3
γ -ray (2 MeV)	27.9 ± 1.1	49.4 ± 1.0
γ -ray (3 MeV)	28.5 ± 0.4	48.9 ± 0.4

We can see from Figure 6.20 and Table 6.12 that the pulse shape analysis performance on the c-channels in SEGA comparable with that from CLOVER presented in this dissertation. There is however, not quite as much separation between DEP and γ -ray events in this data set as there was

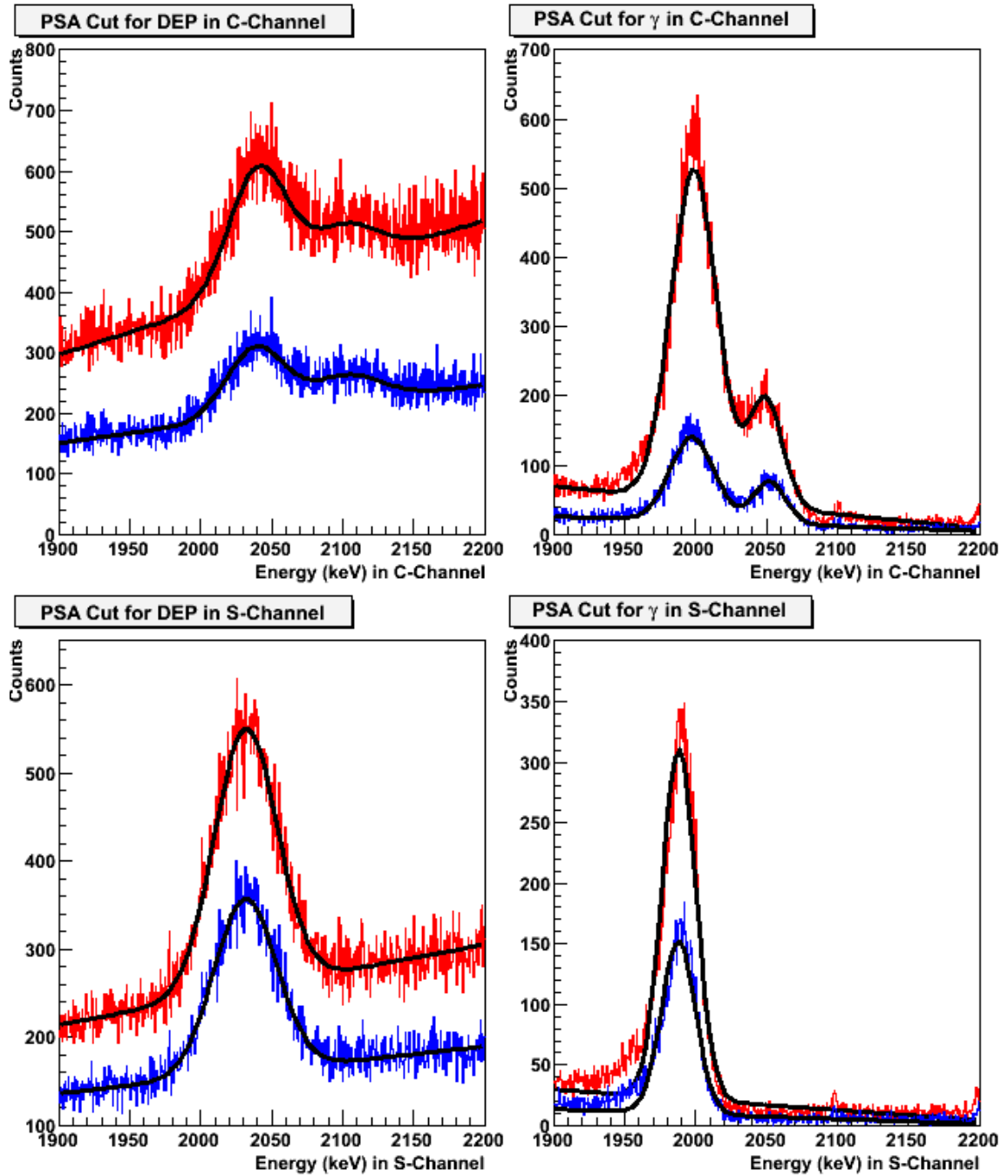


Figure 6.20: Survival probabilities for PSA cuts on FEL data taken with the SEGA detector. The panels are: DEPs in the *c*-channel (top left), γ -rays in the *c*-channel (top right), DEPs in the *s*-channel (bottom left) and γ -rays in the *s*-channel. In each panel, the singles spectrum (either single central or segmentation channels) is in red, and the PSA cut is in blue.

for much of that taken with the CLOVER. We surmise that this is because this data was taken in a preliminary test cryostat supplied by ORTEC. This test cryostat is not ideal from either a crystal mounting or electronics standpoint. There is a nontrivial amount of both microphonic pickup and electronic cross talk from this detector in its current configuration. This is clearly seen by the double peak structure in the central contact spectra (see the top two panels in Figure 6.20). Also, we would expect the time structure of pulses from SEGA to be inherently more complicated because of its high degree of segmentation in the ϕ direction. This means that the spatial structure of the image charges that get induced across the segmentation planes is far more complicated. This complexity means that it is more difficult to capture the structure of current pulses from SEGA with only two pulse shape moments. It will be interesting therefore, to incorporate the higher moment PSA demonstrated in Section 6.2.2 with the CLOVER. There was a modest performance improvement in PSA performance for the CLOVER, and the complexity of the SEGA detector suggests that its corresponding improvement will be more dramatic. It would also be interesting to examine SEGA data using γ -ray tracking techniques, since the configuration of SEGA is much closer to those in the γ tracking experiments. These arrays are described in Section 2.5, and the pulse shape analysis they employ are described in Section 6.2.4. One last point to consider is that the PSA performance in SEGA is markedly better for SEGA's central contact than it is on the outer contacts. We believe this to be due to a number of electronic affects. First, the capacitances of the contacts themselves differ by a factor of four (40 pF on the inner contacts and only 10 on for the outer). Secondly, the DGF4C digitizers used to read out the data from SEGA do not handle contacts with induced image charges well at all. This leads to a number of problems with the calculated energy from that channel. The image charges are a much stronger affect in the outer contacts than on the inner ones, so phenomena caused by them would be much more apparent in the s-channels. In spite of its suboptimal cryostat and data acquisition, we have demonstrated the efficacy of pulse shape analysis for SEGA. Furthermore, this performance should only improve as the detector mounting is upgraded and more sophisticated PSA algorithms get applied to its data.

6.6 Width of Detector Segmentation Boundaries in the CLOVER

Because so many of the detector designs being considered for the MAJORANA use segmented outer contacts, it is interesting to examine the way in which events occurring close to the segmentation boundary share energy across segments. To investigate this, we performed the following experiment with the CLOVER. We scanned a ^{137}Cs source, collimated by a 2-mm hole in a 4-in. lead brick, across the front face of the CLOVER over detector E1. The scanning took place slightly off the

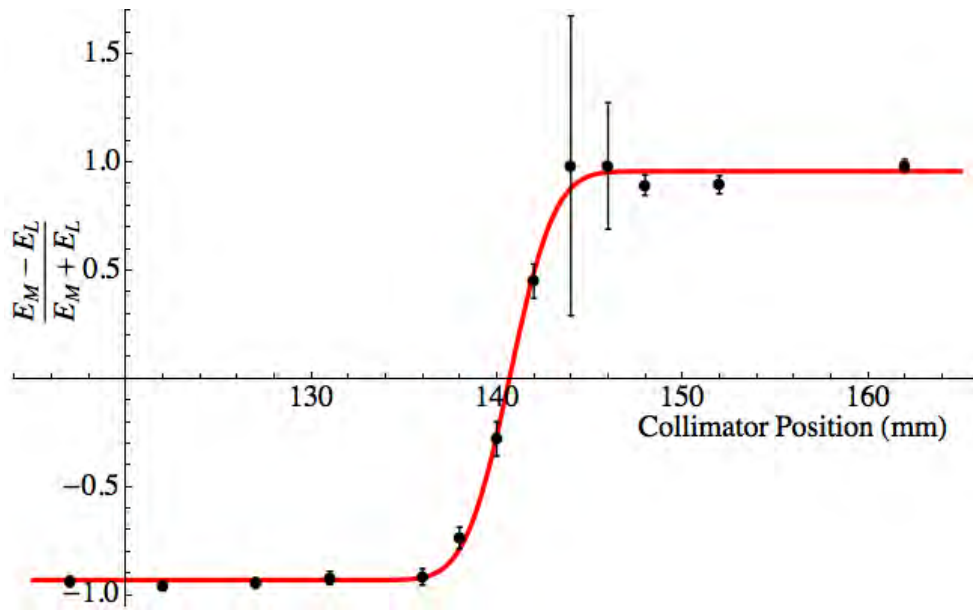


Figure 6.21: A measurement of the border width of crystal 1 of the CLOVER. The average fraction of energy assigned to the left and middle positions is plotted as a function of source location. The curve is a fit to the data. See text for discussion of the collimated source. The absolute value of the position scale is arbitrary.

center of the detector to avoid the central core of the crystal. We moved the source in steps of 2 mm near the segmentation border and in larger steps further from it. The spot size on the front of the CLOVER was 3.5 mm in diameter. We looked at the relative strength of the single γ -ray peak in the ^{137}Cs spectrum in the left and middle position channels. We present the results of this study in Figure 6.21. If the segmentation were perfect (*i.e.* no electrical coupling between them) and the spot from the source were infinitesimally small, Figure 6.21 would look like a step function. To quantify the width of the border between segments, we fit a step function convolved with a Gaussian to the collimator data. Because we knew the size of the spot from the collimator, we could subtract this off from the width from the fit. In doing so, we found the width of the border between the two segments to be 1.9 mm. This means that events occurring within 1 mm of the segmentation border will register counts in both segments. Last, we used γ -rays for this study. While the 662-keV γ -ray from ^{137}Cs are not particularly high in energy, it is certainly true that a fraction of the events that registered as two-segment events could have actually been multi-site in nature. We therefore maintain that the value 1.9 mm for the width of the border region should be treated as an upper limit.

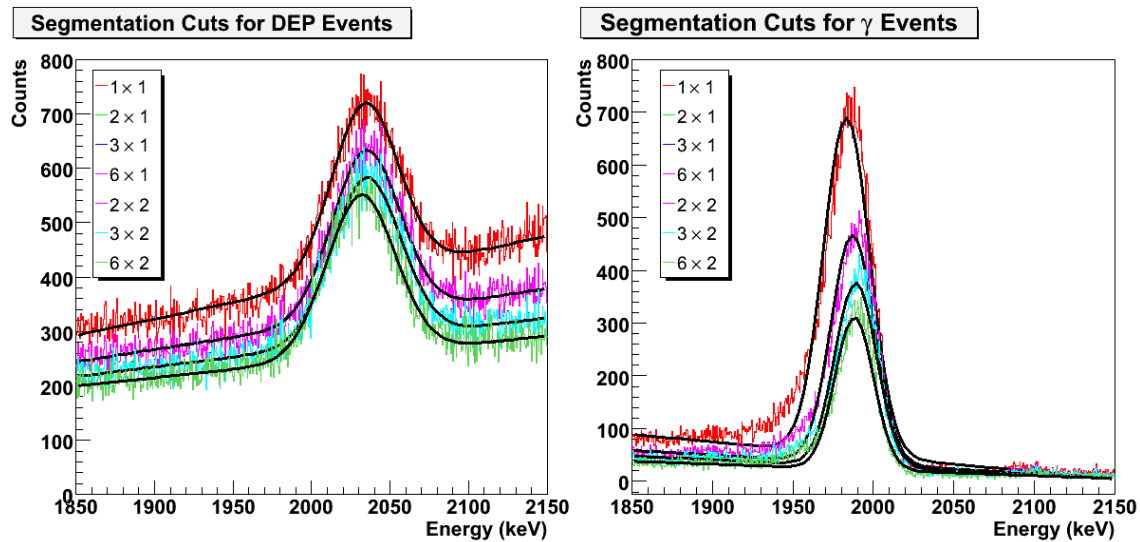


Figure 6.22: Survival probabilities for several segmentation configurations for DEP events (left) and γ events (right) acquired with the SEGA detector in the FEL. The schemes are enumerated by the label $m \times n$, where m is the number of ϕ segments and n is the number of z segments.

6.7 Different Segmentation Schemes With SEGA

We can use the six-fold azimuthal segmentation in SEGA to examine the effects of two and three-fold segmentation as well. The data used for this study came from the FEL runs, and because the beam was well-collimated and pointed nearly through the center of one of the axial segments, there are very few events in the other. This means that the affects of the z -axis segmentation is negligible in this data. The DEP/ γ spectra can be seen in Figure 6.22, and we report the survival probabilities for the different segmentation cuts (compared to the 1×1 spectrum in Figure 6.22) in Table 6.13.

It is very difficult to compare these results to those from the Monte Carlo studies that generated Figure 6.18 partly because the geometry for the detector and the energy of the γ line is different, but mostly because the configuration of SEGA is such that we can only perform PSA after making a single-segment cut. This makes it difficult to perform these cuts independently. It is possible in principle, to perform external segmentation contact (s-channel) cuts independently from PSA on the internal central contact (c-channel). The problem with this plan is that the c-channel PSA efficacy is not good enough to achieve the the radial position difference resolution of $\Delta r = 3$ mm used in the Monte Carlo, making the PSA cut survival probabilities generated for Figure 6.18 different than those attainable with SEGA in its current configuration. It is, however important to remember that the optimal combination of pulse shape and segmentation analysis in SEGA will become more

Table 6.13: Survival probabilities for a variety of segmentation cuts in the SEGA detector from the FEL data runs. The uncertainties here result from the fit to the appropriate spectrum. The segmentation schemes are enumerated using the same convention as in Figure 6.22.

Segmentation	DEP Survival (%)	γ survival (%)
2×1	98.2 ± 1.2	65.6 ± 0.7
2×2	98.1 ± 1.2	65.6 ± 0.7
3×1	96.4 ± 1.1	51.8 ± 0.6
3×2	96.3 ± 1.1	51.7 ± 0.6
6×1	95.6 ± 1.1	41.2 ± 0.6
6×2	95.6 ± 1.1	41.1 ± 0.6

accessible once SEGA gets moved to a permanent cryostat with better electrical and mechanical performance. In spite of the suboptimal PSA performance in SEGA, it is quite encouraging that the 2×1 segmentation performance is quite close to the single segment performance of the CLOVER (a 2×1 segmented detector). SEGA had 2×1 segmentation survival probabilities of 65.6% and 98.2% respectively for γ and DEP events, while the CLOVER's single segment cut survival probabilities were 69.1% and 93.3%.

6.8 Pulse Shape and Segmentation Systematic Uncertainty Summary

We now motivate the choice of specific values for the systematic uncertainty for the pulse shape and segmentation survival probabilities. We begin with the segmentation survival probability. As long as we constrain our discussion of segmentation analysis to simple multiplicity filters for external γ -rays, the systematic uncertainty arising from segmentation analysis is relatively simple. We can measure it directly using calibration data, using the statistical and fit uncertainties from the individual crystals and single-segment spectra. Of course, external γ -rays are not the only backgrounds that we will have to mitigate in MAJORANA or any other low-background experiment. These will, in general, have different survival probabilities arising from the single-segment cut and need to be simulated in the MAJORANA Monte Carlo program. We will then normalize the survival probabilities from the Monte Carlo so that they correctly reproduce the single-crystal and single-segment cuts for calibration data. For those backgrounds, the systematic uncertainty would be a quadrature sum of the counting uncertainty from the simulation and that from the calibration data. If we assume we can take calibration and generate Monte Carlo data sets sufficiently large that we can lower the counting statistics to the 1–2% level in each, the total uncertainty in the segmentation cut should

be at the level of $\approx 3\%$. The absolute value of this efficacy will depend on our ability to understand the location and parent decay of any contamination in the MAJORANA experiment. If we cannot understand the sources of contamination in the experiment, the uncertainty in the segmentation cut will likely be much higher. Generally speaking, the parent nuclide of γ -ray lines in MAJORANA will be easy to understand (simply by their energy), while the location of the contamination causing the events contributing to that line may be more difficult. Continuum events will likely be more difficult both to identify with a specific parent reaction and to spatially localize in the detector.

The survival probability for PSA cuts will be subject to the same systematic considerations as the segmentation cuts described above, meaning that in principle, the PSA cut uncertainties could be as low as 1–3%. There are also a whole other variety of systematic uncertainties (detailed in Section 6.3) that could contribute to uncertainty in the pulse shape cuts. We summarize these now in Table 6.14.

We find generally, that the γ -ray survival is more sensitive to these systematic affects than the DEP survival. Summing the affects in Table 6.14 in quadrature, we reach a total uncertainty of 1.9% for γ -rays and 2.5% for DEPs. Fractionally, this comes to 6.6% and 3.8% respectively. Because several of the PSA systematic uncertainties we examined in this chapter came from ^{56}Co data, we could not arrive at a rigorous total uncertainty for continuum events near $Q_{\beta\beta}$. This is because of the strong γ -ray line at 2034 keV from ^{56}Co . As briefly mentioned at in Section 6.4, we estimate that the fractional uncertainty for continuum events will lie between that of γ -rays and DEPs. We choose a fractional uncertainty of $\approx 5\%$ for the continuum, corresponding to a nominal performance of $45.4 \pm 2.3\%$. This seems to span the the continuum survival probabilities quite well, but we must keep in mind that this is only an estimate.

Much of the work in this chapter has focused on the notion of reducing backgrounds using segmentation and pulse shape analysis. We have been using DEP and γ -ray events as surrogates for single and multi-site events, and quoting survival probabilities that are roughly a factor of two to three different between the two classes of events. It is far more likely however, for background events near $Q_{\beta\beta}$ to be Compton continuum events. The efficacy for rejecting continuum events with PSA and segmentation cuts is not as good as that for γ -rays, tending to hover at 40–45%. If we look back at Reference [38, Section 4.6], we see that the $T_{1/2}^{0\nu}$ sensitivity of the MAJORANA experiment is inversely proportional to the square root of the background level, given the same level of ^{76}Ge exposure. A reduction in background to 40% of its initial value would therefore correspond to an increase in sensitivity of only around 58% ($\sqrt{1/0.4} = 1.58$). Even if the combination of all of the background reduction techniques discussed in this dissertation resulted in a factor of 10–20 reduction

in background, this would correspond only to a factor of roughly 4 increase in $T_{1/2}^{0\nu}$ sensitivity. While this is certainly not a negligible sensitivity increase, it is not the sole reason that we should go to these great lengths to tag and reject backgrounds in addition to building a larger experiment out of cleaner materials than previous $0\nu\beta\beta$ endeavors. Another *extremely* important reason to be able to identify multi-site events in the final MAJORANA spectrum, is the ability to demonstrate the single-site nature of any potential signal seen at or near $Q_{\beta\beta}$, thereby identifying that peak as $0\nu\beta\beta$ to a much higher degree of certainty.

Table 6.14: Summary table of systematic effects impacting parametric pulse shape analysis. We include the name of each effect, a brief description and the change in survival probability beyond that from the fit parameters for γ -ray and DEP events. The effects are quoted for PSA cuts trained on non-coincidence-tagged DEPs.

Effect	Description	γ -ray	DEP (%)
Training overlap ^a	Different numbers of data files in common between training and characterization data	$-2.6 \times \sigma_{Fit}$	$+2.7 \times \sigma_{Fit}$
Event Rate ^a	Rates < 143 Hz	—	—
Different Training Sets	Trained on five independent data sets and analyzed same events	0.1 %	—
Trigger Settings ^a	Difference between two trigger settings minus fit uncertainty	3.5%	—
Analyzed Line	DEP and γ -ray events above 1 MeV from ⁵⁶ Co data set	0.001%	—
Training DEP	Trained on same γ -ray and different DEPs in ⁵⁶ Co. Survivals are from averages above 1 MeV for both event types	1.5%	—
Source Location	Moved source above, in front, and to the side of CLOVER. Survivals are from averages above 1 MeV for both event types in ⁵⁶ Co data	0.8%	—
	Systematic Sum	1.7%	—
	Fit Parameter Uncertainty	0.9%	2.5%
	Total Uncertainty	1.9%	2.5%
	Nominal Performance	$29.0 \pm 1.9\%$	$65.6 \pm 2.5\%$
	Fractional Uncertainty	6.6%	3.8%

^aThese uncertainties can be held to zero in MAJORANA production data.

Chapter 7

VARIATIONS AND UNCERTAINTIES IN THE BACKGROUND MODEL

We present the results of a Monte Carlo study of the effects on the reconstructed $0\nu\beta\beta$ peak from the different components of the sum spectrum of a Ge $\beta\beta$ experiment. We simulate the sum spectrum from from 2.0 – 2.1 MeV from four components:

- a flat continuum background,
- all of the ^{214}Bi peaks in this energy range (with intensities coming from the branching ratios in the table of isotopes),
- the $0\nu\beta\beta$ peak at 2039 keV, and
- a mystery peak like the one potentially seen in the KKDC spectrum [96] at 2030 keV.

The ^{214}Bi peaks in the simulation are found in Table 7.1. We parameterize these components in

Table 7.1: Full-energy γ peaks from ^{214}Bi included in this simulation study.

Peak Energy (keV)	Branching Ratio
2004.5	0.003
2010.7	0.050
2016.7	0.0058
2021.8	0.020
2052.9	0.078
2085.0	0.0089
2089.5	0.055

terms of five arguments that get passed to the Monte Carlo program in the command line:

- overall exposure in $\text{kmol} \times \text{years}$ which determines the overall number of counts in the spectrum,

- continuum level in counts/keV/kg/year,
- ^{238}U level in units tied to the anticipated contamination of the copper which determines the strength of the ^{214}Bi lines,
- $T_{1/2}^{0\nu}$ in years which determines the $0\nu\beta\beta$ peak strength, and
- mystery peak strength expressed as a fraction of the strength of the $0\nu\beta\beta$ peak.

The overall exposure includes: detector mass, enrichment in ^{76}Ge , counting time and detection efficiency. The ^{238}U level corresponds to $\mu\text{Bq/kg}$ if all of the ^{238}U were in the germanium. It is true, however that if there were actually this amount of ^{214}Bi in the germanium, there would be α lines and β components in the spectrum as well, both of which we neglect for this exercise. It is expected that, most of the ^{238}U contamination in the MAJORANA experiment will be in the copper, rather than the germanium. The rationale for the exact values picked for the ^{214}Bi levels is explained in Section 7.1.

We assume analytic forms for probability distributions for each of the four sum spectrum components: Gaussians for each of the peaks and a flat distribution for the continuum. Then, we calculate the number of counts expected in each sum spectrum component from the parameters listed above. After we have an expected number of counts for each component, we then populate the sum spectrum by sampling the probability distribution for that component a number of times Poisson distributed about the expected number. We repeat this process for 10000 experiments for each set of parameters, creating a sum spectrum for each. For each final sum spectrum, we perform a log-likelihood fit to the spectrum from 2030 to 2080 keV including the $0\nu\beta\beta$ peak, one peak on the high-energy side of $Q_{\beta\beta}$, plus a flat background. The peak locations are not fixed, instead they can each range over roughly the lower third and upper two thirds of the fit range.

From this fit, we extract the continuum level and the number of counts in and energy of the $0\nu\beta\beta$ peak and then histogram those values. We do not extract the ^{238}U level because all of the γ lines from that decay chain are sufficiently separated from $Q_{\beta\beta}$ to avoid them bleeding into the $0\nu\beta\beta$ peak. Once we have these histograms for each parameter set (which consists of 10000 experiments) we then take the mean of the histogram as the most likely value. We estimate the uncertainties in the mean of these distributions by integrating out a 1σ probability on either side of that value and normalizing that by the square root of the number of experiments. If we wanted to calculate the anticipated uncertainty of any single measurement, we would neglect this normalization.

7.1 Parameter Space

We chose exposures and background levels based on three general experimental configurations: the KKDC analysis of the Heidelberg-Moscow experiment, and the M60 and M1000 versions of the MAJORANA experiment. For the KKDC-like experiment, we vary the continuum background level and the strength of the mystery peak. For the M60 and M1000 experiments, we vary the continuum background level and $T_{1/2}^{0\nu}$.

Specifically, the parameter spaces for the KKDC, M60 and M1000 experiments can be found in Tables 7.2, 7.3, and 7.4, respectively.

Table 7.2: Parameter space explored for the KKDC-like exposure. The two parameters varied for this configuration were: the background level, and strength of the mystery peak.

Exposure (kmol \times y)	Cont. BG (counts/keV/kg/y)	^{214}Bi level (arb.)	$T_{1/2}^{0\nu}$ (years)	Mystery Peak Strength
0.83	0.11	0.3	1.2×10^{25}	0.54
0.83	0.01	0.3	1.2×10^{25}	0.54
0.83	0.11	0.3	1.2×10^{25}	0.27
0.83	0.01	0.3	1.2×10^{25}	0.27
0.83	0.11	0.3	1.2×10^{25}	0.0
0.83	0.01	0.3	1.2×10^{25}	0.0

The KKDC exposure was chosen to reproduce the number of counts in that spectrum, and the M60 and M1000 exposures were scaled up to match the corresponding detector masses and counting times (the MAJORANA counting time was taken to be five years for both M60 and M1000). The continuum backgrounds are taken from the claimed value from KKDC, the one count/tonne/y/ROI MAJORANA background goal, and filling in the orders of magnitude in between. The ^{214}Bi level was taken to reproduce the number of counts in the 2052.9 keV peak (the strongest one between 2.0 and 2.1 MeV) in the KKDC spectrum. Picking the value for the MAJORANA experiments was done by using the MAJORANA assay goal for copper purity ($0.4 \mu\text{Bq/kg}$) and multiplying that by twice the mass of the close in copper parts ($2 \times 840 \text{ g}$). This corresponds to a reduction of the ^{214}Bi levels from KKDC by a factor of five. The $0\nu\beta\beta$ half-life for the KKDC experiment comes from their best fit value, and that for the MAJORANA exposures takes that order of magnitude, and adds on two more (*i.e.* 10^{25-27} years). The mystery peak strength goes from the number of peaks in the

Table 7.3: Parameter space explored for the M60-like exposure. The two parameters varied for this configuration were: the background level, and $0\nu\beta\beta$ lifetime.

Exposure (kmol \times y)	Cont. BG (counts/keV/kg/y)	^{214}Bi level (arb.)	$T_{1/2}^{0\nu}$ (years)	Mystery Peak Strength
3.34	0.00025	0.06	1.0×10^{25}	0.0
3.34	0.00025	0.06	1.0×10^{26}	0.0
3.34	0.00025	0.06	1.0×10^{27}	0.0
3.34	0.001	0.06	1.0×10^{25}	0.0
3.34	0.001	0.06	1.0×10^{26}	0.0
3.34	0.001	0.06	1.0×10^{27}	0.0
3.34	0.01	0.06	1.0×10^{25}	0.0
3.34	0.01	0.06	1.0×10^{26}	0.0
3.34	0.01	0.06	1.0×10^{27}	0.0

KKDC spectrum to half that and then to zero. The mystery peak was left out of the MAJORANA experiments (for which we instead varied the $0\nu\beta\beta$ half-life).

7.2 Simulation Results

We now present results from this study. For each simulated configuration, we will present a summary plot with shifts in the reconstructed: $0\nu\beta\beta$ peak location, continuum level, and $0\nu\beta\beta$ rate and a sample of one of the 10000 simulated spectra. We will also include histograms of the continuum level number of $0\nu\beta\beta$ events added to the simulation for each of the 10000 simulated experiments.

7.2.1 KKDC-Like Configuration Results

First, we present the results for the KKDC-like exposure in Figure 7.1 and a sample spectrum in Figure 7.2. The first thing to notice is that the location of the reconstructed $0\nu\beta\beta$ peak is largely unaffected by the presence of the mystery peak (the range on this panel of the Figure 7.1 is -20 to $+5$ parts in 10^6 , corresponding to peak shifts of ≈ 0.04 keV). Upon examination of the middle panel, we see that for the higher continuum level, the fit reconstructs the continuum level quite well for the KKDC background level. When we drop the continuum level by roughly a factor of ten however, we see that it is more difficult for the fit to extract the correct value. The higher background curve varies

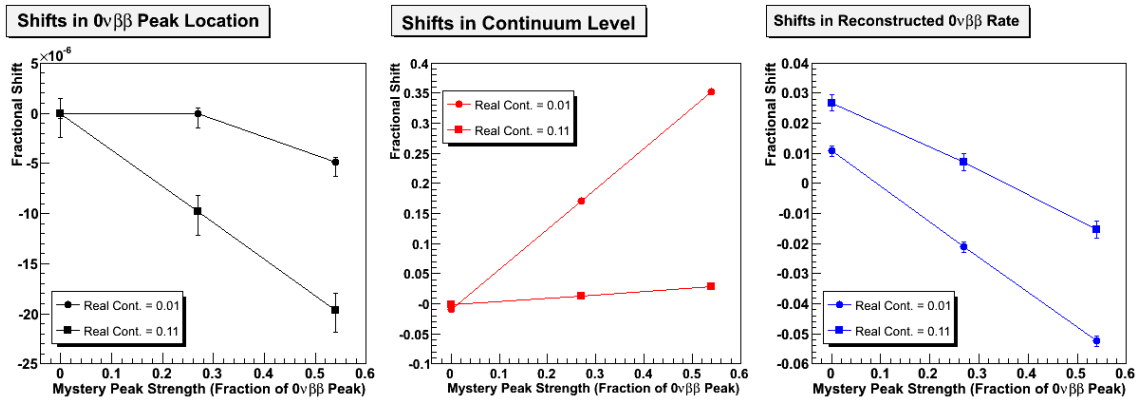


Figure 7.1: Shifts in peak location (left), continuum background level (middle) and $0\nu\beta\beta$ rate (right) as a function of the strength of the mystery peak at 2030 keV for KKDC-like exposures.

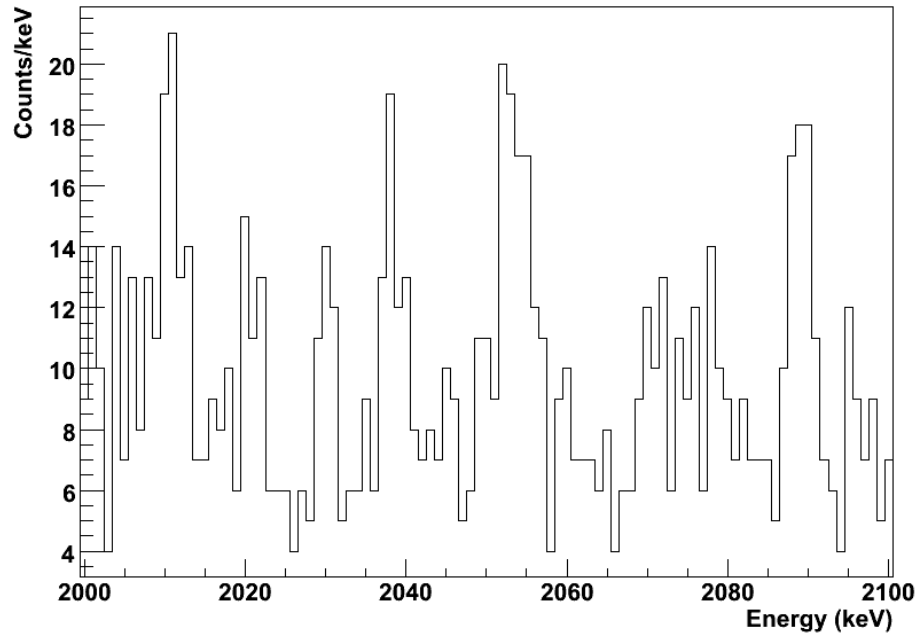


Figure 7.2: One of the 10000 spectra generated for a KKDC-like exposure ($0.83 \text{ kmol} \times \text{y}$). The continuum background was $0.11 \text{ counts/keV/kg/y}$, the ^{214}Bi level was set to 0.3 , $T_{1/2}^{0\nu}$ was $1.2 \times 10^{25} \text{ y}$, and the mystery peak strength was 0.54 that of the $0\nu\beta\beta$ peak.

Table 7.4: Parameter space explored for the M1000-like exposure. The two parameters varied for this configuration were: the background level, and $0\nu\beta\beta$ lifetime.

Exposure (kmol \times y)	Cont. BG (counts/keV/kg/y)	^{214}Bi level (arb.)	$T_{1/2}^{0\nu}$ (years)	Mystery Peak Strength
55.7	0.00025	0.06	1.0×10^{25}	0.0
55.7	0.00025	0.06	1.0×10^{26}	0.0
55.7	0.00025	0.06	1.0×10^{27}	0.0
55.7	0.001	0.06	1.0×10^{25}	0.0
55.7	0.001	0.06	1.0×10^{26}	0.0
55.7	0.001	0.06	1.0×10^{27}	0.0

much less strongly with the presence of the mystery peak, while for the lower background, the fit gets steadily worse as the mystery peak gets stronger. The upward trend in both plots comes from the mystery peak adding counts to the fit's estimate of the background level. The affect is much stronger in the lower background level because the mystery peak adds roughly the same number of counts to a much smaller number of background counts. Last, we find that the fit reconstructs the correct number of counts in the $0\nu\beta\beta$ peak to within $\approx 5\%$. This is, of course correlated with the reconstruction of the continuum. As we would expect, as the fit incorrectly reconstructs the continuum level as too high, it reconstructs the $0\nu\beta\beta$ peak too low. We also include the actual histograms of added and reconstructed continuum and $0\nu\beta\beta$ levels for the KKDC exposure in Figures 7.3 and 7.4. This allows us to see the initial and reconstructed probability distributions that were used to generate and reconstruct the continuum levels in Figure 7.1. The sample spectrum given in Figure 7.2 was generated using the parameters reported as the KKDC result in Reference [96].

7.2.2 M60-Like Configuration Results

Next, we present the M60 results in Figure 7.5 and a sample spectrum in Figure 7.6. The M60 results are the most difficult ones to explain and characterize in this study. First, the sample spectrum given in Figure 7.6 was generated for a continuum level $4\times$ the MAJORANA goal, and $T_{1/2}^{0\nu}$ of 10^{26} y. Even with this relatively conservative set of parameters, the $0\nu\beta\beta$ peak is readily apparent above the background. When we examine the left panel of Figure 7.5, we see that the deviation of the location of the $0\nu\beta\beta$ peak is less than a part in 10^5 for the two shortest half-lives considered. For the longest

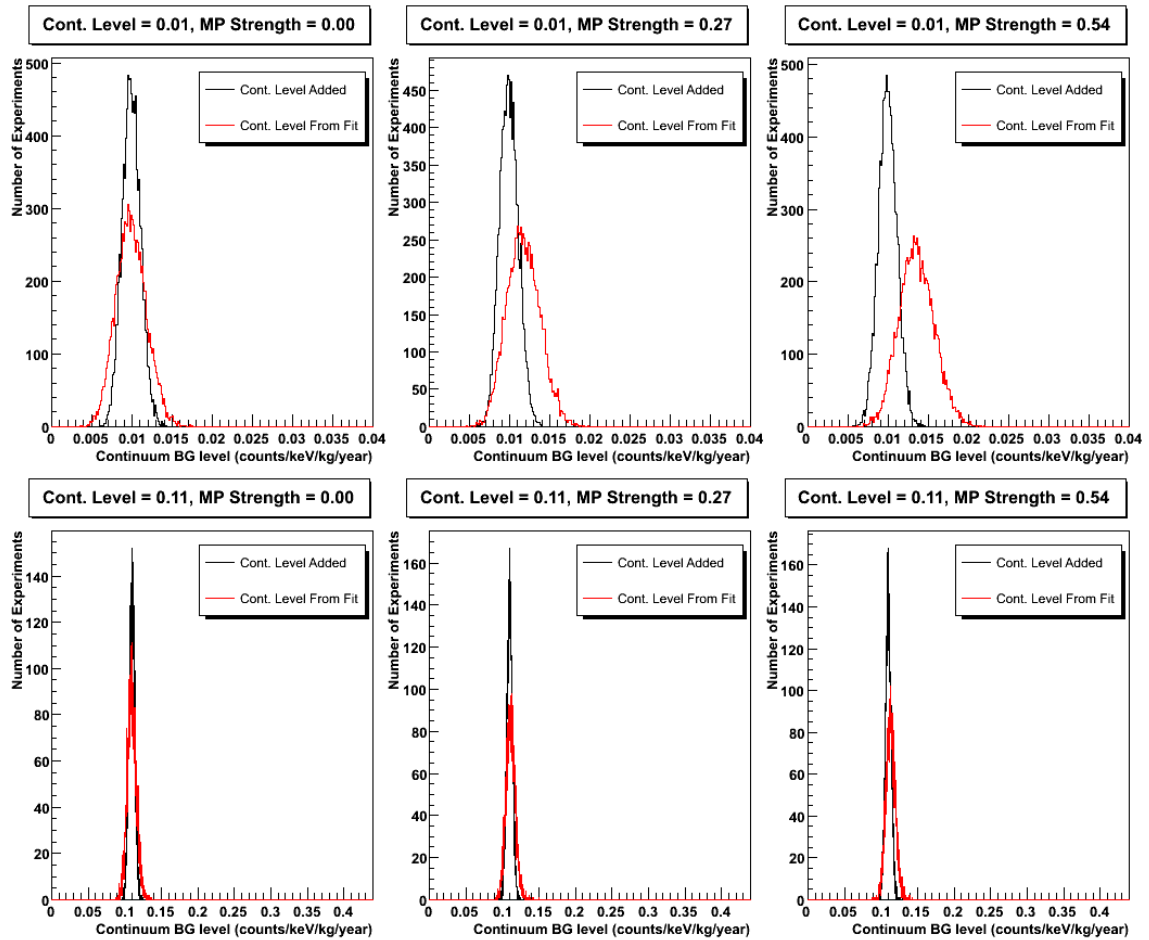


Figure 7.3: Histograms of the continuum level added to the simulation (black) and reconstructed by the fit (red) for each of the 10000 simulated KKDC-like experiments. The top row used a background level of 0.01 counts/keV/kg/y, and the bottom used 0.11 counts/keV/kg/y. The left column was generated for an experiment with no unidentified mystery peak. The middle column had one whose strength was 0.27 that of the $0\nu\beta\beta$ peak. The right column had a mystery peak strength of 0.54 (the level in the KKDC spectrum).

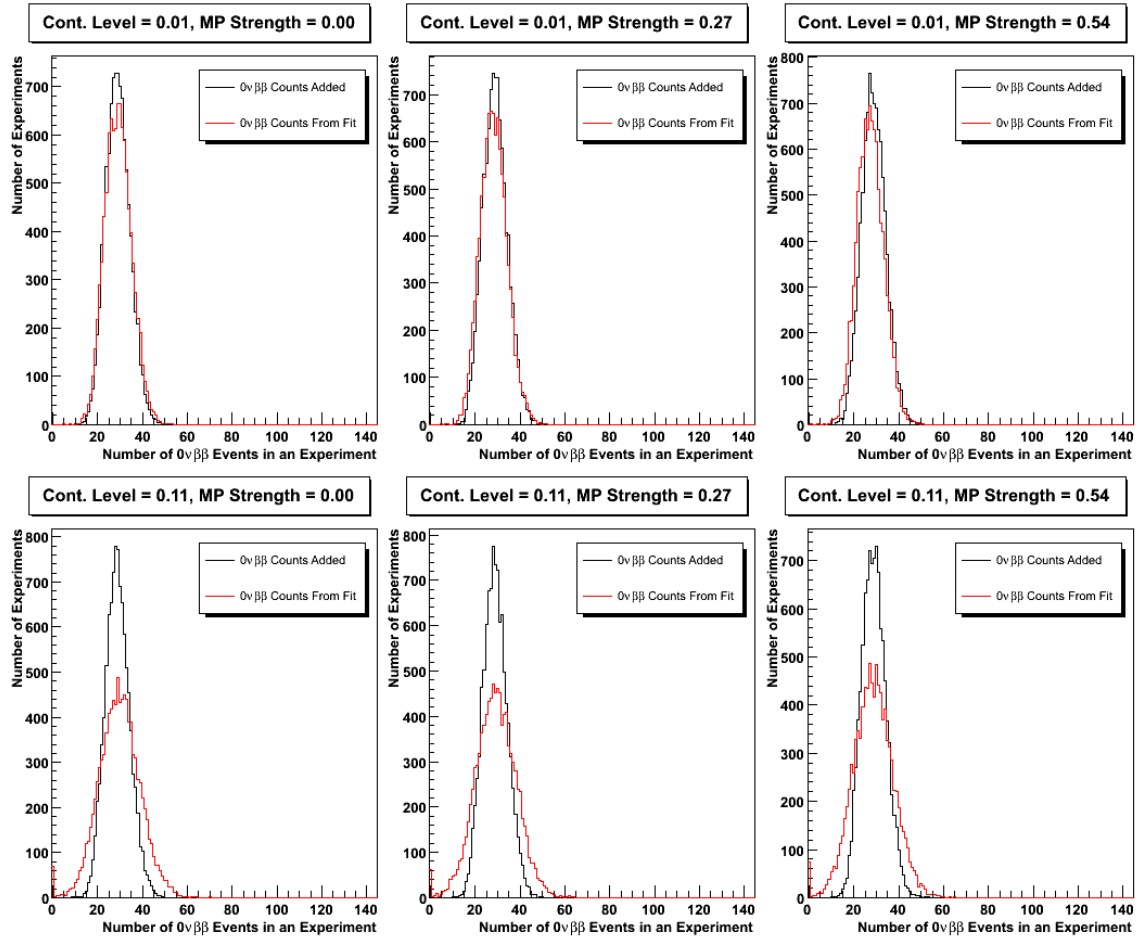


Figure 7.4: Histograms of the number of $0\nu\beta\beta$ events added to the simulation (black) and reconstructed by the fit (red) for each of the 10000 simulated KKDC-like experiments. The top row used a background level of 0.01 counts/keV/kg/y, and the bottom used 0.11 counts/keV/kg/y. The left column was generated for an experiment with no unidentified mystery peak. The middle column had one whose strength was 0.27 that of the $0\nu\beta\beta$ peak. The right column had a mystery peak strength of 0.54 (the level in the KKDC spectrum).

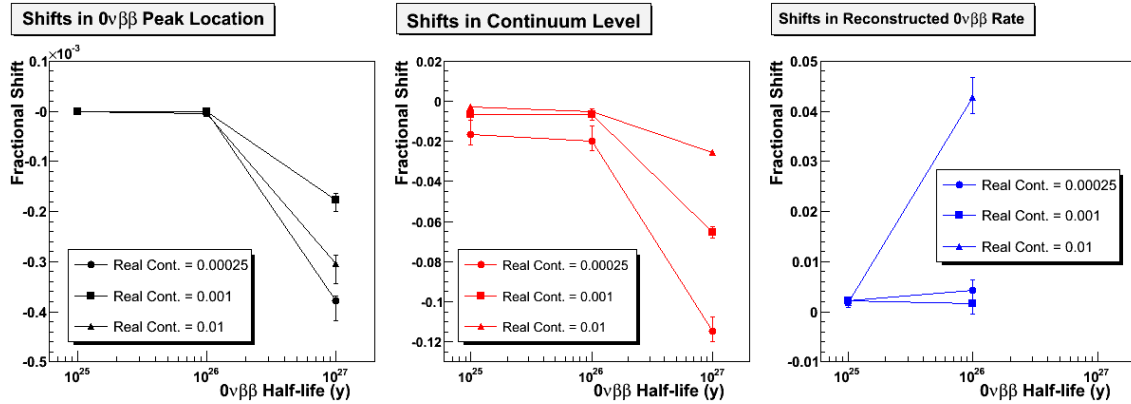


Figure 7.5: Shifts in peak location (left), continuum background level (middle) and $0\nu\beta\beta$ rate (right) as a function of the $0\nu\beta\beta$ half-life for M60-like exposure. The 10^{27} year half-life points for the $0\nu\beta\beta$ lifetime plot have been suppressed because they are off scale. Refer to the text for more details.

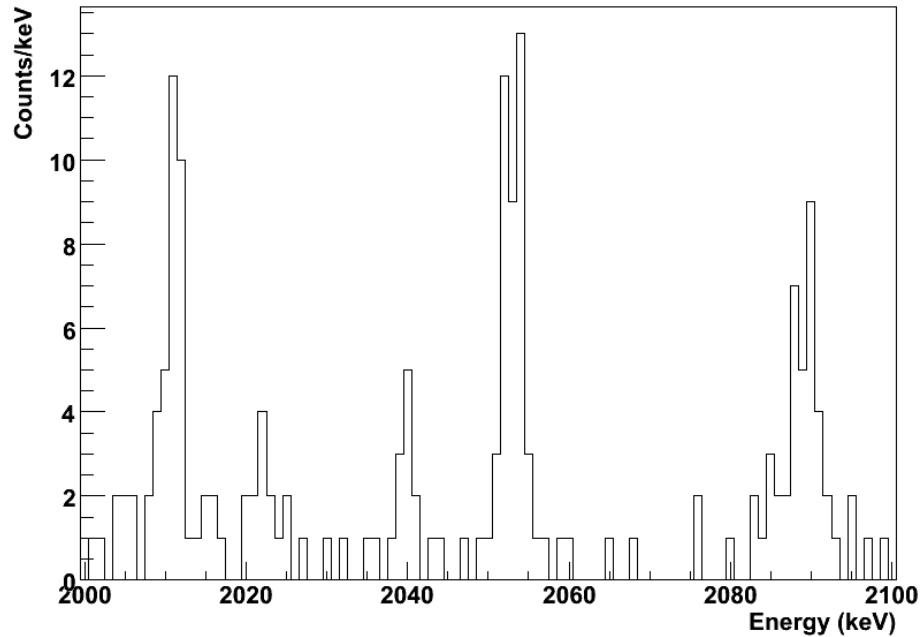


Figure 7.6: One of the 10000 spectra generated for M60-like exposures ($3.34 \text{ kmol} \times \text{y}$). The continuum background was 0.001 counts/keV/kg/y (or $4\times$ the MAJORANA assay goal), the ^{214}Bi level was set to 0.06, $T_{1/2}^{0\nu}$ was 1.0×10^{26} y, and the mystery peak strength turned off.

half-life, the deviation is still very small for the lowest background level, but is worse by roughly an order of magnitude for each of the two higher background levels. We now examine the accuracy with which the fit reconstructs the continuum level and the $0\nu\beta\beta$ peak strength. Understandably, higher continuum levels are better reconstructed than lower ones. We see that as the $0\nu\beta\beta$ peak gets weaker (*i.e.* the half-life gets longer), the continuum seems to lose counts to the $0\nu\beta\beta$ peak. To explain this phenomenon, we must look at the average number of counts from the continuum that enter the sum spectrum for M60-like exposures. They are listed in the Table 7.5. We now make

Table 7.5: Number of counts in the continuum for different continuum levels.

Continuum Level (counts/keV/kg/y)	Counts in Sum Spectrum	Counts in Fit Range	Counts per keV
0.00025	7.5	3.25	0.065
0.001	30	15	0.3
0.01	300	150	3.0

the supposition that the reason the continuum level loses counts to the $0\nu\beta\beta$ and the 2052.9 keV ^{214}Bi peaks is that for continuum levels that give rise to a forest of isolated counts (rather than an identifiable continuum), isolated continuum counts that fall too close to a peak get counted as part of that peak. If we assume that there is roughly 5 keV around each peak, this corresponds to roughly 20% of the 50 keV range for the two peaks in our fit, leading to the loss of approximately 20% of our continuum counts to the peaks. This of course represents an upper limit on this loss. As the peaks get better defined, the Gaussian shape of the underlying probability distribution will tend to narrow the region in which isolated continuum counts would be mistaken for part of a peak. The ^{214}Bi peak in the fit range has an average of 44 counts for all of the M60 parameter space considered. Upon examination of the middle panel of Figure 7.5, we see that for $0\nu\beta\beta$ half-lives of 10^{25} and 10^{26} years (these have ≈ 140 and 14 counts, respectively) the shift is less than 2%. When the $0\nu\beta\beta$ half-life extends up to 10^{27} years (and the peak strength drops to ≈ 1.4 counts), the shape of the $0\nu\beta\beta$ peak becomes quite ill-defined, and it becomes more likely that an isolated continuum event would be mistaken for part of the peak. When there are only an average of 1.4 counts in the $0\nu\beta\beta$ peak, the absorption of only one of the continuum counts to it by the fit constitutes an upward shift in the $0\nu\beta\beta$ rate of over 70%. Furthermore, this shift for very weak $0\nu\beta\beta$ rates is nearly one-sided because the fit will not reconstruct a negative value for the rate. Thus, the shift in reconstructed rate for $T_{1/2}^{0\nu} = 10^{27}\text{y}$ is strongly positive. This situation corresponds the the last data points in Figure

7.5 and the rightmost columns of Figures 7.7 and 7.8 and corresponds to the worst reconstruction for both the continuum level and the $0\nu\beta\beta$ rate. We also find that these configurations have the highest deviation in the reconstructed location of the $0\nu\beta\beta$ peak. We must be extremely careful in analyzing MAJORANA production data if the $0\nu\beta\beta$ peak is just on the edge of our sensitivity when the background level is also low, lest this affect cause the collaboration to mistakenly believe that we have a much stronger signal than we actually do.

7.2.3 M1000-Like Configuration Results

Last, we examine the M1000 results in Figure 7.9, and a sample spectrum in Figure 7.10. The M1000 sample spectrum given in Figure 7.10 was generated for a continuum level $4\times$ the MAJORANA goal, and $T_{1/2}^{0\nu}$ of 10^{27} y. Once again, even with non-ideal parameter set, the $0\nu\beta\beta$ peak is clearly present in the spectrum. Once again, the fit does an excellent job of reconstructing the location of the peak, with a worst-case reconstruction of only five parts in 10^6 (this corresponds to a shift of ≈ 0.01 keV). With the exception of a weak continuum and the strongest $0\nu\beta\beta$ peak (which reconstructs the continuum level approximately 0.2% high), the fit reconstructs the continuum level correctly within error bars or just slightly low ($< 0.3\%$). The $0\nu\beta\beta$ peak strength is also quite well reconstructed for this exposure, with fractional shifts consistent with zero for 10^{25} and 10^{26} years, and 1.0 to 2.5% for 10^{27} years depending on the background level chosen. Once again, we see the inverse correlation between the continuum level and the $0\nu\beta\beta$ level. For the sake of completeness, we also include the added and reconstructed histograms for the continuum and $0\nu\beta\beta$ rate for this exposure as well.

7.3 Conclusion From Background Model Simulations

We found that the shifts and uncertainties resulting from statistical fluctuations in the background and signal levels in a variety of possible MAJORANA configurations can vary over a wide range of possible values. We used maximum likelihood fits to extract different parameters of the experimental configuration corresponding to different components of the final spectrum. Generally speaking, the fidelity with which we could correctly extract those parameters depended, perhaps unsurprisingly, on the number of counts the fit can see from that component of the spectrum. When there are more than ≈ 10 counts in the fit range from a given spectral component, the fit tends to be reconstructed to within 0 – 5%. For this reason, we quote this level as the uncertainty in Table 4.3. It is certainly true however, when there are only a few counts from a part of the spectrum for the fit to access the reconstruction is much poorer than that level. For instance, when we try to reconstruct the number of $0\nu\beta\beta$ counts in the M60-like spectrum for $T_{1/2}^{0\nu} = 10^{27}$ y, the $0\nu\beta\beta$ rate is mis-reconstructed by a

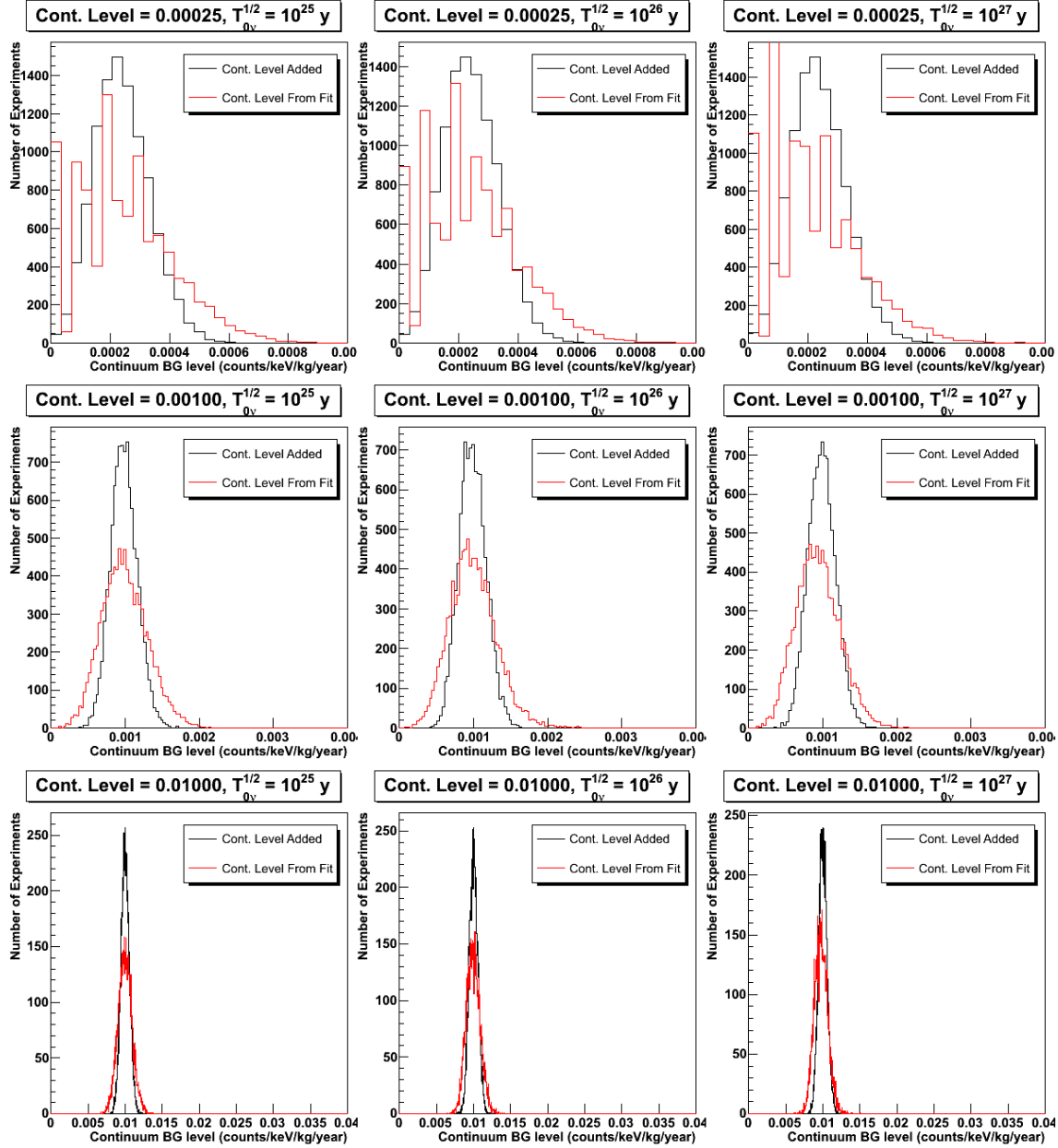


Figure 7.7: Histograms of the continuum level added to the simulation (black) and reconstructed by the fit (red) for the 10000 simulated M60-like experiments. The top row used a continuum background level of 0.00025 counts/keV/kg/y, the middle used 0.001 counts/keV/kg/y, and the bottom used 0.01 counts/keV/kg/y. The left column was created with a $0\nu\beta\beta$ lifetime of 10^{25} y, the middle with 10^{26} y, and the right with 10^{27} y.

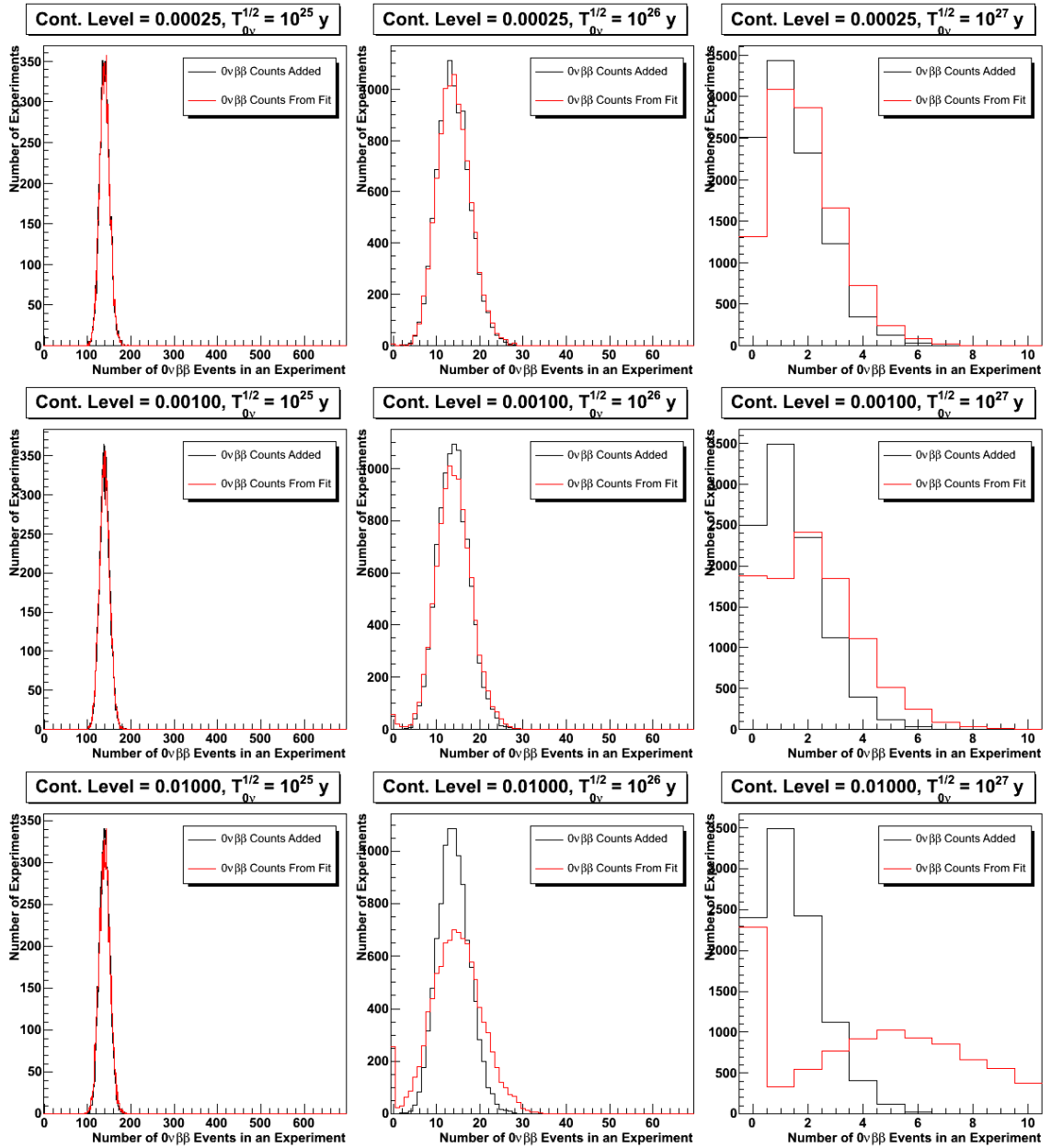


Figure 7.8: Histograms of the number of $0\nu\beta\beta$ events added to the simulation (black) and reconstructed by the fit (red) for the 10000 simulated M60-like experiments. The top row used a continuum background level of 0.00025 counts/keV/kg/y, the middle used 0.001 counts/keV/kg/y, and the bottom used 0.01 counts/keV/kg/y. The left column was created with a $0\nu\beta\beta$ lifetime of 10^{25} y, the middle with 10^{26} y, and the right with 10^{27} y.

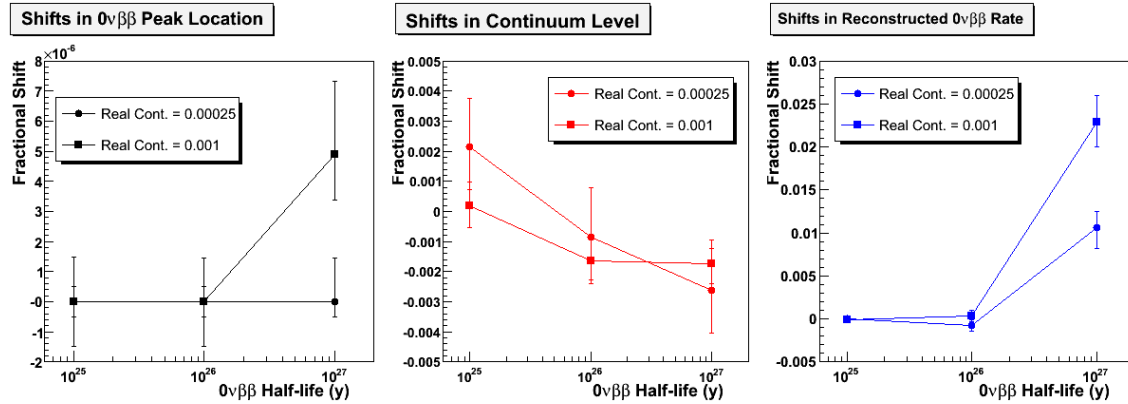


Figure 7.9: Shifts in peak location (left), continuum background level (middle) and $0\nu\beta\beta$ rate (right) as a function of the $0\nu\beta\beta$ half-life for M1000-like exposure.

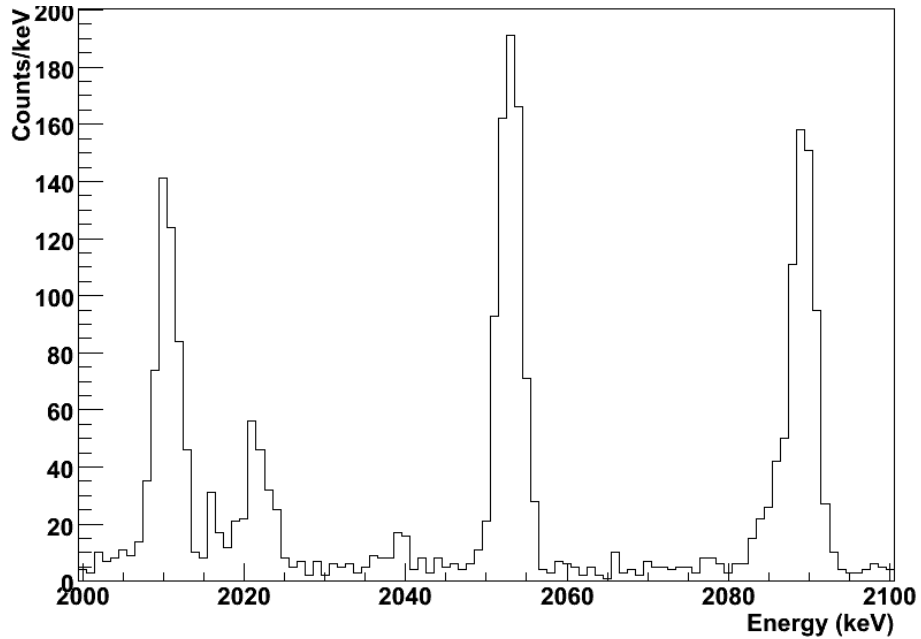


Figure 7.10: One of the 10000 spectra generated for M1000-like exposures ($55.7 \text{ kmol} \times \text{y}$). The continuum background was 0.001 counts/keV/kg/y ($4 \times$ the MAJORANA assay goal), the ^{214}Bi level was set to 0.06, $T_{1/2}^{0\nu}$ was $1.0 \times 10^{27} \text{ y}$, and the mystery peak strength turned off.

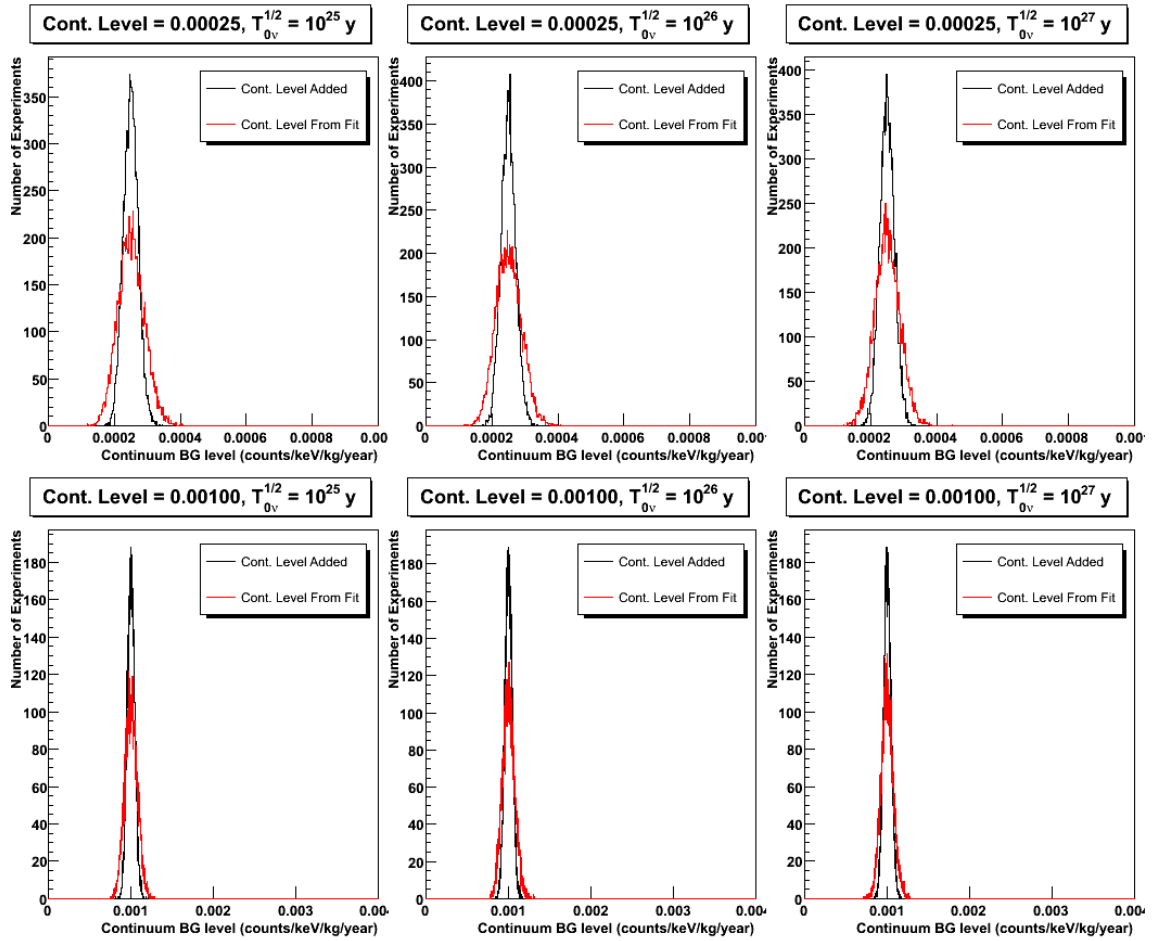


Figure 7.11: Histograms of the continuum level added to the simulation (black) and reconstructed by the fit (red) for the 10000 simulated M1000-like experiments. The top row used a continuum background level of 0.00025 counts/keV/kg/y, and the bottom used 0.001 counts/keV/kg/y. The left column was created with a $0\nu\beta\beta$ lifetime of 10^{25} y, the middle with 10^{26} y, and the right with 10^{27} y.

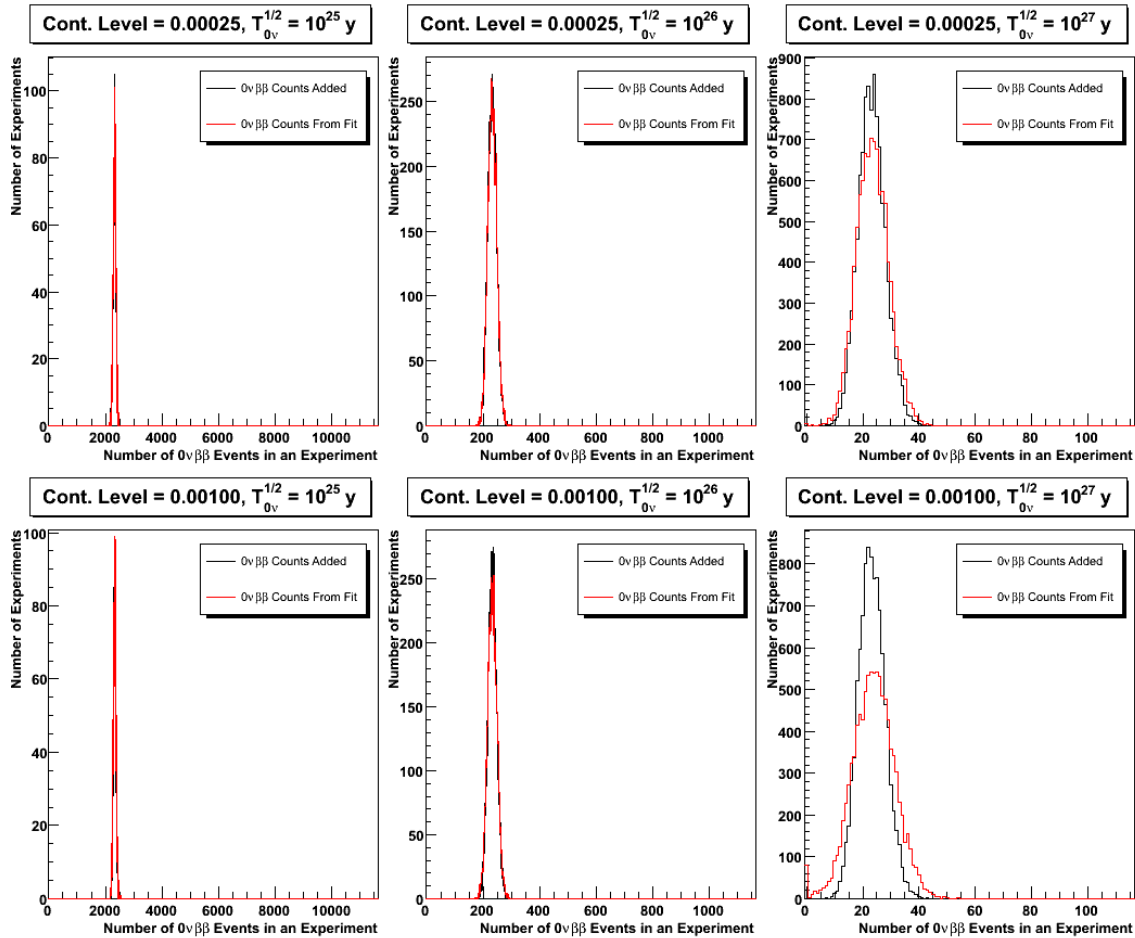


Figure 7.12: Histograms of the number of $0\nu\beta\beta$ events added to the simulation (black) and reconstructed by the fit (red) for the 10000 simulated M1000-like experiments. The top row used a continuum background level of 0.00025 counts/keV/kg/y, and the bottom used 0.001 counts/keV/kg/y. The left column was created with a $0\nu\beta\beta$ lifetime of 10^{25} y, the middle with 10^{26} y, and the right with 10^{27} y.

factor of roughly 1.5 to 4 depending on the continuum level. In this case, there are only 1.4 $0\nu\beta\beta$ counts in the spectrum, and even very small fluctuations in the continuum level can mimic much higher $0\nu\beta\beta$ rates. It is for this reason that lowering the MAJORANA continuum level both through sophisticated background tagging techniques and even more importantly, through careful selection of ultra-clean materials, will be paramount to a successful experiment.

Chapter 8

CONCLUSIONS AND PATH FORWARD

We now review the results from the previous chapters and draw some conclusions from them. We will then suggest some directions for future work on the MAJORANA experiment as well as in the broader field of neutrino physics.

8.1 Global $0\nu\beta\beta$ Analysis

The results of our model separation analysis in Section 1.4 set the scale of the total uncertainty budget for which the global $0\nu\beta\beta$ program should strive in fielding the next round of experiments. As we will see, this should include substantial efforts in refining the nuclear matrix element calculations for $0\nu\beta\beta$, as well as new attempts at measuring $T_{1/2}^{0\nu}$. While Table 1.6 shows that the order in which the $\beta\beta$ isotopes are added to the model separation analysis has a noticeable impact on the results (for more information see Reference [73]), it is clearly not an overwhelming effect. This ordering dependence does seem to indicate that certain models might be better tested with particular isotopes, but given the assumptions regarding the nuclear theory upon which these calculations are based, it would be dangerous to put too much weight on the specific choice of isotope for an experiment based on this work using presently available matrix elements. It is far more reasonable to pick the $\beta\beta$ isotopes for the global program which are most easily studied from an experimental standpoint and have the best understood $M_{0\nu}$ calculations, then perform this analysis to see what can be done to cut down the plausible model space for the underlying physics of $0\nu\beta\beta$.

If we neglect only the right-handed current models (rows 1 – 4 in Table 1.6), the results imply that approximately four experimental results are required to correctly choose the best physics model underlying the $0\nu\beta\beta$ process. For 68% (90%) confidence in choosing the correct model, a total uncertainty (theoretical and experimental) of $\sim 30\%$ ($\sim 19\%$) might be acceptable if four experimental results are available. In this analysis, it is the heavy neutrino exchange model that seems to be the limiting factor in setting the uncertainty levels. We could also restrict our consideration to the light neutrino models. This would serve as a test of the different methods for calculating $M_{0\nu}$, especially if results from other experimental programs begin to rule out the parameter space for other lepton number violating processes to which this global $0\nu\beta\beta$ analysis is sensitive. When we consider only

the light ν exchange models, the requirement for 68% (90%) confidence can be relaxed to $\approx 64\%$ ($\approx 44\%$) uncertainty for four experiments, or 35% (18%) for only three. When all seven models are considered, the required statistical precision becomes more stringent than when one uses fewer models, as one would expect. A 68% confidence-level result would require $T_{1/2}^{0\nu}$ measurements in four isotopes with a precision of $\sim 22\%$ or better (see the final row in Table 1.6). From this analysis, it is clear that only two experimental results is insufficient to perform the separation. Three results also seems to constrain the total uncertainty budget to be smaller than is likely reachable by the next generation of experiments and $M_{0\nu}$ calculations. The general conclusion of this work is that separation is possible if the uncertainties can be made small. It also indicates that additional constraints limiting the possible viable models from non- $0\nu\beta\beta$ experimental results will help discern the underlying mechanism.

8.2 Total Uncertainty Budgets

The uncertainty described above is the total uncertainty: statistical, systematic and theoretical. We use the following form to express it for an experiment:

$$\sigma_{Total} = \sqrt{\sigma_{Stat}^2 + \sigma_{Sys}^2 + 2\sigma_M^2}, \quad (8.1)$$

where σ_{Stat} is the experiment's statistical uncertainty, σ_{Sys} is the experiment's systematic uncertainty, and σ_M is the the uncertainty in $M_{0\nu}$. Remember that the last term in the quadrature sum is doubled because the matrix element appears squared in the expression for the $0\nu\beta\beta$ rate.

We find in Chapter 3 that the theoretical uncertainty from the nuclear matrix elements used to calculate the $0\nu\beta\beta$ rate for a given model currently dominate the total uncertainty level expected for potential results in the next generation of experiments. Table 3.3 estimates the current level of the uncertainty in QRPA calculations to be $\approx 30 - 40\%$. Uncertainty levels in $M_{0\nu}$ of $\approx 30 - 40\%$ correspond to a theoretical $0\nu\beta\beta$ rate uncertainty of $60 - 80\%$. Unfortunately, this consumes the entire available budget described above for any of the model spaces considered. Furthermore, this $M_{0\nu}$ uncertainty only comes from the inputs to the calculation itself. As seen in the recent erratum to Reference [125], these calculations are extremely complicated and there is no guarantee that the current calculations actually contain all the necessary physics to correctly describe the nuclear structure of these isotopes, or that the calculations themselves are free of coding errors.

There are however, a number of reasons to think that the uncertainty in $M_{0\nu}$ will drop over the next few years. As reported in Table 3.2, when using measured $2\nu\beta\beta$ lifetimes to fine tune the calculation of $0\nu\beta\beta$ matrix elements (as was done in Reference [125]), much of the uncertainty in $M_{0\nu}$ comes from from experimental uncertainties in $T_{1/2}^{2\nu}$. The next round of $\beta\beta$ experiments will do much

to address this uncertainty since they will all perform extremely high-statistics measurements of $T_{1/2}^{2\nu}$ on the way to obtaining a $T_{1/2}^{0\nu}$ limit or result. Even for QRPA calculations tuned to reproduce the β decay rates of the intermediate nuclei (as was done in Reference [135]), uncertainties in the rates for these reactions can be addressed with future experimental programs. In particular, future radioactive beam experiments could do much to provide accurate data as inputs for these calculations (there is a plan to perform radioactive beam studies like this at the TRIUMF facility in Canada, but the author is aware of no formal proposals or allocated beam time). The other, perhaps more significant push forward on this front comes from the increasing competitiveness of shell model calculations to address the the problem of $M_{0\nu}$ calculation. Until fairly recently, ^{48}Ca was the only $\beta\beta$ isotope with a small enough atomic number to be treated in the shell model without dramatically truncating the number of states available to the calculation. Continuing advances in both processor speeds and computational methods are beginning to put ^{76}Ge and ^{82}Se in reach of more complete shell model calculations as well. Ultimately, the best way to limit uncertainty in the theoretical values of $M_{0\nu}$ is to treat these nuclei in both the shell model and QRPA. This will have to be done with sufficiently complete calculations that they not only agree with each other in terms of producing the same numerical values of $M_{0\nu}$, but also reproduce other experimentally verifiable quantities for each $\beta\beta$ isotope. In any case, should $M_{0\nu}$ calculations reach uncertainty levels compatible with this global analysis, it will greatly increase the physics reach of $0\nu\beta\beta$, and help to formulate the future program of searches for physics beyond the Standard Model.

The experimental uncertainty will be a combination of statistical and systematic affects in each $0\nu\beta\beta$ result. The statistical uncertainty for each experiment will be decided by nature (from the actual level of lepton number violation) and the experimental exposure for each isotope. If we assume light ν exchange dominates $0\nu\beta\beta$, and that $\langle m_{\beta\beta} \rangle \approx 200$ meV, then a 60-kg MAJORANA experiment would see approximately 38 $0\nu\beta\beta$ events in five live years of running. Assuming \sqrt{N} counting statistics, this corresponds to a statistical uncertainty of $\approx 16\%$. In Chapter 4, we showed that MAJORANA can likely expect a systematic uncertainty of $\approx 11\%$, leaving us with a total experimental uncertainty of 19%. Recalling the factor of 2 that multiplies the $M_{0\nu}$ uncertainty, this leaves only $\approx 12\%$ for the matrix elements given a total uncertainty budget of 30% (required for the five-model analysis) and $\approx 31\%$ for a budget of 64% (required for the light ν only analysis). As mentioned above, the current state of the field and likely future for the calculation of $M_{0\nu}$ mean that the light ν analysis is a strong possibility, while the five-model analysis will be extremely difficult. Still, as the community moves forward in better understanding $M_{0\nu}$ calculations it is possible (even likely) that their numerical values will change for each model. We must therefore monitor the progress in these

efforts, as the total required uncertainty budgets may change in the coming years. Furthermore, input from other experimental programs could also further constrain the available model space, and this too could change the total available uncertainty for this analysis.

There are other motivations that require multiple $0\nu\beta\beta$ experimental results detailed in Reference [51]. Principle among them is need to prove that the observation of $0\nu\beta\beta$ is indeed $0\nu\beta\beta$ and not a heretofore unidentified background. Therefore, a general conclusion the reader can draw from this work is that at least four $0\nu\beta\beta$ experiments along with significant theoretical effort are critical to maximizing the physics reach of a $\beta\beta$ research program [73].

8.3 $0\nu\beta\beta$ and Neutrino Physics as a Whole

Analogously to the way that we can extend the physics reach of a $0\nu\beta\beta$ program by comparing results across several isotopes, we can extend the physics reach of a broader neutrino physics program by comparing results from several types of experiments. The most interesting prospect here is the fact that because the neutrino mass affecting $0\nu\beta\beta$ (assuming light-neutrino exchange dominates) is a different admixture of the mass eigenstates, mixing matrix elements and phases, from that affecting tritium β decay. This means that comparing any positive results from both experimental techniques will allow us to access some information about the phases in the expression for $\langle m_{\beta\beta} \rangle$. The oscillation experiments are also very important to this global neutrino analysis in that they will help the community to reduce uncertainties on the mixing angles and mass differences. A group of very talented scientists preparing to undertake a large neutrino experiment once remarked that these three experimental techniques are like the legs of a three-legged stool—all three must be present for the stool (or the neutrino physics research program) to be of greatest utility to the community [37].

8.4 Systematics and Calibration

In Chapter 4, we examined the list of systematic uncertainties in the expression we will use to calculate a $0\nu\beta\beta$ rate from the number of events passing our signal and background tagging cuts. Chapter 5 dealt with what we will do to minimize their impact through a calibration program. As mentioned above, we can expect a total systematic uncertainty in MAJORANA of $\approx 11\%$. In Chapter 4, we found that the two largest systematic uncertainties for the MAJORANA experiment will be the pulse shape and segmentation cut efficacies and (depending on the actual background level and ^{76}Ge exposure in MAJORANA) fluctuations in the continuum background level. We addressed each of these in Chapters 6 and 7 respectively. We expect our pulse shape cuts to have a fractional uncertainty of 6.6% for multi-site events and 3.8% for single-site events. The segmentation cuts will

have an uncertainty based on the counting statistics per detector segment of our calibration runs, so 1 – 3% is a good estimate. For conservative values of the background level and comparatively low ^{76}Ge exposure, we can expect fluctuations in the continuum near $Q_{\beta\beta}$ to contribute as much as 5% to the systematic uncertainty total (though for lower backgrounds and greater exposure, this can be brought down essentially to zero). Both of these preliminary figures will of course, depend on the details of the final design and implementation of the MAJORANA array. We must therefore revisit them as details about detector design begin to crystalize and actual construction of the MAJORANA apparatus is initiated allowing background levels to be demonstrated experimentally.

We spent Chapter 5 laying out the requirements and challenges associated with calibrating MAJORANA, as well as detailing the calibration plan for the experiment. We also described the prototyping work done at LANL in support of this task, and the lessons learned from it. We now reiterate in brief, the MAJORANA calibration plan. We propose there be four different types of calibration runs: “energy scale,” “pulse shape training,” “contamination response,” and “veto response.” The energy scale runs will be aimed at characterizing the energy scale and resolution of the detector array. They will use the calibration track described in Section 5.3.2 to position a wire source (probably ^{232}Th) inside the MAJORANA shield. Energy scale runs will need to collect enough statistics to fit out the centroid and width of at least ten γ -ray peaks in each detector. We anticipate the schedule for energy scale calibration runs to be in the neighborhood of a few hours per week. The pulse shape training runs will focus on providing training data for the pulse shape analysis software. These will use the same source positioning hardware as the energy scale runs, but require significantly higher statistics. The need for greater statistics comes from the minimum 400 – 500 double escape peak events necessary to teach the PSA software to recognize single-site events. Pulse shape training runs should therefore be much longer, and occur less often. The proposal in our calibration plan is to take pulse shape training runs approximately once every one to two months for roughly two days. The need for pulse shape training runs is of course, predicated on the use of PSA algorithms requiring training data. If we find that unsupervised cuts requiring no training data perform similarly well to the supervised cuts described in Chapter 6 or that the burden of acquiring a sufficient number of training events in each detector is too onerous, the need for pulse shape training runs could be eliminated. Contamination and veto response runs would be special calibration runs designed to characterize the array’s response to localized contamination (*i.e.* “hot spots”), and the efficiency of the active veto system. These would take place fairly frequently during commissioning of the MAJORANA array. After that however, these runs would be extremely rare, only taking place on a roughly quarterly to yearly basis to check for stability against the commissioning data.

8.5 Plans for Future Work

We now lay out some possibilities and suggestions for future work on MAJORANA connected to this dissertation. First, we mentioned, but did not discuss in detail, the initial characterization plan for the MAJORANA detectors. This differs from the calibration program in that calibration must be performed *in situ*, while characterization would take place with detectors in test cryostats prior to their installation in the MAJORANA array. The characterization program will focus on understanding the active volume of and electronic performance of any segmentation scheme applied to MAJORANA detectors. Just characterizing the detectors' active volumes will be a large amount of work both in terms of designing the program and actually implementing it. Work on this task has begun at the Triangle Universities Nuclear Laboratory (TUNL). Second, the details of electronics characterization remain largely unaddressed within the collaboration. As mentioned briefly in Chapter 5, electronics calibration will likely involve interrogating each detector with a precision pulser to characterize and then monitor its: gain, linearity, preamplifier bandwidth and baseline voltage. As with detector characterization, refining the details of this program will take quite a bit of attention from a subset of the collaboration.

In Sections 6.2.3 and 6.2.4, we went over two possible extensions to the MAJORANA pulse shape analysis methods. The former focused on using a family of machine learning techniques known as “boosting” to enhance the discrimination power of parametric PSA. The latter discussed the possibility of using the charges induced in the outer contacts of modest to highly-segmented detectors to perform a full, three-dimensional spatial reconstruction of energy depositions, as is done by the γ -ray tracking arrays. Both options are intriguing possible avenues for future PSA techniques. The extensions to the parametric methods are likely the most versatile, in the sense that they are applicable to more detector designs. The γ -ray tracking techniques require a fairly high degree of detector segmentation, but provide the most information about each event. Also, as discussed above, the collaboration should investigate the feasibility of using unsupervised machine learning techniques for pulse shape analysis because the problem of collecting sufficient training statistics for our current methods is, while not insurmountable, a significant burden that will result in a nontrivial reduction of the time devoted to production data taking in MAJORANA.

There are a variety of other background reduction techniques (in addition to pulse shape analysis and segmentation) currently being investigated for use in the MAJORANA experiment. First, the active veto system for the MAJORANA shield, while it seems fairly simple in principle, will require some careful engineering and characterization work to deploy. Understanding the efficiency of the active veto system for different types of external radiation will be of particular import. The single-

site time coincidence cuts are another area that has tremendous potential for removing continuum background events (specifically from ^{68}Ge decays), but it will require careful study to develop the actual algorithm used to make the cut. Accurately characterizing the efficiency of this cut for tagging both signal and background events will also be critical. Last there is a continuing debate surrounding both the design of the detectors themselves and the DAQ electronics that will be used to read them out. The first choice will be closely tied to the building of the MAJORANA prototype module. The second has more leeway in the timing of the decision, and will be more centered on efforts to incorporate several of the available DAQ hardware options into a single software framework for ease of direct comparison. The detector design decision is of great interest to many parties in the MAJORANA experiment, and will therefore involve a large fraction of the collaboration. The DAQ hardware decision, is probably more appropriate for a future doctoral dissertation or postdoc project, but should not be made prematurely since digitizer electronics are constantly improving.

We conclude this dissertation by briefly reiterating the immense discovery potential of the MAJORANA project and the “forward momentum” built by the collaboration, in terms of R&D progress, funding potential and operational capabilities. Understanding $0\nu\beta\beta$ in ^{76}Ge fills an important part of the broader neutrino physics program, and the MAJORANA experiment is vital to that effort. The next decade will be a very exciting time in the field of neutrino physics, and the MAJORANA experiment is a large part of that excitement.

BIBLIOGRAPHY

- [1] C. E. Aalseth, F. T. Avignone, R. L. Brodzinski, S. Cebrian, E. Garcia, D. Gonzalez, W. K. Hensley, I. G. Irastorza, I. V. Kirpichnikov, and A. A. Klimenko. IGEX ^{76}Ge neutrinoless double-beta decay experiment: Prospects for next-generation experiments. *Physical Review D*, 65:092007, 2002.
- [2] Craig Aalseth. *Germanium Spectrometer Pulse Shape Discrimination for ^{76}Ge Double-Beta Decay*. PhD thesis, University of South Carolina, 2000.
- [3] I. Abt. A new ^{76}Ge double beta decay experiment at LNGS, 2004, hep-ex/0404039.
- [4] A. Ali, A.V. Borisov, and D.V. Zhuridov. Neutrinoless double beta decay: Electron angular correlation as a probe of new physics, 2006, hep-ph/0606072.
- [5] S. W. Allen, R. W. Schmidt, and S. L. Bridle. A preference for a non-zero neutrino mass from cosmological data. *Monthly Notices of the Royal Astronomical Society*, 346:593, 2003.
- [6] R. Alvarez-Rodriguez, P. Sarriguren, E. Moya de Guerra, L. Paceaescu, Amand Faessler, and F. Simkovic. Deformed quasiparticle random phase approximation formalism for single- and two-neutrino double beta decay. *Physical Review C (Nuclear Physics)*, 70(6):064309, 2004.
- [7] C. Arnaboldi. CUORE: a cryogenic underground observatory for rare events. *Nuclear Instruments and Methods A*, 518:775, 2004, hep-ex/0212053.
- [8] C. Arnaboldi. Private communication, to be submitted to physical review c, 2007.
- [9] R. Arnold, C. Augier, J. Baker, A. Barabash, D. Blum, V. Brudanin, A. J. Caffrey, J. Campaigne, E. Caurier, , and D. Dassi. Double- β decay of ^{82}Se . *Nuclear Physics A*, 636:209, 1998.
- [10] X-Ray Instrument Associates. User's manual digital gamma finder (DGF, version 3.02), 2003, <http://www.xia.com>.
- [11] K.S. Babu and R.N. Mohapatra. New vector-scalar contributions to neutrinoless double beta decay and constraints on r-parity violation. *Physical Review Letters*, 75:2276, 1995.
- [12] J.N. Bahcall, H. Murayama, and C. Peña-Garay. What can we learn from neutrinoless double beta decay experiments. *Physical Review D*, 70:033012, 2004.
- [13] B. Balantekin. Review of particle physics. *Journal of Physics G: Nuclear and Particle Physics*, 33:1, 2006.

- [14] A. Barabash. NEMO-3 and SuperNEMO double beta decay experiments. *J. Phys. Conf. Ser.*, 39:347, 2006, hep-ex/0602011.
- [15] A. Barabash. NEMO-3 double beta decay experiment: latest results, 2006, hep-ex/0610025.
- [16] A. S. Barabash. Double-beta-decay experiments: Present status and prospects for the future. *Physics of Atomic Nuclei*, 67:438, 2004.
- [17] A. S. Barabash and the NEMO Collaboration. Investigation of double-beta-decay processes at the NEMO-3 tracking detector. *Physics of Atomic Nuclei*, 68:414, 2005.
- [18] J. Bardeen, L. N. Cooper, and J. R. Schrieffer. Theory of superconductivity. *Phys. Rev.*, 108(5):1175–1204, Dec 1957.
- [19] V. Barger, D. Marfatia, and A. Tregre. Neutrino mass limits from SDSS, 2dFGRS and WMAP. *Physics Letters B*, 595:55, 2004, hep-ph/0312065.
- [20] C. Beausang and J. Simpson. Large arrays of escape suppressed spectrometers for nuclear structure experiments. *Journal of physics. G, Nuclear and particle physics*, 22(5):527 – 558, 1996.
- [21] R. Bernabei, P. Belli, F. Cappella, R. Cerulli, F. Montecchia, A. Incicchitti, D. Prosperi, and C J Dai. Investigation of $\beta\beta$ decay modes in ^{134}Xe and ^{134}Xe . *Physics letters. B*, 546(1-2):23 – 28, 2002.
- [22] T. Bernatowicz, J. Brannon, R. Brazzle, R. Cowsik, C. Hohenberg, and F. Podosek. Precise determination of relative and absolute $\beta\beta$ -decay rates of ^{128}Te and ^{130}Te . *Physical Review C*, 47:806, 1993.
- [23] Philip R. Bevington and D. Keith Robinson. *Data Reduction and Error Analysis for the Physical Sciences*. WCB/McGraw-Hill, second edition, 1992.
- [24] G. Bhattacharyya, H.V. Klapdor-Kleingrothaus, H. Päs, and A. Pilaftsis. Neutrinoless double beta decay from singlet neutrinos in extra dimensions. *Physical Review D*, 67:113001, 2003.
- [25] S. M. Bilenky, C. Giunti, J. A. Grifols, and E. Massó. Absolute value of the neutrino masses: Status and prospects. *Physics Reports*, 379:69, 2003.
- [26] S. M. Bilenky and S. T. Petcov. Nuclear matrix elements of $0\nu\beta\beta$ -decay: Possible test of the calculations, 2004, hep-ph/0405237.
- [27] J. B. Birks. *The Theory and Practice of Scintillation Counting*. Macmillan Co., 1964.
- [28] F. Boehm and P. Vogel. *Physics of Massive Neutrinos*. The Press Syndicate of the University of Cambridge, The Pitt Building, Trumpington St. Cambridge CB2 1RP, 1987.
- [29] Canberra, 2007, <http://www.canberra.com>.

- [30] E. Caurrier, G. Martinez-Pinedo, F. Nowacki, A. Poves, and A. P. Zuker. The shell model as a unified view of nuclear structure. *Reviews of Modern Physics*, 77:427, 2005.
- [31] E. Caurrier, F. Nowacki, A. Poves, and J. Retamosa. Shell model study of the neutrinoless double beta decays. *Nuclear Physics A*, 654:973c, 1999.
- [32] V. Cirigliano, A. Durylov, M. J. Ramsey-Musolf, and P. Vogel. Neutrinoless double beta decay and lepton flavor violation. *Physical Review Letters*, 93:231802, 2004.
- [33] O. Civitarese and J. Suhonen. Light-neutrino mass spectrum, nuclear matrix elements, and the observability of neutrinoless $\beta\beta$ decay. *Nuclear Physics A*, 729:867, 2003.
- [34] ROOT Collaboration, 2007, <http://root.cern.ch>.
- [35] The DUSEL Collaboration, 2007, <http://www.dusel.org>.
- [36] The KATRIN Collaboration. KATRIN: A next-generation tritium beta decay experiment with sub-eV sensitivity for the electron neutrino mass, 2001, hep-ex/0109033.
- [37] The Majorana Collaboration. The majorana zero-neutrino double-beta decay experiment, 2003, nucl-ex/0311013.
- [38] The Majorana Collaboration. The majorana neutrinoless double-beta decay experiment pre-conceptual design proposal, 2006.
- [39] The Planck Collaboration, 2007, <http://www.rssd.esa.int/Planck/>.
- [40] Goodfellow Corporation, 2007, <http://www.goodfellow.com>.
- [41] S. Cowell. Scaling factor inconsistencies in neutrinoless double beta decay. *Physical Review C*, 73:028501, 2006.
- [42] P. Crotty, J. Lesgourgues, and S. Pastor. Current cosmological bounds on neutrino masses and relativistic relics. *Physical Review D*, 69:123007, 2004, hep-ph/0402049.
- [43] F. A. Danevich, A. S. Georgadze, V. V. Kobychyev, B. N. Kropivnyansky, A. S. Nikolaiko, O. A. Ponkratenko, V. I. Tretyak, S. Y. Zdesenko, Y. G. Zdesenko, and P. G. Bizzeti. New results of ^{116}Cd double β decay study with $^{116}\text{CdWO}_4$ scintillators. *Physical Review C*, 62:045501, 2000.
- [44] Frank Deppisch and Heinrich Päs. Pinning down the mechanism of neutrinoless double beta decay with measurements in different nuclei, 2006, hep-ph/0612165.
- [45] M. Doi, T. Kotani, and E. Takasugi. Double beta decay and majorana neutrino. *Progress in Theoretical Physics (Supplement)*, 83:1, 1985.
- [46] G. Douysset, T. Fritioff, C. Carlberg, I. Bergström, and M. Björkhage. Determination of the ^{76}Ge double beta decay Q value. *Physical Review Letters*, 86(19):4259–4262, 2001.

- [47] Hiroyasu Ejiri. Double beta decays and neutrino masses. *Journal of the Physical Society of Japan*, 74:2101, 2005.
- [48] S. R. Elliott and J. Engel. Double beta decay. *Journal of Physics G: Nuclear and Particle Physics*, 30:R183, 2004.
- [49] S. R. Elliott, V. M. Gehman, K. Kazkaz, D-M. Mei, and A. R. Young. Pulse shape analysis in segmented detectors as a technique for background reduction in Ge double-beta decay experiments. *Nuclear Instruments and Methods in Physics Research A*, 558:504, 2006.
- [50] S. R. Elliott and P. Vogel. Double beta decay. *Annual Review Nuclear and Particle Science*, 52:115, 2002.
- [51] Steven R. Elliott. Introduction to the double-beta decay experimental program, 2006, nucl-ex/0609024.
- [52] J. Engel, P. Vogel, X. Ji, and S. Pittel. Double beta decay in the generalized-seniority scheme. *Physics letters. B*, 225(1-2):5 – 9, 1989.
- [53] B. Aharmim *et al.* Electron energy spectra, fluxes, and day-night asymmetries of [sup [bold 8]]b solar neutrinos from measurements with nacl dissolved in the heavy-water detector at the sudbury neutrino observatory. *Physical Review C (Nuclear Physics)*, 72(5):055502, 2005.
- [54] C. Aalseth *et al.* Recent results from the igex double-beta decay experiment. *Nuclear physics. B, Proceedings, supplements*, 48(1-3):223 – 225, 1996.
- [55] C. E. Svensson *et al.* Radioactive beam experiments with large gamma-ray detector arrays. *Nuclear Instruments and Methods in Physics Research Section B: Beam Interactions with Materials and Atoms*, 204:660–665, 2003.
- [56] C. L. Bennett *et al.* First-year wilkinson microwave anisotropy probe (WMAP) observations: Preliminary maps and basic results. *The Astrophysical Journal*, 148:1, 2003, astro-ph/0302207.
- [57] C. L. Kuo *et al.* High-resolution observations of the cosmic microwave background power spectrum with ACBAR. *The Astrophysical Journal*, 600:32, 2004.
- [58] D. N. Spergel *et al.* First-year wilkinson microwave anisotropy probe (WMAP) observations: Determination of cosmological parameters. *The Astrophysical Journal Supplement Series*, 148:175, 2003.
- [59] H. Ejiri *et al.* Spectroscopy of double-beta and inverse-beta decays from ¹⁰⁰Mo for neutrinos. *Physical Review Letters*, 85:2917, 2000.
- [60] M. Apollonio *et al.* Limits on neutrino oscillations from the chooz experiment. *Physics Letters B*, 466:415, 1999.
- [61] M. Tegmark *et al.* Cosmological parameters from SDSS and WMAP. *Physical Review D*, 69:103501, 2004, astro-ph/0310723.

- [62] Ø. Elgarøy *et al.* New upper limit on the total neutrino mass from the 2 degree field galaxy redshift survey. *Physical Review Letters*, 89:061301, 2002.
- [63] R. A. C. Croft *et al.* Toward a precise measurement of matter clustering: Ly α forest data at redshifts 2-4. *The Astrophysical Journal*, 581:20, 2002.
- [64] S. Ahmed *et al.* Measurement of the total active ^8B solar neutrino flux at the sudbury neutrino observatory with enhanced neutral current sensitivity. *Physical Review Letters*, 92:181301, 2004.
- [65] T. J. Pearson *et al.* The anisotropy of the microwave background to $l = 3500$: Mosaic observations with the cosmic background imager, 2002, astro-ph/0205388.
- [66] Y. Ashie *et al.* Measurement of atmospheric neutrino oscillation parameters by superkamiokande i. *Physical Review D (Particles and Fields)*, 71(11):112005, 2005.
- [67] A. Faessler, S. Kovalenko, and F. Šimkovic. Pions in nuclei and manifestations of supersymmetry in neutrinoless double beta decay. *Physical Review D*, 58:115004, 1998.
- [68] A. Faessler and F. Šimkovic. Double beta decay. *Journal of Physics G*, 24:2139, 1998.
- [69] F. Feruglio, A. Strumia, and F. Vissani. Neutrino oscillations and signals in β and $0\nu 2\beta$ experiments. *Nuclear Physics B*, 637:345, 2002.
- [70] E. Fiorini, A. Pullia, G. Bertolini, F. Cappellani, and G. Restelli. A search for lepton non-conservation in double beta decay with a germanium detector. *Physics Letters B*, 25:602, 1967.
- [71] Richard B. Firestone, Virginia S. Shirley, Coral M. Baglin, S. Y. Frank Chu, and Jean Zipkin, editors. *Table of Isotopes*. John Wiley & Sons, Inc., eighth edition, 1998.
- [72] L. Bornschein for the KATRIN Collaboration. KATRIN - direct measurement of neutrino mass in the sub-ev region, 2003, hep-ex/0309007.
- [73] V. M. Gehman and S. R. Elliott. Multiple-isotope comparison for determining $0\nu\beta\beta$ mechanisms. *Journal of Physics G: Nuclear and Particle Physics*, 34(4):667-678, 2007, <http://stacks.iop.org/0954-3899/34/667>, arXiv:hep-ph/0701099.
- [74] Victor M. Gehman. *A Prospective Global Analysis to Extend the Physics Reach of Neutrinoless Double-Beta Decay Experiments, and the Majorana Experiment's Efforts to Mitigate its Systematic Uncertainties*. PhD thesis, University of Washington, 2007 Yes, this is a recursive reference.
- [75] G. Gratta. EXO presentation to NuSAG, 2005.
- [76] S. Hannestad. Neutrino masses and the number of neutrino species from WMAP and 2dFGRS. *Journal of Cosmology and Astroparticle Physics*, 2003(5):4, 2003.

- [77] S. Hannestad. Neutrino cosmology - an update, 2003, hep-ph/0312122.
- [78] H. L. Harney. Reply to the comment on “Evidence for Neutrinoless Double Beta Decay” [Mod. Phys. Lett. A 16 (2001) 2409], 2001, hep-ph/0205293.
- [79] M. Hirsch, H. V. Klapdor-Kleingrothaus, and S. G. Kovalenko. Supersymmetry and neutrinoless double β decay. *Physical Review D*, 53:1329, 1996.
- [80] M. Hirsch, H. V. Klapdor-Kleingrothaus, and S. G. Kovalenko. R-parity-conserving supersymmetry, neutrino mass, and neutrinoless double beta decay. *Physical Review D*, 57:1947, 1998.
- [81] M. Hirsch, H.V. Klapdor-Kleingrothaus, and S.G. Kovalenko. Double beta decay in left-right symmetric models. *Physics Letters B*, 374:7, 1996.
- [82] M. Hirsch, H.V. Klapdor-Kleingrothaus, and S.G. Kovalenko. New leptoquark mechanism of neutrinoless double β decay. *Physical Review D*, 54:4207, 1996.
- [83] M. Hirsch, H.V. Klapdor-Kleingrothaus, and S.G. Kovalenko. On the susy accompanied neutrino exchange mechanism of neutrinoless double beta decay. *Physics Letters B*, 372:181, 1996.
- [84] MA M. Howe. Sudbury neutrino observatory neutral current detector acquisition software overview. *IEEE transactions on nuclear science*, 51(3):878 – 883, 2004.
- [85] Wayne Hu and Max Tegmark. Weak lensing: Prospects for measuring cosmological parameters. *The Astrophysical Journal Letters*, 514:L65, 1999.
- [86] F. T. Avignone III, R. L. Brodzinski, C. K. Guerard, I. V. Kirpichnikov, H. S. Miley, V. S. Pogosov, J. H. Reeves, A. S. Starostin, and A. G. Tamanyan. Confirmation of the observation of $2\nu\beta\beta$ decay of ^{76}Ge . *Physics Letters B*, 256(3-4):559–561, 1991.
- [87] F. T. Avignone III, G. S. King III, and Y. Zdesenko. Next generation double-beta decay experiments: Metrics for their evaluation. *New Journal of Physics*, 7:6, 2005.
- [88] A. Gould K. Freese, J. Frieman. Signal modulation in cold-dark-matter detection. *Physical Review D*, 37:3388, 1988.
- [89] W. Kaminski and A. Faessler. Description of the ground-state pionic double charge exchange reaction on $^{128,130}\text{Te}$. *Nuclear physics. A*, 529(4):605 – 632, 1991.
- [90] David B. Kaplan, Ann E. Nelson, and Neal Weiner. Neutrino oscillations as a probe of dark energy. *Physical Review Letters*, 93:091801, 2004.
- [91] Kareem Kazkaz. *Finding Excited-State Decays of Germanium-76*. PhD thesis, University of Washington, 2006.
- [92] H. V. Klapdor-Kleingrothaus. Neutrino mass from laboratory: Contribution of double beta decay to the neutrino mass matrix. *Nuclear Physics B Proceedings Supplements*, 100:309, 2001, hep-ph/0102276.

- [93] H. V. Klapdor-Kleingrothaus. Reply to a comment of article “Evidence for Neutrinoless Double Beta Decay”, 2002, hep-ph/0205228.
- [94] H. V. Klapdor-Kleingrothaus, A. Dietz, L. Baudis, G. Heusser, I. V. Krivosheina, B. Majorovits, H. Paes, H. Strecker, V. Alexeev, and A. Balysh. Latest results from the HEIDELBERG-MOSCOW double beta decay experiment. *European Physical Journal A*, 12:147, 2001.
- [95] H. V. Klapdor-Kleingrothaus, A. Dietz, I. V. Krivosheina, , and O. Chkvorets. Data acquisition and analysis if the ^{76}Ge double beta experiment in gran sasso 1990 - 2003. *Nuclear Instruments and Methods in Physics Research A*, 522:371, 2004.
- [96] H. V. Klapdor-Kleingrothaus, I. V. Krivosheina, A. Dietz, , and O. Chkvorets. Search for neutrinoless double beta decay with enriched ^{76}Ge in gran sasso 1990 - 2003. *Physics Letters B*, 586:198, 2004.
- [97] H. V. Klapdor-Kleingrothaus, H. Päs, and A. Y. Smirnov. Neutrino mass spectrum and neutrinoless double beta decay. *Physical Review D*, 63:073005, 2001, hep-ph/0003219.
- [98] H.V. Klapdor-Kleingrothaus and Utpal Sarkar. Neutrinoless double beta decay with scalar bilinears. *Physics Letters B*, 554:45, 2003.
- [99] Glenn F. Knoll. *Radiation Detection and Measurement, Third Edition*. John Wiley & Sons, Inc., 111 River St. Hoboken NJ 07030, 2000.
- [100] M. Kortelainen, O. Civitarese, J. Suhonen, and J. Toivanen. Short-range correlations and neutrinoless double beta decay. *Physics letters. B*, 647(2-3):128 – 132, 2007.
- [101] Kenneth S. Krane. *Introductory Nuclear Physics*. John Wiley & Sons, Inc., 111 River St. Hoboken NJ 07030, 1988.
- [102] Isotope Products Laboratories, 2007, <http://www.isotopeproducts.com>.
- [103] O. Lahav. Upper limits on neutrino masses from the 2dFGRS and WMAP: the role of priors. *Journal of Cosmology and Astroparticle Physics*, 2003(04):004, 2003.
- [104] I.-Y. Lee. GRETA - Gamma Ray Energy Tracking Array. In P. Fallon and R. Clark, editors, *Frontiers of Nuclear Structure*, volume 656 of *American Institute of Physics Conference Series*, pages 343–348, March 2003.
- [105] J.D. Lewin and P.F. Smith. Review of mathematics, numerical factors, and corrections for dark matter experiments based on elastic nuclear recoil. *Astroparticle Physics*, 6:87, 1996.
- [106] J. Lindhard, V. Nielsen, M. Scharff, and P. V. Thomsen. Integral equations governing radiation effects. *Matematisk-fysiske Meddelelser udgivet af Det Kongelige Danske Videnskabernes Selskab*, 33:10, 1963.

- [107] V. M. Lobashev, V. N. Aseev, A. I. Belesev, A. I. Berlev, E. V. Geraskin, A. A. Golubev, O. V. Kazachenko, Yu. E. Kuznetsov, R. P. Ostroumov, L. A. Rivkis, B. E. Stern, N. A. Titov, S. V. Zadorozhny, and Yu. I. Zakharov. Direct search for mass of neutrino and anomaly in the tritium beta-spectrum. *Physics Letters B*, 460:227, 1999.
- [108] R. Luescher, J. Farine, F. Boehm, J. Busto, K. Gabathuler, G. Gervasio, H. E. Henrikson, V. Jörgens, K. Lou, and A. Paić. Search for $\beta\beta$ decay in ^{136}Xe : New results from the Gotthard experiment. *Physics Letters B*, 434:407, 1998.
- [109] J.W.F Valle M. Hirsch, J.C. Romão. Bilinear r-parity violating susy: Neutrinoless double beta decay in the light of solar and atmospheric neutrino data. *Physics Letters B*, 486:255, 2000.
- [110] R.N. Mohapatra. New contributions to neutrinoless double-beta decay in supersymmetric theories. *Physical Review D*, 34:3457, 1986.
- [111] K. Muto, E. Bender, and H.V. Klapdor. Nuclear structure effects on the neutrinoless double beta decay. *Zeitschrift fur Physik A*, 334:187, 1989.
- [112] Otto Nachtmann. *Elementary Particle Physics: Concepts and Phenomena*. Springer-Verlag, 1990.
- [113] I. Ogawa. Search for neutrinoless double beta decay of ^{48}Ca by CaF_2 scintillator. *Nuclear Physics A*, 730:215, 2004.
- [114] S. Capelli on behalf of CUORE Collaboration. Cuoricino last results and CUORE R&D, 2005, hep-ex/0505045.
- [115] Committee on Data for Science and Technology, 2007, <http://www.codata.org>.
- [116] Inc. Ortec Ametek, 2007, <http://www.ortec-online.com>.
- [117] G. Pantis, F. Šimkovic, J. D. Vergados, and Amand Faessler. Neutrinoless double beta decay within the quasiparticle random-phase approximation with proton-neutron pairing. *Phys. Rev. C*, 53(2):695–707, Feb 1996.
- [118] H. Päs, M. Hirsch, and H.V. Klapdor-Kleingrothaus. Improved bounds on susy accompanied neutrinoless double beta decay. *Physics Letters B*, 459:450, 1999.
- [119] Presentation from CINPAP 2006 Petr Vogel. Double beta decay outlook, referenced as “Private communication from Nowacki, *et al*, 2007.
- [120] A. Piepke. New techniques: EXO, MOON and SuperNEMO, presented at Neutrino 2006, 2006.
- [121] G. Prézeau, M. Ramsey-Musolf, and Petr Vogel. Neutrinoless double β decay and effective field theory. *Physical Review D*, 68:034016, 2003.

- [122] Gary Prézeau. Light neutrino and heavy particle exchange in $0\nu\beta\beta$ -decay. *Physics Letters B*, 633:93, 2006.
- [123] Norbert Rempe. Personal communication, 2004.
- [124] P. Ring and P. Schuck. *The Nuclear Many-Body Problem*. Springer-Verlag, New York, NY, 1980.
- [125] V. A. Rodin, Amand Faessler, F. Šimkovic, and Petr Vogel. Assessment of uncertainties in QRPA $0\nu\beta\beta$ -decay nuclear matrix. *Nuclear Physics A*, 766:107, 2006.
- [126] V.A. Rodin, A. Faessler, F. Šimkovic, and P. Vogel. Uncertainty in the $0\nu\beta\beta$ decay nuclear matrix elements. *Physical Review C*, 68:044302, 2003.
- [127] C. Saji. SK atmospheric neutrinos, 10–15 February, 2004.
- [128] X. Sarazin. Search for neutrinoless double beta decay with the NEMO-3 detector: First results. *Nuclear Physics B Proceedings Supplements*, 143:221, 2005, hep-ex/0412012.
- [129] J. Schechter and J.W.F. Valle. Neutrinoless double- β decay in $SU(2)\times U(1)$ theories. *Physical Review D*, 25:2951, 1982.
- [130] S. Schönert. New techniques in $0\nu\beta\beta$ germanium experiments, presented at Neutrino 2006, 2006, hep-ex/0404039.
- [131] J. R. Schrieffer. *Theory of superconductivity*. W. A. Benjamin, New York, NY, 1964.
- [132] J. Simpson. The euroball spectrometer. *Zeitschrift für Physik. A, Hadrons and nuclei*, 358(2):139 – 143, 1997.
- [133] J. Simpson. The agata project. *Journal of Physics - Conference Series*, 41(1):72 – 80, 2006.
- [134] S. Stoica and H.V. Klapdor-Kleingtrothaus. Neutrinoless double- β -decay matrix elements within the second quasirandom phase approximation method. *Physical Review C*, 63:064304, 2001.
- [135] J. Suhonen. Nuclear matrix elements of $\beta\beta$ decay from β -decay data. *Physics Letters B*, 605:87, 2005.
- [136] J. Suhonen and O. Civitarese. Weak-interaction and nuclear-structure aspects of nuclear double beta decay. *Physics Reports*, 300:123, 1998.
- [137] The Sloan Digital Sky Survey, 2007, <http://www.sdss.org>.
- [138] T. Tomoda. $0^+ \rightarrow 2^+ 0\nu\beta\beta$ decay triggered directly by the majorana neutrino mass. *Physics Letters B*, 474:245, 2000.

- [139] F. Šimkovic, L. Pancearscu, and A. Faessler. Two-neutrino double beta decay of ^{76}Ge within deformed QRPA. *Nuclear Physics A*, 733:321, 2004.
- [140] F. Šimkovic, G. Pantis, J.D. Vergados, and A. Faessler. Additional nucleon current contributions to neutrinoless double β -decay. *Physical Review C*, 60:055502, 1999.
- [141] F. Šimkovic, A. A. Raduta, M. Veselský, and Amand Faessler. Quasiparticle random phase approximation with inclusion of the pauli exclusion principle. *Phys. Rev. C*, 61(4):044319, Mar 2000.
- [142] F. Šimkovic and A. Faessler. Distinguishing the 0nbb-decay mechanisms. *Progress in Nuclear and Particle Physics*, 48:201, 2002.
- [143] Ch. Weinheimer, B. Degenndag, A. Bleile, J. Bonn, L. Bornschein, O. Kazachenko, A. Kovalik, and E. W. Otten. High precision measurement of the tritium β spectrum near its endpoint and upper limit on the neutrino mass. *Physics Letters B*, 460:219, 1999.
- [144] A. Wodecki, W. Kamiński, and F. Šimkovic. Grand unified theory constrained supersymmetry and neutrinoless double β decay. *Physical Review D*, 60:115007, 1999.
- [145] Y. G. Zdesenko, F. A. Danevich, and V. I. Tretyak. Has neutrinoless double β decay of ^{76}Ge been really observed? *Physics Letters B*, 546:206, 2002.
- [146] K. Zuber. COBRA-double beta decay searches using CdTe detectors. *Physics Letters B*, 519:1, 2001.
- [147] Kai Zuber. Consensus report of a workshop on “matrix elements for neutrinoless double beta decay”, 2005, nucl-ex/0511009.

Appendix A

DARK MATTER SENSITIVITY OF THE MAJORANA EXPERIMENT

We present a summary of the estimation of the dark matter sensitivity of the MAJORANA $\beta\beta$ decay experiment. While the MAJORANA project’s main science goal is the measurement of the absolute mass scale of the electron neutrino, it has been suggested that the technical problems to be overcome in building a next-generation $\beta\beta$ decay experiment are similar to the technical problems in the development of a next-generation dark matter experiment. We present a detailed analysis of the sensitivity of the MAJORANA project for a variety of experimental configurations for both the “signal to noise” and “annual modulation” limits, along with a comparison to past, present and projected future dark matter searches.

A.1 Expected Nuclear Recoil Spectrum From the WIMP Halo

The first step in estimating the sensitivity of any experiment comes in the understanding the characteristics of the signal for which it will be searching. First and foremost, for any WIMP search, the experimenter must be able to measure nuclear recoils rather than (or in addition to) electron recoils since basically all dark matter halo models call for an electrically neutral WIMP. For a complete derivation of the form of the expected nuclear recoil spectrum from a detector’s interactions with a given WIMP halo, see Reference [105] (from which the following treatment is largely taken).

We assume a Maxwellian (*i.e.* thermal) WIMP velocity distribution for the dark matter halo of our galaxy:

$$f(v, v_E) = e^{-\frac{(v+v_E)^2}{v_0^2}} \tag{A.1}$$

Where v is the velocity of an individual WIMP, v_E is the velocity of the Earth relative to the center of the galaxy, and v_0 sets the width of the velocity distribution. Since the mass of any reasonable WIMP candidate gravitationally bound to a galaxy is much greater than its kinetic energy, we assume it is moving non-relativistically and therefore has energy quadratic in its velocity. This gives us an energy spectrum exponential in energy:

$$\frac{dR}{dE_R} = \frac{R_0}{E_0 r} e^{-\frac{E_R}{E_0 r}} \tag{A.2}$$

Where E_R is the energy of the recoiling nucleus, R_0 is the absolute rate of WIMP interactions neglecting the motion of the Earth and the escape velocity of the galaxy (which are surprisingly good approximations for simply capturing the rough shape of the spectrum), E_0 is the energy of a WIMP with velocity v_0 and r is a simple kinematic factor. The absolute rate R_0 from Equation A.2 is most conveniently expressed as:

$$R_0 = \frac{2}{\sqrt{\pi}} \frac{N_0}{A} \frac{\rho_D}{M_D} \sigma_0 v_0 \quad (\text{A.3})$$

Where N_0 is Avogadro's number, A is the atomic weight of the target nucleus, ρ_D is the local density of WIMPs in the galactic halo, M_D is the WIMP mass, σ_0 is the interaction cross section per nucleus, and v_0 is again the scale velocity of the WIMP halo. The kinematic factor from Equation A.2 is:

$$r = \frac{4M_D M_T}{(M_D + M_T)^2} \quad (\text{A.4})$$

Where M_D is again the WIMP mass and M_T is the mass of the target nucleus.

When one includes the motion of the Sun and Earth in the form of the dark matter spectrum (vitaly important for performing any annual modulation analysis), the expression becomes the difference of two error functions:

$$\frac{dR}{dE_R} = \frac{R_0}{E_0 r} \frac{\sqrt{\pi}}{4} \frac{v_0}{v_E} \left[\text{erf} \left(\frac{v_{min} + v_E}{v_0} \right) - \text{erf} \left(\frac{v_{min} - v_E}{v_0} \right) \right] \quad (\text{A.5})$$

Where v_{min} is the velocity corresponding to the minimum WIMP energy able to impart a recoil energy E_R (i.e. in a direct, head-on collision or zero impact parameter). The expression used for v_E is a simple constant plus sine wave for the motion of the Sun around the galaxy plus the projection of the Earth's orbital velocity around the Sun:

$$v_E \approx (244 + 15 \sin(2\pi y)) \frac{km}{s} \quad (\text{A.6})$$

Where y is the time in years since March 2. The time is measured from this date because that is the date corresponding to the phase in Equation A.6 equaling zero. This means that it is on which the Earth's velocity around the sun is perpendicular to the Sun's velocity around the center of the galaxy, that the projection of these two velocities has a positive derivative (i.e. Earth's velocity around the Sun is most closely aligned with that of the Sun around the center of the galaxy on June 2).

To also include the effect of the finite escape velocity of the galaxy, one simply adds in a small correction effectively truncating the velocity distribution at v_{esc} (≈ 600 km/s at the location of the Earth/Sun system). This effect is quite small (less than 1% between 0 and 100 keV). Many performing this analysis prefer to use the simple exponential form of Equation A.2 with two sinusoidally

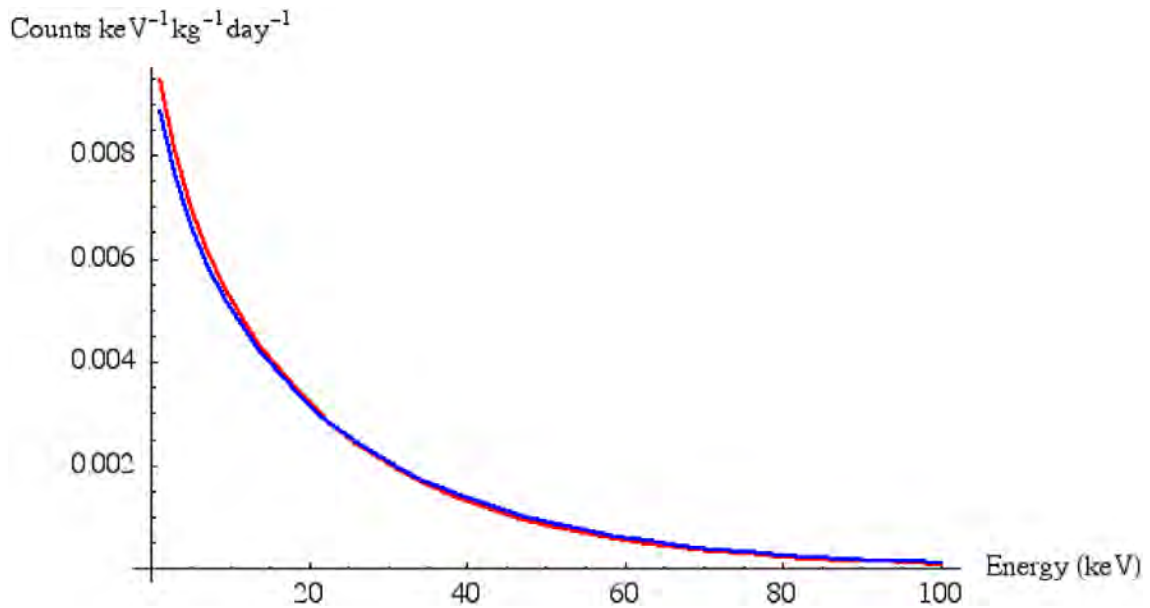


Figure A.1: Summer (red) and Winter (blue) WIMP nuclear recoil spectra including quenching and finite nuclear radius for a WIMP mass $M_D = 100$ GeV and a cross section per nucleon of 3×10^{-43} cm².

modulating correction factors (one in the amplitude of the exponent and one in its argument) to include annual modulation effects. Although the difference in spectral shape is never greater than 1% over the region of interest, it can simplify the analytical form of the WIMP spectrum. This technique is most use to those using a high-level programming language (like C++ or FORTRAN). Since the analysis presented in this report was performed with Mathematica, in which complicated analytical expressions can be constructed easily, the form in Equation A.5 was used in this exercise.

We also multiply in correction factors for finite nuclear radius and nuclear recoil quenching. For a more complete discussion of nuclear recoil quenching, see Reference [106] rather than Reference [105] as Reference [105] has several numerical errors in some of the constants. Last, we renormalize the spectrum so that the absolute rate (the energy integral of the spectrum) is still R_0 . The final version of the spectrum we work with is shown in Figure A.1. The y-axis of figure A.1 is measured in counts/keV/kg/day. This is also called “differential rate units,” or “dru.”

A.2 Explored Experiment Configurations

For much of our design for the MAJORANA experiment, we have used results from the IGEX experiment as a benchmark. We have used this strategy for our dark matter sensitivity as well.

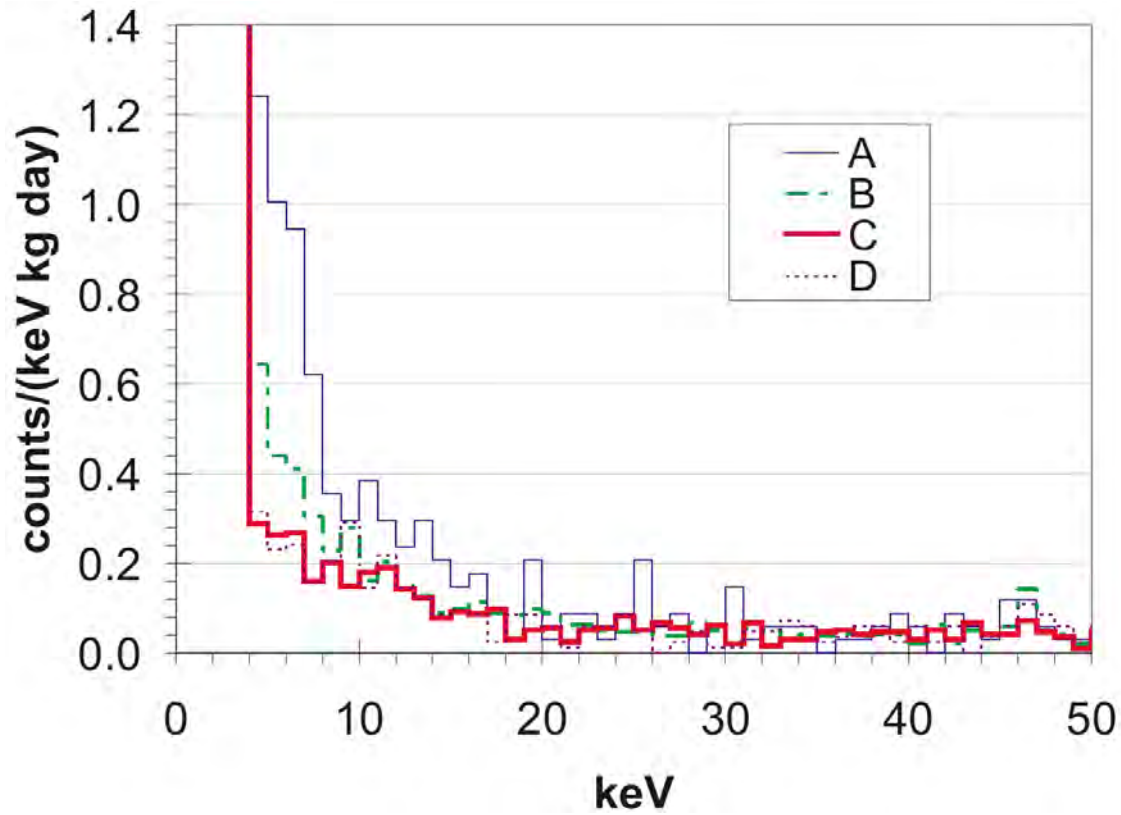


Figure A.2: Results from a neutron moderation study for the dark matter limit in the IGEX experiment. The four curves on the plot correspond to different thicknesses of the neutron moderator in the IGEX shield: (A) no neutron moderator, (B) 20 cm neutron moderator, (C) 40 cm neutron moderator and (D) 80 cm neutron moderator. Curves B and C were actually IGEX production data, and curves A and D were taken later to study neutron backgrounds. The similarity between curves C and D was taken as evidence that the IGEX experiment had eliminated slow neutron backgrounds in their dark matter production data.

There are four main parameters of the experimental configuration varied in this exercise: energy threshold, background level at threshold, asymptotic background level (*i.e.* above ≈ 20 keV), and active mass of germanium. The total parameter space explored can be found in Table A.1.

Table A.1: Experimental parameters used in the calculation of MAJORANA dark matter sensitivity. Text in blue denotes the configuration of the IGEX experiment.

Experimental Parameter	Values Studied
Energy Threshold (keV)	1.0, 4.0 , 10.0
Background at Threshold ($\frac{\text{counts}}{\text{keV kg day}}$)	0.03, 0.06, 0.09
Asymptotic Background ($\frac{\text{counts}}{\text{keV kg day}}$)	0.05 , 0.005
Active Mass (kg)	20, 120, 500

Of particular interest are the active masses used in these calculations as they correspond to proposed phases of the MAJORANA experiment. MEGA will have an active mass of about 20 kg, the mid-scale M-120 proposal has an active mass of 120 kg, and the full proposal of the MAJORANA experiment has an active mass of 500 kg. It is also important to note that a background level of 0.6 dnu corresponds to only a few (3–4) days above ground for the detectors after zone refinement, due to rate at which ^3H is cosmogenically produced.

A.3 MAJORANA *Sensitivity: Signal to Noise*

To calculate an experimental configurations “Signal to Noise” sensitivity, we simply set the expected signal at threshold integrated over the exposure of the experiment equal to the expected background at threshold integrated over the course of the experiment plus two standard deviations (for a 90% confidence level):

$$M_{Active} \int dt \frac{dR}{dE_R}(E_R, M_D, \sigma_N, t) \Big|_{E_R=E_{Thr}} = M_{Active} \int dt Bg(t) + 2\sqrt{M_{Active} \int dt Bg(t)} \quad (\text{A.7})$$

Where M_{Active} is the active mass of the experiment, E_{Thr} is the energy threshold, and $Bg(t)$ is the background at threshold as a function of time. For this exercise, we used a constant background. The sensitivity curve is then obtained by solving for the cross section per nucleon as a function of WIMP mass.

The resulting sensitivities are largely insensitive to the amount of active mass, and strongly dependent on threshold and background, as seen in Figure A.3. The first and perhaps most important

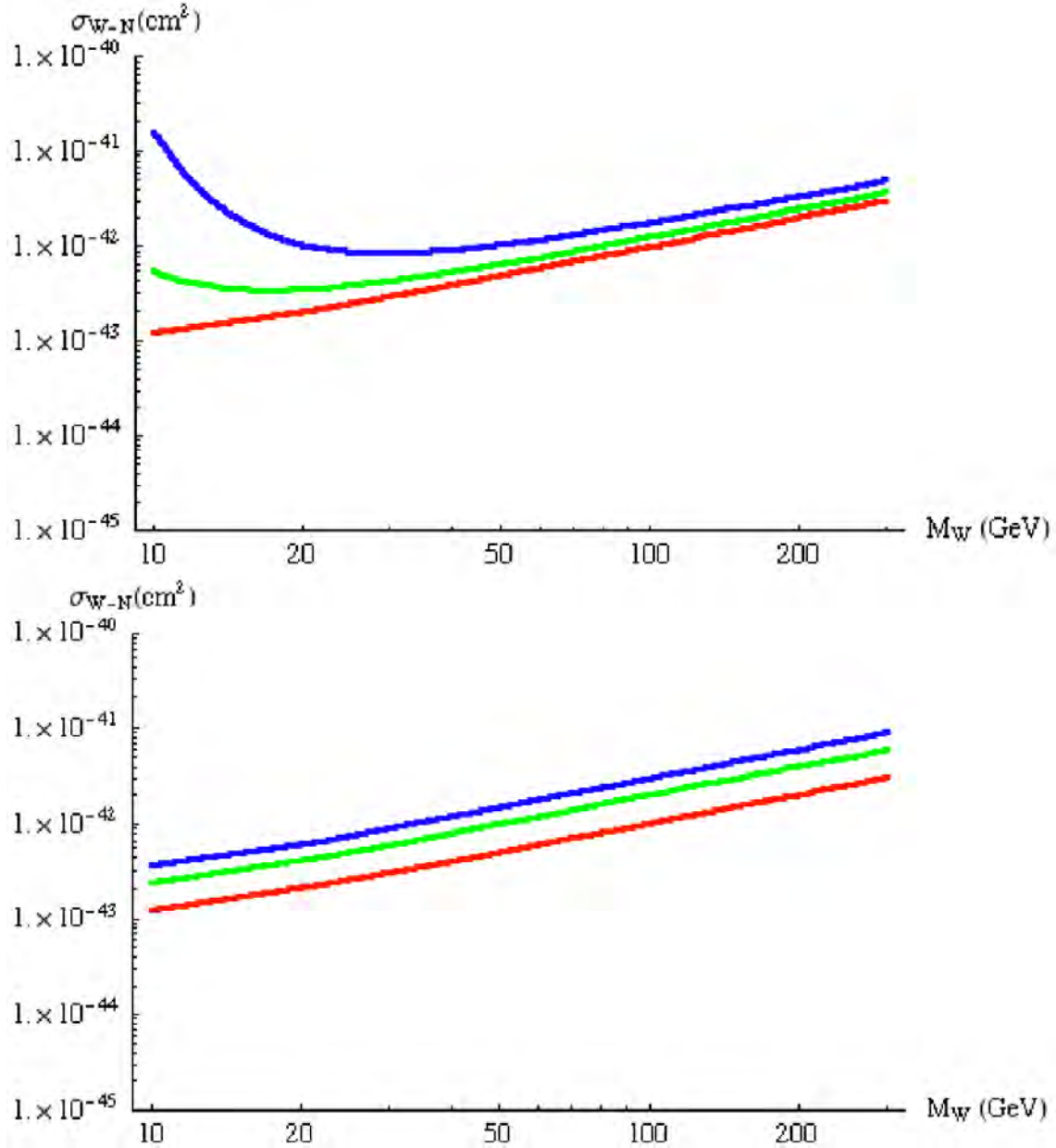


Figure A.3: (Top) Signal to noise sensitivities for the MAJORANA detector with a threshold of 1 keV (red), 4 keV (green) and 10 keV (blue). (Bottom) Signal to noise sensitivities for the MAJORANA detector with a background at threshold of 0.03 dru (red), 0.06 dru (green) and 0.09 dru (blue).

feature of the top panel of Figure A.3 is the fact that at WIMP masses above ≈ 50 GeV the signal to noise sensitivity is largely independent of threshold, and that the difference between 4 and 10 keV is much more important than that between 4 and 1 keV. While it is true that detectors with lower stable thresholds are in general better detectors at all energies, these sensitivity curves show that for the dark matter measurement, it is not “mission critical” to push the threshold all the way down to 1 keV for all detectors in the MAJORANA array. Next, the signal to noise sensitivity scales directly with the background at threshold, therefore a reduction of background by a factor of two will lead to an increase by that same factor in the signal to noise sensitivity of the experiment. This fact coupled with the relative invariance of the signal to noise sensitivity to the active mass of the detector bodes well for the use of a fiducial volume cut in the MAJORANA array as a way to boost our signal to noise sensitivity.

A.4 MAJORANA Sensitivity: Annual Modulation

The method used to extract the annual modulation sensitivity for different MAJORANA configurations is discussed in greater detail in Reference [88]. This method looks for modulation in the rate in the entire dark matter region of interest. The first step is, of course to integrate the spectrum over this energy window. This leaves us a rate in $\frac{\text{counts}}{\text{kg day}}$ (or “integrated rate units,” iru) as a function of time.

$$N(M_D, \sigma_N, t) = \int_{E_{Lo}}^{E_{Hi}} dE_E \frac{dN}{dE_R}(E_R, M_D, \sigma_N, t) \quad (\text{A.8})$$

For these calculations, we used time bins of one month.

The next step is to multiply the rate as a function of time by a sine wave of ω and ϕ consistent with the expected annual modulation, then integrate in time over the duration of the experiment as well.

$$X(M_D, \sigma_N) = \int dt N(M_D, \sigma_N, t) \sin(\omega t - \phi) \quad (\text{A.9})$$

This step is analogous to the use of a “Lock-In Amplifier” to project out the component of a signal with a particular phase and period. We then use the quantity $X(M_{WIMP}, \sigma_{W-N})$ calculated in Equation A.9, normalized by its uncertainty (again assuming Poisson statistical fluctuations to be the leading source of experimental uncertainty) as a figure of merit for the strength of the annual modulation signal. Once we have this figure of merit, we simply step through a set of interesting WIMP masses and increment the WIMP-nucleon cross-section until it is high enough to yield an annual modulation figure of merit corresponding to a 90% confidence level.

There is however a subtlety in this analysis that can cause problems if not properly addressed. Let us again examine the summer/winter plot of the dark matter nuclear recoil spectrum in Figure

A.1. Note the turning point at ≈ 25 keV. At energies lower than this turning point, the rate is higher in summer, and at higher energies it is higher in the winter. This turning point is dependent on the WIMP mass and is calculable from first principles given a dark matter halo model. If the energy analysis window extends on either side of the turning point, the annual modulation signal is suppressed because the energy integral gives contributions with opposite signs from either side. The solution to this problem is quite simple. We calculate the turning point and break the energy analysis window into low and high-energy regions on either side, and then sum the two figures of merit. We perform a similar analysis to that for the signal to noise limit, varying the threshold and background level (this time the background is examined at its “asymptotic” level *i.e.* above ≈ 20 keV). We note a similar structure to the signal to noise limit with regard to the threshold and background levels. Lower threshold gives a better sensitivity at low WIMP mass and little gain above about 50 GeV. Note also that the background level causes the sensitivity to scale similar manner to the signal to noise limits. Also of great importance to the experiment is the active mass available. This comes from the fact that we are not trying to see an absolute rate, but a change in that rate. If the absolute rate is higher, the modulation will be higher as well, making it easier to see. As one might expect, more active mass increases the experiments annual modulation sensitivity.

A.5 Comparison to Other Experiments

An important part of the decision whether or not to allocate significant resources to making a dark matter measurement is its competitiveness with other experiments. Rather than describing these sensitivity curves in great detail, it is more instructive to simply show the sensitivity of a sample of other experiments and draw some conclusions in Section A.6.

A.6 Conclusions

First and foremost it is important to recognize that the MAJORANA detector is not going to exist for at least four to five years, and consequentially, we are not competing against the state of the art detectors now (in the same range as the CDMS result from 2004). We are instead competing against the what the state of the art will be five to ten years from now (in the same range or better than the CDMS II projections). It is also vitally important to keep in mind that the annual modulation sensitivity for the MAJORANA experiment was calculated using very optimistic background assumptions. For instance it was assumed that there was no change in threshold or background in the experiment. It was also assumed that the differential nonlinearity of our ADC systems was perfectly well known and would contribute no systematic error to the count rate in the dark matter region of interest.

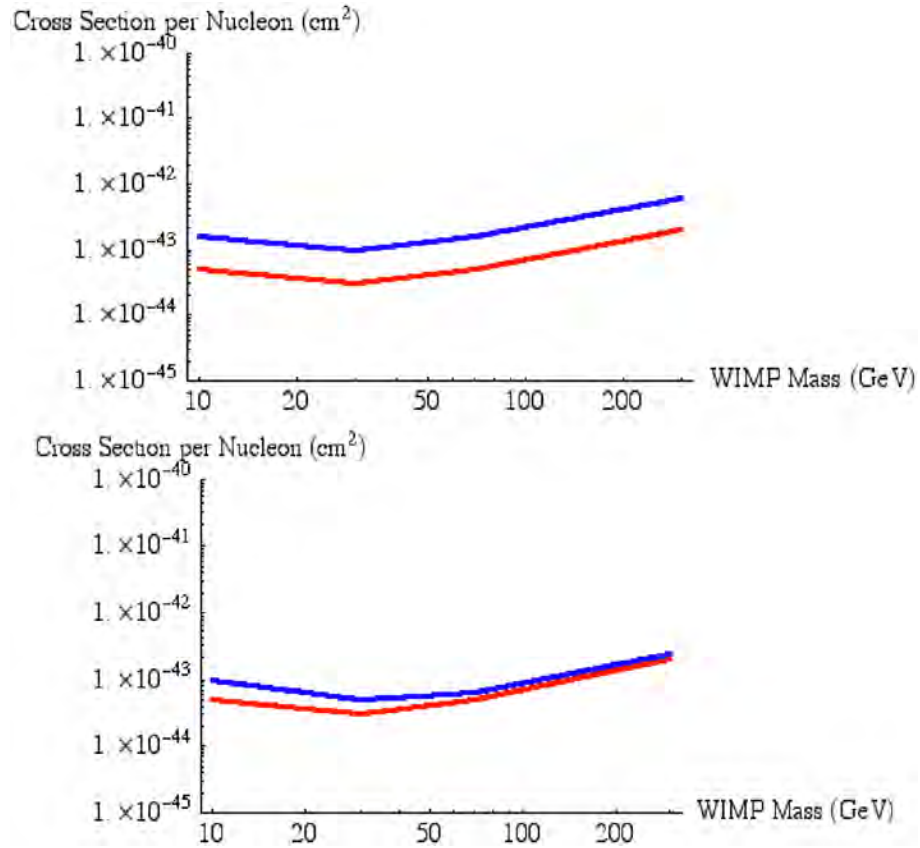


Figure A.4: (Top) Annual modulation sensitivity for thresholds of 1 keV (red) and 4 keV (blue). (Bottom) Annual modulation sensitivity for asymptotic background levels of 0.005 dru (red) and 0.05 dru (blue).

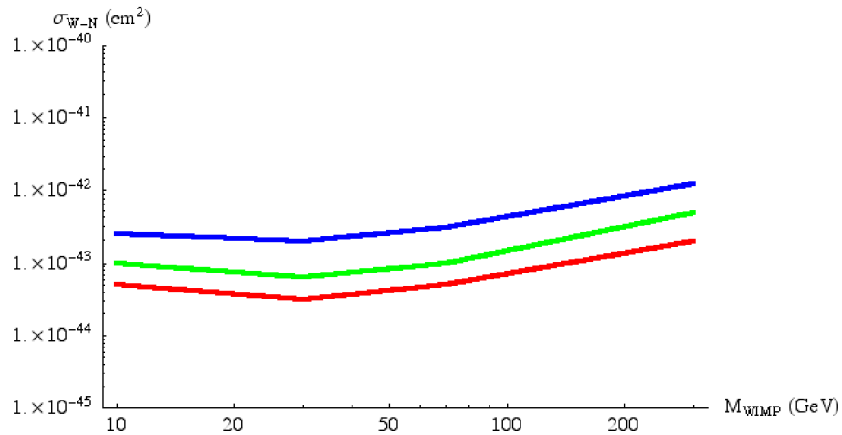


Figure A.5: Annual modulation sensitivity for active detector masses of 500 kg (red), 120 kg (green) and 20 kg (blue).

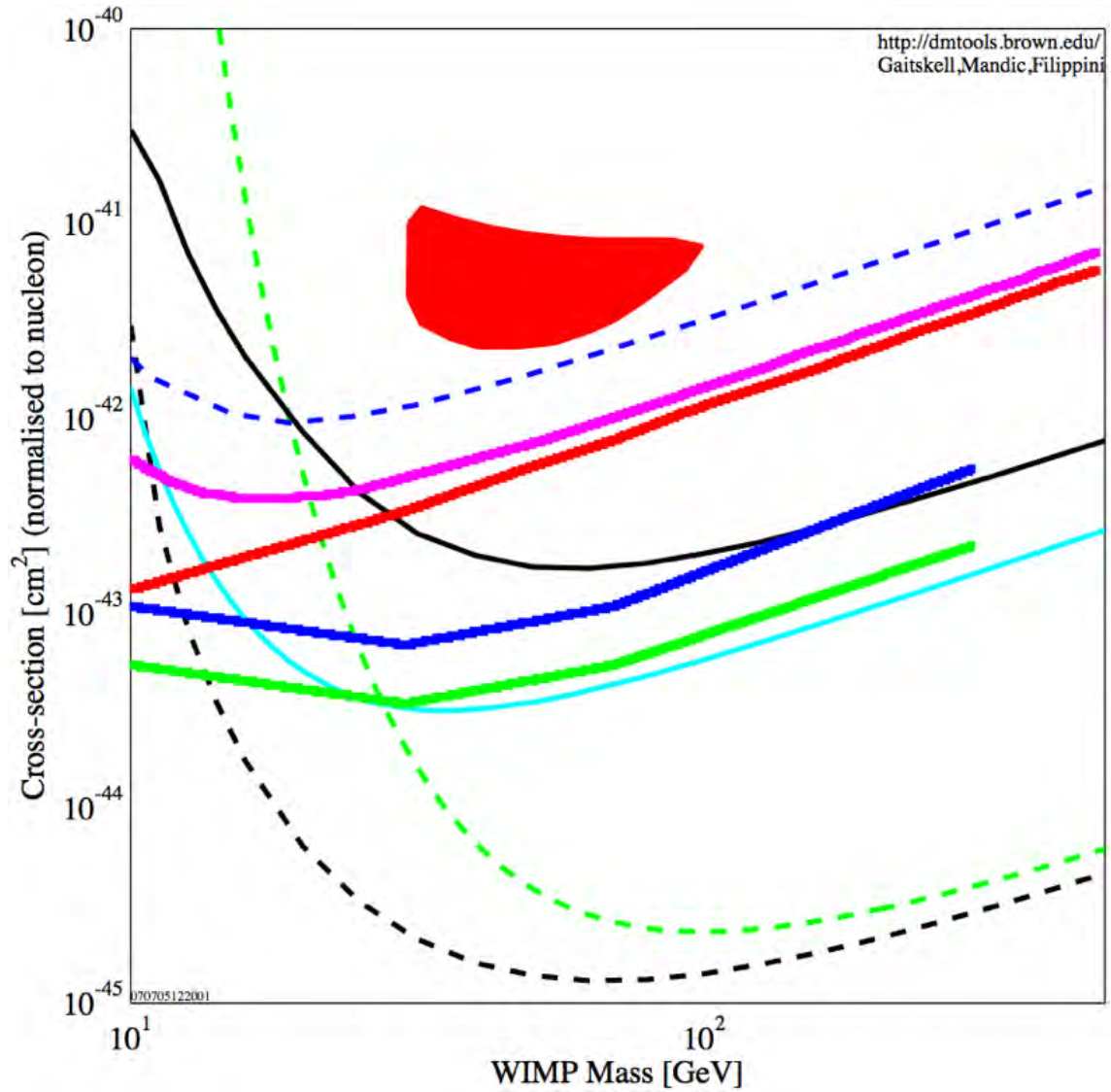


Figure A.6: A variety of dark matter sensitivities from experiments around the world: CDMS 2004–2005 7 keV threshold (black line), SuperCDMS projected sensitivity at SNOLab (black dash), Cuoricino projected sensitivity (blue dash), XENON10 136 kg d (cyan line), XENON100 projected (green dash), DAMA 3σ result-58000 kg days exposure (red fill), MAJORANA signal to noise sensitivity for thresholds of 1 keV (red line) and 4 keV (magenta line), and MAJORANA annual modulation sensitivity for active masses of 120 kg (blue line) and 500 kg (green line).

Effects such as these will serve only to degrade our annual modulation sensitivity, which is only barely competitive with the next generation of dark matter experiments to begin with.

While the annual modulation limit has many systematic uncertainties that will take many person-years of time and effort to fully characterize, the signal to noise limit depends only on the levels of the threshold and background and not on their stability over a sidereal year. Much of the work required to push the threshold and background levels down to those required for the sensitivities depicted in Figure A.6 has to be done for other aspects of the experiment as well (both are important for the use of x ray coincidences to reject ^{68}Ge decays). The assumptions made to calculate the signal to noise sensitivities are also quite conservative by comparison to those required for the annual modulation analysis. It is also of great importance to notice that the signal to noise sensitivities are only about one order of magnitude worse than those for the annual modulation even under these rather conservative assumptions.

It is therefore logical to conclude that the signal to noise measurement really is a limit on dark matter detection that we get essentially “for free,” that is there is little or no work outside of that necessary for other aspects of the experiment required. The annual modulation analysis, on the other hand, would require a significant commitment from the collaboration and would not buy a commensurate improvement in sensitivity.

Appendix B

PREAMP EVALUATIONS FOR SEGA, MEGA AND MAJORANA

B.1 Introduction

The MAJORANA Experiment is a search for neutrinoless double-beta ($0\nu\beta\beta$) decay. We will use high-purity germanium detector diodes to search for the specific signatures of the localized double-beta signal. MAJORANA also plans to use segmented germanium crystals isotopically enriched to 86% ^{76}Ge . There are two feeder experiments to MAJORANA, one being the Segmented Enriched Germanium Assembly (SEGA). SEGA uses a single segmented, isotopically enriched crystal. The other feeder experiment is the Multi-Element Germanium Assay (MEGA), which will use 18 unenriched, unsegmented germanium crystals.

These two feeder experiments as well as the full MAJORANA setup require data be read out from the segments of the germanium crystals using charge-collecting preamplifiers. We have identified five candidate preamps for evaluation, the best of which will be used in the experiments.

B.2 Preamp Requirements

We have two make-or-break requirements for preamp performance. One is preamp response time and the other is single-constant decay to baseline. Both of these requirements are based on the necessity of using Pulse Shape Discrimination to differentiate between the double-beta decay signal and background events.

The digitizing hardware we have identified for use is the XIA DGF4C. This card runs at 40 MHz, which translates to a 25 ns period between samples. The highest frequency we can therefore measure (based on the Nyquist frequency of the DGF4C) is 20 MHz. Our preamps must therefore have a 10%-90% response time to an input pulse of 50 ns.

The software used in measuring the pulse amplitudes includes a correction for ballistic deficit. This correction relies on the preamp exhibiting an exponential decay in the pulse back to baseline with a single time constant in the exponent. This single time constant decay is an absolute necessity for any preamp used in these double-beta decay experiments.

B.3 Supplemental Performance Criteria

We can compare the preamps that pass the basic requirements of Section B.2 on the basis of other performance criteria that do not have a sharp division between acceptance and rejection of the preamp. In no specific order, these criteria are ripple amplitude, ripple frequency, bandwidth, nonlinearity, FET operating points, energy resolution, and cost.

Figure B.1 shows a typical oscilloscope trace of a test input pulse, preamp response, and Fourier transform of the response. The ripple amplitude and period may interfere with the calculation of the response pulse height, and must both therefore be as small as possible. The bandwidth in part governs the speed of response of the preamp, and the bandwidth should be as high as possible to achieve the fastest response time possible. The preamp response must be as linear as possible in the energy input, as deviations from linearity will require more complicated calibrations than a straightforward linear response. Energy resolution is valuable for differentiating background events from $0\nu\beta\beta$ events, and poor energy resolution will require greater statistics. Given an event rate sensitivity of roughly a single event per year, the barrier to acquiring greater statistics is formidable.

The FET will be driven differently for each model of preamp. Some preamps include the capability to adjust the FET operating points: the FET voltage and the FET current. The heat generated by the FET is a function of these operating points. Given that the FET is inside the cryostat, a FET with a lower heat load is desirable.

Finally, if two or more preamps display characteristics that are equivalent from a performance basis, we may choose a preamp based on cost. A one-tonne MAJORANA would use thousands of preamps, so cost comparison may provide a clear choice where performance could not.

B.4 Crystal Characterization

Our test bed setup had the preamps attached to a PGT IGC30 HPGe detector. A fair amount of time had to be spent documenting the crystal behavior. Any anomalous behavior of the crystal may show up in the preamp evaluation, and this crystal-specific documentation may help to separate crystal behavior from preamp behavior. The three measurements of the crystal are depletion voltage, capacitive load, and leakage current.

A depletion region within a diode crystal will grow with reverse bias voltage. As the crystal depletion region grows, the resolution and centroid of any given gamma source peak may fluctuate. When the centroid and resolution no longer change with an increase of bias voltage, the crystal is assured to be fully depleted. Once we know a crystal is fully depleted, we may calculate the capacitance of the crystal. Unfortunately, increasing the reverse bias of the crystal too much can

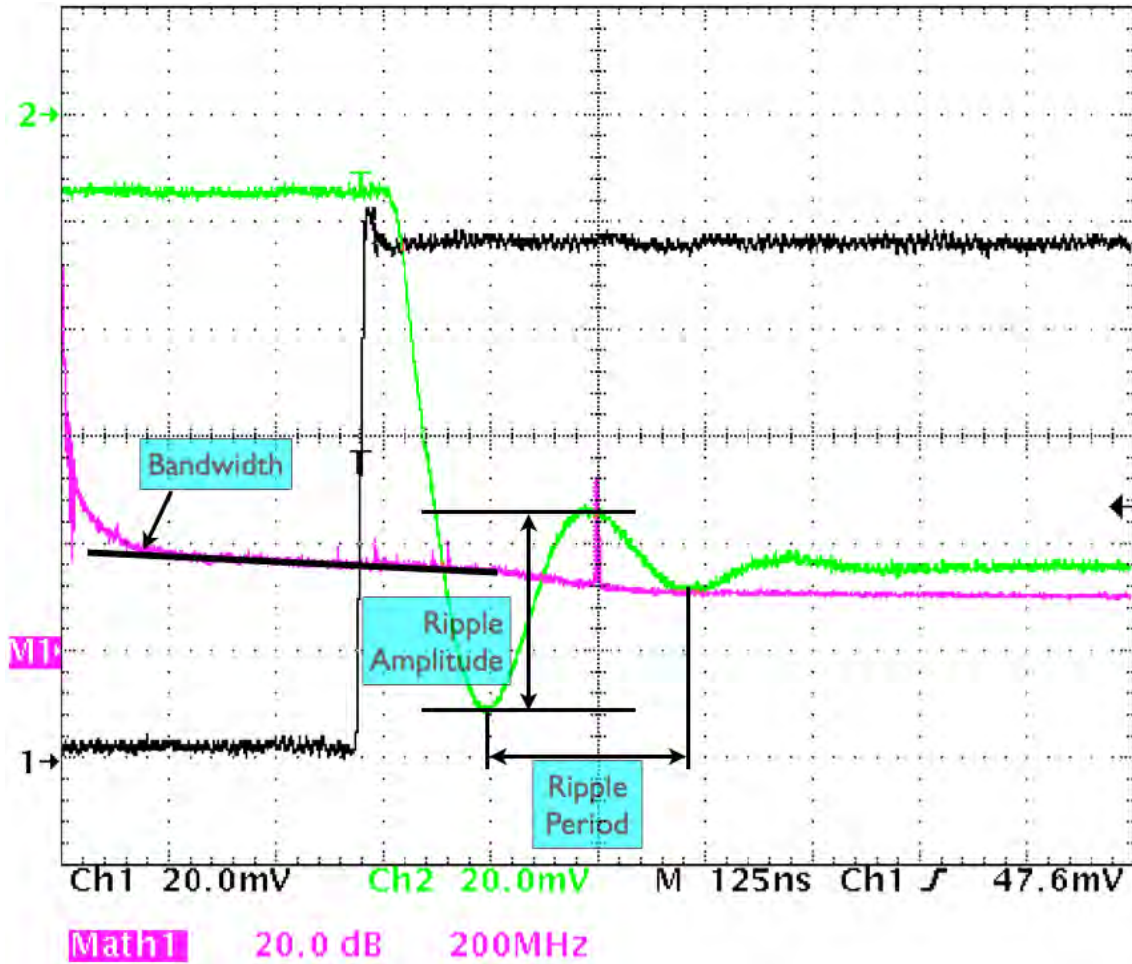


Figure B.1: Oscilloscope trace of a PGT RG-11 preamplifier. This trace shows the typical aspects of a preamp trace relevant to evaluation. The black trace is the input pulse, the green trace is the preamp response, and the purple trace is the Fourier transform of the preamp response. The bandwidth is measured at the point the Fourier transform transforms from $1/f$ to linear.

damage the surface of the crystal. To insure the quality of a crystal diode is high enough to hold a large reverse bias, a leakage current curve is measured. Leakage current increases linearly with reverse bias up to a breakdown point, where leakage current will grow faster than exponentially with bias. The crystal bias must be kept below this runaway voltage. Ideally, a crystal will be fully depleted before the runaway voltage is attained.

To start our measurements, we first run a leakage current curve on our crystal. The PGT ICG30 detector has five wires coming out of the cryostat, connected to the high voltage bias (green), the FET source, (yellow) the FET drain (violet), the preamp feedback circuit (red), and the test input (white). Disconnecting the yellow, violet, and white wires forces all electricity to flow from high voltage through the feedback components. With nothing connected to the bias input, the red wire can be used to measure the leakage current.

There is a slight complication. The feedback components are a capacitor and a resistor connected in parallel with each other, and in series with the crystal (see Figure B.2). As the leakage current settles down to a constant value, the effect of the feedback capacitor can be ignored. The feedback resistor, however, can be somewhat sizeable—nominally 2 G Ω . The effects of the feedback resistor must be taken into account (or assured to be negligible) when measuring the leakage current. We do not, after all, want to measure the bias dependence of the feedback components on the current, but the bias dependence of the crystal diode.

To measure the leakage current, we use a Keithley model 410 “Micro-MicroAmmeter”. Unfortunately (or perhaps fortunately), we are unable to measure any appreciable, stable leakage current greater than 4 pA even though we run the bias up to the manufacturer-recommended +3500 V. Not trusting this result, we use an HP 3458A digital multimeter to measure the leakage current, with the same results (unstable leakage current that does not appreciably go above 4 pA). We determine that the crystal is simply of very high quality. This still leaves the question of whether the feedback resistor is contributing too much to the resistance of the circuit. Assuming the crystal plays no role in limiting the leakage current, a bias of +3500 V applied across 2 G Ω results in a current of 1.76 μ A. Since our leakage current is roughly three orders of magnitude lower than this, we can be assured that the crystal dominates the circuit resistance, and therefore the leakage current. We are now assured of safely running the bias voltage to at least +3500 V. Previous experience with HPGe crystals tells us we may safely run the bias up beyond +3500 V, as we must to verify the PGT-recommended +3500 V depletion voltage. We reconnect the preamp connections and tape a ^{137}Cs source to the end of the crystal. The ^{137}Cs source provides a very strong gamma decay peak at 662 keV. We start with a bias voltage of +100 V and increment the bias in 100 V steps.

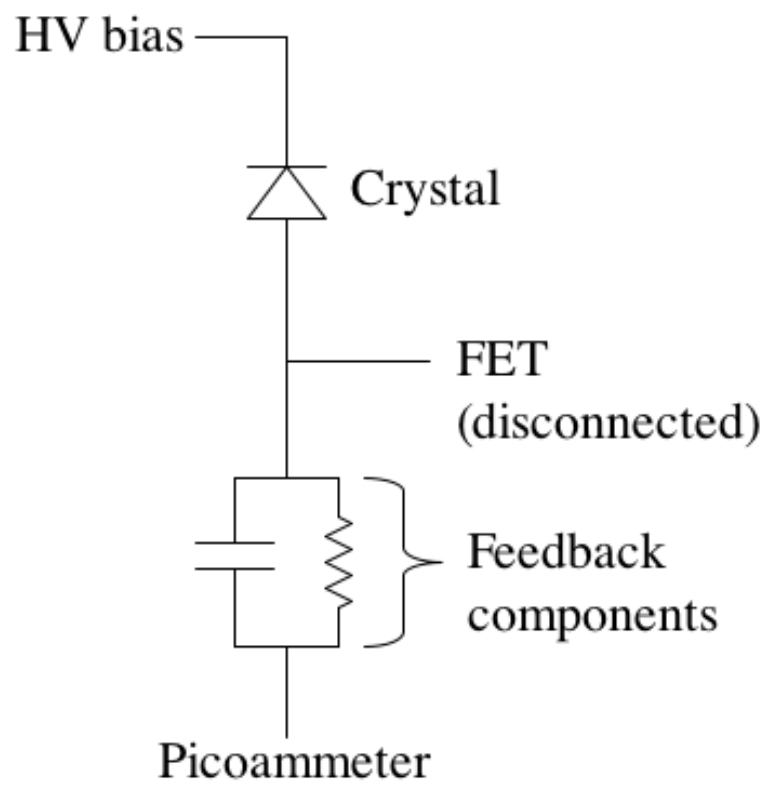


Figure B.2: Leakage current schematic. The crystal is in series with both feedback components, which are in parallel with each other. In a steady-state situation, the effects of the feedback capacitor can be ignored.

We run the output of the preamp into an Ortec 673 Spectroscopy Amplifier and from there into a Canberra Series 35+ pulse height analyzer (PHA). For every bias voltage setting, we collect data for 180 seconds. We then fit a Gaussian distribution curve to the ^{137}Cs peak, and record the centroid and the FWHM in channels (*i.e.* without energy calibration).

The value of the calculated resolution is strongly dependent on the choice of channel window. To insure reproducibility, we decide to alter the Gaussian fit window until it is consistent with a 3σ deviation from the centroid. Still, the windows only tend to be roughly 6 channels wide, and rounding effects play a very noticeable role in the centroid measurement, leading to what appears to be quantized behavior in the centroid curve. We justify our determination of full depletion, however, by looking for no further change in the centroid with increase in bias voltage, as visible in Figure B.3.

Now that the crystal is certain to be fully depleted, we calculate the capacitance of the crystal and leads coming off the FET to determine the impedance of the circuit. Using typical coaxial crystal dimensions of an inner radius of 1 cm, an outer radius of 6 cm, and 7 cm in length gives (with a germanium dielectric constant of 16) a capacitance of about 35 pF. Because we are using a cold FET and a warm preamp, there is about two feet of coaxial cable (13 pF/ft) in parallel with the crystal, giving a total capacitive load of about 50-60 pF.

B.5 Testing methods

We need to test the preamps in a reliable fashion under conditions that are idealized, reproducible, and more extreme than what the preamps will have to contend with when taking actual data.

We start with the waveform generator. We want the pulse to have the following qualities:

- Amplitude roughly equal to that created by a 2 MeV event (we are looking for events at the endpoint energy of double-beta decay from ^{76}Ge : 2039 keV). Energy calibrations on the detector put a 100 mV input pulse at 1980 keV, which is certainly in the ballpark of a 2039 keV event.
- A risetime much faster than the preamp will have to respond to when taking data. This risetime also needs to be appreciably faster than the 50ns response time requirement. We decide on a 10ns linear rise in the leading edge of the pulse.
- Decay constant long to give the preamp adequate time to respond to the leading edge of the pulse. The leading edge should look like a step function when viewed on the scale of 100 ns

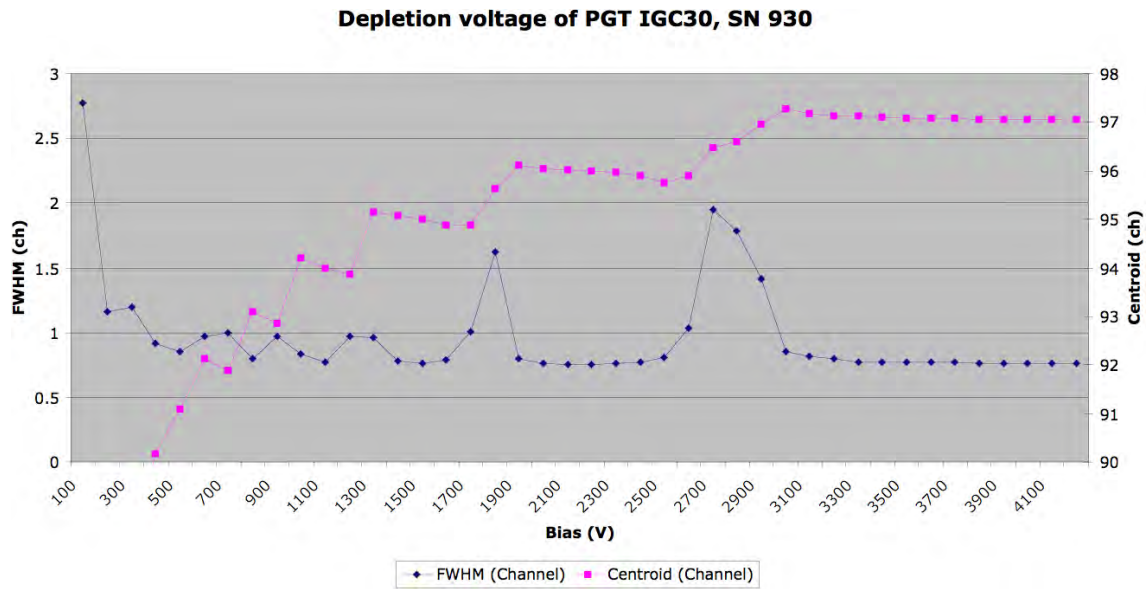


Figure B.3: Resolution and centroid curves for the PGT HPGe detector #930. The nominal depletion voltage determined by PGT is +3500 V, but the curves still relax a bit to +3900 V. We decide to run the detector at +3900 V instead of +3500 V.

or so, but should exponentially decay back to the baseline over the long term. Additionally, the pulse needs to decay to the baseline voltage before the next pulse begins. The noise on the signal is about 2 mV, and it will take 3.9 decay constants for a 100 mV pulse to fall down to 2 mV. The waveform generator, an Analogic 2045, can only store about 500,000 points in a given waveform, so we have to balance out decay length and resolution on the input pulse. After a bit of trial and error, we decide on a decay constant of 150 μ s and a time of 750 μ s between pulses.

- Smooth leading edge
- No bounce

The equation we enter in the Analogic 2045 is:

```
FOR 10n 0 FOR 10n 100m*(t/10n) FOR 750u 100*(1*e^(-1*t/150u)).
```

The resulting pulse is a flat baseline for 10 ns, followed by a linear rise to 100 mV taking 10 ns, followed in turn by an exponential decay with a time constant of 150 μ s. It is shown as the black trace shown in Figure B.1.

We next turn to the Pole/Zero settings. P/Z is used to adjust the preamp response decay back to baseline, as well as any under/overshoot of the baseline. To assure the quality of the P/Z setting, we fit the exponential decay part of the trace to a single-decay exponential with a constant offset and plot the residuals. The residuals plot should not have any discernible structure.

Finally, the preamps will have nonzero energy resolution. To determine the energy resolution of the preamps, we collect gamma rays from various sources spread out over the energy spectrum of interest and record the peak widths (see Table B.1 for the list of sources used and their largest discernable peak energies). The number of liberated charge carriers in the depletion region is proportional to the energy of the event, thus the crystal itself will have a resolution proportional to the square root of the energy. The resolution of the preamp, however, is constant. By plotting resolution versus energy, we can fit the data points to the equation

$$\sigma_{total} = \sigma_p + \sigma_c \sqrt{E} \quad (\text{B.1})$$

where σ_p is the resolution of the preamp and σ_c is the resolution of the crystal. We do not need to worry about the inherent width of the decays (*i.e.* the inverse of the half-life) because the shortest-lived isotope is ^{208}Tl , which has a half-life of about 3 minutes. This half-life gives a decay width of a little over 10^{-17} eV, which is far less than the keV resolutions we know to expect.

Table B.1: Sources for resolution measurement. This table does not show all decay peaks, just the largest ones used in the preamp resolution determination. Data comes from the Lawrence Berkeley National Laboratory.

Isotope	Half-Life	γ Energy (keV)	Decay Ratio (%)
^{26}Al	740 000 y	1808.63	99.73
^{40}K	1 277 000 000 y	1460.83	11
^{60}Co	5.2714 y	1173.237	99.9
		1332.501	99.982
^{133}Ba	10.52 y	80.997	34.06
		302.853	18.33
^{137}Cs	30.07 y	661.66	85.1
^{207}Bi	31.55 y	569.702	97.74
		1063.662	74.5
		1770.237	6.87
^{208}Tl	3.053 m	583.191	84.5
		2614.533	99

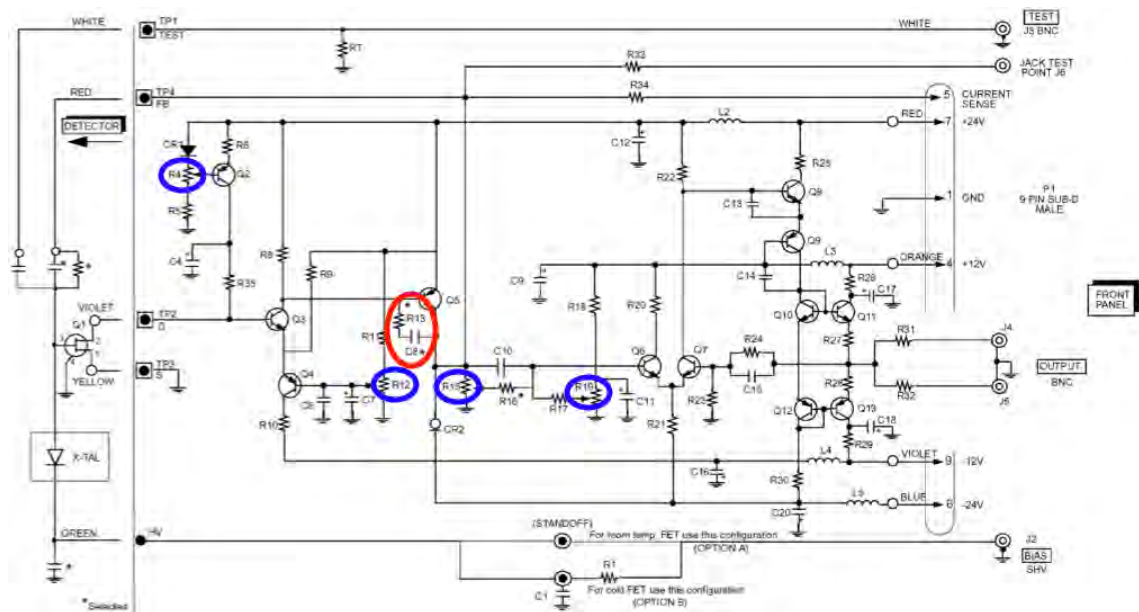


Figure B.4: Circuit diagram for the PGT RG-11B preamp. The bandwidth limiting capacitor, C8, is between stages 1 and 2 of the preamp, circled in red. The adjustment potentiometers R4 (FET current), R12 (FET voltage), R15 (Pole/Zero) and R19 (DC offset) are circled in blue.

B.6 PGT RG-11

The first task is to obtain the best trace available subject to the constraints of Sections B.2 and B.3.

The RG-11 has a bandwidth-limiting capacitor (C8, see Figure B.4) that can be swapped out to reduce the response time to below 50 ns. Unfortunately, some choices for C8 cause a sustained, 8 mV peak-to-peak, 68 MHz ripple in the response (see Figure B.5) that could not be tuned out with the FET current and voltage potentiometers, so the viable choices for C8 were limited. We tried various capacitors for C8, each time with the crystal charged to +3500 V*. What we found is that the smaller the C8, the better the response time but the worse the bounce. We therefore decided to use the largest capacitor that still gives us a response time below 50 ns, and that turned out to be a 100 pF capacitor. In addition to tuning the FET current and voltage, we also attempted to reduce the long time-scale overshoot by adjusting the Pole/Zero of the preamp. This seemed to have very little effect. Our best effort at optimizing the long time scale performance of the RG-11 (using the P/Z and DC offset) can be seen in Figure B.6.

*We had not yet run the depletion voltage curve for this crystal by the time we determined the best bandwidth-limiting capacitor, but the difference in total capacitance between +3500 V and +3900 V is negligible for this purpose.

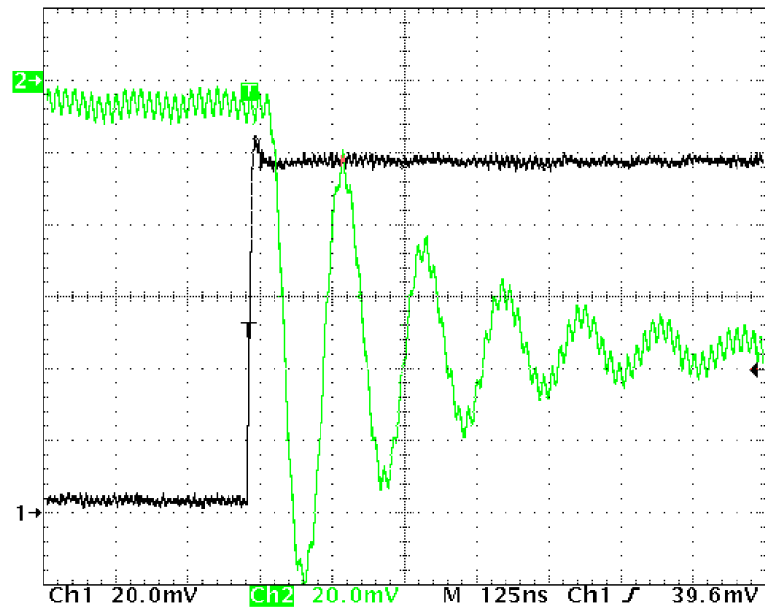


Figure B.5: The FET current and voltage had to be tuned to eliminate a sustained, fast ripple. If the bandwidth limiting capacitor were too small, the FET could not eliminate the ripple. In this case, the capacitor is 30 pF.

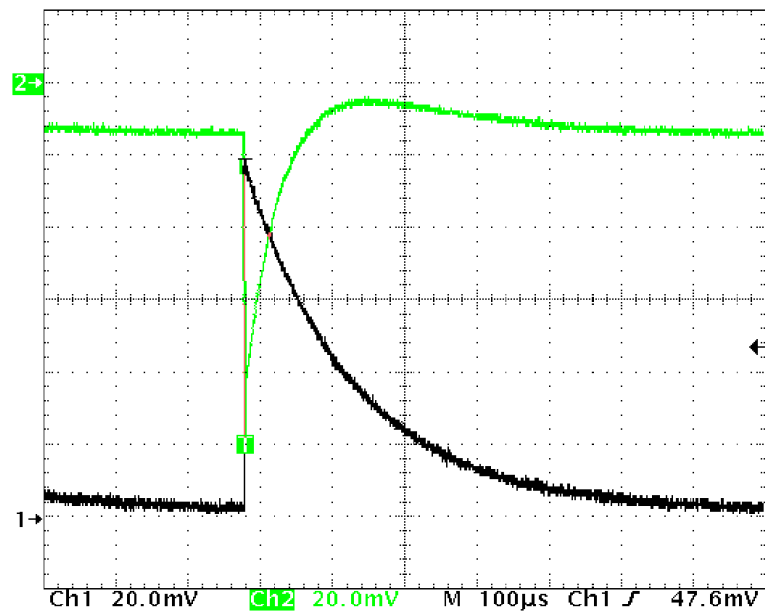


Figure B.6: Long time scale behavior of the RG-11B. The time base is 100 μ s per division.

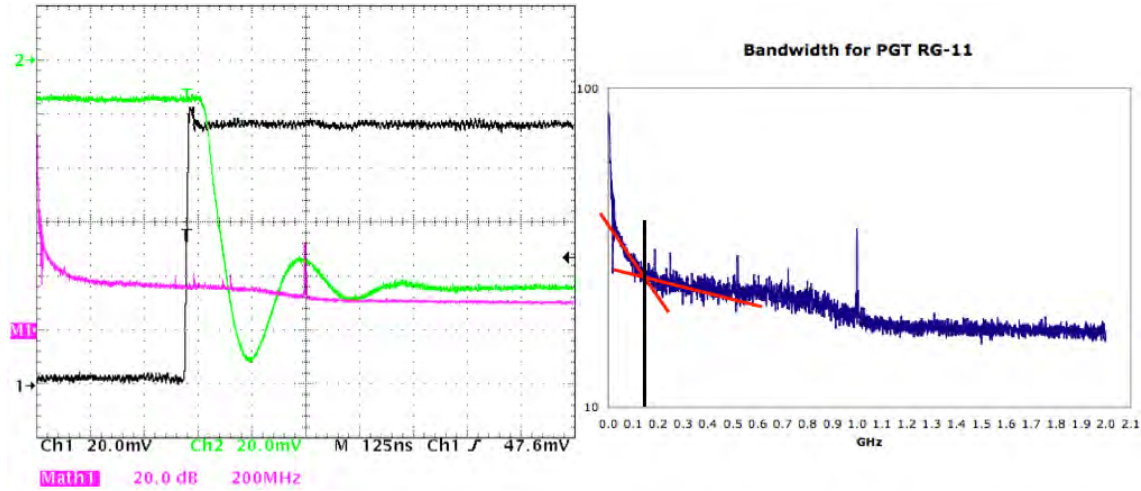


Figure B.7: In the left panel, the black trace is the input pulse, green is the RG-11 response, and purple is the FFT of the preamp response. The right panel is a log-linear re-plotting of the FFT (the purple trace in the left panel). From the FFT, we see that the preamp bandwidth is about 150 MHz.

Once we were satisfied we had appropriately tuned the preamp, we measured its performance characteristics. We used a Tektronics TDS 754D oscilloscope (sometimes known as “The Scope of the Ancients”) to make the measurements. The rise time of the input signal and the fall time of the preamp response were measured by the scope itself. Pulse height, ripple height, and ripple frequency were read directly off the RG-11 response scope trace. The left panel of Figure B.7 shows the oscilloscope-calculated measurements as well as the traces from which we read off the other values. Preamp bandwidth is determined by re-plotting the FFT of the preamp response on a log scale and determining where the $1/f$ behavior of the FFT becomes linear in f (see the right panel of Figure B.7). We measured the voltage across the drain and source of the FET (V_{DS}) by measuring the voltage across test points 2 and 3 on the preamp board. We measured the current through the FET (I_{DS}) by inserting an ammeter between test point 2 and the rest of the preamp. From these two values, we calculated the effective resistance of the FET (R_{DS}) and the power dissipated by the FET ($P_{FET} = V_{DS} \times I_{DS}$). Table B.2 summarizes these results.

We next measured the crystal/preamp response to the list of sources in Table B.1. We collected data for 60 minutes and used the 1060 keV ^{207}Bi line and the 2614 keV ^{208}Tl line to obtain the calibration equation:

$$\text{Energy} = (7.2001 \times \text{channel} - 27.907) \text{ keV} \quad (\text{B.2})$$

(See Figure B.8) The ^{137}Cs peak is missing from Figure B.8 because it exceeded the maximum

number of counts in a bin for the Canberra PHA, and the 569 keV peak of ^{207}Bi and 583 keV peak of ^{208}Tl overlapped. We collected data from ^{137}Cs and ^{208}Tl for 50 minutes, and in a separate data run from ^{207}Bi for 1 hour. We measured the FWHM of each source line and plotted them as a function of line energy. We fit equation B.1 to the data to obtain:

$$FWHM = 5.55535 + 0.000431531\sqrt{E} \quad (\text{B.3})$$

Thus the width of the preamp is $\sigma_{RG-11} = 5.55535$ keV. To find the nonlinearity of the preamp re-

Table B.2: RG-11 performance results.

Measurement	Result
Pulser Risetime	7.581 ns
Pulser Height	95 mV
Preamp Response Time	45.343 ns
Preamp Response Height	68 mV
Preamp Ripple Height	-28 to +10 mV
Preamp Ripple Frequency	4.3 MHz
Preamp Bandwidth	150 MHz
V_{DS}	1.285 V
I_{DS}	1.73 mA
$R_{Channel}$	743 Ω
P_{FET}	2.22 mW

sponse we plotted the centroid of each peak as a function of energy, and fit a second order polynomial to this data:

$$Channel = 3.911195 + 0.139203(Energy) - 1.05942 \times 10^{-7}(Energy)^2 \quad (\text{B.4})$$

Our last test of the RG-11 was to look at the exponential part of the response pulses tail (see Figure B.9) and plot the residuals:

$$Pulse = -0.00159182 - 0.0857911e^{-21139.3t} \quad (\text{B.5})$$

The residuals seem to have no structure to their shape, demonstrating a single-constant exponential decay in the preamp response.

Finally, the last relevant data point in the evaluation of the RG-11 is its cost: \$875 for each preamp in an aluminum box.

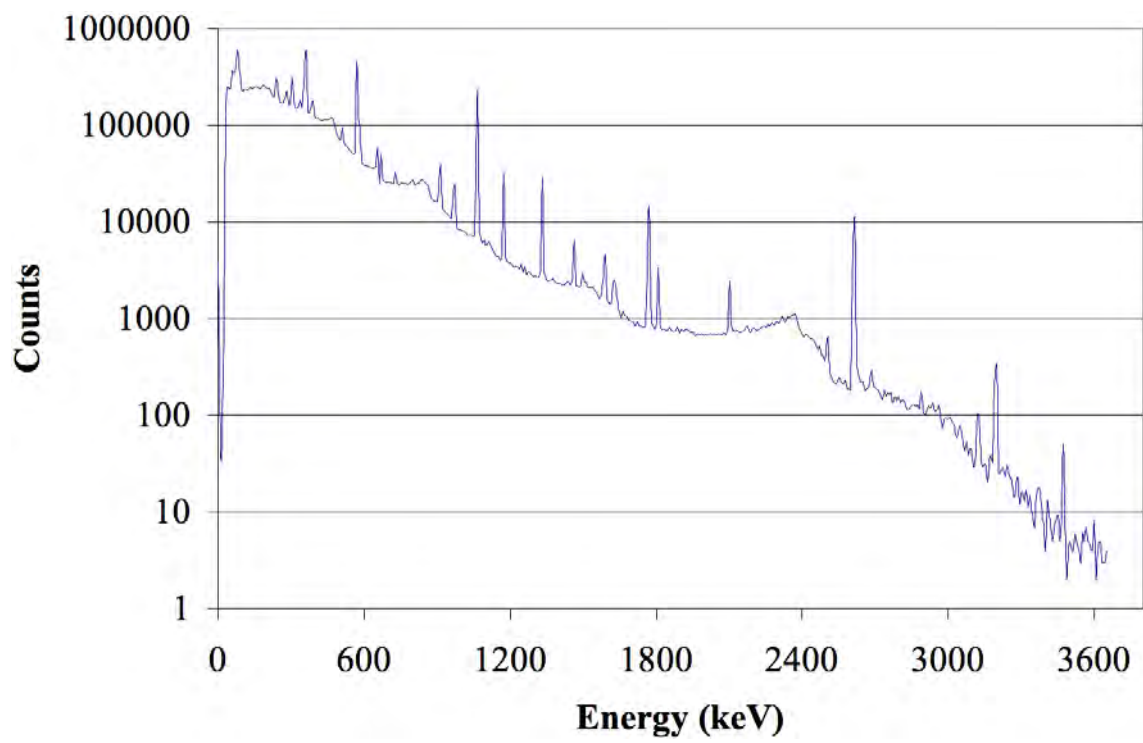


Figure B.8: Calibration Spectrum.

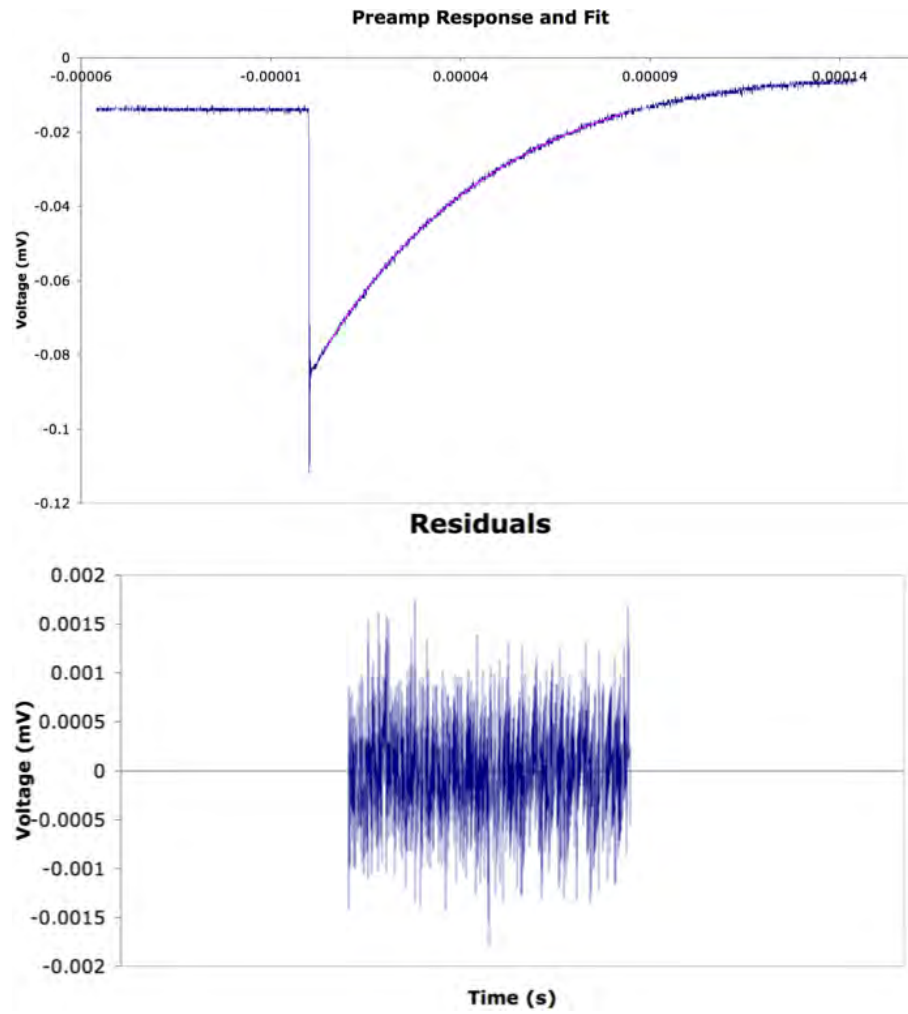


Figure B.9: RG-11 long time scale preamp response with fit and residuals.

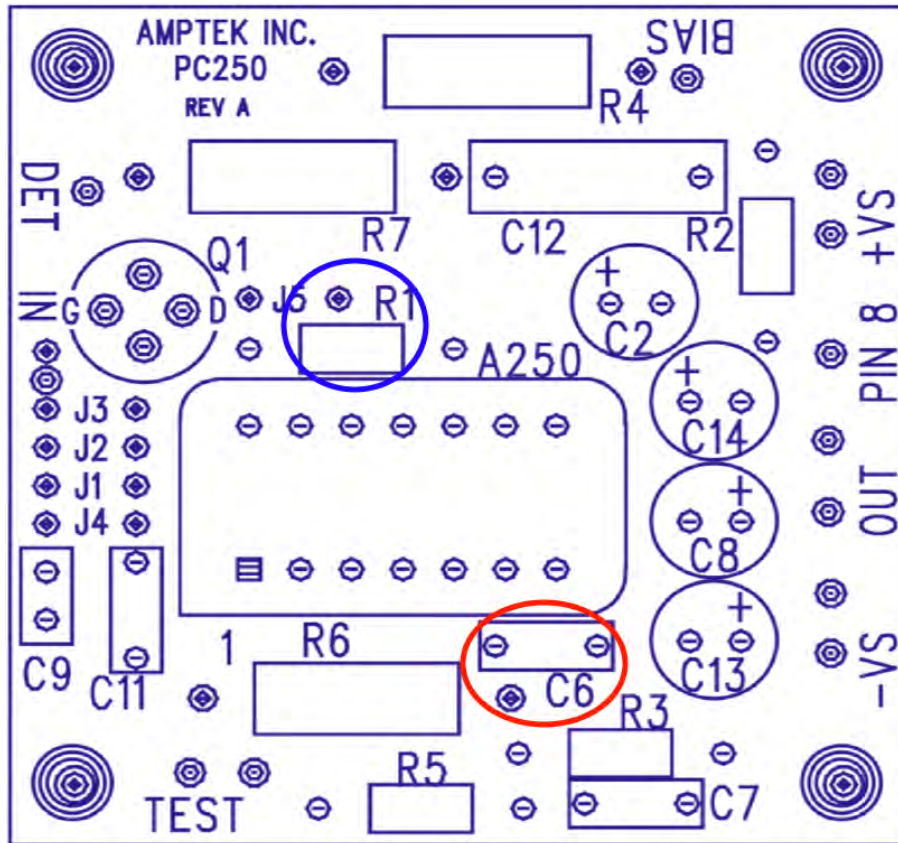


Figure B.10: Circuit diagram for the Amptek PC250 preamp motherboard. The compensation capacitor, C6 is circled in red. The adjustment potentiometer, R1 is circled in blue.

B.7 Amptek A250

As with the PGT RG-11, the first task is to obtain the best preamp response subject to the constraints of Sections B.2 and B.3.

Our A250 did not come from Amptek with bandwidth-limiting components. So, after some trouble with high frequency ($> 10 - 100$ MHz) noise, it became necessary to add a “compensation capacitor” at location C6 (see Figure B.10). Using similar criterion to those in our evaluation of the RG-11 (general noise suppression constrained by response time less than 50 ns), we selected a compensation capacitor value of 5 pF.

After selecting a compensation capacitor, we adjusted R1 (see Figure B.10), and took our standard battery of measurements. The requisite scope traces are in Figure B.11.

We then measured our systems response to the radioactive sources in Table B.1. It is now

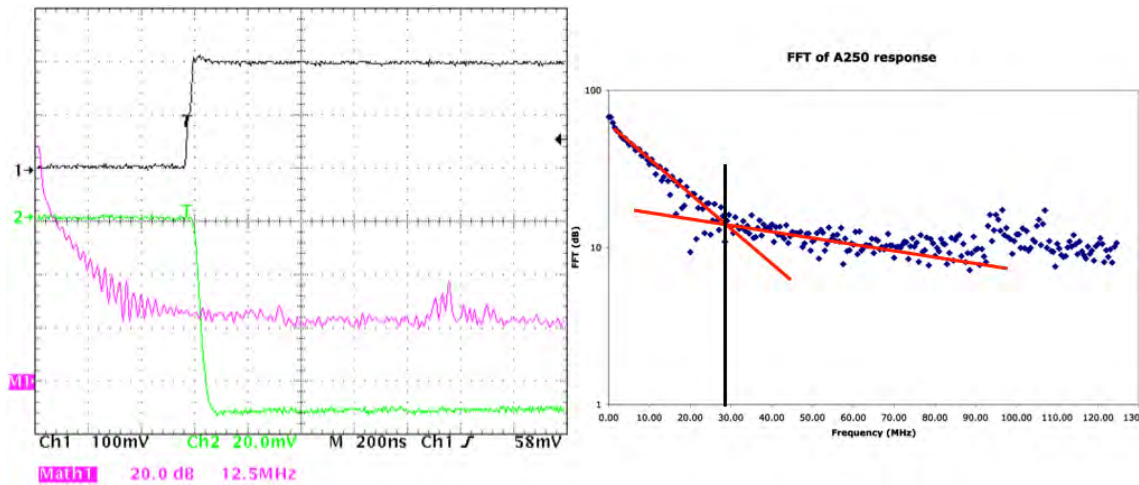


Figure B.11: Left: best trace of the A250 preamp. The black trace is the input pulse, green is the A250 response, and purple is the FFT of the preamp response. Right: log-linear plot of the FFT from the left panel of this figure. From the graph, the preamp bandwidth is read to be ≈ 29 MHz.

necessary to point out that when we evaluated the A250, we used the XIA DGF4C digital data acquisition system to collect our source data (as opposed to the Canberra analog PHA). The DGF4C system has much finer energy resolution than the Canberra system, so some of the calibration numbers will be quite different from those for the RG-11. From our source data, we obtained the calibration equation:

$$Energy = (0.069138 \times channel + 0.186247) \text{ keV} \quad (\text{B.6})$$

We also plotted FWHM for each line source and fit the results to obtain:

$$FWHM = (44.8881 + 0.0391275 \times \sqrt{channel}) \text{ channels} \quad (\text{B.7})$$

Leaving us with a preamp width of 44.8881 DGF4C channels, or (from the slope of the calibration equation) $\sigma_{A250} = 2.88464$ keV. We fit a quadratic to our calibration data to get the nonlinearity:

$$Energy = -0.111373 + 0.0601563 \times channel - 1.00874 \times 10^{-9} \times channel^2 \quad (\text{B.8})$$

Finally, the fit to the exponential response part of the pulse is:

$$V = -0.348906 - 0.05546466e^{-208.846 t} \quad (\text{B.9})$$

This, in turn, gives us a decay constant of $\tau = 4.788$ ms. Happily, there is no apparent temporal structure, demonstrating a single-constant exponential response.

Last, the A250 costs approximately \$500 per preamp, and \$200 per motherboard.

Table B.3: A250 performance results.

Measurement	Result
Pulser Height	200 mV
Preamp Response Time	45.77 ns
Preamp Response Height	72 mV
Preamp Ripple Height	0 mV
Preamp Ripple Frequency	N/A
Preamp Bandwidth	29 MHz
V_{DS}	???
I_{DS}	???
$R_{Channel}$???
P_{FET}	???

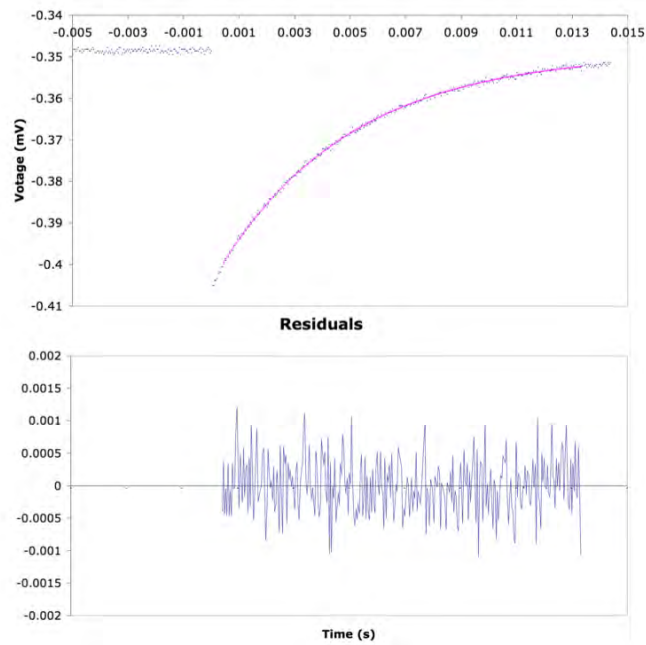


Figure B.12: A250 long time scale preamp response with fit and residuals.

Appendix C

SCINTILLATION LIGHT OUTPUT STUDIES IN CONNECTION TO ALTERNATIVE DESIGNS OF THE MOON $\beta\beta$ DECAY EXPERIMENT

Some of the content of this appendix is discussed briefly in Section 2.4.6. We reproduce it here for the sake of completeness because this is the form of the original write up of this work when it was performed in 2002 and 2003.

C.1 Introduction

The MOON (Molybdenum Observatory Of Neutrinos) experiment is actually designed to be two experiments running concurrently. The first is a neutrinoless double beta decay experiment (*i.e.* to measure the half life of the reaction $^{100}\text{Mo} \rightarrow ^{100}\text{Ru} + 2\beta^- + 0\nu$). The second experiment is designed to measure the flux of neutrinos from external sources (specifically supernovae and the solar p-p reaction) using the scattering of these external neutrinos via the weak interaction with ^{100}Mo . There are several pressing issues to be considered in the design of the MOON. Among these are: scintillation light output, energy resolution, spatial resolution, and detector cleanliness. Aside from a brief discussion of detector cleanliness as a motivation in the next section, we will focus on light output and energy resolution.

C.1.1 Why Liquid Scintillators?

The current design of the MOON experiment involves sandwiching thin layers of Molybdenum foil between large blocks of plastic scintillator. A concept drawing and prototype of this design can be seen in Figure C.1. This design has the advantage of being able to effectively add as much molybdenum as we want by simply making the experiment larger. The main problem with this design is that the many thin layers lead to huge surface areas. These surfaces, in turn, need to be kept clean. This challenge becomes even more daunting when we take into account the fact that half of the surface area consists of plastic scintillator, which can acquire an electric charge thereby attracting contaminants, including dust and radon decay daughters. At CENPA, we have been investigating an alternative to the plastic scintillator/foil sandwich design that may avoid a few of its contamination issues. We have been investigating the possibility of dissolving an organo-

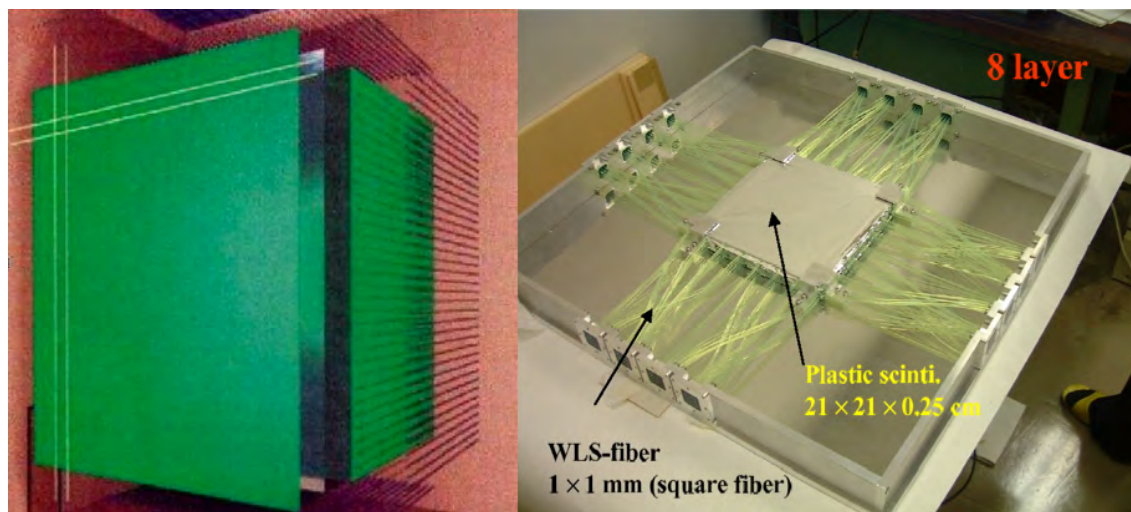


Figure C.1: A concept drawing (left) and prototype of the detector for the MOON neutrino experiment.

metallic compound in an organic liquid scintillator. The fact that our scintillator would be in liquid form would allow us to carefully refine it, and building the tank in the shape of a sphere would allow us to minimize the ratio of surface area to volume, leaving us with less surface area to clean. This design too, has its problems to be overcome. Most notable of these, is finding a combination scintillator/solvent and molybdenum-based solute with a sufficiently high concentration. This has also been addressed by our group, but is not the focus of this document. We will instead focus on the secondary issues of light output and energy resolution.

C.2 Scintillation Light Output

C.2.1 Scintillator Solutions

Throughout the course of this study we have been focused on five common liquid scintillators: benzene, toluene, xylene (actually a mixture of the three different xylene isomers), pseudocumene (PC), and methylnaphthalene (MN). As for organo-molybdenum compounds, we tried: molybdenum carbonyl ($\text{Mo}(\text{CO})_6$), bis(acetylacetonato)-dioxomolybdenum (BAADOM), molybdenum trioxide (MoO_3 —not actually organic, but it is inexpensive, and comparatively non-toxic), and several molybdates (compounds including molybdenum-based poly-atomic ions). We prepared supersaturated solutions of each solute in each solvent, and then spun them in a centrifuge to remove from solution any of the solute that had not actually dissolved. We then measured the concentration of

Mo for each solute/solvent pair using flame atomic absorption (FAA) techniques. Having now measured the solubility of each solute in each solvent and observing the solutions over time to check on stability, we selected the best combination, and tested its light output. This mixture was $\text{Mo}(\text{CO})_6$ in toluene.

C.2.2 Calibration Sources and Fit Techniques

To test the light output of the metal-loaded organic liquid, we require a standard candle. For this, we chose two industry standard liquid scintillators: BC505 from Bicron (based on PC), and a toluene-based liquid scintillator from Aldrich. We were also concerned that the fluors added to liquid scintillators would change the solubility of the Mo compounds in our solutions. We wanted to be able to add the fluors after the Mo, so we needed to perfect our own “recipe” for liquid scintillators based on these five organic molecules. To do this, we also tested the light output of our own “home-brewed” liquid scintillators after adding 2,5-Diphenyloxazole (PPO) and 1,4-Bis(5-phenyloxazol-2-yl)benzene (POPOP) to the base solvents in amounts in accordance with the guidelines in Chapters 3 and 10 of Reference [27]. All in all, we tested the light output of eight different liquid scintillators: our two standard candles, five home-brewed scintillators, and one Mo-loaded toluene solution.

We then took four different radioactive spectra with our eight liquid scintillator mixtures: three γ – ray sources (^{137}Cs , ^{207}Bi , ^{241}Am —usually considered an α source, but it also has a γ line at 59.6 keV). The most useful data came from the two γ sources even though we were only able to measure Compton spectra from them. This was a result of the spectral lines of our two sources (660 keV for ^{137}Cs and 570 keV and 1060 keV for ^{207}Bi) having too high an energy to get a photoelectron peak in our scintillator cell (the γ energies of our sources were much too high to stop in our cell) and too low an energy to create e^+/e^- pairs. For a more detailed discussion, see Chapter 10 of Reference [99].

An “ideal” Compton spectrum (i.e. one measured using a detector with perfect resolution) should have a sharp cutoff corresponding to the maximum energy of an electron scattered by an incoming γ ray of a specific energy. There is a nice discussion of how to calculate the ideal Compton spectrum in Reference [112]. Obviously, any real data will have a less than perfect cutoff. By fitting a Gaussian to the nonzero part of the Compton spectrum above the nominal cutoff energy, we can estimate both the location of the cutoff in our data, and the resolution of the detector. The data were taken using a photo-multiplier tube (PMT)-based scintillation counting setup shown schematically in Figure C.2. The output of the PMT was fed into a multi-channel analyzer residing in the data acquisition computer. The spectrum files were then converted to simple two-column ASCII text files

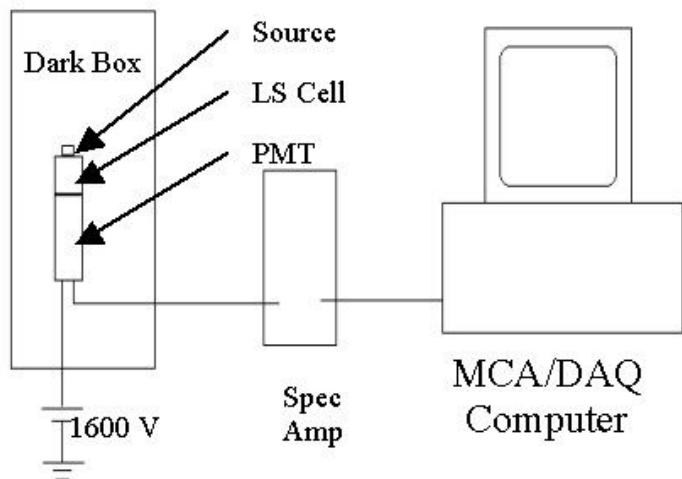


Figure C.2: Scintillation counting setup diagram.

(one column for channel number and the other for counts at that channel). Once we had the data in such a portable format, we used the fitting routines in the “ROOT” analysis software to make the fits. The Gaussian fits had three parameters: overall amplitude, mean and standard deviation.

Since the γ ray is of low energy, it is possible to obtain a photoelectron peak for the ^{241}Am source. We therefore tried fitting Gaussian functions to these spectra. These numbers have little meaning on an absolute scale because the energy of the photo-peak is low enough that the noise in our detector makes a good fit very difficult. The results of the photo-peak fits are, however, meaningful for the relative values of light output and resolution.

C.2.3 Results

The best Compton spectrum cutoff fits we got came from the ^{137}Cs line and the higher energy ^{207}Bi line. The fits for the resolution (σ , not FWHM) from the lower energy ^{207}Bi line were all too high because the cutoff from the lower energy Compton spectrum was blended into the beginning of the one from the higher energy line. Still these are of similar value to the ^{241}Am photo peak fits—meaningless on an absolute scale, but very nice for comparing relative values. Tables of all of these results are included in this appendix.

From the ^{137}Cs line and the high-energy ^{207}Bi line, the Mo-loaded toluene had approximately

Table C.1: Scintillation output results for ^{137}Cs , $E_\gamma = 660$ keV.

Solution	Cutoff (ch)	Cutoff (% BC505)	σ (ch)	σ (% cutoff)
BC505	986.0 ± 18.7	100.0	52.9 ± 6.8	5.4
Com. Toluene	959.8 ± 24.0	97.3	62.0 ± 8.7	6.5
Benzene	498.8 ± 45.5	50.6	72.3 ± 13.2	14.5
Toluene	705.6 ± 30.7	71.6	78.7 ± 12.6	11.2
Xylenes	602.2 ± 44.0	61.1	89.9 ± 14.1	14.9
Pseudocumene	605.5 ± 37.9	61.4	76.9 ± 14.2	12.7
Methylnapthalene	218.7 ± 36.7	22.2	51.7 ± 13.9	23.7
Mo(CO) ₆ in Tol.	425.3 ± 34.3	43.1	68.2 ± 10.9	16.0

Table C.2: Scintillation output results for ^{207}Bi , $E_\gamma = 570$ keV. Note that no fit was possible for the standard candles with this spectral line.

Solution	Cutoff (ch)	Cutoff (% Tol.)	σ (ch)	σ (% cutoff)
BC505	—	—	—	—
Com. Toluene	—	—	—	—
Benzene	383.1 ± 63.9	68.3	103.5 ± 38.3	27.0
Toluene	561.2 ± 57.4	100.0	121.3 ± 36.9	21.6
Xylenes	468.1 ± 61.7	83.4	122.0 ± 42.7	26.1
Pseudocumene	449.7 ± 72.6	80.1	125.4 ± 42.9	27.9
Methylnapthalene	160.2 ± 98.4	28.5	64.6 ± 166.2	40.4
Mo(CO) ₆ in Tol.	326.6 ± 43.7	58.1	92.6 ± 29.4	28.4

60% and 40% respectively of the light output of BC505. As far as energy resolution, the Mo-loaded toluene had roughly 16% at 660 keV from the ^{137}Cs source (compared to 5.3% in BC505), and 9.4% at 1060 keV from the ^{207}Bi (compared to 3.5% for BC505). In both cases the resolution was approximately three times worse in the Mo-loaded toluene than in the BC505. The results for all of the scintillators but the standard candles from the low energy γ line in ^{207}Bi are consistent with these results. We could not get a Gaussian fit for this using line the standard candles because the high-energy Compton spectrum was strong enough to obscure the low-energy cutoff. Interestingly, for all the spectral lines, MN had by far the worst performance of any of the scintillator mixtures. This is one reason that we have yet to extensively test the light output of any BAADOM solutions, since it was most soluble in MN. The results from the ^{241}Am source were quite similar. The Mo-

Table C.3: Scintillation output results for ^{207}Bi , $E_\gamma = 1060$ keV.

Solution	Cutoff (ch)	Cutoff (% BC505)	σ (ch)	σ (% cutoff)
BC505	1225.3 ± 37.0	100.0	42.7 ± 37.2	3.5
Com. Toluene	1221.6 ± 68.2	99.7	60.4 ± 23.5	4.9
Benzene	891.8 ± 60.0	72.8	67.5 ± 30.8	7.6
Toluene	1062.5 ± 40.3	86.7	58.4 ± 20.2	5.5
Xylenes	1020.0 ± 122.6	83.2	71.9 ± 58.7	7.0
Pseudocumene	991.9 ± 111.4	80.9	68.6 ± 49.7	6.9
Methylnaphthalene	413.1 ± 40.7	33.7	88.2 ± 20.6	21.4
Mo(CO) ₆ in Tol.	756.9 ± 111.5	61.8	71.0 ± 60.8	9.4

Table C.4: Scintillation output results for ^{241}Am , $E_\gamma = 59.6$ keV.

Solution	Peak Energy (ch)	Energy (% BC505)	σ (ch)	σ (% cutoff)
BC505	123.1 ± 1.3	100.0	29.7 ± 2.0	24.1
Com. Toluene	103.2 ± 1.7	83.8	25.8 ± 2.0	25.0
Benzene	56.0 ± 1.5	45.5	15.3 ± 1.6	27.4
Toluene	78.4 ± 0.7	63.7	20.9 ± 1.2	26.6
Xylenes	65.5 ± 2.3	53.2	17.9 ± 2.9	27.4
Pseudocumene	63.8 ± 0.9	51.8	18.5 ± 1.4	29.0
Methylnaphthalene	25.0 ± 2.3	20.3	10.4 ± 17.9	41.6
Mo(CO) ₆ in Tol.	42.5 ± 2.1	34.5	15.5 ± 2.1	36.5

loaded toluene had 34.5% of the light output of BC505, but the resolutions were much closer: 36.5% and 24.1% at 59.6 keV, respectively. This is possibly due to the fact that the ^{241}Am photo peaks were nearly at the bottom of the MCA operating range.

Whether the Mo-loaded liquid scintillator we tested will be adequate in terms of light output and energy resolution is still largely undecided. The resolutions we were able to measure were at much lower energies than $Q_{\beta\beta}$ for ^{100}Mo (3.034 MeV). The highest energy we were able to characterize was the Compton cutoff for the 1.06 MeV γ -ray line in our ^{207}Bi source at 206 keV. Therefore to answer the question more definitively, we would need to characterize the scintillators at energies more comparable to 3.034 MeV. To do this, we would need to perform these tests in a much larger test cell instrumented with more PMTs to boost the efficiency for capturing higher energy events.

VITA

Vic Gehman has been a graduate student at UW since the fall of 2001. He spent his first two years of grad school in Seattle completing the usual cannon of coursework, and then took a position as a Graduate Research Assistant at Los Alamos National Laboratory in August of 2003. There, he has continued his work on the MAJORANA Experiment, focusing on characterizing possible systematic effects in MAJORANA and designing the calibration plan for the experiment. Of particular interest to him, has been ways to improve the efficacy of and characterize the uncertainty in pulse shape and segmentation analysis. Now that he has completed his dissertation work, he will continue on at LANL as a Postdoctoral Research Associate, splitting his time between dark matter and double-beta decay research.